Large-scale Vertical Velocities in the Global Open Ocean via Linear Vorticity Balance

Diego Cortés Morales

THESE DE DOCTORAT
DE SORBONNE UNIVERSITE

Spécialité: Océanographie Physique

Ecole Doctorale: 129 - Sciences de l'Environnement d'Ile de France

réalisée au

Laboratoire d'Océanographie et du Climat Expérimentale et Approche Numérique

pour obtenir le grade de

Docteur de Sorbonne Université

Large-scale Vertical Velocities in the Global Open Ocean via Linear Vorticity Balance

présentée par

Diego CORTÉS MORALES

Soutenance prévue le 11 Janvier devant le jury composé de :

Rapporteur	Remi TAILLEUX	Reading University
Rapporteur	Stéphanie BARRILLON	MIO, Marseille
Présidente du jury	Sabrina SPEICH	ENS, Paris
Examinateur	Jonathan GULA	LOPS, Brest
Examinateur	Hervé GIORDANI	Météo France, Toulouse
Directeur de thèse	Alban LAZAR	LOCEAN, Paris
Co-Advisor de thèse	Juliette MIGNOT	LOCEAN, Paris
Co-Advisor de thèse	Diana RUIZ PINO	LOCEAN, Paris

Abstract

At oceanic basin scales, vertical velocities are several orders of magnitude smaller than their horizontal counterparts, setting a formidable challenge for their direct measurement in the real ocean. Therefore, their estimations need a combination of observation-based datasets and theoretical considerations.

Historically, scientists have employed various techniques to estimate vertical velocities across different scales constrained by the available observations of their time. Various approaches have been attempted, ranging from methods utilizing *in-situ* horizontal current divergence to those based on intricate omega-type equations. However, the Sverdrup balance has captured the attention of researchers due to its robust and straightforward description of ocean dynamics. The linear vorticity balance (LVB), expressed as $\beta v = f\partial_z w$, constitutes one of the fundamental components of the Sverdrup balance. Unlike the former balance, the LVB provides information along the vertical dimension at any depth, establishing a connection between vertical movement and the meridional transport above. This balance serves as the cornerstone of this thesis.

In order to advance on the theoretical prospect of estimating the vertical velocities, we first identified the annual mean climatological circulation in linear vorticity balance within an eddy-permitting Ocean General Ciruclation Model (OGCM) simulation. Initially, this analysis was conducted over the North Atlantic Ocean and subsequently expanded to encompass the entire global ocean, focusing on larger scales than 5°. The analysis revealed the feasibility of computing vertical velocities beneath the mixed layer using the LVB approach across large fractions of the water column in the interior regions of tropical and subtropical gyres and within some layers of the subpolar and austral circulation. Departures from the LVB were observed in the western boundary currents, strong zonal tropical flows, subpolar gyres and smaller scales due to the nonlinearities, mixing and bathymetry-driven contributions to the vorticity budget.

The extensive validity of the LVB in the global ocean provides a relatively simple foundation for estimating the vertical velocities through the indefinite depth-integrated LVB. In the OGCM, the w estimates accurately reproduce the time-mean amplitude and interannual variability of the vertical velocity field within substantial portions of the global ocean. Accordingly, we build the OLIV3 (Observation-based Linear Vorticity ocean Vertical Velocities estimates) w product applying observation-based geostrophic velocities from ARMOR3D to the indefinite depth-integrated LVB formalism, with wind stress data from ERA5 serving as boundary condition at the surface. This product contains annual-mean vertical velocities spanning the global upper ocean at 5° horizontal resolution and 40 isopycnal levels during the 1993-2018 period.

A comparative analysis between the OLIV3 product and four alternative products, including one OGCM simulation, two reanalyses and an omega-equation observation-based reconstruction, is conducted using various metrics assessing the multidimensional features of the ocean vertical flow. In the subtropical gyres and Eastern tropical gyres, where the LVB holds as a valid assumption, the OLIV3 product demonstrates a remarkable ability to replicate the baroclinic structure of the upper ocean, exhibiting satisfactory spatial consistency and notable agreement in terms of temporal variability when compared to the two reanalyses and the OGCM simulation. However, further investigation is required for its use by the scientific community.

Keywords: Vertical Velocities, Linear Vorticity Balance, Sverdrup Balance, Data Product

Résumé

À l'échelle des bassins océaniques, les vitesses verticales présentent des valeurs nettement inférieures à celles des vitesses horizontales, imposant ainsi un défi considérable en ce qui concerne leur mesure directe dans l'océan. Par conséquent, leur évaluation nécessite une combinaison d'ensembles de données observationnelles et de considérations théoriques. Diverses méthodes ont été tentées, allant de celles qui se fondent sur la divergence du courant horizontal in situ à celles qui reposent sur des équations complexes de type oméga. Cependant, l'équilibre de Sverdrup a attiré l'attention des chercheurs, y compris la nôtre, en raison de sa description robuste et simple de la dynamique des océans. L'équilibre de vorticité linéaire (LVB), exprimé par $\beta v = f\partial_z w$, constitue l'une des composantes fondamentales de l'equilibre de Sverdrup. La LVB fournit des informations sur la dimension verticale à chaque profondeur, établissant un lien entre le mouvement vertical et le transport méridien. Cet équilibre constitue la pierre angulaire de cette thèse.

Afin de progresser dans la perspective théorique de l'estimation des vitesses verticales, nous analysons la circulation climatologique moyenne annuelle avec l'équilibre de vorticité linéaire au sein d'une simulation de modèle de circulation générale océanique (OGCM) eddy-permitting. Au départ, cette analyse a été effectuée dans la région de l'océan Atlantique Nord, puis étendue à l'ensemble de l'océan mondial, en mettant l'accent sur des échelles supérieures à 5°. L'analyse a révélé la faisabilité du calcul de vitesses verticales robustes sous la couche de mélange en utilisant l'approche LVB pour de grandes fractions de la colonne d'eau dans les régions à l'interieur des gyres tropicaux et subtropicaux, ainsi que dans certaines couches de la circulation subpolaire et australe à des échelles de temps annuelles et interannuelles. Des déviations par rapport à la LVB se produisent dans les courants de la frontière occidentale, les flux tropicaux zonaux forts, les gyres subpolaires et les échelles plus petites en raison des non-linéarités, des mélanges et des contributions au bilan de vorticité induites par la bathymétrie.

L'étude de la validité de la LVB dans l'océan global fournit une base relativement simple pour l'estimation des vitesses verticales à travers de la LVB intégrée indéfinie en profondeur. Dans l'OGCM, les estimations de w ont la capacité de reproduire avec précision l'amplitude temporelle moyenne et de la variabilité interannuelle des vitesses verticales dans des portions substantielles de l'océan global. En conséquence, nous construisons ici le produit OLIV3 (Observation-based Linear Vorticity ocean Vertical Velocities estimates) dérivé des vitesses géostrophiques ARMOR3D basées sur des observations et appliquées à la LVB intégrée indéfinie en profondeur, avec les données de forçage du vent ERA5 comme conditions limites à la surface. Ce produit contient des vitesses verticales moyennes annuelles couvrant l'ensemble de l'ocean supérieur globale à une résolution horizontale de 5° et 40 niveaux isopycnaux pendant la période 1993-2018.

Une analyse comparative entre le produit OLIV3 et quatre autres produits de vitesse verticale, comprenant une simulation OGCM, deux réanalyses et une reconstruction basée sur des observations appliquées à l'équation oméga, est proposée. Diverses métriques sont utilisées pour évaluer les caractéristiques multidimensionnelles de la circulation verticale de l'océan. Dans les gyres subtropicaux et tropicaux d'est, où la LVB est une hypothèse valide, le produit OLIV3 démontre une capacité remarquable à reproduire la structure barocline de l'océan, présentant une cohérence spatiale satisfaisante et un accord notable en termes de variabilité temporelle lorsqu'il est comparé aux deux réanalyses et à la simulation OGCM. Cependant, des études complémentaires sont nécessaires pour son utilisation par la communauté scientifique.

Mots-clés: Vitesse Verticales, Balance de Vorticité Lineaire, Balance de Sverdrup, Produit de Données

Acknowledgements

I express my sincere gratitude to my advisors, Alban Lazar and Diana Ruiz Pino, for the invaluable opportunity to pursue my passion for oceanography in Paris. Their guidance not only nurtured my scientific skills in data analysis and visualization but also honed my transversal abilities in administrative management, project applications, event organization of scientific seminars and workshops, which are essential for a successful scientific career. I extend my appreciation to Juliette Mignot, whose involvement in the supervision team in early 2023 significantly contributed to advancing and completing this thesis within the established deadlines.

I would like to acknowledge to my thesis jury members, Remi Tailleux and Stephanie Barrillon, to accept to be part of it and for dedicating their time and expertise to read, correct, and improve this thesis manuscript. I also extend my gratitude to Sabrina Speich, Hervé Giordani, and Jonathan Gula for their invaluable support during the thesis defense. I also want to thank my thesis committee members, Jonathan Gula, Josep Lluis Pelegrí, and Gilles Reverdin, for their scientific interest and insightful discussions. I am particularly grateful to Jonathan Gula for the two-month invitation to UCLA, where I had the opportunity to delve into the mathematical aspects of the full vorticity equation.

I would like to express my sincere gratitude to Jean Marc Molines for providing the NEMO OCCITENS simulation data, which formed the backbone of this thesis, and for sharing his codes for post-processing the model outputs. I would like to acknowledge the discussions that have helped for the advancement of the thesis and explored new perspectives shared by Gurvan Madec, Francesco d'Ovidio, Serge Janicot, Julie Deshayes, Francis Codron, and Pascale Bouruet-Aubertot from LOCEAN and outside it, Remi Tailleux, Andrea Doglioli, Stephanie Barrillon, Robin Waldman, Mara Freilich, Maike Sonnewald, Jim McWilliams, Jeroen Molemaker, Han Lei, Bruno Buongiorno Nardelli, Alexander Haumann, Florian Sevellec, Bárbara Barcelló Llull, Irene Polo, Marta Martín Rey, and particularly to Belén Rodriguez Fonseca, whose encouragement was critical in pursuing this PhD project. I also wish to express my appreciation to the former master's students, Siny Ndoye and Philippe Estrade, whose prior work during the past decade on this exciting topic laid the foundation for my thesis.

This thesis has received a LEFE MERCATOR funding in the framework of the LVBW-3Dclim project which has advocated about the importance of the topic presented in this thesis, allowed us to present our work outside the French borders in four scientific congresses (EGU2022, AGU2022, EGU2023 and PIRATA-TRIATLAS2023), organise one workshop in LOCEAN and visit UCLA (USA).

I am also thankful to all the direction and staff of the LOCEAN for their kind and friendly welcoming, their moral support, and for providing a comfortable environment to work and collaborate. I would also like to extend my gratitude to the Doctoral School, particularly to its management team, for their consistent support and guidance throughout this journey.

I would like to thank to all my colleagues at the laboratory who accompanied me throughout these three years and three months, sharing moments of laughter and support. Without their support, this thesis would not have been possible. I am particularly grateful to my roommate, Angel García Gago, for the support, meaningful conversations, and wonderful moments we shared during this project. I couldn't have asked for a better roommate. Finally, I reserve my deepest thanks for my family, including mamá, papá, abuela, David, Rodri, Claudia, and Sansón. Their unwavering support, strength, trust, patience, and sacrifices have been my driving force.

And what if one of the gods does wreck me out on the wine-dark sea? I have a heart that is inured to suffering and I shall steel it to endure that too. For in my day I have had many bitter and painful experiences in war and on the stormy seas. So let this new disaster come. It only makes one more.

— Homer, *The Odyssey*

Contents

List of Figures

List of Tables

Acronyms

AC Açores Current. 34

ADCP Acoustic Doppler Current Profiler. 2

BPT Bottom Pressure Torque. 10, 48, 56, 160

BVB Barotropic Vorticity Balance. 8, 10, 50, 56, 160

CC Canary Current. 34

CROCO Coastal and Regional COmunity model. 24, 105

DIVB Depth-Integrated Vorticity Balance. ix, 160

ECMWF European Center for Medium-Range Weather Forecasts. 18

ECCO Estimating the Circulation and Climate of the Ocean. xiii, xiv, 20, 81, 82, 84–97, 99, 101, 104

ERA-Interim ECMWF Re-Analysis -Interim. 18

ERA5 ECMWF Re-Analysis v5. xiii, 19, 20, 81, 83, 103

GLORYS GLobal Ocean ReanalYsis and Simulations. xiii, xiv, 20, 81, 82, 84, 86–89, 91, 94, 95, 97, 99, 101, 104

GLVB Geostrophic Linear Vorticity Balance. xi, 43, 44, 104

IDILIV Indefinite Depth-Integrated LInear Vorticity. viii, xiii, xiv, 13, 15, 17, 19, 20, 46, 61, 62, 69, 71, 74, 76–79, 81–86, 88, 89, 91, 95–101, 103, 105, 108, 109

IDILIV3 Indefinite Depth-Integrated LInear Vorticity Vertical Velocities Estimates. xiv, xv, 17, 21, 65, 72, 91, 94, 95, 97, 98, 100, 101, 105

LONM Level Of No Motion. 9, 11, 59, 101, 105

LONVM Level Of No Vertical Motion. 9, 12

LVB Linear Vorticity Balance. vii–xiv, 11, 12, 14, 15, 17, 23–25, 29, 35, 37, 39, 41, 43–59, 62, 70, 71, 73–75, 77–79, 81, 82, 84, 85, 87, 91, 93, 95–98, 101, 103, 104, 106, 107, 109, 110, 158, 161

MDT Mean Dynamic Topography. 19

MLD Mixed Layer Depth. xv, 18, 168

NECC North Equatorial Counter Current. 34

NEMO Nucleus for European Modelling of the Ocean. 18, 20, 87, 104

OCCIPUT Oceanic-Chaos-Impacts,Structure,Predictability. 18

OGCM Ocean General Circulation Model. viii, 15, 20, 24, 25, 69, 81, 83

OLIV3 Observation-based Linear Vorticity Vertical Velocities estimates. vii, ix, xiii–xv, 15, 17, 19–21, 81–101, 103–108, 171

QG Quasi Geostrophic. 6, 7, 21

R Correlation coefficient. 107

SOFAR Sound Fixing And Ranging. 2

RMSE Root Mean Squared Error. 65, 89, 98, 100, 107

SEC Southern Equatorial Current. 51

SECC Southern Equatorial Counter Current. 51

SLA Sea Level Anomaly. 5, 19, 20

SPG Subpolar Gyre. 42–44, 49, 56, 59, 62, 78

SQG Surface Quasi Geostrophic. vii, 7

SSH Sea Surface Height. 3, 30

SSS Sea Surface Salinity. 19

SST Sea Surface Temperature. 5, 19, 20

STG Subtropical Gyre. xii–xiv, 42, 43, 49, 54, 56, 64, 72, 86–89, 92, 98, 100, 108

TG Tropical Gyre. 42, 46, 51, 54, 72

TWI Thermal Wind Imbalance. 6

WBC Western Boundary Current. 54, 62, 78, 96–98, 104–106

WOA World Ocean Atlas. vii, 3

WOCE World Ocean Circulation Experiment. vii, 3, 4

Eppur si muove (And yet it does moves)

— Galileo Galilei *apocriphal, 1633*

1 Introduction

1.1 Importance of Understanding the Oceanic Vertical Velocity Field

Vertical movements in the ocean constitute a fundamental element for understanding the ocean's dynamics. They are critical mechanisms for the exchange of various properties between (and within) the ocean's interior and the surface in continuously interacting with the atmosphere. These mechanisms encompass the transfer of essential components such as heat, salinity, CO_2, oxygen, and nutrients (Leach, 1987; Fischer et al., 1989). Furthermore, the vertical velocity (w) contributes to shaping the intricate patterns of the ocean's thermohaline circulation, which is recognised as a primary driver of global carbon cycle and Earth's climate variability (Klein and Lapeyre, 2009; Mahadevan, 2016; DeVries et al., 2017). The vertical flow also plays a crucial role in driving the deep ocean circulation. Notable examples of deep ocean vertical velocity include its role in the Stommel theory[1] (Stommel, 1948) and its impact as a necessary element in maintaining the balance when the viscosity is considered (Munk, 1966).

The dynamical processes occurring within the thermocline are of particular importance. This layer of the water column represents the transitional zone between the wind-driven flow of the upper ocean and the circulation patterns within the intermediate, deep and abyssal oceans (Poole and Tomczak, 1999). Vertical exchanges of water masses within the upper ocean have a regulatory role in the air-sea interactions, including heat fluxes and carbon sequestration, often referred to as the "physical carbon pump" (Iudicone et al., 2011; Iudicone et al., 2016). In addition, the mesoscale and submesoscale vertical exchanges significantly influence the functioning of marine ecosystems. Subduction processes, for instance, ventilate the thermocline, alter the water mass characteristics of the ocean's interior, and impact the ocean's biogeochemistry (Freilich and Mahadevan, 2021). Furthermore, primary production in the ocean and the horizontal distribution of phytoplankton and its chlorophyll biomass are strongly influenced by near-surface mesoscale and sub-mesoscale upwelling (Bubnov, 1987; Lévy et al., 2005). Vertical movements within the thermocline also control the marine "biological carbon pump" through the injection of nutrients from deeper layers into the surface euphotic zone and the organic matter export out of the euphotic zone (e.g. Siegel et al., 2016; Freilich and Mahadevan, 2019; Uchida et al., 2019; Yang et al., 2021).

[1] Stommel theory equation: $\beta V = \hat{\mathbf{k}} \cdot \nabla \times (\tau^{wind}/\rho_0) + \hat{\mathbf{k}} \cdot \nabla \times (\tau^{bot}/\rho_0)$

Despite these insights, the comprehensive effects of mesoscale vertical motions on biochemical tracer budgets, water mass transformations and upwelling/downwelling processes remain largely uncharted territory. In the intermediate and deep oceans, vertical motions are associated with diverse processes, each characterised by distinct dynamics and magnitudes. These processes include internal waves and three-dimensional turbulent motions characterised by high-frequency and small-scale non-geostrophic flows occurring at spatiotemporal eddy scales (e.g., Polzin et al., 1997; D'Asaro et al., 2007; Waterman et al., 2013; Sheen et al., 2013) and near-bottom frictional Ekman currents along sloping topographic boundaries (e.g. Garrett et al., 1993). Additionally, mesoscale eddy flows along sloping isopycnals contribute to driving vertical flows (e.g. Marshall and Speer, 2012; Freilich and Mahadevan, 2019).

Since the pioneer study of Stommel and Arons (1959) on deep vertical velocities, numerous equations have been developed to estimate this key component of the ocean dynamics, leading to the present-day four-dimensional reconstruction of vertical velocities through the omega equation (Buongiorno Nardelli et al., 2018; Buongiorno Nardelli, 2020). Nevertheless, this methodology still has limitations, as it relies on parameterisations and assumptions in the three-dimensional flow. Consequently, the basin-scale view of the ocean's vertical flow remains one of the open questions of physical oceanography. Therefore, the primary objective of the thesis is to address this open question by studying an alternative, simpler, and more easily interpreted formalism for estimating the vertical velocity field over the global ocean. First, our study of w will enhance our understanding of ocean circulation and its controlling factors, providing valuable insights into ocean circulation theories. Second, the alternative and reliable estimate of observation-based ocean w will serve as the foundation for assessing and comprehending the vertical exchanges of mass and tracers in the global ocean. These exchanges play a pivotal role in regulating the Earth's climate. It is thus imperative to examine their effects, particularly in a world experiencing escalating greenhouse gas concentrations and temperatures.

1.2 Complexities of Vertical Velocity Field Characterisation

While the importance of vertical velocities in shaping the oceans has been recognised for decades, directly measuring the ocean's vertical circulation has proven to be a formidable challenge. This challenge arises primarily because of the extremely weak vertical velocity field associated with large-scale ocean circulation. It is on the order of magnitude of 10^{-5} m s^{-1} near the surface, decreasing to 10^{-6} within the thermocline, and reaching 10^{-7} - 10^{-8} m s^{-1} in the ocean interior, several orders of magnitude smaller than those of the horizontal velocity field (e.g. Stommel and Arons, 1959; Schott and Stommel, 1978). Given that the Earth's rotation and the ocean's stratification place significant constraints on the large-scale motions, there is a strong variation in the amplitude of the vertical velocity field across scales. Literature estimates of oceanic vertical velocities span nearly four orders of magnitude, depending on the specific spatial scale under consideration. Consequently, except for experiments relying on processing Lagrangian neutrally buoyant RAFOS (Sound Fixing And Ranging (SOFAR) spelt backwards), Acoustic Doppler Current Profiler (ADCP)s, or the new Sentinel V (ADCP that includes an additional fifth vertical beam alongside the classical four) acquiring fine-scale vertical velocities in the order of 10^{-2} - 10^{-4} m s^{-1} (e.g., Bower and Rossby, 1989; Song et al., 1995; Rossby, 2016; D'Asaro et al., 2018; Comby et al., 2022), direct observations of vertical velocities are limited.

Operational oceanography is built upon analysing the spatiotemporal distribution of the parameters that characterise the state of the ocean. In theory, the vertical velocity field could be derived from measurements, particularly for the physical components of the system, which typically include temperature and salinity (density), pressure and horizontal velocities. However, a fundamental challenge in estimating the time-varying ocean circulation stems from the need for more observations even with current technology. The scarcity is primarily sue limitations in resolution, coverage and technology (Wunsch, 2015). These issues reflect our limited understanding of boundary layer dynamics and incomplete parameterisation of processes occurring at the unresolved scales, such as turbulent mixing, diffusion, and submesoscale phenomena (e.g. Hamlington et al., 2014; Canuto, 2015; Bachman et al., 2017; Li et al., 2017). Moreover, forecasting the ocean circulation is complicated by the inherently nonlinear nature of the equations governing the system, which typically require numerical solutions.

1.3 *In-Situ* Ocean Observation: Methods and Variables

Approaches with the goal of retrieving the three-dimensional mesoscale dynamics solely grounded on observations have received limited attention until now. This is primarily due to the constraints in the resolution of the available observation-based data and the challenges associated with estimating geostrophic horizontal velocities solely from thermohaline and altimetry measurements. Researchers must navigate the complexity of dynamical models, the required computational resources, *a priori* statistical information and assumptions, and the quantity and quality of available data. Satellite-based remote sensing of Sea Surface Height (SSH), together with temperature and salinity measurements, can offer valuable insights into ocean circulation through geostrophic dynamics (Jones et al., 1998; Hausmann and Czaja, 2012; Reul et al., 2014; Rio et al., 2016). Nonetheless, despite the global coverage of remote sensing observations, they only provide a surface picture of the ocean. To enhance our understanding of the ocean, it becomes imperative to implement *in-situ* observational efforts. This includes profiling and surface drifters, CTDs, expendable bathythermographs (XBTs), moorings, and current meters, which furnish real-time, *in-situ* global temperature, salinity, and horizontal velocity vertical profiles.

1.3.1 World Ocean Atlas (WOA) and World Ocean Circulation Experiment (WOCE)

The history of subsurface open-ocean observations is relatively brief. It begins with the pioneering voyage of the *HMS Challenger*, which aimed to collect temperature and salinity data in the open ocean, spanning from the surface water to the ocean's interior (Wyville Thomson and Murray, 1885a; Wyville Thomson and Murray, 1885b).

The temperature and salinity measurements from the entire history of physical oceanography have been assembled by Levitus (1982) as a function of position and depth. This enormous effort has become one of the most commonly used global climatology in the ocean interior and has subsequently been refined and enlarged in the World Ocean Atlas (first produced in 1994) and its latest form WOA23 (Locarnini et al., 2023; Reagan et al., 2023). The World Ocean Circulation Experiment (WOCE) in the 1990s aimed to improve the understanding of the oceans' role in the climate system by combining *in-situ* measurements, including those from ships of opportunity, with satellite SSH (Thompson et al., 2001). WOCE was primarily designed to produce the first truly global, time-evolving estimate of the circulation, including the scarce

current meter records that would serve as the main reference for defining the major ocean phenomena (Siedler et al., 2013). The most significant technical advance during WOCE was the development of a neutrally buoyant float known as Autonomous Lagrangian Circulation Explorer (ALACE) (Davis, 1991; Davis et al., 1992). Additionally, WOCE provided an impetus for the systematic global use of moorings and also brought changes in our approach to data handling, leading to rapid data reporting, internationally accepted quality control standards and the open exchange of observational data.

This project eventually led to the implementation of a global network of automatic Argo profilers, which are now a mainstay of our observing network.

1.3.2 Argo Floats

Building upon the knowledge garnered during the final decade of the 20th century from WOCE, the Argo program (http://www.argo.ucsd.edu/) was born as a global initiative involving the deployment and maintenance of an array of floats by an international consortium comprising contributions from more than 30 nations. This collaborative effort has established a comprehensive global ocean climate monitoring network (Roemmich et al., 1999). Argo's primary objective is to measure the physical properties of the global ocean. Floats within this network are programmed to park at a depth of 1000 decibars for a 10-day interval, after which they adjust their buoyancy to dive to 2000 decibars and ultimately ascending to the sea surface. Argo floats measure the vertical structure of temperature and salinity during the ascent phase until they reach the sea surface. The data are subsequently sent to a land station via a satellite, and the floats return to their initial depth, repeating this 10-day drift and profiling cycle (Freeland, 2013).

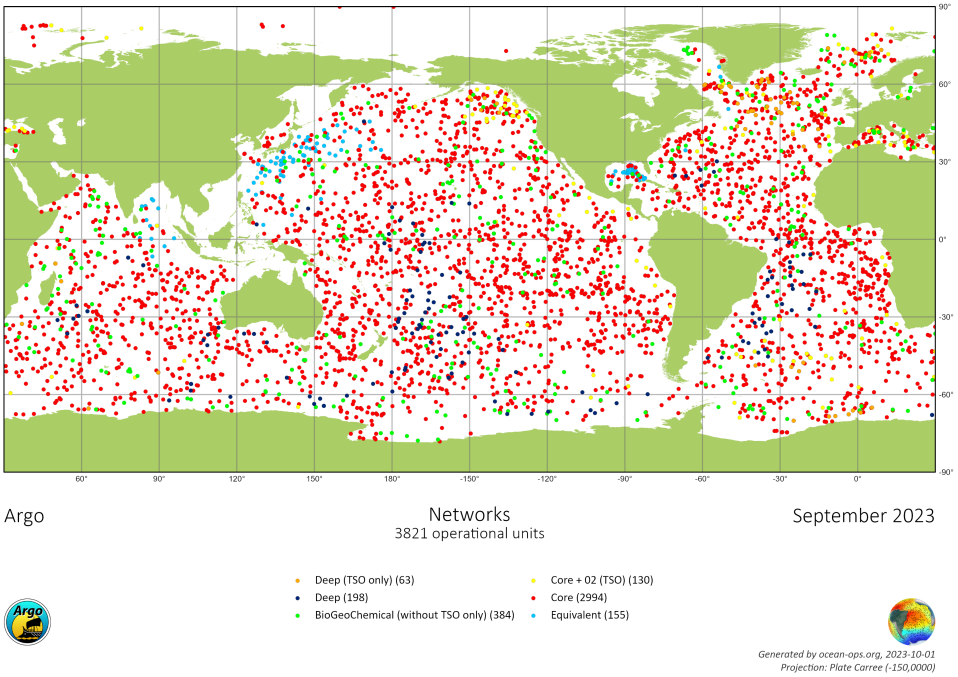

Figure 1.1: Operational units of Argo program at October 1st, 2023. Source: https://argo.ucsd.edu/about/status/.

The deployment of Argo floats began in 1999, but it was not until 2007 that the network reached its goal of 3000 active floats operating at the same time, simultaneously achieving a nearly uniform spatial distribution over the ocean. Today, despite the presence of close to 4000 active floats (see Figure 1.1),

certain regions of the ocean, such as the Northern Hemisphere Western Boundary Currents, exhibit an overabundance of floats, while others, like the Arctic and Antarctic Oceans, continue to have poor spatial coverage (Wong et al., 2020). As a result, efforts are required to deploy additional floats (Smith et al., 2019; Wilson et al., 2019).

Acknowledging the global coverage provided by remote sensing observations, along with the available *in-situ* vertical profiles of temperature and salinity, Guinehut et al. (2012) pioneered the development of a 4D gridded estimate of the ocean's state (ARMOR3D). Their approach involved merging remote sensing observations, including Sea Surface Temperature (SST) and Sea Level Anomaly (SLA), with *in-situ* temperature and salinity vertical profiles obtained from instruments such as XBTs, CTDs, moorings and Argo floats. In particular, the temperature and salinity fields in the ARMOR3D dataset (Guinehut et al., 2012), based on *in-situ* and satellite observations, allowed for the computation of the geostrophic velocity field using the thermal wind equation (Mulet et al., 2012)[2]. **The geostrophic meridional transport and an observation-based wind stress dataset are used in this study to estimate the global vertical motions of the real ocean under the assumption of Linear Vorticity Balance (Chapter 5).**

1.4 Previous Efforts in Vertical Velocity Field Estimation

The reconstruction of geostrophic velocities, derived from observed thermohaline fields, in conjunction with data collected from current meters, expands the possibilities for connecting the three components of ocean circulation. However, the capabilities offered by the available observations at specific times throughout the observations' history are intrinsic to the evolution and progression of the various approaches for estimating the vertical velocity field.

Numerous early estimations of w were conducted utilising profiles of tracer measurements applied to tracer fluxes (e.g. Stommel and Arons, 1959; Robinson and Stommel, 1959; Wyrtki, 1961; Munk, 1966; Wunsch, 1984) or the application of mooring and profile measurements of horizontal currents to the continuity equation[3] (Stommel and Schott, 1977; Schott and Stommel, 1978; Wyrtki, 1981; Roemmich, 1983; Bubnov, 1987; Halpern and Freitag, 1987; Halpern et al., 1989; Weingartner and Weisberg, 1991). These studies reached a consensus regarding the order of magnitude of the various ocean layers ranging from 10^{-5} m s^{-1} near the surface, gradually decreasing to 10^{-6} m s^{-1} within the thermocline, and reaching values between 10^{-7} and 10^{-8} m s^{-1} in the intermediate and deep oceans. Yet, while the vertical velocity field can be diagnosed from the horizontal velocity divergence using vertical integral in standard primitive equation numerical models, this approach does not apply to observation-based data at global scales. This limitation arises from the scarcity of current measurements available and the potential for prominent instrumental errors when computing the divergence from measured horizontal velocities. One example of retrieving the vertical flow from observations via continuity equation is presented by Freeland (2013), who calculated a single observation-based w value at 700 decibar within an approximately 25x20° region, assuming a null vertical flow at the surface. Over the last decade, researchers have explored alternative approaches for assessing large-scale baroclinic vertical velocities. These alternative methods include the use of observations of isopycnal displacement (Giglio et al., 2013; Christensen et al., 2023), moorings

[2] This geostrophic velocity field is provided in the ARMOR3D dataset

[3] $\partial_x u + \partial_y v + \partial_z w = 0$, where u, v and w are the three components of the flow

data applied to the momentum and density equations (Sévellec et al., 2015) and biogeochemical tracers (Garcia-Jove et al., 2022). More theoretical approaches have just now gained more attention, including using the Bernoulli function to estimate w (Tailleux, 2023).

1.4.1 Omega equation

A widely used indirect approach for diagnosing vertical velocities involves the utilisation of the Quasi Geostrophic (QG) omega equation:

$$f^2 \frac{\partial^2 w}{\partial z^2} + \nabla_h (N^2 \cdot \nabla_h w) = 2\nabla_h \cdot Q \tag{1.1}$$

where N^2 is the Brunt-Väisäla frequency, f is the Coriolis parameter, w is the vertical velocity and Q the Hoskin Q-vector:

$$Q = \frac{g}{\rho_0}\left(\frac{\partial v_g}{\partial x}\frac{\partial \rho}{\partial y} + \frac{\partial u_g}{\partial x}\frac{\partial \rho}{\partial x}, \frac{\partial u_g}{\partial y}\frac{\partial \rho}{\partial x} + \frac{\partial v_g}{\partial y}\frac{\partial \rho}{\partial y}\right) \tag{1.2}$$

with g the gravitational acceleration, u_g the geostrophic velocity and ρ the density, originally developed to study atmospheric frontogenesis (Holton, 1973; Hoskins and Draghici, 1977; Hoskins et al., 1978). The Q-vector approach used in this theory was derived from the concept of Thermal Wind Imbalance (TWI):

$$f\partial_z \boldsymbol{u} - (g/\theta_0)\partial_{y,x}\theta = f\partial_z \boldsymbol{u}_{ag} \tag{1.3}$$

wherw $\boldsymbol{u}_{ag}$ are the ageostrophic horizontal currents.

In the QG case, the ageostrophic motion is crucial to restore the thermal wind balance that the geostrophic motion tends to balance. By measuring the three-dimensional fine-scale density field, researchers in the late 20th and early 21st centuries quantified the upper-ocean vertical circulation using the QG omega equation over limited areas (e.g. Tintoré et al., 1991; Pollard and Regier, 1992; Rudnick, 1996; Allen et al., 2001; Nardelli et al., 2001; Gomis et al., 2001; Garabato et al., 2001; Rodriguez et al., 2001). Notably, the omega equation has the advantage of being a diagnostic equation. As a result, a single snapshot is sufficient to determine the vertical motion at a certain time. However, this equation demands a fine spatial discretisation involving spatial derivatives along all three spatial dimensions and assumptions about the vertical flow at the boundaries.

In recent years, further efforts have been made to compute the w field using the omega equation. These efforts involve updating the Q-vector to account for processes that were neglected in the original QG methodology while maintaining the Hoskins framework (e.g., Sanz and Viúdez, 2005; Nagai et al., 2006; Giordani et al., 2006), as demonstrated in studies by Buongiorno Nardelli et al. (2018); Ruiz et al. (2014); Ruiz et al. (2019); Tzortzis et al. (2021) and Buongiorno Nardelli (2020). Buongiorno Nardelli et al. (2018); Buongiorno Nardelli (2020) managed to reconstruct a 4D ocean state vertical velocity field (OMEGA3D) at a 0.25° horizontal spatial and weekly resolutions, combining *in-situ* observations and satellite data (ARMOR3D; Mulet et al., 2012; Guinehut et al., 2012) within the thermocline. Their findings indicated good agreement, at first order, in the subtropical band, particularly away from upwelling areas in the tropical band, when compared to other w simulations and reanalyses. However, the QG mesoscale and submesoscale vertical velocity field derived from the ARMOR3D fields could be underestimated due

to the smoothing applied to these ARMOR3D fields (Pascual et al., 2014; Barceló-Llull et al., 2016; Mason et al., 2017). Unfortunately, the lack of independent temperature, salinity and geostrophic velocity *in-situ* observations has hindered further studies.

1.4.2 Surface Quasi Geostrophic (SQG) equation

Continuing with the QG theory, Lapeyre and Klein (2006) started a different line of research based on the expected QG (Blumen, 1978; Held et al., 1995) behaviour of mesoscale motions. It proposes that the three-dimensional flow can be decomposed into a Surface Quasi Geostrophic (SQG) contribution associated with surface density anomalies, and an interior contribution that does not consider the density anomalies at the surface but considers the potential vorticity changes in the ocean interior. In this framework, the SQG depends primarly on the surface density anomaly and stratification, with the associated stream function decreasing with depth. Satellite observations of SST can be used to estimate this contribution to the flow, which proves valuable for estimating surface circulation. The SQG approach has been widely employed in various studies to reconstruct the upper-ocean three-dimensional physical ocean properties, including the vertical velocity field. Notable works attempting to reproduce the vertical flow from SQG using numerical simulations include studies by Klein et al. (2009); Ponte and Klein (2013); Wang et al. (2013); Qiu et al. (2020). Additionally, LaCasce and Mahadevan (2006) provides an estimation of the vertical flow using satellite and in-situ observed data. While the w field can be determined by the density and the characteristics of the basin-scale stratification as demonstrated by previous literature, it is noted that the SQG methodology applies solely to the upper layers (above 500 m), and only to circulation associated with dynamical structures exhibiting a signature at the ocean surface (Lapeyre and Klein, 2006). Furthermore, while the reproduced amplitudes are reasonably accurate, an observation-based study by Mahadevan (2016) has revealed that the reconstructed w field exhibits weak values compared to the flow patterns reproduced by primitive equations.

1.5 Vertical Velocity Estimation via Linear Vorticity Balance

The two complex methods for estimating vertical velocities, the QG omega equation and the SQG, require establishing vertical and lateral boundary conditions. This involves making assumptions about the vertical velocity field at these boundaries. To pursue a simpler approach for describing the vertical flow, we propose to go back to the fundamental principles of physical oceanography with the continuity and momentum equations, which serve as a diagnostic, mathematical instrument for constraining the relation between horizontal and vertical flow within the ocean.

1.5.1 Equations of Motion: Navier-Stokes and Continuity Equation

Starting with the Navier-Stokes equations (Pedlosky, 1979) under Boussinesq approximation and the continuity equation provides a comprehensive description of the ocean dynamics. From here, we simply the equations by disregarding phenomena at scales and in regions of secondary interest, which reduces the complexity of the ocean system to a level that aligns with the desired requirements.

$$\frac{\partial u}{\partial t} + \boldsymbol{u}\nabla u - fv = -\frac{1}{\rho}\frac{\partial p}{\partial x} + \frac{1}{\rho}\left[\frac{\partial \tau_{xx}}{\partial x} + \frac{\partial \tau_{xy}}{\partial y} + \frac{\partial \tau_{xz}}{\partial z}\right] + \vartheta\nabla^2 u \tag{1.4}$$

$$\frac{\partial v}{\partial t} + \boldsymbol{u}\nabla v + fu = -\frac{1}{\rho}\frac{\partial p}{\partial y} + \frac{1}{\rho}\left[\frac{\partial \tau_{yx}}{\partial x} + \frac{\partial \tau_{yy}}{\partial y} + \frac{\partial \tau_{yz}}{\partial z}\right] + \vartheta\nabla^2 v \tag{1.5}$$

$$\frac{\partial u}{\partial x} + \frac{\partial v}{\partial y} + \frac{\partial w}{\partial z} = 0 \tag{1.6}$$

The $\boldsymbol{u}$ represents the three-dimensional velocity field, with u, v, and w being the zonal, meridional and vertical components, respectively, f denotes the Coriolis parameter, ρ the reference density, and p the pressure at each depth. τ_{ij}, where i and j are any x, y, and z, represent the Reynolds stress tensor components, and ϑ is the kinematic viscosity. The Reynolds stress tensor components can be described as:

$$\tau_{xx} = 2\rho A_h \frac{\partial u}{\partial x};\ \ \tau_{yy} = 2\rho A_h \frac{\partial v}{\partial y} \tag{1.7}$$

$$\tau_{xy} = \tau_{yx} = \rho A_h \left(\frac{\partial v}{\partial x} + \frac{\partial u}{\partial y}\right) \tag{1.8}$$

$$\tau_{xz} = \rho A_v \frac{\partial u}{\partial z} + \rho A_h \frac{\partial w}{\partial x};\ \ \tau_{yz} = \rho A_v \frac{\partial v}{\partial z} + \rho A_h \frac{\partial w}{\partial y} \tag{1.9}$$

A_h and A_v represent the horizontal and vertical turbulent viscosity coefficients.

1.5.2 A Depth-Integrated Ocean

Numerous researchers have examined the Barotropic Vorticity Balance (BVB) to address the various dynamic regimes in the ocean interior. To derive this equation, the curl of depth-integrated momentum equations (Eq. 1.4 and 1.5) is taken (Hughes and De Cuevas, 2001):

$$\underbrace{\frac{\partial \Omega}{\partial t}}_{\substack{\text{time}\\ \text{rate}}} = \underbrace{-\nabla\cdot(f\overline{\boldsymbol{u}_h})}_{\substack{\text{planetary}\\ \text{vorticity}\\ \text{advection}}} + \underbrace{\hat{\mathbf{k}}\cdot\nabla\times\frac{\tau^{wind}}{\rho_0}}_{\text{wind curl}} - \underbrace{\hat{\mathbf{k}}\cdot\nabla\times\frac{\tau^{bot}}{\rho_0}}_{\substack{\text{bottom}\\ \text{drag curl}}} + \underbrace{\frac{\mathbf{J}(P_b,h)}{\rho_0}}_{\substack{\text{bottom}\\ \text{pressure}\\ \text{torque}}} + \underbrace{\hat{\mathbf{k}}\cdot\nabla\times(\overline{\boldsymbol{u}_h}\cdot\nabla)\overline{\boldsymbol{u}_h}}_{\substack{\text{nonlinear}\\ \text{advection}}} + \underbrace{\hat{\mathbf{k}}\cdot\nabla\times(A_h\nabla^2\overline{\boldsymbol{u}_h})}_{\substack{\text{horizontal}\\ \text{diffusion}}} \tag{1.10}$$

In this equation, the overbar corresponds to a vertically integrated variable, $\Omega = \partial_x\bar{v} - \partial_y\bar{u}$ denotes the barotropic relative vorticity, $\boldsymbol{u}_h$ is the horizontal velocity field, and τ^{wind} and τ^{bot} are, respectively, the wind and bathymetry stress at the upper and lower ocean interface. $\frac{\mathbf{J}(P_b,h)}{\rho_0}$ is the Jacobian of the bottom pressure (P_b) and the bathymetry (h).

Considering only the planetary vorticity advection and wind curl terms of Eq. 1.10, the Sverdrup balance can be recovered. Sverdrup introduced the first dynamical interpretation of oceanic gyres (Sverdrup, 1947). His theory is based on the balance between the beta effect induced by meridional transport, and the curl (vertical vorticity) of the turbulent momentum stress at the ocean surface by the winds:

$$\beta \bar{v} = \hat{\mathbf{k}} \cdot \nabla \times \frac{\tau^{wind}}{\rho_0} \tag{1.11}$$

where β is the meridional gradient of f: $\partial_y f$.

Sverdrup, 1947 assumes that *"the horizontal velocities and the horizontal pressure gradient must vanish at a moderate depth below the sea surface"*. Therefore, the Sverdrup theory relies on the existence of a level of no motion (LONM).

Despite its fundamental contribution to the understanding of ocean dynamics, the extent to which the Sverdrup balance accurately describes the observed global ocean circulation has only received scarce attention. One primary reason for the scarcity of analyses of the Sverdrup balance is the limited availability of subsurface velocity observations until the last decade.

Various observational and modelling studies have exmined the applicability of Sverdrup balance in describing the tropical and subtropical open ocean circulation. Many of these underscore the importance of the assumptions in formulating the Sverdrup balance. Both the existence and localisation of a level of no vertical motion (LONVM), as well as the linearity of the ocean vorticity balance are necessary for closing the vorticity budget within the framework of the Sverdrup balance (Roemmich and Wunsch, 1985; Wunsch and Roemmich, 1985; Lu and Stammer, 2004; Zhang and Vallis, 2007; Wunsch, 2011; Hausmann and Czaja, 2012; Gray and Riser, 2014; Thomas et al., 2014; Yeager, 2015). Nevertheless, there was no *a priori* reason to assume that the flow could not reach the ocean floor. The assumption that the horizontal velocities and pressure gradient must vanish in the ocean interior was mainly justified by the resulting circulation patterns.

Several studies employing models, reanalyses, and hydrographic-based data have proposed that the Rossby waves propagating from the eastern boundary play a fundamental role in establishing the Sverdrup circulation in the ocean interior. The fastest waves are barotropic (with time scales ranging from hours to months), quickly establishing a barotropic interior flow mode (Willebrand et al., 1980; Andres et al., 2011; Andres et al., 2012). Subsequently, the first baroclinic mode wave, having time scales spanning years to decades (Tailleux and McWilliams, 2001), confines the Sverdrupian flow to the thermocline (Anderson and Gill, 1975; Anderson and Killworth, 1977; Williams et al., 2014; Forget and Ponte, 2015). Outside the tropical and subtropical latitudes, the Rossby wave phase velocities are slower than the background flow velocity (decreasing from approximately 10^{-5} m s^{-1} within the tropical band to less than 10^{-6} m s^{-1} at high latitudes (Killworth et al., 1997). Indeed, at extratropical and subpolar latitudes, the wind-stress changes occur faster than the ocean adjustment and break the Sverdrup balance (Hughes and De Cuevas, 2001). This ocean response to the atmospheric forcing raises a pertinent question regarding the appropriate period for testing the validity of the Sverdrup balance. While Sverdrup (1947) and most oceanographic textbooks suggest that the Sverdrup balance emerges after averaging over some years, they do not specify a specific duration. In contrast, some authors (e.g., Niiler and Koblinsky, 1985; Vivier

et al., 1999) chose to investigate the Sverdrup balance time dependence. These studies, with a focus on time scales smaller than a month, demonstrated that the surface and subsurface signals are out-of-phase, requiring the removal of the Rossby wave contribution at the surface to achieve equilibrium.

Hence, below the tropical and subtropical thermocline, as well as in regions such as high latitudes and the western boundary regions, where no level of no motion exists, the Sverdrup balance does is no longer applicable. Breaking down the BVB equation (Eq. 1.10) provides an understanding of how the idealised Sverdrup balance case can be affected by topography, pressure or a specific circulation regime.

The terms of the BVB involving planetary vorticity advection, wind curl and bottom drag curl (second, third and fourth terms in Eq. 1.10) illustrate the classical Stommel theory equation (Stommel, 1948). The Stommel theory considers a flat-bottom ocean with a significant influence on the water column. The bottom forcing is applied through the bottom friction stress ($\hat{\mathbf{k}} \cdot \nabla \times \tau^{bot}/\rho_0$), which in their theory can be parameterised by a linear drag, and it should drive the return meridional flow. The Stommel model effectively accounted for the east-west asymmetry within the subtropical gyres due to a changing Coriolis parameter with latitude and flow intensification at the western boundaries. Later, Munk (1950) argued that the ocean flow does not reach the ocean bottom. This study considers that the drag is not an appropriate descriptor, and the contribution of the viscous term allows a return flow along the western boundary. Furthermore, the nonlinear contribution ($\hat{\mathbf{k}} \cdot \nabla \times (\bar{\boldsymbol{u}} \cdot \nabla)\bar{\boldsymbol{u}}$) was further described by Veronis (1966).

The barotropic vorticity equation (Eq. 1.10) includes a pressure-dependent term know as the Bottom Pressure Torque (BPT): $\mathbf{J}(P_b, h) = \hat{\mathbf{k}} \cdot (\nabla P_b \times \nabla h)$ (Holland, 1973; Hughes and De Cuevas, 2001). Similar to the process occurring at the surface, the bottom pressure torque arises from variations in bottom pressure along isopycnal contours. These variations force a non-negligent torque on the horizontal flux above the bathymetry (Jackson et al., 2006). This implies that the interaction between deep flow and seafloor in the presence of varying topography can also induce the vertical flow.

Conversely, suppose the wind-driven and bathymetry-driven transports overlap at a certain depth. In that case, the assumption of a level of no motion is not appropriate, leading to the Sverdrup balance losing accuracy to a significant extent. Nonetheless, hydrographic observations, models, and reanalyses studies over the tropical and subtropical bands (e.g. Hautala et al., 1994; Wunsch, 2011; Lu and Stammer, 2004; Liang et al., 2017) have reported mid-depth vertical velocities sufficiently small to be considered negligible.

Numerical models (Bryan and Cox, 1972; Bryan et al., 1995; Hughes and De Cuevas, 2001), mooring data (Bryden, 1980) and scaling analyses (Wunsch and Roemmich, 1985 and Khatri et al., 2023) indicate that topography forcing is significant below the thermocline within the subtropics interior. In the barotropic vorticity studies that encompass the entire water column, a balance is found between the bottom pressure torque, surface wind stress curl and the meridional transport of planetary vorticity, defined as "Topographic-Sverdrup balance" by Holland (1967). Note that the bottom pressure torque does not dissipate energy; therefore, it can only balance the flow rather than drive it (Jackson et al., 2006).

It is well-established that the Sverdrup balance breaks down in the western boundary currents, where the underlying assumptions of linear vorticity balance break down (e.g. Roemmich and Wunsch, 1985; Bryan et al., 1995). In these regions, bottom pressure torque and nonlinear terms balance the return flow along the western boundary. Therefore, these regions exhibit characteristics of being largely inviscid, as friction is not necessary for clossing the vorticity budget (Hughes, 2000; Hughes and De Cuevas, 2001, Gula et al., 2015, Schoonover et al., 2016; Le Bras et al., 2019; Sonnewald et al., 2019; Yeager, 2015;

Waldman and Giordani, 2023; Khatri et al., 2023). The fundamental role of topography in western boundary currents was initially demonstrated by Holland (1973), who observed that the continental slope enhances the poleward current, compensated by an offshore return flow.

Studies based on observations such as Luyten et al. (1985) and Wunsch and Roemmich (1985) have raised doubts about the applicability of the Sverdrup balance to address the circulation in the subpolar gyres. In high latitudes, where the stratification is weak and Rossby wave velocities are slow, as previously discussed, it is expected that bottom pressure torque and bottom drag curl terms ($\hat{\mathbf{k}} \cdot \nabla \times \tau^{bot}/\rho_0$) in Eq. 1.10 become significant components in the force balance (Lu and Stammer, 2004; Spence et al., 2012; Yeager, 2015; Le Corre et al., 2020; Le Bras et al., 2019; Sonnewald et al., 2019; Le Bras et al., 2019; Sonnewald and Lguensat, 2021; Yeager, 2015; Styles et al., 2022). In such regions, the absence of a proper level of no motion suggests there is no isolation between the upper and lower ocean, and thus, no level where the meridional transport effectively absorbs the vertical flow generated by wind stress at the ocean surface.

The validity of the Sverdrup balance will also depend on the scale under consideration. While the equation remains valid on scales larger than 5° (e.g. Wunsch, 2011; Thomas et al., 2014), it breaks down at small scales due to the nonlinear vorticity terms becoming significant (Lu and Stammer, 2004; Khatri et al., 2023). Therefore, the spatial resolution considered plays a critical role not only in assessing the constraints of the Sverdrup balance but also in understanding the contribution of each term in the barotropic vorticity equation (Eq. 1.10) for closing the vorticity budget, as highlighted by e.g., Hughes and De Cuevas, 2001; Yeager, 2015; Le Corre et al., 2020; Styles et al., 2022; Khatri et al., 2023.

1.5.3 Linear Vorticity Balance (LVB)

The Sverdrup Balance is built under several assumptions and constraints: a linear, barotropic ocean, with a Level Of No Motion (LONM). By removing the constraint of a depth-integrated ocean, it becomes possible to estimate the vertical velocity field using the Linear Vorticity Balance (LVB):

$$\beta v = f \frac{\partial w}{\partial z} \tag{1.12}$$

where βv is the meridional advection of planetary vorticity and $f \frac{\partial w}{\partial z}$ is the vortex stretching. The LVB relates the direction of the meridional flow with the change in depth of the vertical flow, or, in other words, the change in the vorticity of a water parcel due to changes in latitude represented by the meridional advection of the planetary vorticity is balanced by a change in the thickness of the water column expressed by the vortex stretching generated by the vertical transport.

One possible derivation of the Sverdrup Balance is based in the vertical integral of the linear vorticity balance. When comparing the vertical integral of the LVB (Eq. 1.12) from the ocean-atmosphere interphase to a given depth level with the Sverdrup balance (Eq. 1.11), it becomes evident that at the upper boundary, the vertical velocities respond to atmospheric forcing according to Ekman theory, where the vertical velocity associated with the Ekman pumping in the Ekman layer (w_{Ek}) is written as:

$$w_{Ek} = \hat{\mathbf{k}} \cdot \nabla \times \frac{\tau^{wind}}{\rho_0 f} \tag{1.13}$$

The Sverdrup balance relies on a level of no vertical motion LONVM at the lower boundary of the integration layer. The LVB is indeed only one of the building blocks necessary for the validity of Sverdrup's theory, being the existence and depth of the LONVM, the other necessary components. However, this connection was not immediately established, and their link emerged sometime later in the literature (Vallis, 2006).

The LVB approach, which will be thoroughly examined, enables the assessment of the vertical dimension of the ocean dynamic that the Sverdrup balance misses in Chapter 3. All considerations regarding the dynamics of a barotropic ocean help us comprehend the potential limitations of solely relying on a linear description for the baroclinic case. By introducing the additional vertical dimension to the vorticity analysis, the upper and lower boundary forcings are not explicitly considered, unlike in the barotropic case. **A secondary question to address in Chapter 3 pertains to whether boundary forcings implicitly influence the linear baroclinic description.** This would suggest that the boundary-driven pathways are transported into the ocean interior. This potential connection between baroclinic results at a specific depth and previous studies conducted in a barotropic ocean forms a significant aspect of our investigation.

The derivation of Eq. 1.12 is rooted in the same set of equations as the barotropic vorticity balance: the Navier-Stokes and continuity equations (Eqs. 1.4, 1.5, and 1.6). However, unlike the barotropic vorticity balance, which requires depth integration, the vorticity equation is derived by taking the curl of the Navier-Stokes equations at each level:

$$\frac{\partial(1.5)}{\partial x} - \frac{\partial(1.4)}{\partial y} \tag{1.14}$$

The vorticity balance equation then arises after considering the continuity equation and neglecting the viscosity terms:

$$\underbrace{\frac{\partial \zeta}{\partial t}}_{\substack{\text{time}\\ \text{rate}}} + \underbrace{\beta v}_{\substack{\text{planetary}\\ \text{vorticity}\\ \text{advection}}} + \underbrace{\boldsymbol{u}\nabla\zeta}_{\substack{\text{relative}\\ \text{vorticity}\\ \text{advection}}} + \underbrace{\hat{\boldsymbol{k}}[\nabla_h w \times \frac{\partial \boldsymbol{u}_h}{\partial z}]}_{\substack{\text{vortex}\\ \text{tilting}}} = \underbrace{f\frac{\partial w}{\partial z}}_{\substack{\text{vortex}\\ \text{stretching}}} + \underbrace{\zeta\frac{\partial w}{\partial z}}_{\substack{\text{relative}\\ \text{vortex}\\ \text{stretching}}} + \underbrace{\frac{1}{\rho}\nabla \times [\rho A_h \nabla^2 \boldsymbol{u}_h}_{\substack{\text{horizontal}\\ \text{diffusivity}}} + \underbrace{\rho A_v \partial_z^2 \boldsymbol{u}_h]}_{\substack{\text{vertical}\\ \text{mixing}}} \tag{1.15}$$

Where the $\boldsymbol{u}_h$ represents the horizontal velocity field and $\zeta = \partial_x v - \partial_y u$ denotes the relative vorticity. The left-hand side of the Eq. 1.15 encompasses the terms associated with the time-variation of relative vorticity, the planetary vorticity total advection, the relative vorticity total advection and the vortex tilting. The right side of Eq. 1.15 includes the terms related to the vortex stretching term, the horizontal eddy viscosity term and the vertical eddy viscosity (Vallis, 2006).

After considering large-scale oceanic flows occurring at scales on the order of hundreds of kilometres and far from the lateral boundaries, the Earth's rotation exerts a pivotal influence on the flow that a significant degree of rigidity, preventing the development of turbulences and being able to be described by the vorticity equation (Rhines, 1986). Therefore, in this regime, where the Rossby (Ro: Advection/Rotation = V/fL) and Ekman (Ev: Horizontal (Vertical) Friction/Rotation = $A_h(A_v)/fL^2$) numbers are much smaller than 1, to conserve the potential vorticity, the vorticity vortex stretching must be compensated by meridional flow in changing latitudes (Coriolis parameter: f), resulting in the LVB (Eq. 1.12).

This implies that an alternative approach for estimating the vertical velocity field becomes theoretically possible within the framework of the LVB (Charney, 1955). The Indefinite Depth-Integrated LInear Vorticity (IDILIV) formalism allows estimating the vertical velocity field at each depth level:

$$w(z) = w(z_{ref}) - \int_{z}^{z_{ref}} \frac{\beta v}{f} dz' \tag{1.16}$$

The current state of the observations at basin scales only allows retrieving geostrophic flows. Therefore, we derive the three-dimensional w by vertically integrating the geostrophic component of the LVB (GLVB):

$$w_{GLVB}(z) = w(z_{ref}) - \int_{z}^{z_{ref}} \frac{\beta v_g}{f} dz' \tag{1.17}$$

In fact, the geostrophic LVB and the w_{GLVB} can be derived from the divergence of the geostrophic flow in a β-plane (Pedlosky, 1996):

$$\frac{\partial u_g}{\partial x} + \frac{\partial v_g}{\partial y} + \frac{\partial w_g}{\partial z} = 0 \tag{1.18}$$

Where $u_g = -1/f\rho_0 \partial_y p$, $v_g = 1/f\rho_0 \partial_x p$ and p is the pressure. Considering a β-plane, the geostrophic LVB is retrieved:

$$\beta v_g = \frac{\partial w_g}{\partial z} \tag{1.19}$$

Where w_g is the geostrophic component of the vertical flow. According to the GLVB, when accounting for the β-plane effect, the geostrophic meridional transport of the planetary vorticity is compensated by the vortex stretching induced by the vertical transport. By applying the indefinite depth-integral to Eq. 1.19, we obtain the equation for $w_{GLVB}(z)$ (Eq. 1.16):

$$w_g(z) = w_g(z_{ref}) - \int_{z}^{z_{ref}} \frac{\beta v_g}{f} dz' \tag{1.20}$$

Therefore, the w_{GLVB} can be considered as the geostrophic component of the total vertical flow.

In Chapter 4, we will use the geostrophic linear vorticity balance to describe and reproduce large-scale vertical motions in the ocean interior. The Indefinite Depth-Integrated LInear Vorticity alternative provides not only a viable foundation for estimating the vertical velocities but also offers a straightforward and intuitive means to understand basin-scale motions.

1.6 Key Questions

The current observational capacities for the geostrophic flow and the potential of the Sverdrup Balance to characterise ocean dynamics leads to the main goal of the thesis: computing and assessing a global estimation of the large-scale vertical flow. This objective, in turn, poses the main question of the thesis: **Can the geostrophic component of vertical velocity account for the large-scale vertical circulation in the "real" ocean?**

In order to answer the central inquiry of the thesis, three specific questions will be explored using model and observation-based datasets in the following chapters:

- **To what spatial and temporal extent is the ocean in Linear Vorticity Balance?**
- **Can the geostrophic meridional transport effectively explain the vertical motions, and specifically, can the thermocline geostrophic currents be explained by the Ekman pumping?**
- **Does the available observation-based wind stress and geostrophic meridional transport data allow for the estimation of three-dimensional vertical velocities assuming an ocean in Linear Vorticity Balance?**

1.7 Integration of the Thesis Topic and Objectives in a National and International Context

The topic and objectives of this thesis have garnered extended appreciation within both the national and international scientific communities.

In the national realm, the LEFE MERCATOR organisation has funded the project LVBW-3Dclim centred on the thesis theme. This support aims to facilitate the communication and publication of results within and beyond the French borders. Notably, the scientific committee responsible for project selection has shown strong advocacy for this initiative, expressing a highly positive view of its significance: "The Scientific Committee commended the project's focus on generating a tangible product of vertical velocities based on observations, employing a simplified approach while rigorously evaluating and testing the validity of the approximation..."

Regarding the international context, under this project's umbrella, we have shared our findings at four international conferences, conducted an international workshop in LOCEAN involving primarily French researchers, and facilitated a scientific visit abroad. This experience has allowed us to identify the strengths and limitations of our approach.

1.8 Thesis structure

To address these questions, we have built a framework based on ocean general circulation model (OGCM) data and subsequently applied it to observation-based data to retrieve observation-based vertical velocity field estimates. The OGCM-based approach will demonstrate the capability of the linear vorticity balance to describe the ocean dynamics at each depth. This step will assess the spatiotemporal extent of the linear equation in the ocean interior and its capability to retrieve the vertical velocity field through the Indefinite Depth-Integrated LInear Vorticity (IDILIV) approach. Hereafter, the observation-based meridional transport and wind stress will be applied to the IDILIV approach to obtain the Observation-based Linear Vorticity Vertical Velocities estimates (OLIV3) product. Chapter 2 introduces the various datasets based on models, reanalyses and observations. Chapter 3 will revisit the Linear Vorticity Balance (LVB) validity perspective within an OGCM simulation across scales, from the North Atlantic Ocean to a global perspective, with a particular focus on its time dependency. It also includes a section dedicated to identifying the terms required to close the vorticity budget in the regions where the linear vorticity balance does not hold. Chapter 4 will focus on deriving the vertical velocity field from the simulation, serving as a *perfect model test* for the framework's robustness. Chapter 5 will explore the capacity of the LVB to estimate w in the real ocean using an observation-based product and assess its potential to reproduce the characteristics of the field compared to existing datasets. Finally, Chapter 6 will concisely summarise the key findings and offer potential direction for future research.

Our research paper *Vertical Velocity 3D Estimates from the Linear Vorticity Balance in the North Atlantic Ocean* (Cortés-Morales and Lazar, submitted) is embedded in Chapters 3 and 4. This paper assesses the spatial and temporal extent to which the linear vorticity balance effectively accounts for the vorticity budget and its capability to estimate the vertical velocity field in an OGCM simulation over the North Atlantic Ocean as a case study. For the complete manuscript submitted to the *Journal of Physical Oceanography (JPO)*, please refer to the Appendix A. A detailed explanation of the construction of the distance-to-shore dependent filter used in the study, a detailed decomposition and comparison between depth-integrated vorticity equations, together with time-dependent and global maps as a visual aid for the reader, are presented in the Appendix B.

Si tu veux construire un bateau, ne rassemble pas tes hommes et femmes pour leur donner des ordres, pour expliquer chaque détail, pour leur dire où trouver chaque chose... Si tu veux construire un bateau, fais naître dans le cœur de tes hommes et femmes le désir de la mer.

— Antoine de Saint-Exupéry *Le Petit Prince, 1943*

2

Methodology and data

2.1 Preamble

We have developed a two-step protocol to attempt the estimation of vertical velocities. The first step involves building a framework based on the linear vorticity balance and exploring its possibilities to describe the ocean's vertical circulation within an OGCM simulation. This encompasses both the spatiotemporal assessment of the equation in the ocean interior and its capability to retrieve the vertical velocity field when indefinite depth-integrated.

The capacity of the LVB to close the ocean's vorticity budget will be evaluated considering the relative error between the terms of the equation. The two sides of the LVB (Eq. 1.12) are first estimated to assess the extent to which the LVB accounts for the circulation description in an OCGM simulation. From these, its relative error (Δ_{LVB}) relative to the mean between both terms in Eq. 1.12 is estimated as follows:

$$\Delta_{LVB} = \frac{(\beta v - f\partial_z w)}{0.5(|\beta v| + |f\partial_z w|)} \cdot 100 \tag{2.1}$$

The Δ_{LVB} defined in this way measures the offset of the Eq. 1.12 (taking as expected value the average between both terms) and is zero where the LVB is exactly correct. The regions where the Δ_{LVB} is smaller than 10% are considered as LVB valid areas at first order.

From there, the geostrophic component of the vertical flow is computed by applying the OGCM simulation geostrophic meridional velocities to the indefinite depth-integral of LVB[1] (Eq. 1.20), referred as IDILIV3[2]. Furthermore, its effectiveness as an estimator of the total vertical flow is assessed.

The second step includes applying the depth-integrated linear vorticity approach to observation-based data to reconstruct the vertical flow (Observation-based Linear Vorticity Vertical Velocities estimates (OLIV3)). Finally, we evaluate the quality of the observation-based vertical velocity through an intercomparison study with existing estimates of vertical velocity.

[1] Hereafter Indefinite Depth-Integrated LInear Vorticity (IDILIV) approach

[2] Indefinite Depth-Integrated LInear Vorticity Vertical Velocities Estimates (IDILIV3)

2.2 Development of the Framework within an OGCM Simulation

The first step of the protocol developed in Chapters 3 and 4 is based on the Nucleus for European Modelling of the Ocean (NEMO) (Madec et al., 2019). This system embeds various model components, including an ocean general circulation model (OPA, Océan PArallélisé), a sea-ice model (LIM, Louvain-la-Neuve ice model), and ecosystem models with various levels of complexity (see the NEMO website http://www.nemo-ocean.eu/). Every NEMO component solves partial differential equations discretised on a three-dimensional grid using finite-difference approximations (Bessières et al., 2017). Particularly, the study has been conducted with the OCCITENS simulation from Oceanic-Chaos-Impacts,Structure,Predictability (OCCIPUT) project (Penduff et al., 2014; Bessières et al., 2017) (simulation number 3 from 50 simulation ensemble) performed over the period 1960-2015 (after a spin-up of 26 years) at eddy-permitting resolution (1/4°) ORCA025 grid (Arakawa type C cell) forced by DFS5.2 (Dussin et al., 2016) forcing set.

The NEMO OGCM OCCITENS simulation provides four-dimensional estimates of oceanic variables that would be difficult to produce from observations alone, such as the vertical velocity field. Thermohaline and sea surface height fields are used to compute the neutral density field and the isopycnal surfaces within the ocean interior following Jackett et al. (2006) formula. The geostrophic velocity field is computed using the geostrophic equation applied to the pressure field, which is calculated using sea surface height and integration of the hydrostatic equation. The code used to compute the geostrophic velocities is available at https://github.com/meom-group/CDFTOOLS. The Mixed Layer Depth (MLD) taken from the NEMO OGCM OCCITENS simulation is computed within the model using a density criterion of 0.01 kg m^{-3} of density change from the surface following the de Boyer Montégut et al. (2004) methodology.

The wind stress provided by the NEMO OGCM OCCITENS simulation is computed applying the DFS5.2 forcing set Dussin et al. (2016) to the bulk formulae developed by Large and Yeager (2004). This forcing set contains ECMWF Re-Analysis -Interim (ERA-Interim)-Interim atmospheric reanalysis produced at European Center for Medium-Range Weather Forecasts (ECMWF) (Dee et al., 2011). ERA-Interim provides the surface atmospheric variables required to drive global ocean hindcast simulations for the period 1979-2015. The ERA-Interim dataset must be supplemented with the ERA40 dataset, which covers the period from 1958 to 1978, in order to fill the gaps in the simulation period (Dussin et al., 2016). The wind stress computation in the NEMO code uses a drag coefficient computed following Hellerman and Rosenstein (1983).

The outputs of the NEMO OGCM OCCITENS simulation are available upon request. Please contact Thierry Penduff at thierry.penduff@cnrs.fr.

2.2.1 Complete Vorticity Balance Computation

Due to the need to minimise the cross anomaly error in the non-linear vorticity balance terms during time averaging, a CROCO (Coastal and Regional COmunity model) simulation with a 12h time step computation is employed in Section 3.2.2.2 of Chapter 3. The CROCO simulation is based on the Regional Oceanic Modeling System (ROMS; Shchepetkin and McWilliams, 2005). This simulation is configured over the North Atlantic basin with a 3 km horizontal resolution and 100 bathymetry following levels during 2003.

The outputs of the CROCO simulation are available upon request. Please contact Jonathan Gula at jonathan.gula@univ-brest.fr.

2.3 Observation-based Linear Vorticity Vertical Velocities estimates (OLIV3)

Once the framework based on the IDILIV equation to reconstruct the vertical flow is built and validated using the NEMO OCCITENS simulation output, the next step in the 2-step protocol is the application to observation-based datasets. In this study, we introduce a new product of geostrophic vertical velocities (Observation-based Linear Vorticity Vertical Velocities estimates (OLIV3)), obtained by applying the geostrophic meridional velocities from ARMOR3D dataset to the IDILIV equation (Eq. 1.20) and using the Ekman pumping derived by the wind stress from ERA5 as boundary condition.

The OLIV3 presented in Chapter 5 covering the period 1993-2019 at 0.25° horizontal resolution over 71 isopycnal levels is available at: https://doi.org/10.5281/zenodo.11506778. The 50 vertical level version of OLIV3 is available at: https://doi.org/10.5281/zenodo.11520783. The low-resolution version used in the intercomparison study is available upon request.

2.3.1 Ocean Interior Observation-Based Three-Dimensional Fields

The observation-based geostrophic meridional velocities used as input is the global ARMOR3D dataset (Guinehut et al., 2012; Mulet et al., 2012). This product is distributed by the *Copernicus Marine Environment Monitoring Service* (CMEMS; https://doi.org/10.48670/moi-00052). The geostrophic velocity fields are estimated in three successive steps: The first step of this method consists in deriving synthetic temperature and salinity fields from Sea Level Anomaly (SLA; AVISO+, 2015) and Sea Surface Temperature (SST) and Sea Surface Salinity (SSS) observations (Reynolds et al., 2007; Droghei et al., 2018) using a multiple/simple linear regression method and covariances calculated from historical *in-situ* observations (Cabanes et al., 2012). The historical dataset has been constructed using all temperature and salinity profiles available in the EN3 dataset (Ingleby and Huddleston, 2007) and completed with the Argo float observations available (http://www.coriolis.eu.org) (Ollitrault and Rannou, 2013). The second step involves combining the synthetic estimates with thermohaline profiles employing an optimal interpolation method (Bretherton et al., 1976). In the third step, the geostrophic velocities are computed through the thermal wind equation referenced at the surface geostrophic velocities estimated from the altimetric maps of absolute dynamic topography (computed as the sum of the SLA and the MDT) (Mulet et al., 2012).

ARMOR3D dataset provides weekly temperature, salinity and geostrophic velocity fields at 0.25° resolution over 50 vertical levels with different spacing depending on depth from the surface down to 5500 m depth covering the 1993-2019 period. ARMOR3D data can be downloaded at *https://data.marine.copernicus.eu/product/MULTIOBS_GLO_PHY_TSUV_3D_MYNRT_015_012*.

2.3.2 Observation-Based Surface Forcing

The Ekman pumping vertical velocity (w_{Ek}) used as boundary condition to initialise the IDILIV approach is computed using the wind stress from ERA5. ECMWF Re-Analysis v5 (ERA5) provides hourly, daily, and monthly estimates for a large number of atmospheric, ocean-wave and land-surface quantities. This product is the fifth-generation European Centre for Medium-Range Weather Forecasts (ECMWF) reanalysis of the global climate and weather for the past eight decades. Data are available from 1940 to the present. ERA5 updates the ERA-Interim reanalysis. Data have been regridded to a regular lat-lon grid of 0.25°. ERA5 monthly-averaged wind stress can be downloaded in the Copernicus Climate Change Service (C3S) Climate Data Store (CDS), *DOI: 10.24381/cds.f17050d7*.

2.4 Intercomparison Study Datasets

The last step in the study is to compare the features reproduced by OLIV3 to those estimated by a set of available datasets containing the OGCM simulation output used to build the framework, two reanalyses and one observation-based product that uses the omega equation for retrieving the vertical flow.

2.4.1 GLORYS12 reanalysis

One of the two reanalyses utilised in the intercomparison study is the GLobal Ocean ReanalYsis and Simulations (GLORYS) (Verezemskaya et al., 2021, Jean-Michel et al., 2021), with a spatial resolution of 1/12°, and 50 vertical levels from the surface until 5728 m depth covering the period 1993–2019, hereafter referred to as GLORYS12v1. The GLORYS12v1 model component is NEMO (Madec et al., 2019). Observational data assimilation is carried out employing a Kalman filter (Lellouche et al., 2018). Along-track altimeter SLA, satellite SST and sea ice concentration, and *in-situ* temperature and salinity profiles are jointly assimilated. A three-dimensional variational (3D-VAR) scheme corrects the low-frequency large-scale biases in temperature and salinity. GLORYS12v1 data can be downloaded at *https://tds.mercator-ocean.fr/thredds/glorys12v1/glorys12v1_pgn_monthlymeans.html*.

2.4.2 ECCOv4r4 reanalysis

The second reanalysis product used for comparison is the Estimating the Circulation and Climate of the Ocean (ECCO) in its fourth release of version 4 (Forget et al., 2015; Fukumori et al., 2018), hereafter referred to as ECCOv4r4. This dataset covers the 1992-2017 period. ECCOv4r4 is based on the MIT General Circulation Model (Adcroft et al., 2004) and applies a 4D-VAR assimilation scheme to a wide set of observations (including satellite altimetry, *in-situ* temperature and salinity profiles from Argo, satellite sea surface salinity and temperature, and ocean bottom pressure), minimising observation analysis biases in the least square sense. The ECCOv4r4 has a zonal resolution of 1° and it varies spatially from 0.25° to 1° in the meridional dimension, with the highest resolution in high latitudes and lowest resolution in mid-latitudes, with 50 vertical levels where the deepest ocean bottom is set to 5678m below the surface, with decreasing resolution when increases the depth. ECCOv4r4 data can be downloaded at *https://www.ecco-group.org/products-ECCO-V4r4.htm*.

The vertical velocity field is diagnosed from the continuity equation in both reanalyses.

2.4.3 OMEGA3D product

The only available estimate of vertical velocities at a global scale based on observations is the OMEGA3D product (Buongiorno Nardelli et al., 2018; Buongiorno Nardelli, 2020). This dataset was obtained by applying the adiabatic Quasi Geostrophic (QG) omega equation (Giordani et al., 2006). Two datasets are taken as input for the OMEGA3D processing: ARMOR3D thermohaline and geostrophic velocity dataset (Guinehut et al., 2012; Mulet et al., 2012) and ERA-Interim (Dee et al., 2011) surface air-sea fluxes. The OMEGA3D product contains the quasigeostrophic horizontal velocity field, the ageostrophic horizontal velocity field and the vertical velocity field over a 0.25° horizontal grid with 75 vertical levels from the ocean surface until 1500 m depth covering the 1993-2018 period. The full OMEGA3D product is available at *https://doi.org/10.25423/cmcc/multiobs_glo_phy_w_rep_015_007*.

Product Name	OLIV3	NEMO OCCITENS output	NEMO OCCITENS IDILIV3	GLORYS12v1 output	ECCOv4r4 output	OMEGA3D output
Type of Product	Observation-based	OGCM	OGCM	Reanalysis	Reanalysis	Observation-based
Equation	LVB	Continuity	LVB	Continuity	Continuity	Omega Equation
Atmospheric Forcing	ERA5	ERA Interim	ERA Interim	ERA Interim/ ERA5	ERA Interim	ERA Interim
Horizontal velocities	ARMOR3D	NEMO OCCITENS	NEMO OCCITENS	GLORYS12v1	ECCOv4r4	ARMOR3D
w Type	w_g	w_{tot}	w_g	w_{tot}	w_{tot}	w_{QG}
Horizontal resolution	0.25 °	0.25 °	0.25 °	0.083 °	1 °	0.25 °
Horizontal levels	50 (0-5500m)	75 (0-5902m)	75 (0-5902m)	50 (0-5728m)	50 (0-5678m)	75 (0-1500m)
Time resolution	Annual	Weekly	Annual	Monthly	Monthly	Weekly
Available time period	1993-2019	1960-2015	1960-2015	1993-2019	1992-2015	1993-2018

Table 2.1: Characteristics of the OLIV3, NEMO OCCITENS simulation output, NEMO OCCITENS simulation IDILIV3, GLORYS12v1 reanalysis, ECCOv4r4 reanalysis and OMEGA3D estimates used in the intercomparison section in Chapter 5.

It is said by the Eldar that in water there lives yet the echo of the Music of the Ainur more than in any substance that is in this Earth; and many of the Children of Ilúvatar hearken still unsated to the voices of the Sea, and yet know not for what they listen.

— J.R.R. Tolkien, *The Silmarillion*

3

Towards Linear Vorticity Balance Validity in an OGCM simulation

On the role of understanding the large-scale circulation, the Sverdrup balance (Sverdrup, 1947) stands as a pivotal theory connecting the meridional geostrophic transport with the wind stress. Its simplicity and robustness in describing ocean dynamics have attracted numerous researchers since its conception, particularly in depicting the climatological meridional ocean's transport over subtropical and tropical gyres. Nevertheless, this approach encounters limitations in explaining the vertically integrated circulation near coastlines and at higher latitudes (Wunsch, 2011, Gray and Riser, 2014 and Thomas et al., 2014).

Developed in a flat-bottom model without considering varying bathymetry, the Sverdrup balance hypothesis assumes zero vertical movements at the bottom of the wind-driven layer. As a result, the vertical motions generated by the curl of the wind stress at the surface induce the meridional transport within the wind-driven layer. However, the necessary vertical velocity gradient from the surface to the level of no vertical motion has yet to be thoroughly explored. The Linear Vorticity Balance (LVB), from which the Sverdrup balance is derived, serves as a foundation framework for conducting a depth-dependent description of basin-scale circulation. This approach provides a basis for comprehending ocean dynamics, accounting for the complexities arising from the different ocean regimes throughout the water column.

3.1 Preamble

Numerous studies over the past decade have demonstrated the efficacy of the Sverdrup Balance in describing the large-scale barotropic oceanic circulation. However, there is a noticeable gap in research attention when it comes to evaluating its baroclinic version, the Linear Vorticity Balance (LVB). Therefore, this chapter presents the possibilities of describing the ocean dynamics from a linear perspective using the LVB ($\beta v = f\partial_z w$). Here, we introduce a new concept: the tachocline ("Tacho-", from Greek "tachos", refers to "velocity, speed", and "-cline", from Greek klinein, means "to slope"), representing a region with velocity amplitude changing rapidly with depth. The equation is explored using the eddy-permitting NEMO OGCM OCCITENS simulation to assess the extent to which it explains the basin-scale circulation, both spatially and temporally (at scales larger than 5° and one year), first in the North Atlantic, as a case study, evaluating its constraints with a one-year CROCO OGCM simulation, and secondly expanding the LVB validity study to the global oceans.

Given a 56-year time-mean circulation and spatial scales larger than 5°, the LVB holds over most of the tropical and subtropical upper ocean and about half of the basin within the intermediate and deep oceans. The oceanic extension explained by the geostrophic component of the LVB is significantly reduced compared to the total LVB below the upper tachocline, with this reduction being maximal in the intermediate ocean. Here, the ageostrophic component of the velocity opposes its geostrophic counterpart to absorb the vertical flow contribution to the vorticity budget. Shorter timescales reduce the LVB validity, diminishing this reduction with increasing depth and becoming negligible in the deep ocean. Departures from the LVB occur near the western boundary currents, strong zonal tropical flows, and the subpolar gyres. The deviation from linear equilibrium in the upper tachocline regions arises from the influence of non-linear and mixing terms, with the horizontal advection of relative vorticity as the primary contributor to balance the linear residue.

The chapter is organised as follows: The assessment of the time-mean LVB validity using a NEMO OCCITENS simulation in the North Atlantic as a case study is included in Section 3.2.1.4. The extension to the global ocean of the assessment of the LVB validity is addressed in Section 3.3. Within Subsection 3.2.1 is embedded the part centred on the LVB diagnostics of a paper submitted for publication in *Journal of Physical Oceanography (JPO)* [1]). The evaluation of the contribution of the geostrophic and ageostrophic components of the LVB to the validity and the temporal constraints of the LVB using the NEMO OCCITENS simulation, together with the study of the non-linearity contribution to the vorticity budget closure using a CROCO simulation are discussed in Subsection 3.2.2.

[1] (reformatted for the thesis manuscript). For the complete manuscript submitted in *JPO*, please refer to the Appendix A.

3.2 Diagnosing the Performance of Linear Vorticity Balance in Describing North Atlantic Ocean Dynamics

3.2.1 Foundations of the Linear Vorticity Balance: Unraveling Spatial and Temporal Dimensions

This section will delve into the spatial and temporal variability of the Linear Vorticity Balance (LVB), employing the North Atlantic Ocean across the entire water column as a case study. It will endeavour to determine the regions where the LVB accurately characterises basin dynamics, focusing on climatological timescales ranging from 1 year to 56 years at spatial scales larger than 5°.

3.2.1.1 Introduction

One of the most influential theories that explain the ocean's general circulation is the Sverdrup balance, which connects the meridional geostrophic transport with the wind stress at basin scales (Sverdrup, 1947). The Sverdrup balance theory describes the time-mean barotropic ocean transport over the subtropical and tropical gyres (STG and TG), assuming a level of no vertical motion. Sverdrup (1947) proposes that the Sverdrup balance should emerge after extended time-averaging. Subsequent research on this theory has suggested that the oceanic response to the atmospheric forcing needed for the Sverdrup balance to hold can occur within the first-mode baroclinic Rossby wave propagation timescales (Tailleux and McWilliams, 2001). Hence, the Sverdrup balance approach fails to explain the vertically integrated circulation in regions where the Rossby wave has longer timescales than the studied period, such as in high latitudes. This formulation is also inadequate near the coasts, where the assumption of a level of no vertical motion is no longer valid (Wunsch, 2011; Gray and Riser, 2014 and Thomas et al., 2014).

Recent studies have examined the limitations of the Sverdrup balance through the complete vorticity balance, which includes viscosity, frictional, non-linear, and bottom pressure torque terms to close the vorticity budget. The importance of frictional and bottom pressure torque terms in the North Atlantic subpolar gyre interior has been highlighted by Spence et al. (2012), Yeager (2015) and Le Corre et al. (2020). In the Gulf Stream, it is necessary to add the non-linearities to the bottom pressure torque term to accurately account for the atmospheric forcing (Hughes and De Cuevas, 2001, Gula et al., 2015 and Schoonover et al., 2016). The global ocean exhibits similar features, as noted by Hughes and De Cuevas (2001) and Sonnewald et al. (2019). Remarkably, the depth dependency of the vorticity balance is little studied. In an Ocean General Circulation Model (OGCM), Lu and Stammer (2004) and Waldman and Giordani (2023) identify the Sverdrupian nature of the centre of the oceanic gyres within the upper and intermediate oceans and show that topographic forcing drives the vorticity budget closure in the deep ocean.

In order to conduct a baroclinic analysis of the basin-scale circulation, the linear vorticity balance (LVB) serves as an appropriate and well-known starting point:

$$\beta v = f \partial_z w \tag{3.1}$$

Where f is the Coriolis parameter, β is the meridional gradient of f. v and w are the meridional and vertical components of the velocity. When the flow is in LVB, it becomes possible to relate the shear of the vertical velocity field directly and locally to the meridional velocities. When integrated vertically from the surface to a level of no vertical motion, the LVB results in the Sverdrup balance. For a geostrophic and incompressible flow on a β-plane, the LVB represents the continuity equation and expresses a local mass balance between meridional divergent flow and an opposing vertical convergent movement, and vice-versa. Figure 3.1 illustrates this interpretation schematically for the geostrophic component of two stationary tropical and subtropical circulation gyres in the North Atlantic upper ocean.

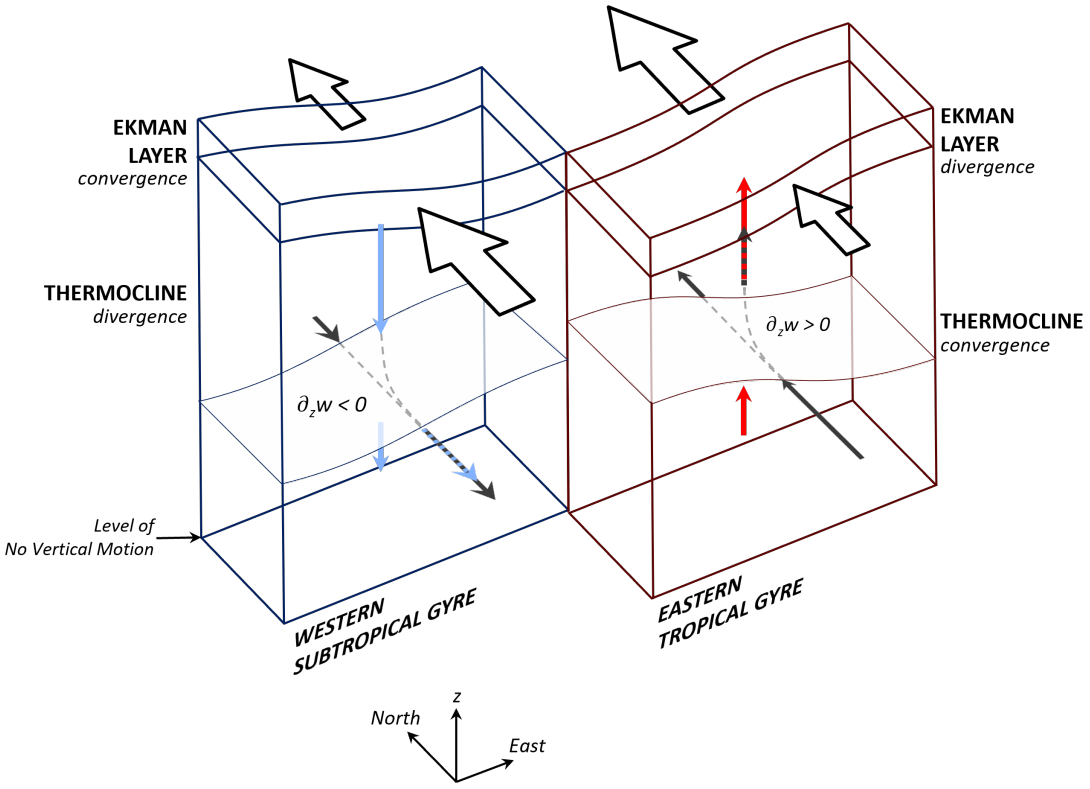

Figure 3.1: Vertical and geostrophic meridional circulation over a typical Northern Hemisphere STG (northernmost cube) and TG (southernmost cube) within the thermocline. The tendency to reduce the amplitude of the downward (upward) flow in the thermocline must be offset by a divergent (convergent) flow in the STG (TG) to absorb (feed) the Ekman transport to the oceanic surface. Thus, the meridional circulation in the thermocline is determined by the divergence of equatorward transport and the convergence of poleward transport.

Indeed, the inverse dependence on latitude of the meridional geostrophic transport (v_g) results in the convergence of the poleward transport within the cyclonic tropical gyre (TG) thermocline, pushing up the thermocline waters and supplying mass to the diverging Ekman flow, forced by the Trade winds, whose intensity increases with latitude. Further north, the intrinsic divergence of the equatorward transport of the subtropical gyre (STG) progressively absorbs the Ekman layer mass excess from the converging flow, leading to downward movements (Tomczak and Godfrey, 1994). A comparable logic can be used in the geostrophic deep ocean and the bottom Ekman layer. However, there is no independent forcing like wind stress in the deep ocean to estimate a boundary condition for the ageostrophic component of w.

As illustrated for the thermocline, geostrophic vertical movements are essential to global circulation. They redistribute water masses between layers, shaping them (Stramma and England, 1999), they ventilate the thermocline (Gordon, 1981), and also participate in driving the deep circulation (Drake et al., 2020).

However, the w field in the open ocean is several orders of magnitude smaller than the horizontal circulation (approximately 10^{-6} m s^{-1} in the centre of oceanic gyres). Currently, direct observations of such weak intensities are not yet technically possible (e.g., Comby et al., 2022).

The main objective of this study is to develop a comprehensive baroclinic analysis of the LVB and its geostrophic case at all depths, in climatological and interannual scales across the North Atlantic, in an OGCM simulation. This analysis will address the oceanic circulation patterns' ability to react to the surface and bottom boundaries forcing, transmitting the forcing to the ocean interior.

3.2.1.2 Methodology and data

3.2.1.2.1 The Linear Vorticity Balance

The vorticity balance can be obtained by applying the continuity equation to the vertical component of the curl of the steady-state momentum Navier-Stokes equations under Boussinesq approximation:

$$\partial_t \zeta + \beta v + \mathbf{u}\nabla\zeta + \hat{\mathbf{k}}(\nabla_h w \times \partial_z \mathbf{u}_h) = (f+\zeta)\partial_z w + \frac{1}{\rho}\nabla \times [\rho A_h \nabla^2 \mathbf{u}_h + \rho A_v \partial_z^2 \mathbf{u}_h] \tag{3.2}$$

Where ζ is the relative vorticity, $\mathbf{u}$ and $\mathbf{u}_H$ are the three-dimensional and horizontal velocity fields, respectively. u, v and w represent the zonal, meridional and vertical components of the velocity. A_H and A_V are the horizontal and vertical turbulent viscosity coefficients, respectively. The terms on the left-hand side of Eq. 3.2 are the relative vorticity time variation, the planetary vorticity advection, the relative vorticity advection and vortex tilting term. On the right side of Eq. 3.2, the terms are the vortex stretching term and the horizontal and vertical eddy viscosity terms (Vallis, 2006).

The Rossby number ($Ro = V/fL$, where L and V are the characteristic length and horizontal component of the flow) relates the inertial to Coriolis forces. Therefore, this ratio can be used for a magnitude analysis of the vorticity equation. Most term dimensions in Eq. 3.2 can be expressed in terms of Ro. The continuity equation indicates that the vertical velocity scale is related to the horizontal velocity by $V/L = W/D$ where W and D are the vertical component and thickness of the flow. With T the characteristic time of the flow and expressed as $T = 1/fRo$:

$$\begin{gathered}\left[\partial_t \zeta = \frac{fRo}{T}\right] = f^2Ro^2; \quad [\mathbf{u}\nabla\zeta] = f^2Ro^2; \quad \left[(\partial_x w \partial_z v) - (\partial_y w \partial_z u)\right] = f^2Ro^2; \quad [\zeta\partial_z w] = f^2Ro^2 \\ [\beta v] = f^2Ro; \quad [f\partial_z w] = f^2Ro;\end{gathered} \tag{3.3}$$

Considering a low Rossby number ($Ro << 1$) describes large-scale ocean flow of $O(100km)$, the terms explicitly dependent on the Coriolis force are dominant contributors in the balance of forces (Pedlosky, 1979). Far from frictional boundaries, the Ekman numbers (horizontal $Ek = 2A_H/fL^2$ and vertical $Ek = 2A_V/fD^2$) are low (Ek << 1), and rotation dominates over friction. Therefore, the eddy viscosity-related terms ($\frac{1}{\rho}\nabla \times [\rho A_H \nabla^2 \mathbf{u}_H] = f^2 RoEk$; $\frac{1}{\rho}\nabla \times [\rho A_V \partial_z^2 \mathbf{u}_H] = f^2 RoEk$) can be overlooked. Taking the first-order balance of Eq. 3.2 while considering the regime flows mentioned above and averaging over a sufficiently long period to neglect time-variation contribution, the Eq. 3.1 emerges.

In this chapter, both sides of Eq. 3.1 are first estimated to assess the extent to which the LVB describes the circulation in the OCGM. Their relative error (Δ_{LVB}) relative to the mean between both terms in Eq. 3.1 is estimated as follows:

$$\Delta_{LVB} = \frac{(\beta v - f\partial_z w)}{\frac{1}{2}(|\beta v| + |f\partial_z w|)} \cdot 100 \tag{3.4}$$

Δ_{LVB} measures the deviation of Eq. 3.1 from the perfect equilibrium and is zero where the LVB is exactly correct. The regions where the $|\Delta_{LVB}|$ is smaller than 10% are considered LVB-valid areas at first order.

The western boundary region (4° width-band), characterised by a high Rossby number, as well as the equatorial band (0-5°N), where the Coriolis parameter f becomes too small, have been masked and not considered in our quantitative analyses. Additionally, given the significant impact of mixing terms within the mixed layer, we exclude the region between the surface and the maximum mixed layer depth from our analysis when determining the zonal percentage of the basin explained by the LVB.

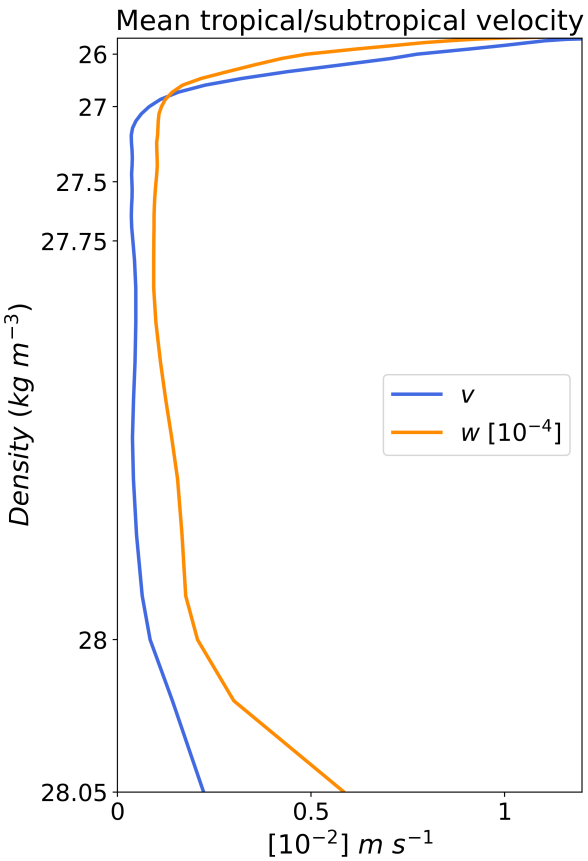

Figure 3.2: Spatial-mean of absolute velocity field over the tropical and subtropical bands (5°-35°N), excluding the 4° width band along the western boundary as well as the mixed layer. The distance between σ levels on the y-axis is proportional to their average width within the basin.

In this model study, we will divide the tropical and subtropical oceans into three distinct dynamic layers visible in Figure 3.2. First, we introduce a new concept: the tachocline. This concept represents a region in a dynamically stratified water column which separates rapid flowing waters from an almost steady region, with velocity amplitude decreasing rapidly with depth. The name "tachocline" is inspired by the construction of concepts such as thermocline, halocline or pycnocline. "Tacho-", from Greek "tachos", refers to "velocity, speed", and "-cline", from Greek klinein, means "to slope". Therefore, in Figure 3.2, we observe an upper tachocline covering the depth range of the thermocline (not shown) and a lower tachocline within the deep ocean. Between these layers, the intermediate ocean is characterised by minimal and barotropic velocities. In this study, we have identified the maximum mixed layer as the upper boundary condition of the upper tachocline and the isopycnal surface σ 27.1 kg m^{-3}, averaged across the subtropical (20-35°N) and tropical bands (5-20°N), as the lower boundary. Note that the subtropical upper tachocline extends to approximately σ 27.1 kg m^{-3}, while the tropical upper tachocline reaches around σ 26.75 kg m^{-3}. In the mid-latitudes (35°-50°N), the upper tachocline

extends to σ 27.5 kg m^{-3} (Figure B.11b in Appendix B). The intermediate ocean is bounded by σ 27.1 and 28 kg m^{-3}. Lastly, the lower tachocline in the deep ocean is bounded from above by σ 28 kg m^{-3} and from below by the seabed.

Given our interest in assessing the horizontal circulation patterns and the extension of the LVB description of each of these three domains, we identified three representative isopycnal surfaces at σ 26, 27.78 and 28.05 kg m^{-3}.

3.2.1.2.2 The Spatial Filtering

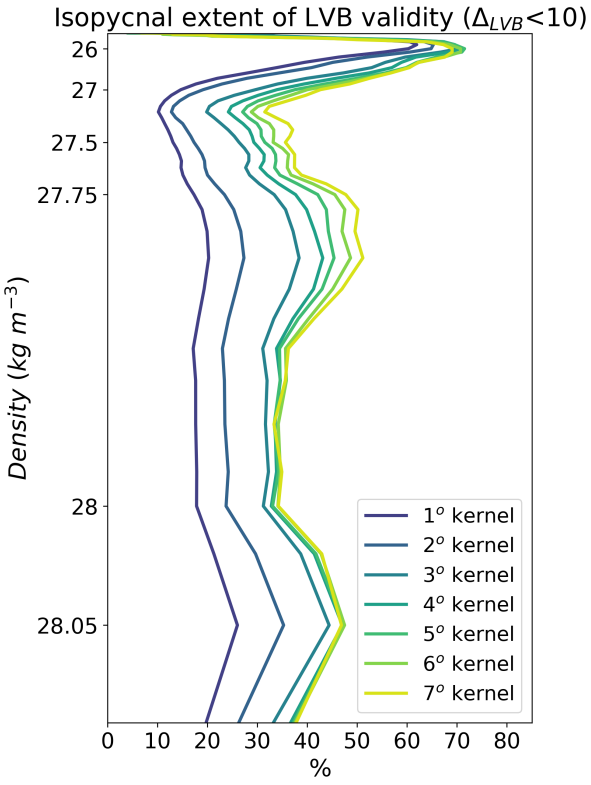

Figure 3.3: 56-year average LVB validity extent (%) over isopycnal levels in the unmasked region outside the 4° belt from the western boundary, as a function of spatial smoothing size from 1 to 7 ° kernel.

Previous studies on the validity of the Sverdrup balance, including Thomas et al. (2014), Wunsch (2011) and Gray and Riser (2014), and studies analysing the complete barotropic vorticity, such as Gula et al. (2015), Le Bras et al. (2019), Sonnewald et al. (2019) and Khatri et al. (2023), have highlighted the significant impact of model spatial resolution and horizontal low-pass filtering on the role and assessment of each term of the vorticity balance. To account for the spatial resolution dependency of the LVB, we conducted a low-pass sensitivity analysis with filter kernel sizes ranging from 1 to 7° (Figure 3.3). The w in the OGCM is a diagnostic variable derived from the horizontal flow in the continuity equation, exhibiting smaller structures than the horizontal velocity field. Hence, prior to the above analysis, a 1° filter is applied to the w field to remove the spatial high-frequency and match its scale to that of the horizontal flow components.

Figure 3.3 displays the 56-year average LVB validity extension as a function of depth and filter scale ranging from 1 to 7°. As the filtering kernel size increases, the LVB validity extension for a given isopycnal surface expands within the intermediate and deep oceans. This occurs because the filter ensures that the motion is of a sufficiently large scale for the LVB to remain valid. However, for larger scales, particularly within the upper ocean where the open ocean circulation already exhibits basin-scale features at its native resolution, the filter extends the error near the coasts. Thus, 5° filter maximises the LVB validity extension across the water column. It reduces errors along the lateral boundaries, smooths out small-scale structures within the intermediate and deep oceans, and preserves the core circulation patterns. This choice lets us focus on the large-scale ocean dynamics the LVB formulation can successfully describe.

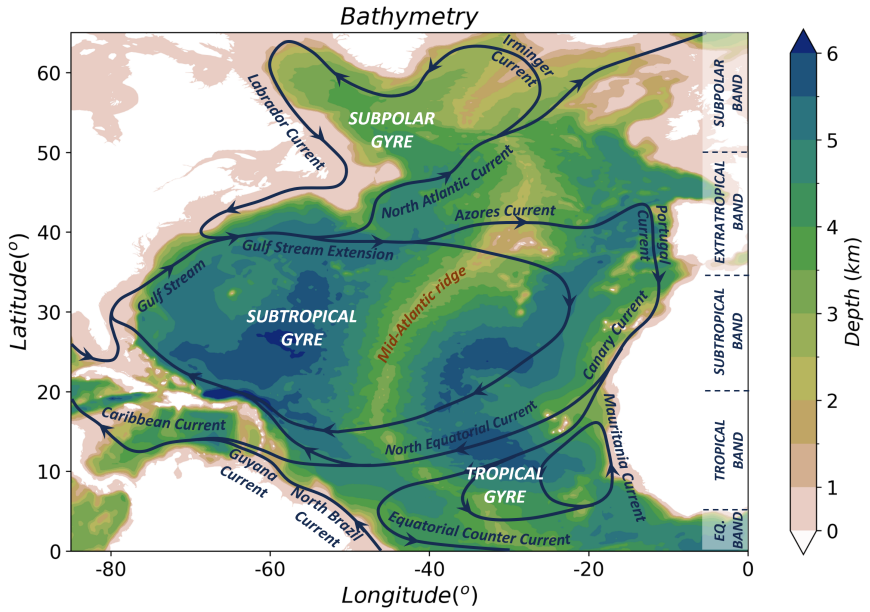

Figure 3.4: Main oceanic gyres and surface currents of the North Atlantic Ocean. The primary bands into which the basin is divided are indicated on the right-hand side of the panel. The shading represents the bathymetry of the basin. Adapted from Schmitz Jr and McCartney (1993) and Tomczak and Godfrey (1994).

3.2.1.3 The Climatological Velocity Field in OCCITENS Simulation

The 56-year average of the OGCM vertical and horizontal velocity field is presented in Figures 3.5, 3.6 and 3.7 over three isopycnal surfaces (σ 26, 27.78 and 28.05 kg m^{-3}), representing the upper tachocline, corresponding to the upper tachocline in the upper ocean, the intermediate ocean, and the lower tachocline in the deep ocean. Figures 3.5 and 3.7 also depict the Ekman pumping vertical velocity (w_{Ek}) and the bottom vertical velocity, respectively, offering insights into how boundary conditions influence the circulation in the ocean interior. Note that in Figure 3.5b, we represent $-w_{Ek}$, considering that, since $w_{tot} = w_g + w_{Ek} = 0$ at the surface, then $w_g(0) = -w_{Ek}(0)$.

The tropical gyre (TG; Figure 3.5a), as described by Schott et al. (2004), displays a counterclockwise circulation around the Guinea Dome (Stramma et al., 2005). On the other hand, the subtropical gyre (STG; Schmitz Jr and McCartney, 1993) is characterised by a clockwise circulation. Strong zonal flow is evident in the southern part of both gyres, the equatorial band and the open ocean Gulf Stream extension. The geostrophic surface circulation (streamlines in Figure 3.5b) is calculated from the Sea Surface Height (SSH), which is primarily influenced by wind forcing (Vallis, 2006). The similarity between the surface and thermohaline horizontal pathways demonstrates that the horizontal circulation within the upper tachocline is primarily driven by the atmospheric forcing (Huang and Russell, 1994).

The Ekman pumping vertical velocity (w_{Ek}) (Figure 3.5b) shows an upwelling over the TG with its maximum occurring near the eastern boundary from between 10-20°N. Over the STG, the downwelling is centred at 50°W over the southern part of the STG. The Gulf Stream region, including its separation from the coast and its open ocean extension, is characterised by upward movements. The subpolar gyre (SPG) exhibits an upwelling centred in the southeastern part of Greenland with a coastal downwelling along Greenland. These results are consistent with previous computations of w_{Ek} using observed datasets (e.g. Xie and Hsieh, 1995).

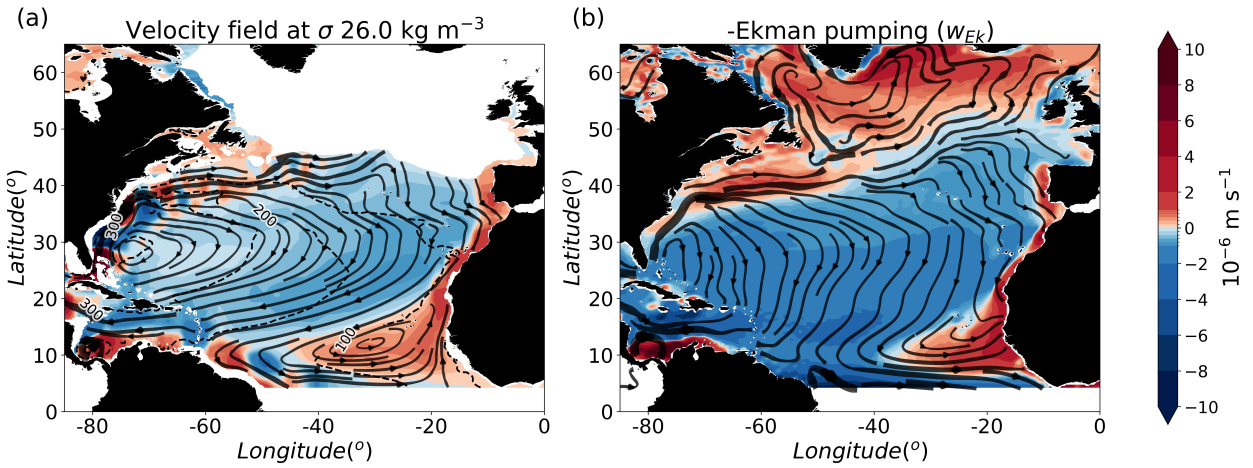

Figure 3.5: 56-year average velocity field from OCCITENS simulation over σ 26 kg m^{-3} representative of the upper tachocline-upper ocean. Horizontal velocities are represented by streamlines, coloured-filled contours represent vertical velocities. The black-dashed contours represent the depth of the isopycnal surfaces (in meters) (a). Time-mean Ekman pumping computed from OCCITENS simulation wind stress (b). Note the minus sign to equate the Ekman pumping to the geostrophic component of the vertical velocity at the surface (Section B.4 in Appendix B). The streamlines represent the geostrophic velocity at the ocean surface. The equatorial band (0-5°N) has been masked.

The vertical velocity field within the upper tachocline-upper ocean (shading in Figure 3.5a) is largely similar to w_{Ek} spatial patterns (Figure 3.5b), evidencing the role of the atmospheric forcing as the primary contributor to the vertical flow within the upper ocean (Huang and Russell, 1994). The sign and amplitude of w_{Ek} evidently shape the isopycnal surfaces (Gill, 1982). Over σ 26 kg m^{-3}, the cyclonic circulation of the TG is associated with positive w (Lazar et al., 2002) with maximum upwelling values within the Canary upwelling system (Arístegui et al., 2009). Conversely, the anticyclonic circulation of the STG is characterised by negative velocities, which deepen the isopycnal surfaces. In addition, the Gulf Stream is associated with an overall downwelling along the coast and an upwelling after its separation from the continent, featuring meanders and eddies. The differences in intensity between the upper ocean w and w_{Ek} illustrate the baroclinic nature of the field within the upper tachocline, as depicted in Figure 3.2.

Let us examine now the intermediate ocean that we chose to bound by σ 27.1 kg m^{-3}, representing the bottom of the permanent upper tachocline and 28 kg m^{-3} where the circulation starts significantly intensifying as shown in Figure 3.2. The σ 27.78 kg m^{-3} surface (Figure 3.6) extends across the entire basin, revealing the cyclonic SPG and northernmost anticyclonic STG circulation. Comparing the tropical and subtropical bands in Figures 3.5b and 3.6, it is evident that the influence of surface circulation is limited to north of 35°N. South 35°N the w_{Ek} no longer dominates the spatial patterns of the vertical motions in the intermediate ocean. Here, the w field has a spatial scale of a few degrees without coherent large-scale structure, in accordance with Ollitrault and De Verdière (2014). While the magnitude of the w field changes rapidly with depth within the upper tachocline, it remains relatively constant in the intermediate ocean (Figure 3.2). Between 40 and 50 °N, the vertical flow exhibits values of the same order of magnitude as within the upper tachocline. The equatorward and downward flow is associated with the STG shifted towards the north with depth (Stramma, 1984). In subpolar latitudes, the SPG cyclonic circulation is associated with upwelling.

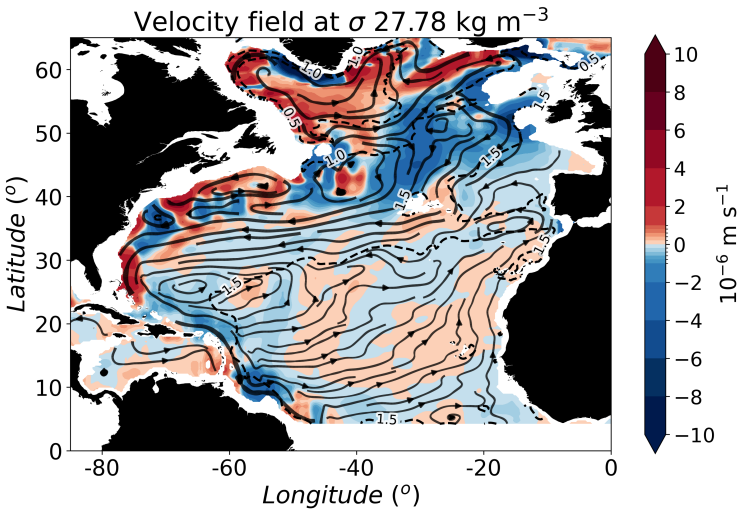

Figure 3.6: 56-year averaged velocity field from OCCITENS simulation over σ 27.78 kg m^{-3} representative of the intermediate ocean. Horizontal velocities are represented by streamlines and coloured-filled contours represent vertical velocities. The black-dashed contours represent the depth of the isopycnal surfaces (in kilometres). The equatorial band (0-5°N) has been masked.

Regarding the deep tachocline circulation in the deep ocean, Figure 3.7a displays the three-dimensional flow pathways over σ 28.05 kg m^{-3}. The western and eastern basins separated by the Mid-Atlantic Ridge (Figure 3.7b) show clockwise basin scale circulations constrained by the topography. Indeed, the interaction of the deep horizontal circulation with bathymetry generates a vertical velocity field at the bottom (Figure 3.7b), expressed as $w_B = -\mathbf{u}_B \cdot \nabla D$ (where $\mathbf{u}_B$ is the horizontal velocity vector at the seabed, and ∇D is the spatial gradient of the bathymetry) (Zhang and Vallis, 2007). Again, the similarities between the deep ocean and bottom vertical velocity fields (panels a and b in Figure 3.7) highlight that the deep ocean vertical flow is controlled by the bottom horizontal circulation and the varying bathymetry. This result is consistent with the high spatial correlation between the bottom and deep ocean vertical velocities obtained by Liang et al. (2017). However, note that the OGCM's reconstruction of the deep circulation has limited confidence. The deep and abyssal flows remain undersampled with scarce observations in the real ocean (Levin et al., 2019). Therefore, obtaining a clear large-scale picture of the climatological circulation within the deep ocean is challenging, and the patterns and amplitudes shown in Figure 3.7a should be interpreted with caution, as they are specific for the OGCM's case.

Given these three large circulation patterns, we aim to assess the extent to which the LVB characterises them and allows a relationship between the meridional and vertical flows.

3.2.1.4 Linear Vorticity Balance Validity Extension Across Averaged Periods

First, we analyse the multidecadal climatology of the two LVB terms within the upper tachocline-upper ocean, intermediate ocean and lower tachocline-deep ocean. This section seeks to evaluate the LVB as a function of depth, quantifying its ability to capture climatological ocean dynamics in layers that are remote from the impact of wind and bathymetry forcings. Moreover, this approach is expected to offer insights into regions within the basin where reconstructing the w field using an indefinite integral of the LVB is feasible, thus enhancing our understanding of circulation patterns. In the final subsection, we will explore the dependency of the extension of LVB validity to the average period.

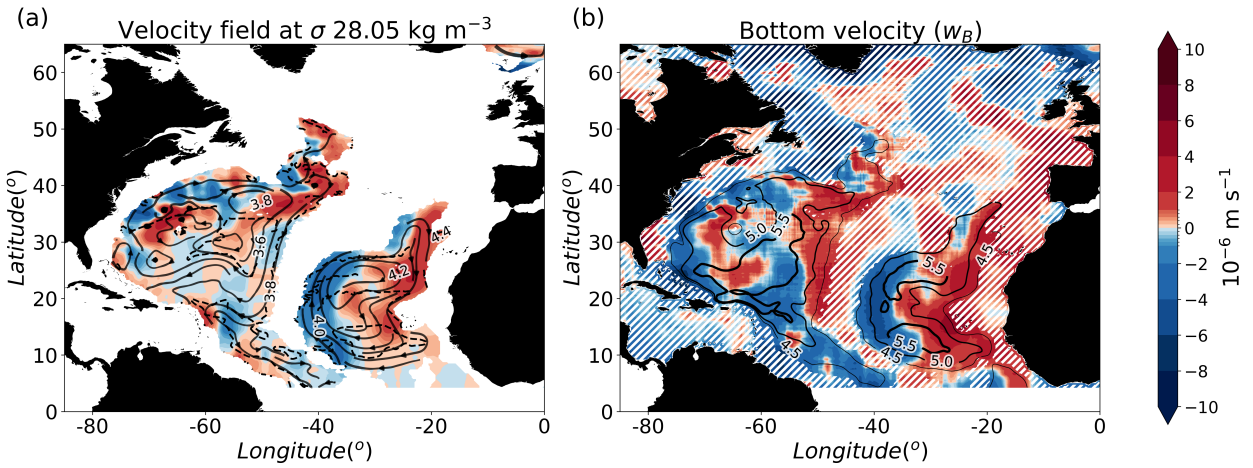

Figure 3.7: 56-year averaged velocity field from OCCITENS simulation over σ 28.05 kg m^{-3} representative of the deep ocean. The black-dashed contours in panel (a) represent the depth of the isopycnal surface (in kilometres). OGCM simulation vertical velocities on the deepest level (b). Note that Madec et al. (2017) uses the topographic induced vertical velocity (Zhang and Vallis (2007)). The contours in panel (b) indicate the seafloor depth at 4500, 5000 and 5500 m (from thinner to thicker contours). The dashed line in panel (b) represents the Mid-Atlantic Ridge border used to split the North Atlantic basin into western and eastern sub-basins. White hatching masks the regions above σ 28.05 kg m^{-3} for comparison purposes.

3.2.1.4.1 Upper Tachocline-Upper Ocean

The $|\Delta_{LVB}|$ displayed over σ 26 kg m^{-3} in Figure 3.8c allows us to unveil where and to what extent this balance characterises the 56-year averaged meridional and vertical circulation. The $|\Delta_{LVB}|$ exhibits values smaller than 10%, considered as LVB-valid regions, in the eastern part of the TG where the poleward Mauritanian Current (MC; Figure 3.4; Fernandes et al., 2005) and the basin-wide equatorward North Equatorial Current (NEC; Figure 3.4; Schott et al., 2002), except for the recirculation core of the gyre, adjacent to the Gulf Stream, with a much weaker flow. For these LVB-valid areas, it appears that the vortex stretching ($f\partial_z w$; Figure 3.8b) is balanced by the planetary vorticity transport (βv; Figure 3.8a). It corresponds to positive (negative) vorticity contribution over poleward (equatorward) flow regions. The sign of the vortex stretching term corresponds to the general downward decrease of the amplitude of the upper tachocline flow (Figure 3.2). In the northwestern part of the TG (solid contours in Figure 3.8b from 30-50°W and 10-15°N), the LVB holds within the NEC exhibiting negative $\partial_z w$ values, unlike the rest of the TG. The divergence of the equatorward flow in shallow layers (not shown) evacuates the downwelling waters from the Ekman layer, changing the sign of the vertical flow. This change displaces the gyre to the north and west with depth, as shown by Elmoussaoui et al. (2005). Note that the Ekman pumping-induced upwelling reaches 35°W at the surface, while the σ 26 kg m^{-3} upwelling in the upper tachocline's tropical gyre extends up to 50°W.

In order to integrate the LVB from the surface to the depth or sigma of interest, it must hold throughout the entire depth range. Therefore, we now examine the vertical extension of the LVB regimes in more detail. Figure 3.9 shows the zonal fraction of LVB valid area at each isopycnal surface and latitude. To address the Eastern Atlantic currents separately from the contribution of the western boundary currents that reduce this fraction, the North Atlantic basin is divided between western and eastern halves separated by the Mid-Atlantic Ridge (Figure 3.7b). To the south, it confirms that the TG departs largely from the LVB,

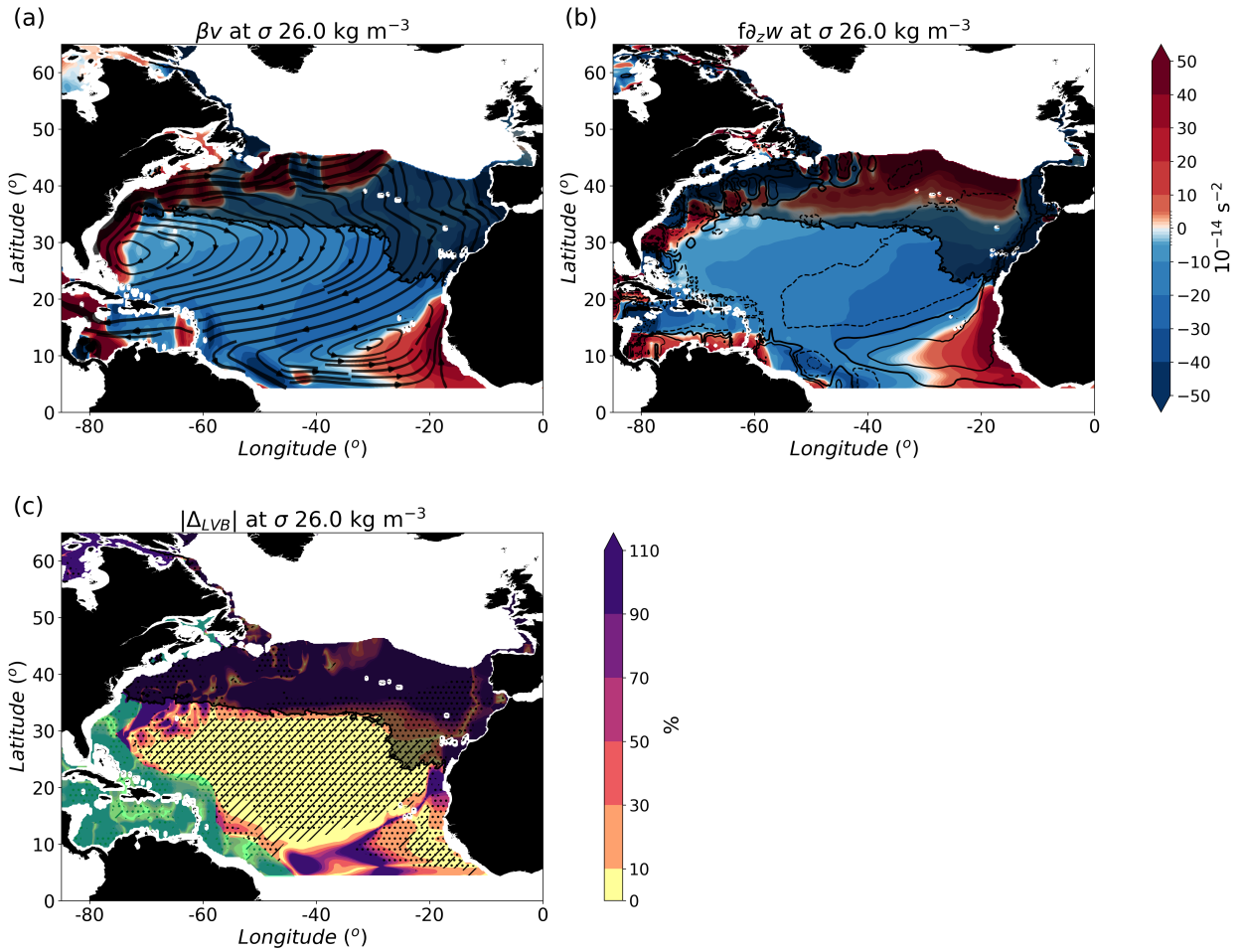

Figure 3.8: Time-mean 5° filtered LVB terms (advection of planetary vorticity and vortex stretching) and $|\Delta_{LVB}|$ (Eq. 3.1) (c) over σ 26 kg m^{-3} (a, b). Horizontal velocities are represented with streamlines over (a) panel (Same as Figure 3.5). Positive (continuous contours) and negative (dashed contours) vertical velocities have been plotted on panel (b). Dotted areas in panel (c) represent the regions where the meridional velocity field is in geostrophic balance with a relative error smaller than 10%. Hatched areas represent the regions where the geostrophic LVB is valid at 10%. The black and green translucent regions indicate the maximum mixed layer mask and the 4° width-band along the western boundary masked region for the zonal percentage extent of valid area computation.

except south of 12°N (Figure 3.9b) where the flow, corresponding to the MC, is essentially meridional. At tropical latitudes, the thermocline (and therefore the upper tachocline) is thin (Salmon, 1982), and the LVB hold accordingly over a shallower extension. However, in the North Equatorial Counter Current (NECC; Figure 3.4; Schott et al., 2002), with a predominantly zonal character, the zonal extent LVB's validity drops to a few spots with a maximum of 60% in the western tropical upper tachocline (Figure 3.9a). The LVB validity extends zonally across up to 90% of the basin until σ 27.1 kg m^{-3} in the central region of the subtropical band, between 20-30°N. Currents such as the equatorward Canary Current (CC; Figure 3.4; Stramma et al., 2005) and the NEC in the interior of the STG are almost entirely in LVB. At higher subtropical latitudes, between 30-35°N, in the vicinity of the Açores Current (AC; Figure 3.4; Klein and Siedler, 1989), the LVB accounts for about 80% of the zonal extent of the eastern and western sub-basins. The limited extent of LVB validity in the western half of the North Atlantic basin between 35-40°N (Figure 3.9a) illustrates the importance of non-linearities in the Gulf Stream. Moving between 40-50°N, the LVB

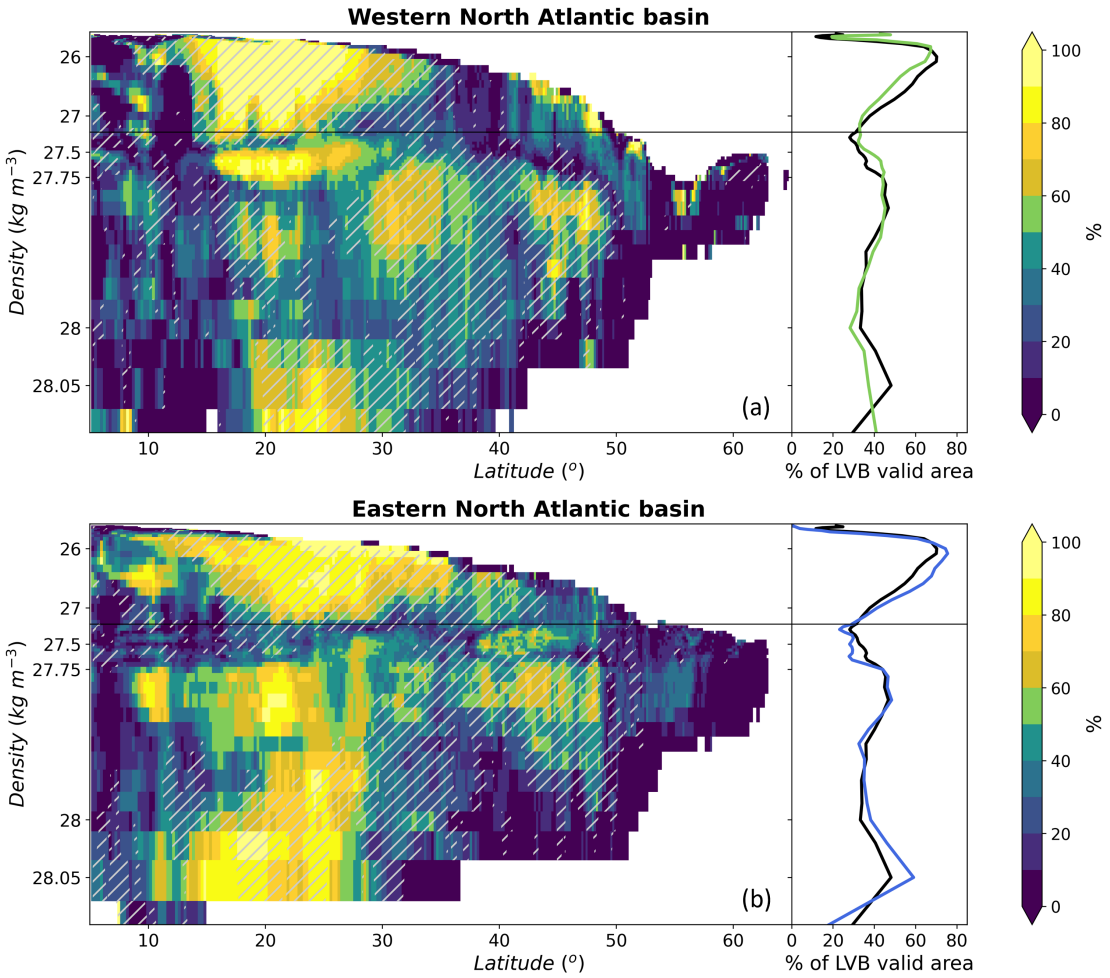

Figure 3.9: Zonal extent (%) of LVB validity (LVB relative error <10%) at each isopycnal surface level and latitudinal grid point (surface and subsurface tropical band not represented) considering only the western (a) and eastern (b) part of the North Atlantic basin defined by the Mid-Atlantic Ridge. The hatching represents net equatorward circulation when the meridional circulation is zonally averaged over solely LVB-valid regions. The distance between σ levels on the y-axis is proportional to their average width within the basin. Note a zoom between the surface and σ 27.1 kg m^{-3}. The red arrows indicate the isopycnal levels chosen as representative of the upper, intermediate and deep oceans. The coloured and black profiles within the side panels represent the (a) western, (b) eastern and complete basin percentage of LVB valid area at each sigma level.

also plays a significant role in the region where the poleward flow of the North Atlantic Current (NAC; Figure 3.4; Rossby, 1996) is found. It covers up to 90% of the zonal extent near the surface in the western basin below and more than 50% around σ 27.5 in the eastern basin.

In addition, to evaluate the capability of observation-based geostrophic meridional transport in describing vertical motions, the extent where the geostrophic component of the LVB (GLVB; Eq. 1.19) and the geostrophic balance (GB) can be considered valid ($|\Delta_{GLVB} = |0.5 \cdot (\beta v_g - f\partial_z w)/(|\beta v_g| + |f\partial_z w|) \cdot 100||$, $|\Delta_{GB}| = |0.5 \cdot (v_g - v_t)/(|v_g| + |v_t|) \cdot 100| < 10\%$) (depicted by hatched and dotted areas in Figure 3.8c). This analysis demonstrates that the LVB is geostrophic within the STG and the eastern part of the TG. The overall overlap of the areas where the GLVB and geostrophic balance are valid suggests that while the geostrophic balance is necessary to close the geostrophic linear vorticity balance, it may not be needed for the total case.

3.2.1.4.2 Intermediate ocean

As the flow decreases below the upper tachocline, one expects the smaller terms of the vorticity balance to become more important compared to the linear terms. However, there is a qualitative agreement between βv and $f\partial_z w$ terms over σ 27.78 kg m^{-3} (Figure 3.10a, b) away from the western boundaries where both terms are mainly positive. Further north, the sign changes, but the terms still agree quite well at first glance. Their values are one order of magnitude larger there than over the tropical and subtropical bands, associated with a more intense circulation. This circulation is predominantly southwestward between 30-50°N, below the North Atlantic Current, and northeastward at higher latitudes. They contribute respectively with positive and negative vorticity to the LVB.

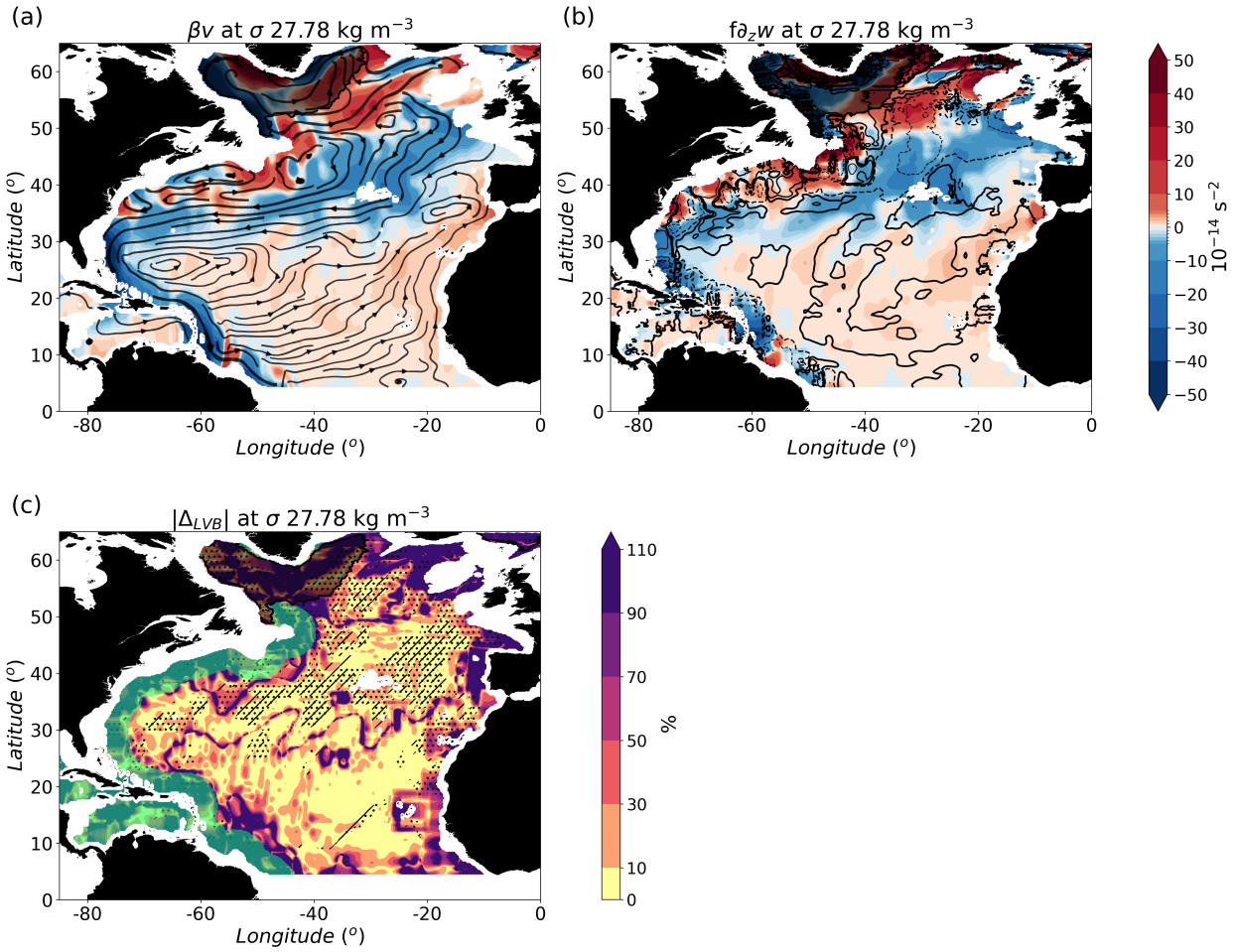

Figure 3.10: Time-mean 5° filtered LVB terms (advection of planetary vorticity and vortex stretching) and $|\Delta_{LVB}|$ (Eq. 3.1) (c) over σ 27.78 kg m^{-3} (a, b). Horizontal velocities are represented with streamlines over (a) panel (Same as Figure 3.5). Positive (continuous contours) and negative (dashed contours) vertical velocities have been plotted on panel (b). The dotted areas in panel (c) represent the regions where the meridional velocity field is in geostrophic balance with a relative error smaller than 10%. Hatched areas represent the regions where the geostrophic LVB is valid at 10%. The black and green translucent regions indicate the maximum mixed layer mask and the 4° width-band along the western boundary masked region for the zonal percentage extent of valid area computation.

Figure 3.10c shows that the LVB holds, but irregularly, across most of the eastern tropical, subtropical and extratropical bands, away from lateral boundaries. The discrepancy in the eastern boundaries, evident in the upper and intermediate ocean, is likely a result of the diabatic effect of eddy fluxes originating

from the eastern boundary currents (Cessi and Wolfe, 2013). The intermediate ocean exhibits smaller LVB-valid areas than the upper layers, particularly in the western half of the tropical-subtropical domain, where alternative meridional bands with relative error larger than 10% are visible. However, the LVB validity extends until reaching the northernmost region of the anticyclonic STG, around 55°N. The LVB zonal extent reaches up to 70% of the basin width away from the masked regions within the subtropical, extratropical and eastern tropical latitudes (Figure 3.9). Moreover, poleward of 50°N, the zonal extent of the LVB drops drastically, only accounting for only a maximum of 50% in the eastern half of the basin.

Regarding the nature of the LVB, as expected, one notices that the geostrophic component of LVB is dominant for geostrophic flow north of about 30° (Figure 3.10c). There, the steeper isopycnal surfaces (contours in Figure 3.6) compared with the subtropical and tropical bands drive more intense geostrophic currents.

3.2.1.4.3 Lower Tachocline-Deep ocean

In the lower tachocline-deep ocean, the validity of the LVB holds over most of the basin except in the Gulf Stream, its adjacent recirculation region and the narrower regions of the abyssal sub-basins within the tropics and mid-latitudes (Figures 3.9 and 3.11). The deep ocean upwelling and downwelling horizontal distribution is generally associated with negative and positive vortex stretching values, respectively, in contrast with the sign of this term in the upper ocean. Drawing a parallel with the upper tachocline within the upper ocean, the velocity field in the deep ocean, induced by the interaction of the varying topography and the horizontal circulation ocean bottom, diminishes towards shallower depths (see also Figure 3.2). This vertical shear matches the meridional transport direction in the areas where the LVB is valid within the deep ocean.

In such proximity to the seabed, the isopycnal surfaces are highly influenced by the topography, promoting larger horizontal density gradients (closer and topography following contours in Figure 3.6 compared with Figure 3.7a). Note that the GLVB (hatched regions in panel c) characterises large fractions of the deep circulation, particularly those associated with steeper topography.

In order to synthesise the results one step further, the zonal extent of valid LVB considering the whole North Atlantic basin is displayed in left panels (black lines) in Figure 3.9. The extent of LVB exhibits a prominent relative maximum in the upper tachocline, intermediate and deep oceans. The largest maximum is located in the upper tachocline at σ 26.25 kg m^{-3} with a valid zonal extent of over 70%. Two additional relative maxima above 50% of valid zonal extent occur in the intermediate ocean at σ 27.78 kg m^{-3} and in the deep ocean at σ 28.05 kg m^{-3}.

3.2.1.4.4 Sensitivity to averaged period length

The LVB validity analysis was conducted so far on the longest multidecadal climatological dataset available to us. However, it is often not feasible to obtain such a long time frame when using observations, reanalyses, or shorter runs. One limitation in the linear vorticity description of the ocean lies in the time required for the ocean adjustment, determined to first order by the propagation velocity of the first baroclinic

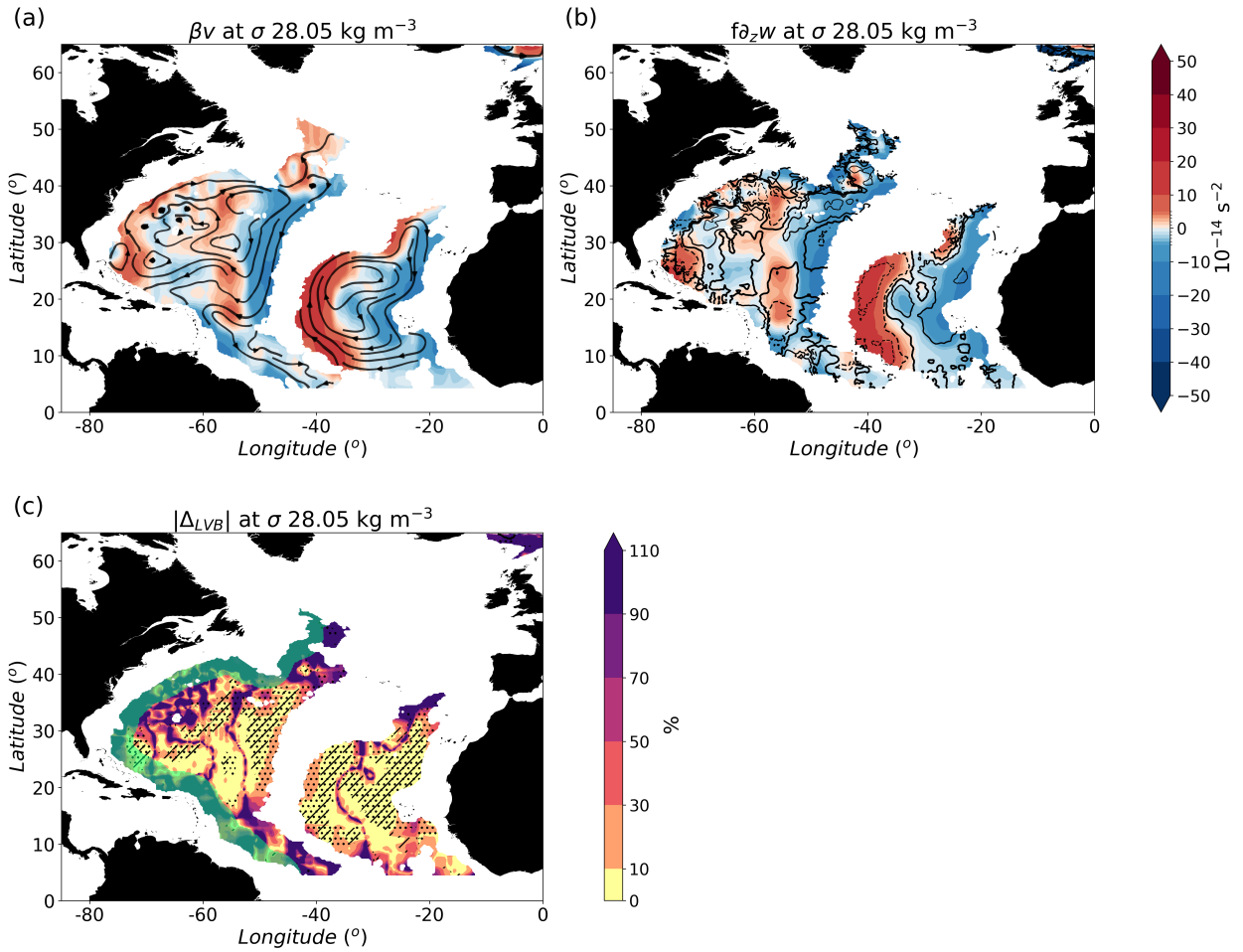

Figure 3.11: Time-mean 5° filtered LVB terms (advection of planetary vorticity and vortex stretching) and $|\Delta_{LVB}|$ (Eq. 3.1) (c) over σ 28.05 kg m^{-3} (a, b). Horizontal velocities are represented with streamlines over (a) panel (Same as Figure 3.5). Positive (continuous contours) and negative (dashed contours) vertical velocities have been plotted on panel (b). The dotted areas in panel (c) represent the regions where the meridional velocity field is in geostrophic balance with a relative error smaller than 10%. Hatched areas represent the regions where the geostrophic LVB is valid at 10%. The black and green translucent regions indicate the maximum mixed layer mask and the 4° width-band along the western boundary masked region for the zonal percentage extent of valid area computation.

Rossby wave, which decreases towards higher latitudes (Hughes and De Cuevas, 2001, Wunsch, 2011 and Thomas et al., 2014). Therefore, a sensitivity study as a function of the averaging period lengths and latitude is advocated.

In Figure 3.12, the temporal dependence of the LVB validity is assessed by computing its zonal extent as a function of the number of years in the climatology for three representative σ levels in the unmasked region, and averaged meridionally over four different latitudinal bands.

Within the upper tachocline, particularly the subtropical band, a large difference of about 20% is found between 1-year and 56-year climatologies, and each increment up to about 14 years significantly improves the results. Nevertheless, the extension of the LVB validity shows only a marginal increase of up to 7 years in the intermediate ocean and 3 years in the deep ocean. The decay of the extent of LVB validity in the upper tachocline is more noticeable in the subtropical band than in the tropical band (by a factor of ~ 4). However, the decrease in the validity extension within the intermediate ocean at shorter timescales is more pronounced in the tropics than in extratropics.

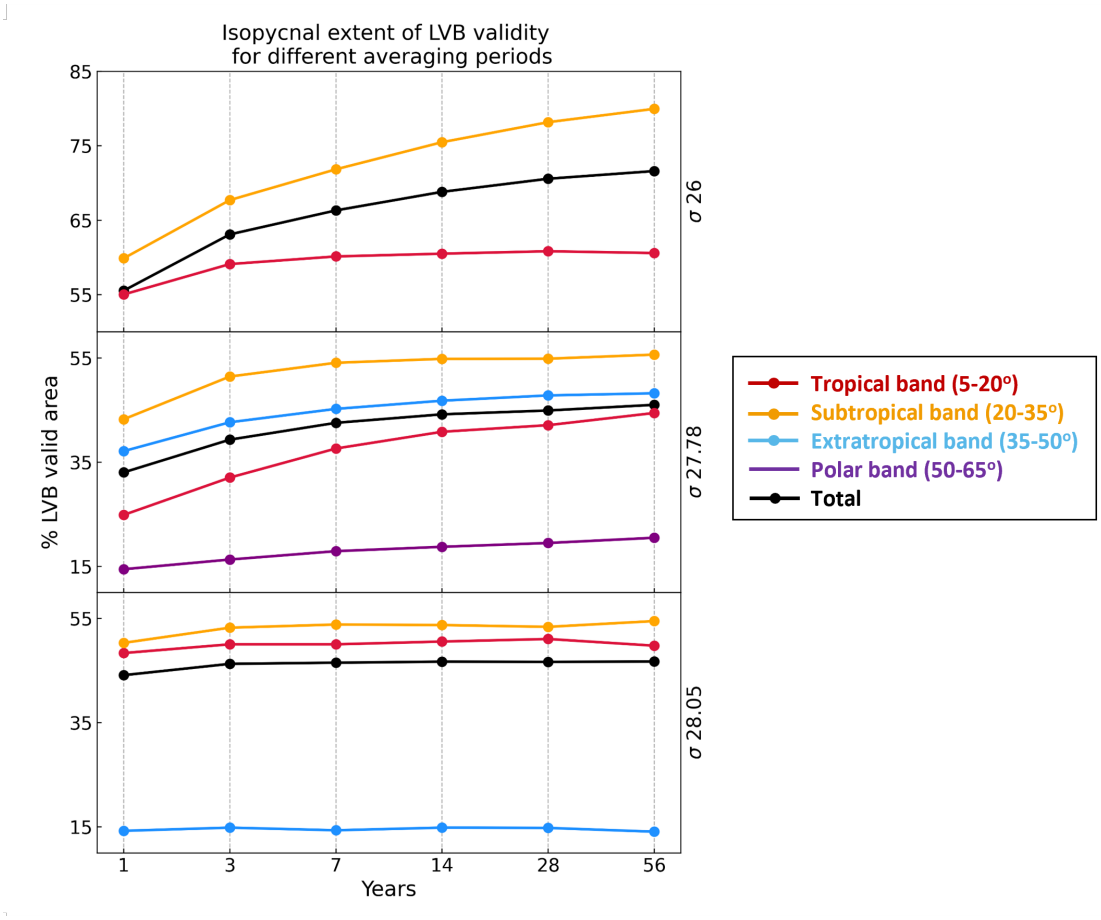

Figure 3.12: Mean zonal extent (%) of LVB validity dependent on the averaged period over the 5-20°N, 20-35°N, 35-50°N, 50-65°N bands and the full basin over σ 26 (a), 27.78 (b) and 28.05 (c) kg m^{-3}.

3.2.1.5 Discussion on the Relevance of the Linear Vorticity Balance for Interpreting the Ocean Circulation

The large domain within the upper tachocline in GLVB allowed us to explain the major currents of the North Atlantic by revisiting the principles of the linear theory of large-scale circulation. By flowing equatorward, the geostrophic component of currents like the NEC, the CC and the AC are divergent, absorbing downwelling Ekman Layer waters accordingly. To the contrary, poleward currents like the NECC and the MC converge and provide upper ocean waters to balance the divergent Ekman transport above, feeding the local TG upwelling. Thus, the applicability of the LVB suggests that the direction of the geostrophic meridional component of the flow of the upper tachocline is influenced by both the sign of the divergence of the Ekman transport above and the decrease in vertical velocity amplitude with depth across the upper tachocline. This latter view corresponds to the classic interpretation of the Sverdrup balance when applied to the upper ocean.

The LVB brings a novel baroclinic analysis of the classical barotropic description of the ocean made by the Sverdrup balance. However, let's recall that the Sverdrup balance needs the LVB and proper boundary conditions. The extensive areas within the upper tachocline identified in LVB are comparable to valid regions observed in Sverdrup balance studies using reanalyses (Wunsch, 2011 and Thomas et al., 2014) or observation-based dataset (Gray and Riser, 2014). Nevertheless, the eastern part of the TG,

described by the LVB in this study, does not satisfy the Sverdrup balance according to previous studies such as Wunsch (2011) and Gray and Riser (2014). Such apparent contradiction for flow in LVB occurs when the w field, chosen as boundary condition to close the Sverdrup balance, is inaccurately estimated. This poorly constrained boundary w field is often at the bottom thermocline (e.g. Kounta et al., 2018), but it can also be the surface w field. The latter generally suffers from considering the Ekman pumping as the sole contributor to the vertical flow in the Ekman layer while neglecting the contribution of the β-plane geostrophic divergence, as explained in the present study.

The departure from the LVB at the large spatiotemporal scales analysed in the present paper can be only explained by the importance of non-linear terms in the vorticity balance (Eq. 3.2). Previous researchers have turned to a barotropic approach to investigate their contribution. Numerous studies have studied the barotropic vorticity balance (BVB) to address the vorticity source and sink mechanisms that the Sverdrupian description of the ocean cannot fully account for.

In both the Gulf Stream region and the SPG, the LVB does not hold along the entire water column (panel c in Figures 3.8, 3.10 and 3.11). In these areas, additional terms are needed to close the vorticity budget. In the Gulf Stream, the bottom pressure torque (BPT) effectively balances the barotropic planetary vorticity advection, with the wind forcing being negligible (e.g. Hughes and De Cuevas, 2001, Gula et al., 2015 and Schoonover et al., 2016). Regarding the SPG, Le Corre et al. (2020) demonstrates that the bathymetry forcing (bottom drag curl) and atmospheric forcing, although with lesser influence, are needed to balance the BPT contribution. The observed reduction in the validity extent of the LVB at shorter timescales, visible in Figure 3.12, may be attributed to the influence of small-scale non-linear flows within the open ocean. Similarly, a model study by Khatri et al. (2023) evidences an increase in non-linear dynamics when diminishing the scale of the low-pass filter. These results are coherent with the fact that oceanic flows' temporal and spatial dimensions often vary with a certain level of proportionality (e.g. Dickey, 1991). A key question remains whether OGCM grid's spatial resolution might change the vorticity balance significantly, even after low-pass space filtering.

Over a substantial portion of the open ocean STG where we have shown that the LVB holds, previous studies (e.g. Sonnewald et al., 2019 or Khatri et al., 2023) evidence the necessity of the BPT to close the vorticity budget. To further compare our baroclinic results with barotropic studies, we may also refer to studies considering the depth integration of the vorticity balance (DIVB; see Section B.2 in Appendix B). In Waldman and Giordani (2023), a comparison between the BVB and DIVB approaches supports the equivalence at first order between the bottom pressure torque (BPT) term and the bottom vortex stretching ($f w_b$; where w_b is the vertical velocity at the bottom of the ocean, and being the bottom boundary condition of the $f\partial_z w$ term). Therefore, the mainly geostrophic horizontal velocities at the deep ocean close to the lateral boundaries (dotted surfaces in Figure 3.11c), together with the minimal contribution of non-linear terms to the deep ocean vorticity budget (small $|\Delta_{LVB}|$ in Figure 3.11c), allows considering that the BPT is equal to the bottom vortex stretching (Zhang and Vallis, 2007). Consequently, the large volume of the tropical and subtropical ocean explained by the LVB throughout the water column aligns with the regions where the Sverdrup and Topographic Sverdrup balances (where BPT closes the Sverdrup balance budget; Holland (1967)) hold within the open ocean (Khatri et al., 2023).

3.2.1.6 Summary on the OGCM LVB Validity

In this numerical study based on an eddy-permitting OGCM simulation, we have shown that the linear vorticity balance (LVB) approximation, spatially filtered with a 5° low-pass filter and averaged over 56 years, is valid within the upper ocean across most of the STG and eastern TG. The dominance of the LVB diminishes in the intermediate ocean, particularly at tropical latitudes and the western half of the basin. In the deep ocean, the topography-induced circulation is largely explained by the LVB, notably over the abyssal plains. Throughout the entire water column, significant departures from the balance are observed in the Gulf Stream region, the equatorial band, the subpolar gyre, and regions with a mainly zonal flow. Here, the vorticity equation can no longer be assumed linear, and the non-linear terms, not studied in the present work, become essential to close the vorticity budget. Over the upper ocean, the mainly geostrophic nature of the LVB determines how the meridional component of the flow responds to the geostrophic vertical divergence. However, the geostrophic LVB holds over more limited extensions within the intermediate ocean and the deep tachocline, reducing its *a priori* usefulness in deriving the geostrophic w from the geostrophic flow below the upper tachocline.

The duration of the averaging period conditions the occurrence of the LVB, although not in a uniform way. A general degradation in the extent of LVB validity occurs when the average period is reduced, with the maximum reduction observed being 20% within the upper ocean. This reduction may be attributed to the enhancement of small-scale structures at shorter timescales. Nevertheless, the increase in LVB-valid extension becomes marginal after several decades, decreasing to 3 years in the intermediate and deep ocean.

The extensive validity of the geostrophic LVB within the upper and lower tachoclines implies that the linear theory of large-scale circulation offers a simple yet reliable explanation for the direction of the meridional geostrophic flow. In the upper tachocline, a convergent (divergent) flow is needed to feed (absorb) the Ekman layer's upward (downward) pumping. This condition, in turn, establishes the direction of the geostrophic meridional flow since only the poleward (equatorward) flows are convergent (divergent). It corresponds to the mere satisfaction of the continuity equation for geostrophic circulation. A similar interpretation can be applied to circulation in vast portions of the deep ocean tachocline when considering the sign of the bottom vertical velocity.

3.2.2 Complementary diagnostics and analyses over the North Altantic basin

3.2.2.1 Decomposition of Linear Vorticity Balance into Geostrophic and Ageostrophic Components

The geostrophic meridional velocities alone do exhibit a weaker capacity in balancing the vortex stretching generated by the vertical motions compared with the total component (Figures 3.8, 3.10 and 3.11). As a result, a question arises concerning the role of ageostrophic meridional velocities in compensating for the insufficiency of geostrophic velocities in specific regions to balance the vortex stretching contribution. This section focuses on the impact of ageostrophic meridional movements on the closure of the linear vorticity budget.

The geostrophic planetary advection (βv_g) depicted in Figure 3.13 exhibits comparable spatial features and intensities when compared to the total advection of planetary vorticity (panel a in Figures 3.8, 3.10, and 3.11), even in regions where the meridional flow is not geostrophic.

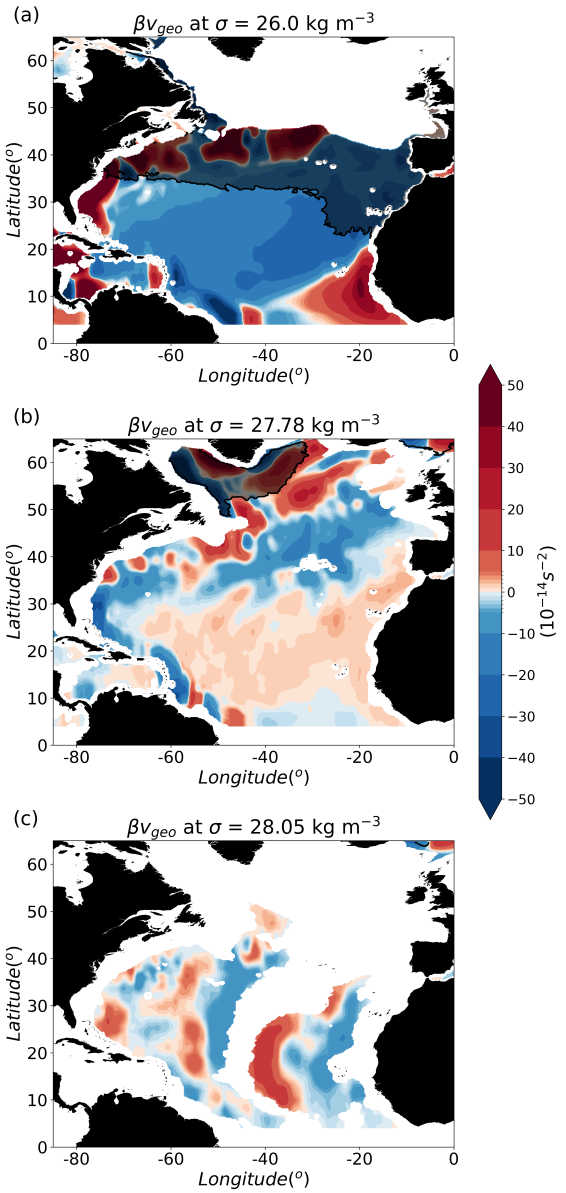

Figure 3.13: Time-mean 5^o filtered geostrophic advection of planetary vorticity (βv_g) over σ 26 (a), 27.78 (b) and 28.05 (c) kg m^{-3}. The black translucent regions indicate the maximum mixed layer mask.

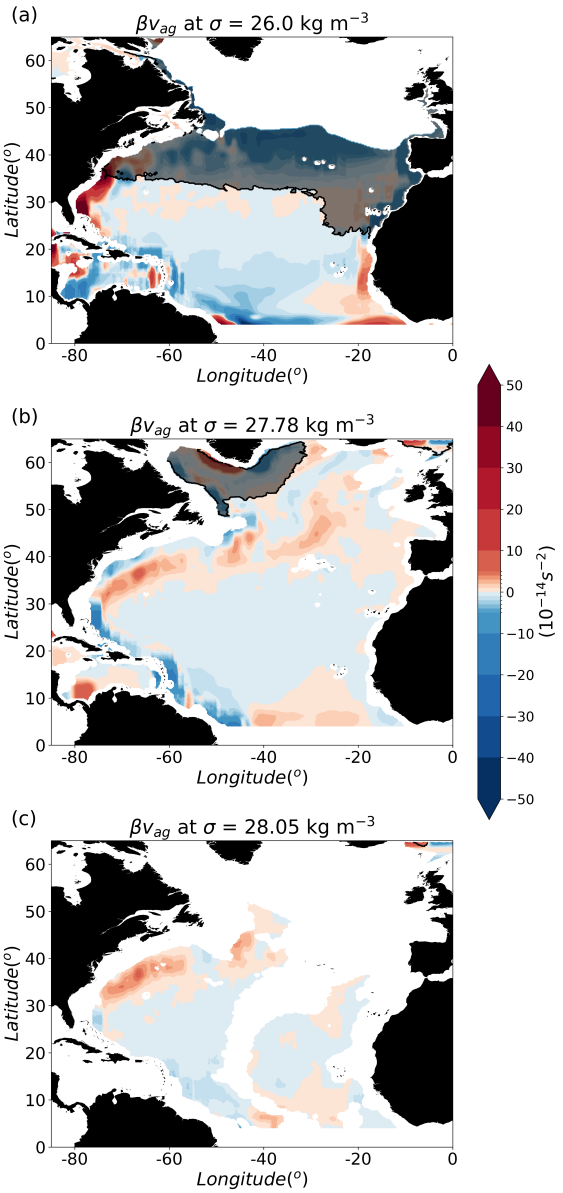

Figure 3.14: Time-mean 5^o filtered ageostrophic advection of planetary vorticity (βv_{ag}) over σ 26 (a), 27.78 (b) and 28.05 (c) kg m^{-3}. The black translucent regions indicate the maximum mixed layer mask.

In contrast, the ageostrophic component of the advection of planetary vorticity (βv_{ag}; Figure 3.14), computed as the residual between the total and geostrophic components of the velocity, maintains the same spatial pattern sign throughout the water column. The βv_{ag} term exhibits a positive contribution to the vorticity in the TG and the Gulf Stream below the mixed layer and a negative value within the STG region, resulting in a contribution to the vorticity budget of the same sign to the geostrophic term within the upper tachocline. The extratropics and SPG exhibit a higher level of complexity: In the northernmost part

of the STG, there is a positive contribution; additionally, a substantial positive vorticity value is observed in the western coastal region of the SPG, while a negative influence is detected along the southeastern coast of Greenland (Figure 3.14a).

To evaluate the contribution of the ageostrophic term in the closure of the vorticity budget, the median ratio between the ageostrophic and geostrophic contribution of the planetary vorticity advection is computed in the regions where the LVB is valid, but its geostrophic component (GLVB) is not. Figure 3.15a illustrates how, within the upper tachocline, the percentage of valid area using total and geostrophic LVB is very similar. In the LVB valid regions where the geostrophic LVB is not maintained, the ageostrophic component of βv helps the geostrophic component to balance the vortex stretching marked by the positive values of the 30th/70th percentile region between 5-25% (Figure 3.15b).

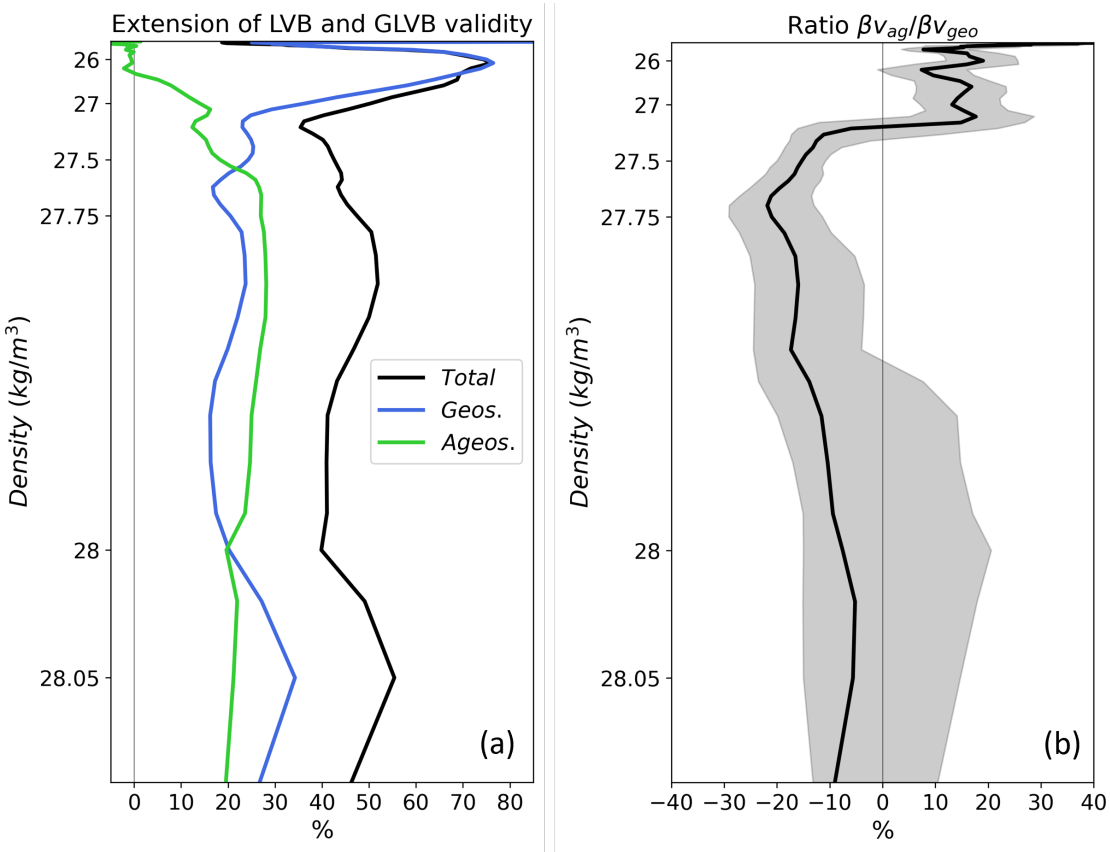

Figure 3.15: Percentage of LVB (black), geostrophic LVB (blue) valid area and their difference (green) at each sigma level (a). Median of the percentage of the ratio between ageostrophic and geostrophic components of the advection of planetary vorticity ($\beta v_{ag}/\beta v_g \times 100$ (solid line)) within the LVB valid areas excluding the GLVB valid areas. The shaded envelope contains the values of the percentage of the ratio between percentiles 30th and 70th (b).

Below σ 26.5 kg m^{-3} towards deeper layers (Figure 3.15a), the strength in describing the ocean of the geostrophic LVB decay faster than the LVB (approx. between 10-30%), being able to hold in only around 20% of the intermediate ocean and up to 35% in the deep ocean. Again, between σ 27 and 27.25 kg m^{-3}, the ageostrophic component helps βv_g to absorb the vorticity generated by the vortex stretching term. Below these depths, the ageostrophic advection of planetary vorticity opposes the geostrophic term by absorbing the vorticity generated by the geostrophic currents unbalanced by the vortex stretching (Figure

3.15a). Analysing the whole intermediate ocean, the ageostrophic term appears to extract between a median of 10% in the upper intermediate ocean and 20% in the lower intermediate ocean of the vorticity generated by the geostrophic component.

Both the percentage of the area where the ageostrophic component is needed for the LVB to be valid and its median contribution decreases towards the deep ocean (Figure 3.15). The decrease of the median is due because the ageostrophic contribution brings vorticity of the same negative sign throughout the basin (Figure 3.14), while the geostrophic contribution changes sign following the circulation around the basins (Figure 3.7), resulting in weaker spatial synchronicity between the ageostrophic and geostrophic components in the studies areas compared with shallower depths (shaded envelope in Figure 3.15b). Focusing on both sides of the Mid-Atlantic Ridge at the deep ocean (Figure 3.14c), as an example, the ageostrophic term extracts vorticity from the geostrophic component in the eastern side of the ridge, where the geostrophic velocities contribute with positive vorticity. The ageostrophic component adds to the geostrophic counterpart in the western side, where they have the same negative contribution.

In conclusion, the ageostrophic component of the meridional velocity has a small contribution to the absolute value of the vorticity provided; but a non-negligible impact on the agreement between the terms of the LVB, especially when using a limit as restrictive as $|\Delta_{LVB}| < 10$. Its impact, both in extent and amplitude, is greatest in the intermediate layer, where the total meridional velocities are smaller than in the upper tachocline and the deep ocean. These findings enable a transition from a qualitative comparison of the LVB and GLVB (Section 3.2.1.4) to a quantitative assessment. This quantitative evaluation can provide reasoning for the errors that may arise when using solely the geostrophic meridional velocity field to estimate vertical velocities, as will be discussed in Chapter 4.

3.2.2.2 Expanding the Frontiers of the Linear Vorticity Balance equation: Contribution of the non-linearity

This section was conducted at the University of California Los Angeles (UCLA) in May and June 2023, with the generous support and guidance of Professor Jonathan Gula.

The depth-dependent analysis of the LVB at large scales has shown its limitations in describing the dynamics in the Gulf Stream region, the SPG and the mainly zonal flow areas in the western tropical band, as well as in the scenario where the analysed scales are reduced below 5° discussed in Section 3.2.1.2.2. Trying to unravel the physics that drives these regions, it is proposed in this section the analysis of the contribution of the non-linear, mixing and time-dependent terms in the vorticity equation (Eq. 3.2) to close the vorticity budget where the LVB does not hold (see Section 3.2.1.4). Due to the need to minimise the error in the non-linear vorticity balance terms during time averaging, a CROCO OGCM simulation with a 12h time step computation during 2003 is used (see Chapter 2 for details). The large extension of the areas explained by the LVB, even when considering annual timescales (Section 3.2.1.4.4), allows exploring the vorticity balance validity using a one-year simulation This approach is adopted due to the limitations in computing power and available time. The simulation yields yearly averages of the online computed momentum terms from the horizontal momentum equation:

$$\partial_t \boldsymbol{u}_h + (\boldsymbol{u}\nabla)\boldsymbol{u}_h + (f\hat{k}\times\mathbf{u}_h) = -\frac{1}{\rho}\nabla_h p + \frac{1}{\rho}[\rho A_h \nabla^2 \boldsymbol{u}_h + \rho A_v \partial_z^2 \boldsymbol{u}_h] \tag{3.5}$$

where f is the Coriolis parameter, $\mathbf{u}$ and $\mathbf{u}_h$ are the 3D and horizontal velocity field respectively where u, v, w are the zonal, meridional and vertical components of the velocity. A_h and A_v are the horizontal and vertical turbulent viscosity coefficients, respectively. The terms on the left-hand side of Eq. 3.5 are the momentum time variation, the non-linear advection of momentum and the Coriolis term. On the right side of Eq. 3.2, the terms are the pressure gradient, horizontal diffusion and vertical mixing of momentum. Applying the curl to Eq. 3.5 allows retrieving the vorticity equation. When the curl is applied, the momentum term associated with the pressure is removed.

$$\partial_t \zeta + \nabla \times (\boldsymbol{u}\nabla)\boldsymbol{u}_h + \nabla \times (f\hat{k} \times \boldsymbol{u}_h) = \frac{1}{\rho}\nabla \times [\rho A_h \nabla^2 \boldsymbol{u}_h + \rho A_v \partial_z^2 \boldsymbol{u}_h] \tag{3.6}$$

From left to right, the terms correspond to the time rate of the vorticity term, non-linear advection term, Coriolis term, vertical mixing term and horizontal diffusion term. In this study, the vorticity terms are computed at horizontal levels rather than the inherent bathymetry following levels of the CROCO simulation.

Note that while Eq. 3.2 and Eq. 3.6 both represent the vorticity balance, the Eq. 3.2 expresses the decomposition of the advection and Coriolis terms. The only available variables from the CROCO simulation were the momentum trend diagnostics stored as annual mean. This constraint impedes the computation of fully decomposed terms in the vorticity balance (Eq. 3.2), necessitating the utilisation of the three-dimensional velocity field at high frequencies. Nonetheless, the computation of the low-frequency decomposed terms can provide an order of magnitude for the vorticity contribution.

Combining Eq. 3.2 and 3.6, it is possible to decompose the Coriolis and non-linear advection terms. The rotational of the Coriolis term (Eq. 3.7) arises as the residue of the LVB (Eq. 3.1):

$$\nabla \times (f\hat{k} \times \boldsymbol{u}_h) = \beta v - f\partial_z w \tag{3.7}$$

In the areas where the LVB is valid (panel c in Figures 3.8, 3.10 and 3.11), this residual value is expected to be at least one order of magnitude smaller than the contributions of the advection of planetary vorticity and vortex stretching terms. Furthermore, the curl of non-linear advection of momentum can be expressed as follows:

$$\nabla \times (\boldsymbol{u}\nabla)\boldsymbol{u}_h = \boldsymbol{u}\nabla\zeta + \hat{k}[\nabla_h w \times \partial_z \boldsymbol{u}_h] - \zeta\partial_z w \tag{3.8}$$

The decomposition of the non-linear advection of momentum results in the advection of relative vorticity, vortex tilting and relative vortex stretching terms. Additionally, it is possible to further decompose the non-linear advection term into its vertical and horizontal contributions:

$$\nabla_h \times (\boldsymbol{u}_h\nabla_h)\boldsymbol{u}_h = \boldsymbol{u}_h\nabla_h\zeta - \zeta\partial_z w \tag{3.9}$$

$$\nabla_h \times (w\partial_z)\boldsymbol{u}_h = w\partial_z\zeta + \hat{k}[\nabla_h w \times \partial_z \boldsymbol{u}_h] \tag{3.10}$$

Therefore, the vortex stretching relative to the relative vorticity ($\zeta\partial_z w$), along with the horizontal advection of the relative vorticity ($\mathbf{u}_h\nabla_h\zeta$) can be determined from the rotational of the horizontal advection of momentum (Eq. 3.9). Conversely, the vertical advection of relative vorticity ($w\partial_z\zeta$) and the vortex tilting term ($\hat{k}[\nabla_h w \times \partial_z \boldsymbol{u}_h]$) are solely derived from the rotational of the vertical advection of momentum (Eq. 3.9). This approach allows isolating the terms that contain the variable w without its vertical derivative and analysing their impact on the vorticity budget. Proving that the vorticity contribution of these terms is negligible compared to the terms dependent on the vertical gradient of w would enhance the LVB framework for estimating vertical velocities through the Indefinite Depth-Integrated LInear Vorticity (IDILIV) approach (see Chapter 4) while maintaining the same formalism.

Since the goal here is to reconstruct the vertical velocity field from observations, and given the limited observations below 1500 m depth, the analysis will be concentrated on the upper ocean. Referring to the isopycnal surface depths of the sigma levels in Figures 3.5 and 3.6, the σ 26 and 27.78 kg m^{-3} poleward 40°N fall within the region of interest. The time-average 5° filtered terms of the vorticity equation (Eq. 3.6) over σ 26 kg m^{-3} from CROCO simulation is presented in Figure 3.16. There is no need for *a priori* filtering since no approximations are applied to the vorticity balance. However, it permits focusing on unveiling the dominant non-linear contributors to the vorticity at large scales where the terms in the LVB are insufficient to close the vorticity budget, as demonstrated in Section 3.2.1.4.1.

To further illustrate the dependence of spatial scales on the vorticity balance terms, Khatri et al. (2023) demonstrated that a stronger kernel enhances the barotropic linear contributions to the vorticity budget closure while diminishing the influence of non-linear terms. The expansion of the areas explained by a barotropic linear description at larger spatial scales is coherent with the increased LVB validity extension in the centre of the gyres with longer averaging periods (see Section 3.2.1.4.4). This finding indicates that the spatial scale selection and the timescale play a significant role in shaping the contributions to the vorticity balance.

The Coriolis (Figure 3.16c) and non-linear advection (panel b) terms account for almost all the vorticity in the upper ocean regions below the mixed layer (panel g) except for the eastern boundary where the vertical mixing (panel d) is needed to close the vorticity budget. The Coriolis term exhibits remarkable similarity to the relative error previously obtained with the NEMO OCCITENS simulation (Figure 3.8), displaying small values in the regions where the LVB is valid ($|\Delta_{LVB}| < 10\%$) and large values along the lateral boundaries and the western part of the tropical band.

Both small departures within the LVB valid areas defined in Section 3.2 and the large departures in the areas where the LVB does not hold are mainly balanced by the non-linear advection term. Concerning the rest of the vorticity balance terms, the time rate of the relative vorticity (Figure 3.16a), vertical mixing (panel d) and horizontal diffusion (panel e) term are completely negligible in the open ocean and the Gulf Stream region below the mixed layer (translucent black region in Figure 3.16). In the western part of the tropical band, the vertical mixing and horizontal diffusion terms offer a marginal but necessary contribution compared with the non-linear advection and Coriolis terms. Close to the eastern boundary, the vertical mixing term exhibits a similar magnitude to the non-linear and Coriolis terms. An apparent contradiction appears in this region when comparing the small relative error in the NEMO OCCITENS study (Figure 3.8c) with the non-negligible LVB residue (Figure 3.16c). However, the stronger upwelling near the African coast, compared to the rest of the TG region, contributes to the relative error reduction.

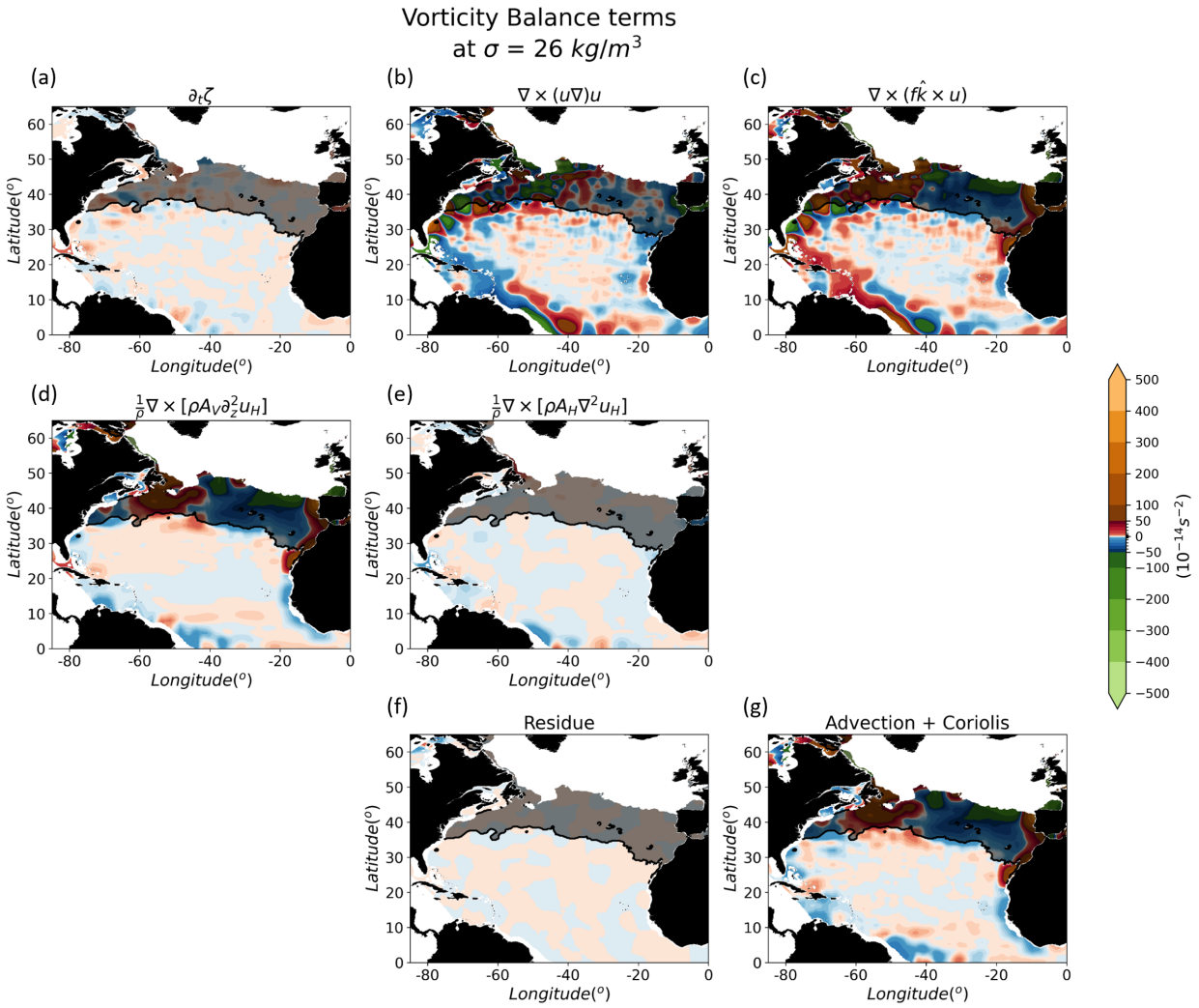

Figure 3.16: Time variation of relative vorticity (a), non-linear advection of vorticity (b), Coriolis term (c), vertical mixing (d), horizontal diffusion (e) from Eq. 3.6, their residue (f) and the residue between non-linear advection and Coriolis terms (g) over σ 26 kg m^{-3}. The black translucent regions represent the areas above the 2003 winter mixed layer defined by the NEMO OCCITENS simulation.

The online analysis prompts the question of which vorticity term within the non-linear advection term (Eqs. 3.9 and 3.10) dominates the vorticity contribution. To address this, the non-linear advection term averaged over one year is decomposed (Figure 3.17). The decomposition reveals that the horizontal components of the advection of relative vorticity (panels a and b) emerge as the dominant contributors to the vorticity budget everywhere. These terms, which generally exhibit an opposite nature (see colorbar in Figure 3.17), are largely compensating each other in the regions where the LVB terms agree to a good order of approximation. In contrast, the vertical component of the relative vorticity advection, the relative vortex stretching, and the vortex tilting term (panels c-e) are completely negligible in the interior of the open ocean. This decomposition unveils the critical role played by the horizontal advection of relative vorticity in balancing the effects of small-scale structure in the open ocean poorly explained by the LVB, reinforcing the importance of the LVB in explaining the large-scale dynamics.

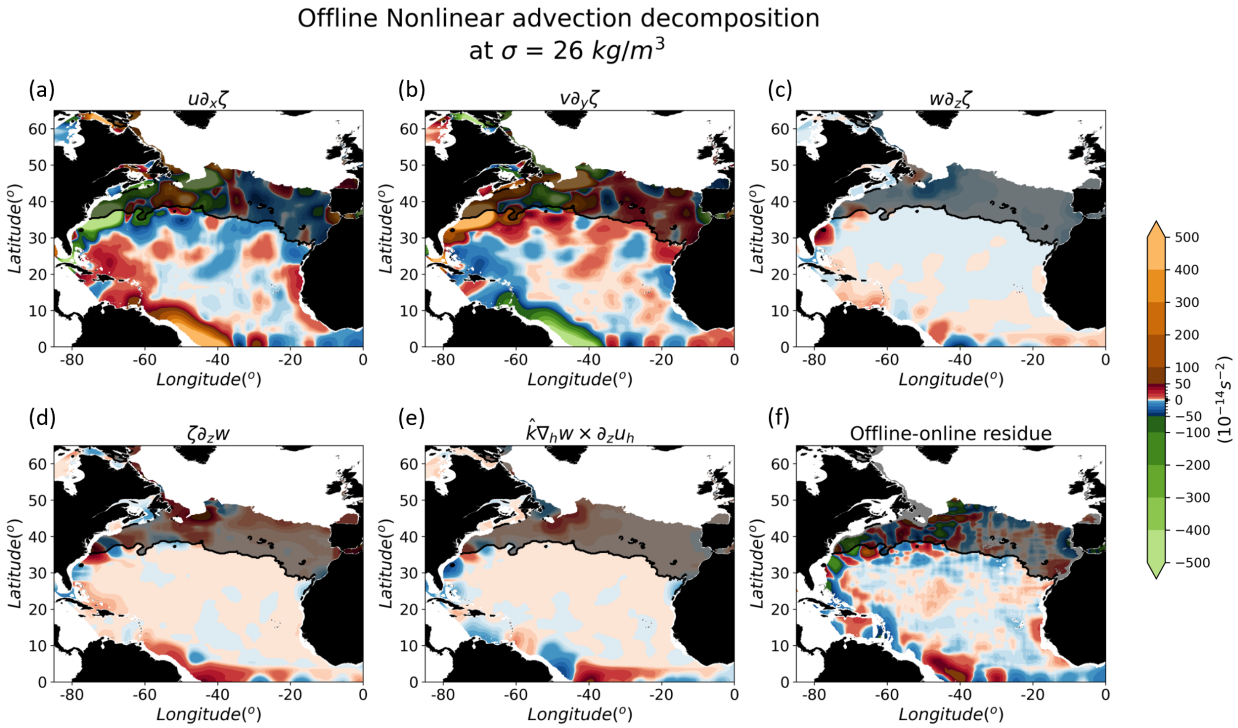

Figure 3.17: Offline-computed zonal advection of relative vorticity (a), meridional advection of relative vorticity (b), vertical advection of relative vorticity (c), relative vortex stretching (d), vortex tilting (e) from Eqs. 3.9, 3.10 and (f) residual between the online and offline non-linear advection term over σ 26 kg m^{-3}.

In the Gulf Stream region, known for large horizontal velocities featuring meanders and eddies, the LVB fails to fully explain the dynamics, even when large filtering is applied (Figure 3.8). The large horizontal velocities in the Gulf Stream give rise to the meridional and zonal advection of relative vorticity that can reach values two orders of magnitude larger than the values of the LVB terms for the interior of the oceanic gyres (see colorbar in Figure 3.17). In this region, the horizontal advection of relative vorticity (panels a and b) exhibit an opposing pattern of vorticity contribution. However, they do not fully balance each other. Thus, they contribute to close the vorticity budget, effectively subtracting the LVB residual (Figure 3.16). This finding aligns with Lu and Stammer (2004) that assessing the barotropic vorticity balance in three distinct ocean layers demonstrates how the non-linear advection plays a significant role in balancing the Coriolis residue in the upper ocean layer. Indeed, the primary contribution of the horizontal advection of relative vorticity obtained here diverges somewhat from the works centred in the barotropic vorticity balance, such as Gula et al. (2015), where the Bottom Pressure Torque (BPT) is identified as the key term responsible for closing the Coriolis residue. In their work, the non-linear advection term opposes the BPT, being necessary to close the vorticity. However, it is not the dominant term.

The remaining terms in Eq. 3.8, vertical advection of relative vorticity, relative vortex stretching and vortex tilting, obtained from the decomposition of the non-linear advection (panels c - e in Figure 3.17) are not negligible in the Gulf Stream region and the western tropical band. The vertical advection of vorticity and the vortex tilting term exhibit quite similar but opposite contributions in the Gulf Stream. Similarly, the relative vortex stretching term seems to absorb the vorticity generated by the vortex tilting term in the western tropical band. Note that the relative vortex stretching term subtracts the vorticity according to the negative sign in Eq. 3.8 (Figure 3.17).

Therefore, within the upper tachocline, the closure of the vorticity budget is primarily driven by the horizontal advection of relative vorticity. Indeed, the strength of the non-linear contribution found in this study may appear relatively stronger compared to studies that isolate the upper tachocline from the bottom contribution. As highlighted by Yeager (2015), who compares the magnitude of the different terms in the barotropic vorticity balance using a coarse and high-resolution model, revealed that the non-linear advection term exhibits a larger contribution in the high-resolution case. In addition, Smith et al. (2000) supports that higher resolution models provide a more accurate representation of mesoscale eddy energy in both magnitude and geographic distribution.

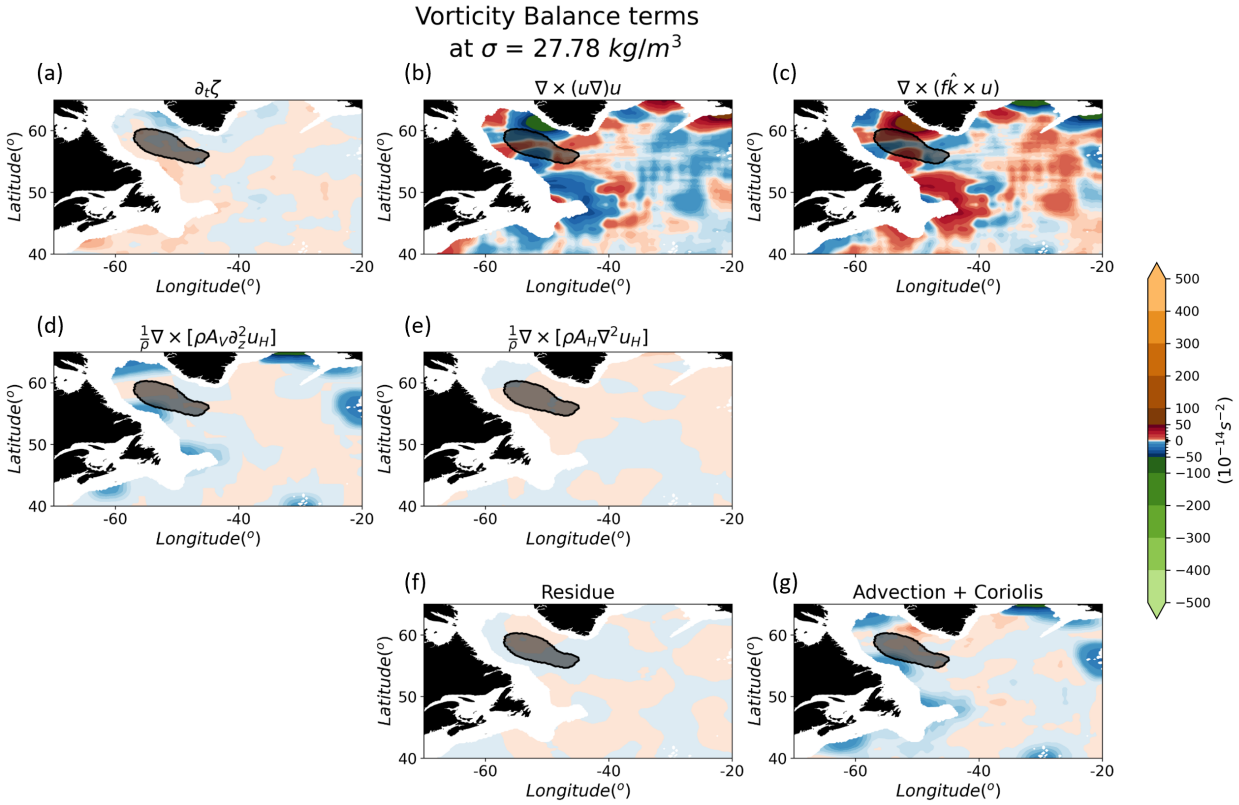

Figure 3.18: Time variation of relative vorticity (a), non-linear advection of vorticity (b), Coriolis term (c), vertical mixing (d), horizontal diffusion (e) from Eq. 3.6, their residue (f) and the residue between non-linear advection and Coriolis terms (g) over σ 27.78 kg m^{-3}. The black translucent regions represent the areas above the 2003 winter mixed layer defined by the NEMO OCCITENS simulation.

To examine the contribution of the various terms in Eq. 3.6 to the vorticity budget at higher latitudes, Figure 3.18 displays the terms of the equation over σ 27.78 kg m^{-3} poleward 40°N. Focusing on the SPG and northernmost part of the STG, the LVB residual (Figure 3.18c) has the same order of magnitude than in the subtropical upper tachocline (Figure 3.16c). Like the upper tachocline, in this layer, the non-linear advection term (Figure 3.16b), and within it the horizontal advection (panels a and b in Figure 3.19), is once again essential to absorb the residual LVB (Figure 3.18b). Moreover, the mixing term is necessary near the lateral boundaries to close the vorticity budget.

The results obtained from the decomposition of the non-linear advection in both upper tachocline and intermediate ocean should be interpreted with caution, given that the one-year average calculation does not account for the average of the cross-term anomalies or covariance of the terms (Figures 3.17f and 3.19f). Given two variables X and Y, with means $\overline{X}$ and $\overline{Y}$ and anomalies X' and Y':

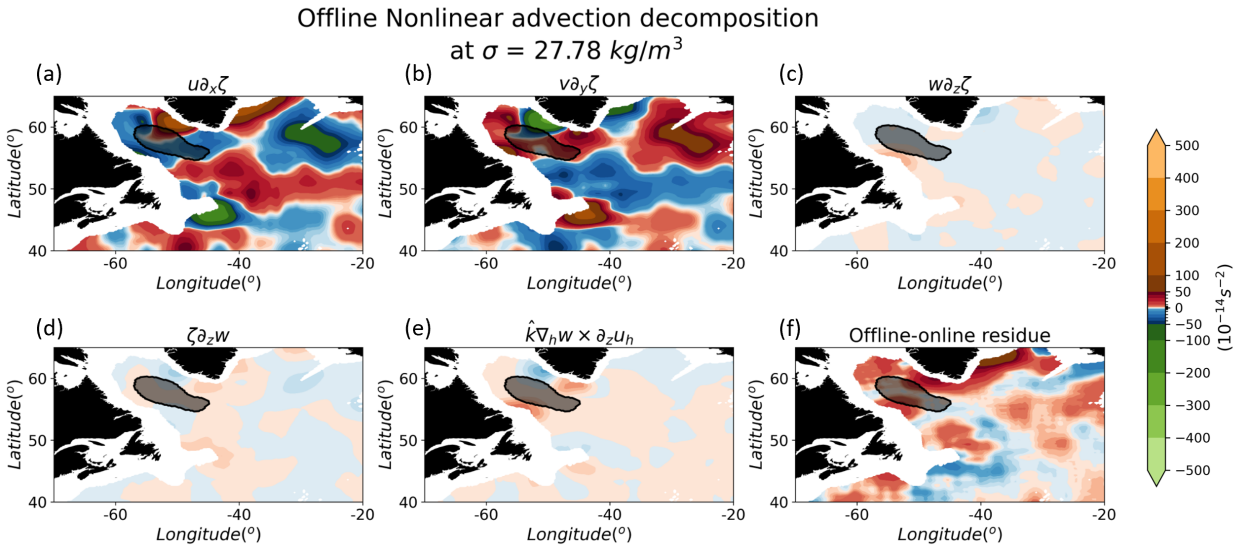

Figure 3.19: Offline-computed zonal advection of relative vorticity (a), meridional advection of relative vorticity (b), vertical advection of relative vorticity (c), relative vortex stretching (d), vortex tilting (e) from Eqs. 3.9, 3.10 and (f) residual between the online and offline non-linear advection term over σ 27.78 kg m^{-3}.

$$\overline{XY} = \overline{(\overline{X} + X')(\overline{Y} + Y')} = \overline{X}\,\overline{Y} + \overline{X'Y'} \tag{3.11}$$

$$\overline{X'Y'} = \overline{XY} - \overline{X}\,\overline{Y} = Cov(X, Y) \tag{3.12}$$

The residue between the online and offline computations of the non-linear advection terms is computed in Figures 3.17f and 3.19f. The large discrepancies between the calculations of the non-linear advection term highlight the significance of the neglected cross terms in the closure of the vorticity budget (~ 0-1 order of magnitude smaller than the online-offline computation). Choosing a shorter averaging time is expected to reduce the impact of the cross-term anomalies, minimising the departure between online and offline cases.

3.3 Moving Towards the Linear Vorticity Balance validity at Global Scale

So far, the examination of the extension to which the LVB can accurately describe the three-dimensional ocean circulation has been focused on the North Atlantic basin. However, much of the previous works on the study of the Barotropic Vorticity Balance (BVB) cited in the Introduction, such as Hughes and De Cuevas (2001), Lu and Stammer (2004), Sonnewald et al. (2019) or Waldman and Giordani (2023) and on the Sverdrup balance such as Wunsch (2011), Gray and Riser (2014) and Thomas et al. (2014) are conducted on a global scale. In these studies, the various oceanic basins exhibit dynamic responses similar to those of the North Atlantic basin, where the centre of the oceanic gyres, far from the lateral boundaries and high latitudes, can be considered linear.

Here, the linear vorticity balance analysis will be extended, both in its total and geostrophic case, to the global ocean. This section provides a four-level view of isopycnals (σ 26, 27.78, 28.05 and 28.12 kg m^{-3}, considered representative examples of the upper tachocline-upper ocean, the intermediate ocean and the lower tachocline-deep ocean). Besides, a vertical view of the LVB validity areas will be provided to evaluate further the vertical extent of the dynamical regimes where the LVB is maintained.

In Section 3.2, a sensitivity study of the LVB's validity was presented on the scale of North Atlantic Ocean dynamics (Figure 3.3). Although the distance-to-shore filter, with maximum filtering of 7° at the centre of the ocean basins and a minimum of 2° at the lateral boundaries, (for more information, please refer to Appendix B) yielded the best results throughout the water column, a simpler and more reproducible 5° filter was chosen in the sections included in the paper submitted to the JPO journal. However, in the following sections focused on expanding the North Atlantic analysis to global scales, the improved distance-to-shore filter was applied to the LVB terms.

3.3.1 Upper tachocline

Within the upper tachocline, the LVB (Figure 3.20) explains most of the ocean dynamics in the subtropical and eastern tropical bands, where the normalised difference between the terms of the LVB is negligible. However, a general departure from the LVB approach, with relative error exceeding 10%, is observable over the equator band (5°S/N), the western part of the Pacific and Atlantic tropical gyres, the Indian tropical band and especially in the western boundary currents. We quantify the vertical penetration of the LVB validity in Figure 3.21, where the zonal extent of the domain of LVB validity is displayed as a function of the neutral density. This figure confirms that the LVB valid regions distinguished in Figure 3.20) are transmitted quite effectively across the upper tachocline, reaching the deepest levels at subtropical latitudes.

3.3.1.1 Tropical band

In the tropical band, the LVB holds valid ($|\Delta_{LVB}| < 10$) within the Southern Atlantic and Pacific TGs, below the mixed layer (translucent black mask in Figure 3.20) throughout the upper tachocline regime (Figures 3.21a and 3.21b). Even though the LVB explains the North Atlantic TG dynamics over σ 26 kg m^{-3} (Figure 3.20), its extension throughout the upper tachocline is lesser than the South Atlantic and only at the lower half of the upper tachocline (Figure 3.21b). Notably, only the eastern part of the North Atlantic TG is well described by the LVB, in contrast to the South Pacific and Atlantic TGs where the LVB explains a larger fraction of the gyre. Unlike the Atlantic Ocean, the North Pacific Ocean upper tachocline has a general departure from the LVB validity over the tropical band.

In the Indian Ocean equator/low-tropical band (10°S/N), the zonal component dominates the horizontal flow in the Southern Equatorial Counter Current (SECC) and Southern Equatorial Current (SEC) throughout the water column (Figure 3.21). In the Southern Hemisphere, the SEC flow becomes meridional, and the LVB does not hold ($|\Delta_{LVB}| > 10$) because the vertical velocity field is too weak to balance the meridional velocity field (Figures B.12a and B.13a in Appendix B). Regarding the Northern Indian Ocean, the only LVB valid area is found over the Arabian Sea. This validity is also maintained through the upper tachocline but is

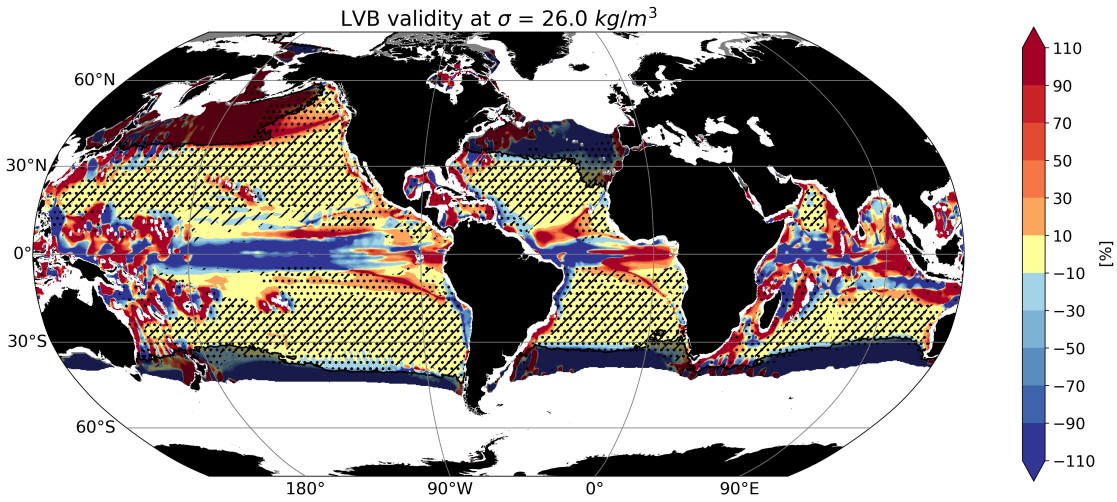

Figure 3.20: Global LVB relative error (Δ_{LVB}; Eq. 3.1) over σ 26 kg m^{-3}. Dotted areas represent regions where the meridional velocity field is in geostrophic balance with a relative error smaller than 10%. Hatched areas represent geostrophic LVB validity ($\Delta_{GLVB} < 10$). The translucent black regions indicate the maximum mixed layer mask.

lost in the intermediate ocean with LVB valid zonal extension dropping below 30% (Figure 3.21c). Despite the LVB errors in the North Indian Ocean, the LVB terms (see Figures B.12a and B.13a in Appendix B) exhibit some similar features in the upper ocean, primarily in the western part of the basin.

The limited performance of the LVB in North Pacific tropical band (Figure 3.20) aligns with the large Sverdrup balance errors obtained by previous works using a 1° reanalysis and OGCM simulation (Thomas et al., 2014), a 2° OGCM simulation (Lu and Stammer, 2004)and a 5° reanalysis (Wunsch, 2011). The small extension of LVB validity in Figure 3.20 aligns with the results for the Sverdrup Balance validity obtained by Wunsch (2011) employing a 5° kernel. Khatri et al. (2023) also reveals a small extension of the Sverdrupian areas at these latitudes when a filter around 2° is applied. However, in contrast with our findings with a 5° filter outside the 5° equator band, this recent study illustrates that this filter enhances the linear components' ability to describe more accurately the three-dimensional dynamics within the North Pacific tropical band.

The small extension of the LVB validity within the Southern tropical Indian Ocean contrast with the Sverdrupian description found in previous works (e.g. Wunsch, 2011, Thomas et al., 2014, Sonnewald et al., 2019, Gray and Riser, 2014, Khatri et al., 2023). The similarities between the Sverdrupian regions defined by previous studies based on reanalyses and observations with diverse spatial resolutions and their discrepancies with the LVB validity extension addressed here may be attributed to the native grid of the datasets. Even after smoothing the vorticity balance terms, specific dynamic phenomena intrinsic to the native grid can be retained through the scales. For example, the substantial influence of the non-linear terms on the vorticity balance when using a high-resolution model, in contrast to the minimal contribution observed with a coarser-resolution model, both with the same 2° kernel filtering (Yeager, 2015). This dependence on the native grid may explain the discrepancies identified between the NEMO OCCITENS-based LVB validity presented here and the works using ECCO reanalysis and observation-based data characterised by a native 1° horizontal resolution grid (e.g. Wunsch, 2011, Thomas et al., 2014, Gray and Riser, 2014, Sonnewald et al., 2019). It also offers a possible explanation for the need for a 5° kernel filtering in the dataset used by Khatri et al. (2023) (with a 0.25° native grid) in order to achieve the extension

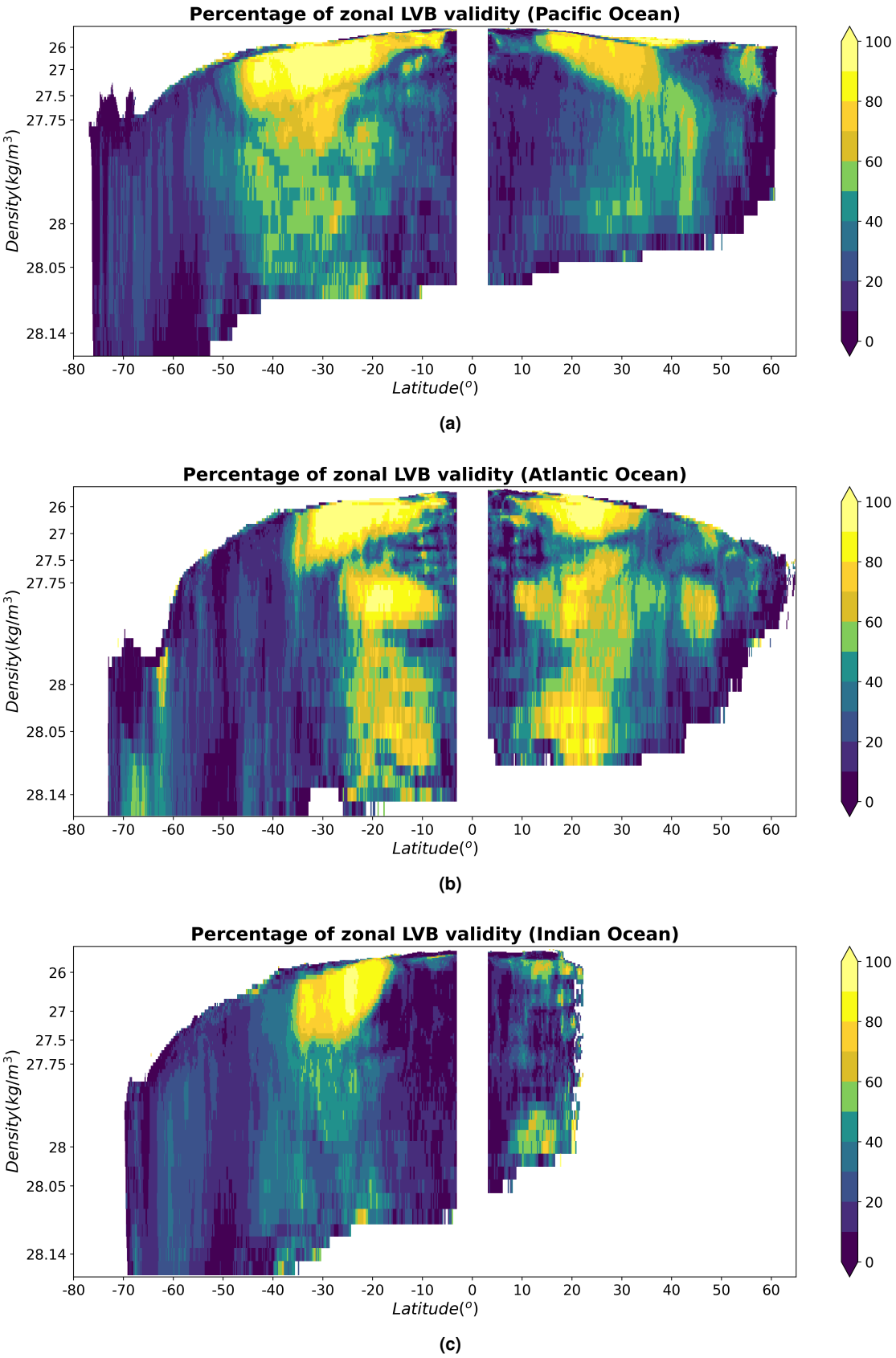

Figure 3.21: Zonal extent (%) of LVB validity (LVB relative error <10%) at each isopycnal surface level and latitudinal grid point (surface and subsurface tropical band not represented) excluding the 4° width band along the western boundaries as well as the mixed layer considering separately the (a) Pacific, (b) Atlantic and (c) Indian Ocean basins bounded by 65°W and 20°E in the Southern Ocean. The distance between σ levels on the y-axis is proportional to their average width within the basin.

for the Sverdrupian regions found by the ECCO and observation-based studies. The distance-to-shore filter applied to the LVB terms here has a size above 5° poleward 5°S/N, yet it fails to fully explain the dynamics. A spatial scale sensitivity study of the LVB's validity could help uncover whether the discrepancies observed between the LVB in the OGCM and the Sverdrup Balance in various datasets in previous works are a result of the necessity for more intensive filtering of the model terms or if there exists a discrepancy in parameterisations resulting in the non-linear vorticity's contribution enhancement.

3.3.1.2 Subtropical band

The subtropical gyres in the five global basins are largely described by the LVB (Figure 3.20), bounded from the west by the Western Boundary Current (WBC) and from above by the mixed layer. Unlike in the Atlantic basin, the LVB cannot fully explain the dynamics near the Pacific and Indian eastern boundaries in the upper upper tachocline. Nevertheless, the Δ_{LVB} remains relatively small, ranging between 10-30% in the lower upper tachocline. The various panels in Figure 3.21 illustrate how the southern hemisphere upper tachocline is overall better resolved by the LVB compared with the northern hemisphere. In the southern hemisphere, the WBC are less intense and less extensive, so the applied mask removes their contribution to the LVB error more efficiently than in the northern hemisphere.

The poor results for the LVB validity obtained in the easternmost part of the Pacific and Indian STGs align with the discrepancies between the terms in the Sverdrup balance from previous works (e.g. Lu and Stammer, 2004, Wunsch, 2011, Gray and Riser, 2014 and Thomas et al., 2014). These departures from the linear description demonstrate that, in general, the wind-driven transport in the eastern coastal regions cannot be entirely evacuated by oceanic transport alone at subtropical latitudes. While the LVB at σ 26 kg m^{-3} shows good results in the Atlantic basin (Figure 3.20), the LVB validity at each depth is necessary but not sufficient for the Sverdrup balance.

Therefore, there are scenarios where the Sverdrup balance may not be equivalent to the LVB in a single depth (or isopycnal surface). i) The LVB validity might not be consistently maintained throughout the upper tachocline, leading to an inability of the meridional transport to fully subtract the atmospheric forcing in the layer. ii) There may be regions where a level of no motion does not exist, requiring a vertical velocity at the bottom of the layer to close the balance. The extension of the LVB validity within the subtropical band shown in 3.20 is maintained with minimum changes across the upper tachocline of the three basins (Figure 3.21). This indicates a close alignment with the Sverdrupian regions identified in early works. Nevertheless, tropical regions, particularly in the Northern Hemisphere, exhibit a reduced valid LVB extent that is not retained along the upper tachocline. This finding and the disparities in the filtering strength methodology may explain the discrepancies observed when compared the LVB approach to the regions defined in Sverdrup balance by previous studies.

The discrepancies between the Sverdrupian regions found in earlier investigations raise the question of these areas' confidence level. Some studies employ a common integration depth for the whole global ocean (e.g. Lu and Stammer, 2004 and Thomas et al., 2014). Gray and Riser (2014) while integrating the SB using a constant depth for each ocean basin, explore the required depth of integration necessary for the meridional transport to effectively evacuate the atmospheric forcing, thus validating the Sverdrup balance hypothesis. This depth exhibits a dependence on latitude, being shallower in tropical latitudes than in subtropical latitudes except in the TG eastern boundaries. This level of integration is consistent

with the latitude-dependent vertical extent of the validity of the LVB in the OGCM simulation (Figure 3.21). In the eastern coastal regions, characterised by large Sverdrup balance errors in the study conducted by Gray and Riser (2014), a depth of integration is not identified within the layer of available observations. The absence of the level of no vertical motion, thus, prevents from finding the region in Sverdrup balance. However, the LVB holds to a good level of approximation here, suggesting that a linear description is possible.

Wunsch (2011) computes the Sverdrup balance using a variable depth where the vertical velocities are minimised, between 1000-2500m depth. However, even using these depths, the Sverdrup balance does not close within the eastern boundaries of the tropical gyres. The selection of the integration depth for the meridional transport, despite being based on the minimum vertical velocity field, does not agree with the latitudinal dependency observed in the OGCM simulation (Figure B.11 in Appendix B). A notable consideration regarding the work of Wunsch (2011) is his choice to use the w field at 117 m depth identified with the Ekman pumping as boundary condition. This choice of depth, together with the assumption that the vertical velocities in the ocean interior serve as a representation of the pumping, clash the rapid degradation of spatial synchronicity between the two fields obtained with the OCCITENS simulation (see Figure 4.8 in Section 4.2.2.2.2). As we delve in Section B.4 in Appendix B, the geostrophic velocities within the Ekman layer play a role in absorbing part of the vertical component from the Ekman pumping. This phenomenon diminishes the total vertical velocities and distinguishes between the Ekman pumping vertical velocities at the ocean surface and the vertical velocities at the bottom of the Ekman layer. Furthermore, such a constant depth approach involves utilising vertical velocities from both the upper tachocline, at low latitudes, and the mixed layer, across the rest of the ocean, indiscriminately as upper boundary condition. Consequently, the description of the oceanic circulation based on the validity of the Sverdrup balance should thus be treated with caution.

The LVB validity in the global deep lower upper tachocline (σ 27 kg m^{-3} in Figure 3.21) exhibits discrepancies between hemispheres. In the Northern Hemisphere, the western boundary currents become more zonal poleward 30°N (Figure B.11 in Appendix B), resulting in a reduction in the zonal extension of the LVB validity. In contrast, in the Southern Hemisphere, the WBC does not follow the same zonal derive as its northern counterpart. However, south of 35°S for the Atlantic and Indian basins and 45°S for the Pacific basin, the LVB is no longer suitable to explain ocean dynamics in the converging region between the southern subtropical regime and the Antarctic Circumpolar Current throughout the entire water column (Figure 3.21). In this band, topographic and non-linear terms are not negligible and are necessary to close the vorticity budget (e.g. Hughes and De Cuevas, 2001, Sonnewald et al., 2019 and Khatri et al., 2023). More intense filtering (around a 20° kernel, as shown by Khatri et al. (2023)) can reduce the contribution of the non-linear terms and increase the influence of the bottom pressure torque contribution.

Expanding the analysis of the validity of the geostrophic LVB and the geostrophic balance to other regions of the globe allows for studying the possibilities of using the geostrophic meridional velocities from observations (such as ARMOR3D; Guinehut et al., 2012; Mulet et al., 2012) to reproduce the vertical velocity field. The almost perfect correspondence between the total LVB valid areas with the geostrophic LVB and geostrophic balance valid areas (hatched and dotted surfaces in Figure 3.20) makes evident that the meridional transport is generally geostrophic and maintains the geostrophic LVB in the upper tachocline regions explained by the LVB.

3.3.1.3 Extratropical and Subpolar bands

At higher latitudes, over the Alaska Gulf, the northernmost part of the Pacific STG is in LVB validity (Figure 3.20). However, close to the intergyre region, between 40-50°, the Δ_{LVB} increases until 10-30% towards the western half of the basin, resembling the results observed in the North Atlantic basin. The validity of the LVB within the eastern part of the SPG remains consistent across the entire upper tachocline between 50-60°N (Figure 3.20). The LVB validity found in the Pacific SPG diverges from the LVB valid areas in the Atlantic extratropical and subpolar latitudes identified in Section 3.2.1.4. In the North Atlantic, the LVB solely explains the STG, while the SPG needs the addition of non-linear terms to close the vorticity budget. In prior research on the BVB (e.g. Hughes and De Cuevas, 2001; Lu and Stammer, 2004; Waldman and Giordani, 2023; Khatri et al., 2023), it has been observed that non-linear and topography-dependent terms play a more significant role in closing the vorticity budget in subpolar latitudes of the North Atlantic basin compared to the North Pacific.

3.3.2 Intermediate and Deep Oceans

Below sigma 27.1 kg m^{-3}, where the wind forcing is no longer driving the circulation (Figure 3.2) a significant loss of LVB validity occurs over the STGs and the entire tropical band (Figure 3.22a), aligning with the results obtained in the North Atlantic analysis in Section 3.2 of this chapter. At these depths, the Southern Atlantic and Pacific basins behave more favourably in terms of LVB validity than the Northern Hemisphere (Figures 3.21a and 3.21b). Nevertheless, retaining LVB validity between 30-60°S for the Atlantic basin and 35-60°S for the Indian basin and 45-60°S for the Pacific basin is found difficult.

In Section 3.2 of this chapter, it has been demonstrated the ability of the LVB to describe the relation between the deep circulation and the bottom forcing over the North Atlantic (Figure 3.11). Extending the analysis for the global oceans, the LVB effectively explains the circulation in the abyssal plains of the South Atlantic, the Pacific around 30°S, and the Abyssal Plains contained in the band 20-40°S in the Indian Ocean (Figure 3.22b). In most of the areas where the LVB is valid, the ageostrophic component of the meridional velocity is found to be negligible. This suggests that the dynamics within these regions are largely governed by geostrophic balance, simultaneously making true the geostrophic LVB assumption. Under idealised conditions with geostrophic movements (dotted surface in Figure 3.22b), the BPT can be considered equivalent to the bottom vortex stretching (Zhang and Vallis, 2007), which dominates the vertical motions at these depths.

Despite the relative poor performance of the LVB in the Northern Hemisphere in the subpolar band over dense waters below sigma 27.78 kg m^{-3} (Figure 3.21), the equation is valid within several regions in the Southern Ocean below sigma 28 kg m^{-3} (Figures 3.22b and 3.23). This validity is observed poleward 60°S below the mixed layer, which is substantially deep due to the weak-stratified ocean. Remarkably, the areas over the Weddell Abyssal Plain where the LVB holds are aligned with the Topographic Sverdrup Balance description supported by Khatri et al. (2023). Again, the geostrophic motions that dominate these depths allow approximating the BPT to the bottom vortex stretching, further establishing a connection between the LVB and Sverdrup balance approaches.

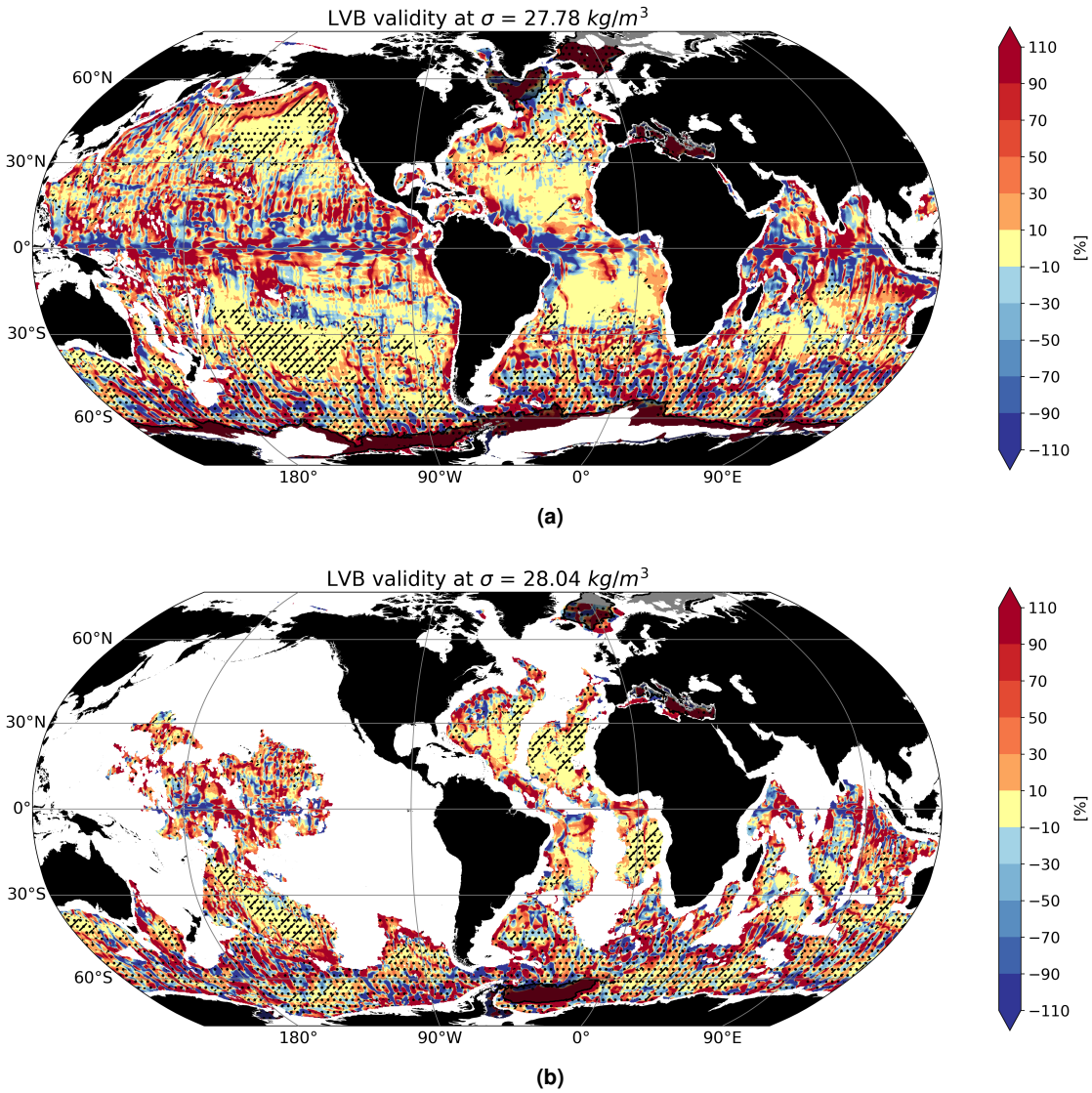

Figure 3.22: Global LVB relative error (Δ_{LVB}; Eq. 3.1) over σ 27.78 (a) and 28.05 (b) kg m^{-3}. Dotted areas represent regions where meridional velocity field is in geostrophic balance with a relative error smaller than 10%. Hatched areas represent geostrophic LVB validity ($\Delta_{GLVB} < 10$). The translucent black regions indicate the maximum mixed layer mask.

In the Pacific and Indian basins, poleward 45° at a denser isopycnal surface (σ 28.12 kg m^{-3}) over the deep ocean (Figure 3.23), several regions were identified with promising results in the LVB validity. Within these areas, regions exhibit Δ_{LVB} between -30 and 30%, alongside LVB valid areas extending as far as 65°, near Antarctica. These valid LVB areas over the Southern Oceans are notably associated with the Abyssal Plains: the Bellingshausen Abyssal Plain (southern 55°S), the Humboldt Abyssal Plain, the Mornington Abyssal Plain, the Wilkes Abyssal Plain and Enderby Abyssal Plain (an extension of Weddell Abyssal Plain). Therefore, assuming the model input's reliability in the deep ocean, the LVB demonstrates a strong ability to capture the dynamics in the regions surrounding the Abyssal Plains in the Southern Oceans.

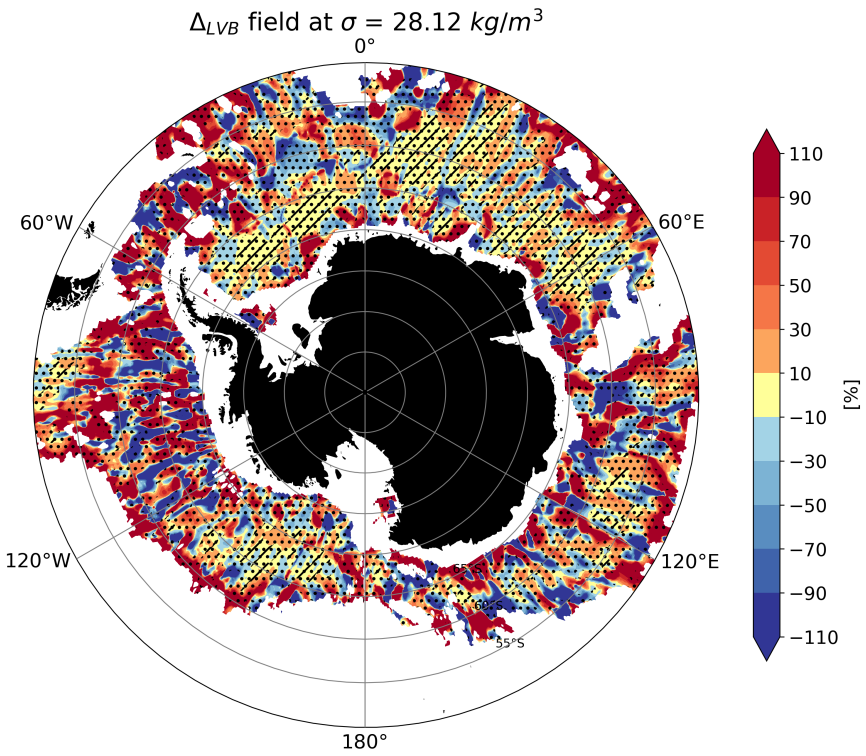

Figure 3.23: Same as Figure 3.22b for the Southern Ocean over σ 28.12 kg m^{-3}.

3.4 Conclusions

A thorough baroclinic evaluation of the climatological dynamical regimes described by the Linear Vorticity Balance (LVB) has been conducted within the ocean interior of the global oceans. Using the NEMO OGCM OCCITENS state estimate, this evaluation reveals variations in the extent to which the LVB closes the vorticity budget across the water column. Notably, the largest extent occurs within the upper tachocline and the deep ocean.

The LVB holds, at scales larger than 5°, within the upper tachocline, below the mixed layer, in most of the subtropical gyres, eastern Pacific and Atlantic tropical gyres, as well as a portion of the Pacific subpolar gyre. The extension of the LVB validity within the upper tachocline provides an alternative and simpler explanation for the direction of the flow compared to the classical potential vorticity scheme. According to the LVB for the geostrophic flow, convergent/divergent meridional transport is required to match the Ekman layer's divergent/convergent wind-driven motions. Therefore, the determination of the meridional flow direction arises from the convergent nature of poleward flows and the divergent nature of equatorward flows. However, notable deviations from the LVB validity are observed within western boundary currents, the equatorial band (and tropical band in the Indian Ocean case), the western half of the Pacific and Atlantic tropical gyres and the Atlantic subpolar gyre. In the intermediate ocean, the efficacy of the linear vorticity balance to describe the ocean diminishes in comparison with the upper layer, particularly at tropical latitudes, the western halves of the global oceans, and the circumpolar circulation. This reduction in extension is attributed to the relatively weak vertical circulation at these depths, leading to an enhanced contribution from the non-linear terms to the vorticity budget. Unlike total meridional velocities, the geostrophic component fails to effectively balance the vortex stretching term in the tropical and subtropical intermediate

ocean. In the deep ocean, topography-induced vorticity is largely explained by the linear vorticity balance, notably over the abyssal plains and in austral circulation regions. Regions where the geostrophic linear vorticity balance holds maintain geostrophic equilibrium throughout the water column.

A notable result that emerges from analysing the LVB within the North Atlantic is that its performance to describe the basin circulation basin declines as the averaging period is shortened. This reduction lessens with depth and becomes negligible in the deep ocean. Even at annual timescales, the extension of the LVB validity only decreases by approximately 15% from its maximum extension at longer periods within the upper tachocline. This suggests that the LVB remains a robust formulation for accurately representing ocean dynamics at annual timescales.

While the applicability extension of the LVB and Sverdrup balance (e.g. Wunsch, 2011, Thomas et al., 2014; Gray and Riser, 2014) is nearly identical, discrepancies arise (e.g. in the Atlantic eastern boundary). These differences underscore the importance of a precise localisation and existence of the assumed Level Of No Motion (LONM) to close the Sverdrup balance, even in regions characterised by the Linear Vorticity Balance. The geostrophic circulation observed near the lateral boundaries in the deep ocean allows a connection between the baroclinic analysis with previous studies of the barotropic vorticity balance through the "Topographic-Sverdrup Balance" (Khatri et al., 2023). Describing boundary-driven features by the LVB suggests the transport of these forcings throughout the water column, emphasising the need to assess ocean dynamics from a baroclinic perspective to determine their penetration into the water column.

The deviation from Linear Vorticity Balance in the upper tachocline is explored with a one-year CROCO simulation in the North Atlantic. The offline decomposition of the vorticity equation reveals that, within the upper tachocline, the horizontal advection of relative vorticity plays a crucial role in balancing the linear vorticity residue in the Gulf Stream region, the subpolar gyre and the western half of the tropical band at scales larger than 5°. In the open ocean, contributions from the vortex tilting, vortex stretching due to relative vorticity, vertical advection of relative vorticity, time evolution of relative vorticity, vertical mixing, and horizontal diffusivity terms are entirely negligible. In regions where the LVB is no longer valid, such as the Gulf Stream, western tropical and SPG, the vorticity contribution of non-linear and mixing terms (except for the time evolution of relative vorticity) exhibits a non-negligible but relatively small impact (by a factor of ~ 0.1) on vorticity balance compared to each component of the horizontal advection of relative vorticity. The vertical mixing term in the eastern boundary and the mixed layer effectively balances the LVB and horizontal advection of relative vorticity residue.

After identifying the four-dimensional regimes described by the LVB and recognising the current limitations in measuring only large-scale geostrophic currents, Chapter 4 will explore the question: **Can the geostrophic meridional transport effectively explain the vertical motions, and specifically, can the upper ocean geostrophic currents be explained by the Ekman pumping?**

Just keep swimming,
just keep swimming,
just keep swimming swimming swimming,
what do we do we swim swim.

— Dory, *Finding Nemo, 2003*

4

Exploring the Potential of Geostrophic Meridional Transport in Estimating Vertical Motions in an OGCM simulation

Vertical movements in the ocean are of paramount importance for comprehending its circulation patterns, as they play a vital role in maintaining the thermocline and driving the deep circulation, as highlighted by Stommel and Arons (1959). However, the magnitude of the vertical velocities in the open ocean is significantly smaller than the horizontal circulation, with values on the order of approximately 10^{-6} m s^{-1} within the upper ocean and even smaller values at deeper layers. These small magnitudes have made direct observations of w in the open ocean challenging.

The linear vorticity balance's validity within the water column, away from the equator, the western boundaries and the polar gyres (as detailed in Chapter 3), supports the effort to utilise this equation vertical velocity estimation.

Historically, one of the challenges in estimating vertical velocities was the need for an initial localisation to start the vertical integration. Researchers often establish a level of no motion, which assumes null vertical movements, to serve as a reference level. This level of no motion is also crucial to close the Sverdrup Balance. However, the assumption and definition of this reference level introduce uncertainties that affect result accuracy. To address this limitation, we use the Ekman pumping vertical velocities at the ocean surface as boundary condition rather than relying on a single level in the ocean interior.

Using the OGCM geostrophic meridional velocities applied to the Indefinite Depth-Integrated LInear Vorticity (IDILIV) approach to estimate the geostrophic vertical velocities provides an opportunity to explore its feasibility of reproducing the total vertical flow in the ocean interior. This assessment involves comparing the obtained estimates with the model's simulation output. The main goal of this chapter is to set the IDILIV framework to build an observation-based vertical velocity field. These estimations could then be further employed in tracer studies requiring a quantitative understanding of the contributions of the vertical transport.

4.1 Preamble

The Linear Vorticity Balance (LVB) reproduces the oceanic dynamics across a significant portion of the water column in the open ocean, particularly in global subtropics and eastern tropics, and Northern Hemisphere Pacific and Atlantic extratropics, focusing on frequencies smaller than one year and spatial scales greater than 5 degrees using a NEMO OCCITENS simulation (see Chapter 3). These findings provide the basis for estimating the geostrophic component of the vertical velocity field within the LVB's validity region through the Indefinite Depth-Integrated LInear Vorticity (IDILIV) approach, employing the Ekman pumping vertical as a boundary condition.

This chapter examines the capability of the IDILIV approach to serve as an estimator of the four-dimensional features of the vertical velocity. The IDILIV approach reproduces open ocean large-scale vertical circulation with the same order of magnitude as the NEMO OCCITENS simulation total w, considered as reference, in the North Atlantic complete water column during the 1960-2015 period and the global upper ocean during 1993-2015, excluding Western Boundary Current (WBC) regions and Northern Hemisphere Subpolar Gyres (SPGs). The closest alignment is found within the upper tachocline, which suggests that errors in the LVB lead to deviations from the model's output. The differences between the two fields, although within the same order of magnitude as the time average, are smaller than the interannual amplitude. The IDILIV approach accurately reproduces the interannual variability, with consistently very high correlation across the majority of the global upper ocean and the North Atlantic intermediate and deep oceans, particularly in regions distant from western boundaries and the equator band. This underscores the dominance of geostrophic meridional transport in driving the annual variability. The non-linear components play a secondary role in the interannual variability of the total flow but significantly influence the vertical flow amplitude.

The accurate reproduction of the localisation and order of magnitude of the time-mean large-scale open ocean circulation, together with the accurate synchronicity performed by the geostrophic vertical velocity, serves as a starting point from where to use the geostrophic meridional transport based on observations to estimate an observation-based geostrophic velocity field in the following chapter.

The chapter is organised as follows: The evaluation of the geostrophic vertical velocity field computed applying the Indefinite Depth-Integrated LInear Vorticity (IDILIV) approach to NEMO OCCITENS simulation outputs in the North Atlantic as a case study is included in Section 4.2. The extension to the global upper ocean of the Indefinite Depth-Integrated LInear Vorticity (IDILIV) approach is addressed in Section 4.3. Within Subsection 4.2.1.3 is embedded the part centred on the Indefinite Depth-Integrated LInear Vorticity (IDILIV) approach to compute geostrophic vertical velocities of a paper submitted for publication in *Journal of Physical Oceanography (JPO)* [1]). The evaluation of the assumption of linearity on the NEMO OCCITENS simulation and the spatiotemporal correlation between the vertical circulation in the ocean interior with the vertical boundary forcing is explored in Subsection 4.2.2.

[1] (reformatted for the thesis manuscript). For the complete manuscript submitted in *JPO*, please refer to the Appendix A.

4.2 North Atlantic Vertical Velocity Estimation through the Indefinite Depth-Integrated LInear Vorticity (IDILIV) Approach

This initial section will address the capacity of the geostrophic meridional transport to reproduce the vertical motions defined by the OGCM simulation, employing again the North Atlantic Ocean across the entire water column as a case study. It will endeavour to determine the regions where the basin vertical dynamics are accurately characterised, focusing on climatological timescales ranging from 1 to 56 years.

4.2.1 IDILIV Vertical Velocity Estimates: Expectations from Ideal Scenario

4.2.1.1 Introduction

The reconstruction of horizontal geostrophic velocities, derived from observed thermohaline fields, in conjunction with data collected by current metres, expands the possibilities for connecting the three components of ocean circulation.

Many early estimations of w utilised measured profiles of tracers to estimate tracer fluxes (e.g. Stommel and Arons, 1959; Robinson and Stommel, 1959; Wyrtki, 1961; Munk, 1966; Wunsch, 1984), or the application of mooring measurements of horizontal currents to the continuity equation (Stommel and Schott, 1977; Schott and Stommel, 1978; Wyrtki, 1981; Roemmich, 1983; Bubnov, 1987; Halpern and Freitag, 1987; Halpern et al., 1989; Weingartner and Weisberg, 1991). These studies reached a consensus on the order of magnitude of the w in the different ocean layers ranging from 10^{-5} m s^{-1} near the surface, gradually decreasing to 10^{-6} m s^{-1} within the upper ocean, and reaching values between 10^{-7} and 10^{-8} m s^{-1} in the intermediate and deep oceans. However, while the vertical velocity field can be diagnosed in primitive equation numerical models by solving the continuity equation, this approach has been limited by the scarcity of observation-based data at global scale and the potential for prominent instrumental errors when computing the divergence from measured horizontal velocities. One example of retrieving the vertical flow from observations via continuity equation is presented by Freeland (2013), who calculated observation-based barotropic w at 700 dbar within an approximately 25x20° horizontal box. Over the last decade, researchers have explored alternative approaches for assessing large-scale baroclinic vertical velocities. These include the use of observations of isopycnal displacement (Giglio et al., 2013; Christensen et al., 2023), moorings data applied to the momentum and density equations (Sévellec et al., 2015) and biogeochemical tracers (Garcia-Jove et al., 2022). More theoretical approaches have now gained more attention, such as using the Bernoulli function to estimate w (Tailleux, 2023). In recent years, several attempts have been made to compute the w field using the omega equation ($f^2 \frac{\partial^2 w}{\partial z^2} + \nabla_h (N^2 \cdot \nabla_h w) = \nabla \cdot Q$; Giordani et al., 2006), as demonstrated by studies conducted by Buongiorno Nardelli et al. (2018); Ruiz et al. (2019) and Buongiorno Nardelli (2020). Buongiorno Nardelli et al. (2018) developed a three-dimensional w product within the upper ocean (OMEGA3D) from an Argo and satellite based dataset (Mulet et al., 2012; Guinehut et al., 2012).

An alternative approach to estimate the w field from observations is theoretically possible within the geostrophic LVB framework, as suggested by Charney (1955). This alternative also offers a simple and intuitive method to understand basin-scale motions in LVB. In the present paper, we aim to develop a comprehensive baroclinic analysis of the LVB and its geostrophic case at all depths, in climatological

and interannual scales across the North Atlantic, in an OGCM simulation. This analysis will address the oceanic circulation patterns' ability to react to the surface and bottom boundaries forcing, transmitting the forcing to the ocean interior. Lastly, and from the perspective of future developments based on the use of global geostrophic currents computed from observations, we will assess the feasibility of using an indefinite vertical integration of the geostrophic LVB in order to reconstruct the three-dimensional distribution of the OGCM's vertical flow.

4.2.1.2 Methodology and data: Vertical Velocities Estimation from the Linear Vorticity Balance

The current state of the observations at basin scales only allows retrieving geostrophic flows. Although we are have assessed the validity of the total LVB in Chapter 3, this Chapter aims to evaluate the feasibility of reconstructing w from observation-based data and LVB. Therefore, we derive the three-dimensional geostrophic w by vertically integrating the geostrophic component of the LVB (GLVB), as we have presented in the Introduction (Eq. 1.20)

$$w_g(z) = w_g(z_{ref}) - \int_z^{z_{ref}} \frac{\beta v_g}{f} dz' \tag{4.1}$$

In order to compute $w_g(z_{ref})$, one method assumes a level of no motion where all velocity vector components are null. However, while recent studies (e.g. Koelling et al., 2020) support this assumption, the depth of this level is uncertain for computations based on data from the real ocean. Alternatively, satellite observations provide variables with extensive spatial and temporal coverage, making them adequate for use as boundary conditions. Therefore, we propose estimating $w_g(z_{ref})$ at the surface.

The total vertical velocity (w) is the sum of the ageostrophic (w_{ag}) and the geostrophic (w_g) components. Since the vertical velocity must vanish at the ocean surface in a steady state, both components are opposite (Pedlosky, 1996). For this purpose, let us recall that w_{ag} is generated by the divergence of the wind-driven ageostrophic flow. When neglecting any other ageostrophic flow, it is therefore sufficient to estimate the Ekman pumping vertical velocity at the surface ($w_{Ek}(z=0)$). dissipation brings the wind-driven flow to zero at its bottom, allowing us to consider its vertical component as null there (Ekman, 1905). Therefore, vertically integrating the Ekman transport over this layer thickness yields:

$$w_{Ek}(z=0) = -\hat{\mathbf{k}} \cdot \nabla \times \frac{\tau^{wind}}{\rho_0 f} \tag{4.2}$$

Where $z=0$ denotes the surface (Pedlosky, 1996), ρ_0 represents the water density at the surface, and τ_{surf} is the wind stress.

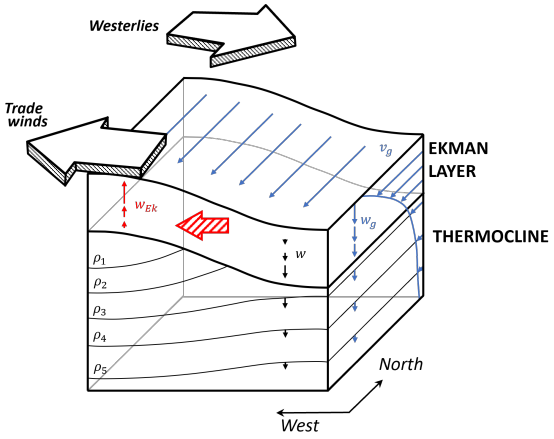

Figure 4.1: Velocity scheme within the Ekman Layer and the upper tachocline for the Subtropical Gyre (STG). At the ocean surface (z = 0), the total w should be 0. Thus, the Ekman pumping vertical velocity (w_{Ek}) generated by the wind stress over the ocean surface is balanced by the geostrophic component of the w (w_g), defined as the divergence of the geostrophic flow (v_g). As the depth nears the bottom of the Ekman Layer, w_{Ek} diminishes to 0, decreasing more rapidly than the geostrophic component, thereby generating a maximum of w at this depth.

The classical view of the Ekman pumping vertical velocity locates it at the bottom of the Ekman layer, neglecting the geostrophic contribution to the horizontal flow (Marshall and Plumb, 2007). However, this is the geostrophic component of the vertical flow at the surface (see Section B.4 in Appendix B for a detailed computation). Indeed, the contribution of the geostrophic flow divergence in the Ekman layer is found to be about 10 (30)% of the Ekman pumping amplitude in the upper 50 (100) m depth (Figure B.6 in Appendix B). In the context of the Ekman pumping described in Eq. 4.2, e.g. over the downwelling gyre, the Ekman transport convergence within the Ekman layer is balanced by a downward vertical flow from the Ekman layer into the ocean interior, evacuating water masses accumulating due to the Ekman flow.

Thus, we derive the expression for the the geostrophic vertical velocity or $w_{IDILIV3}$[2] as a function of depth:

$$w_{IDILIV3}(z) = w_g(z) = -w_{Ek}(z=0) - \int_z^0 \frac{\beta v_g}{f} dz' \tag{4.3}$$

4.2.1.3 Estimation of Vertical Velocities

4.2.1.3.1 Time-mean

Following the methodology presented in Section 4.2.1.2, we computed the geostrophic vertical velocity ($w_{IDILIV3}$ hereafter) applying the Eq. 1.16 to the geostrophic meridional velocities and w_{Ek} (Figure 3.5 b) as surface boundary condition at an annual frequency. The multidecadal mean of $w_{IDILIV3}$ is presented in Figure 4.2 over the three representative σ surfaces.

The $w_{IDILIV3}$ field appears to be qualitatively similar to the reference OGCM output in the open ocean throughout the water column, as illustrated in Figure 4.2. It captures the horizontal patterns across most of the subtropical, extratropical and eastern tropical bands, far from the western boundary and the western part of the tropical band, where large LVB errors were observed. However, when quantitatively evaluating our estimate with the mean square error (RMSE) normalised by the 56-averaged target model output (RMSE/$\overline{w}$; contours in Figure 4.2), it shows significant amplitude biases.

Within the upper tachocline, the RMSE/$\overline{w}$ (contours in Figure 4.2a) shows values below 0.5 in most of the STG and TG, with values above 1 found in the western boundaries and zonal tropical currents where flow is not in GLVB. The bias exceeds the 56-year averaged reference within most of the intermediate ocean (Figure 4.2b). Only in some regions of the eastern part of the extratropical bands the $w_{IDILIV3}$ reproduce the vertical motion of the OGCM's simulation output with a normalised RMSE smaller than 0.5. These regions in extratropical latitudes coincide with areas described by GLVB (Figure 3.10c). The overall coherence of the deep vertical pathways between the $w_{IDILIV3}$ (Figure 4.2c) and the reference evidences the lesser influence of the Ekman forcing compared with the bathymetry. However, $w_{IDILIV3}$ fails in accurately reproducing the amplitude of the OGCM w in most of the basin. Overall, despite the very satisfying qualitative agreement of the reconstruction, the relatively large biases indicate that while the geostrophic component of w establishes the order of magnitude of the total vertical flow, the ageostrophic components (coming from the ageostophic planetary vorticity advection and the non-linear contribution of the vorticity balance) is necessary to close the vorticity budget.

[2] Indefinite Depth-Integrated LInear Vorticity Vertical Velocities Estimates

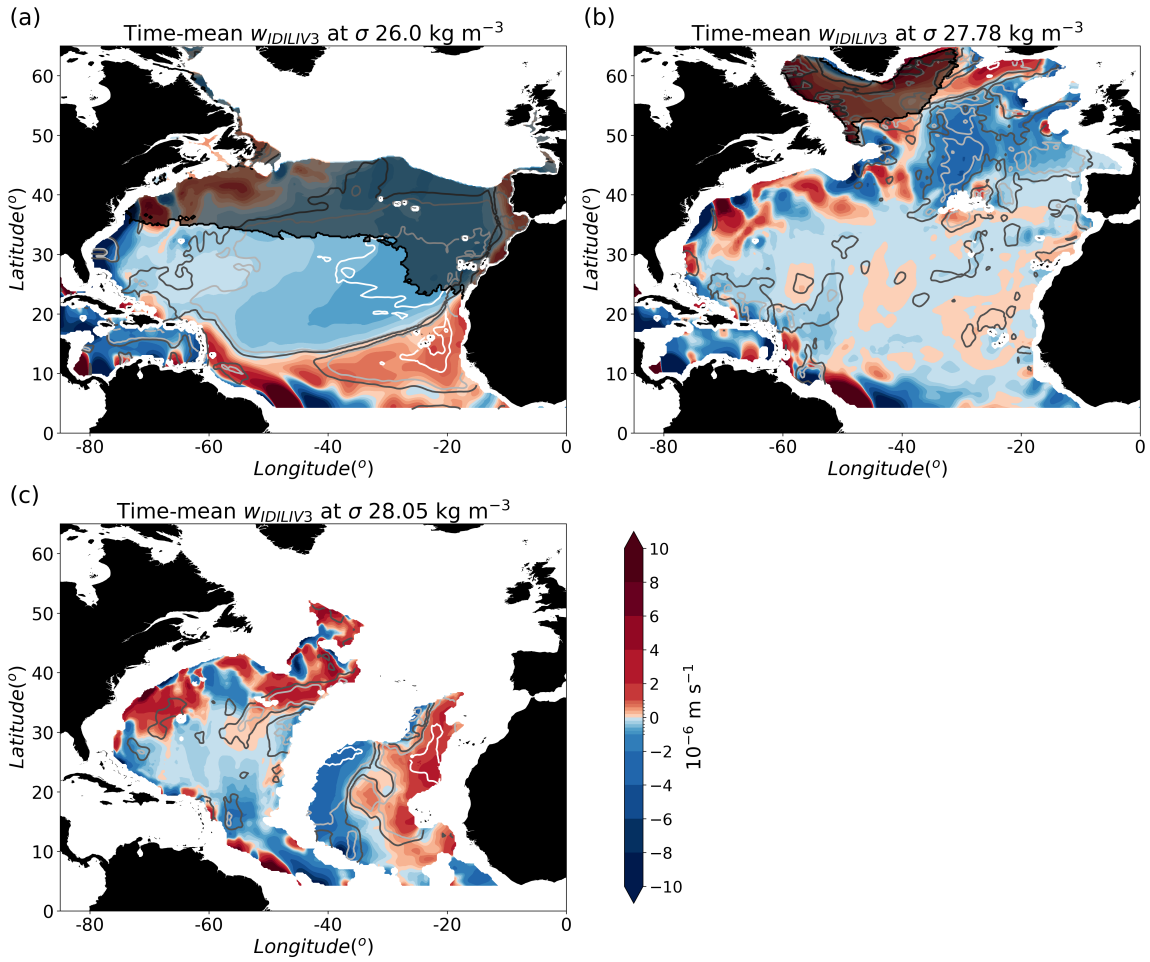

Figure 4.2: Time-mean vertical velocity estimate ($w_{IDILIV3}$) and RMSE/$\overline{w}$ (0.1 (white), 0.5 (light grey), 1 (dark grey) contours) of $w_{IDILIV3}$ estimate with OGCM w output over σ 26 (a), 27.78 (b) and 28.05 (c) kg m^{-3} using OGCM data. The black translucent region indicates the maximum mixed layer mask. The equatorial band has been masked.

After analysing the average of the entire available period, the feasibility of employing the LVB at timescales shorter than the longest multidecadal climatological dataset available enables an exploration of the temporal dimension in the vertical velocity estimates.

4.2.1.3.2 Temporal variability

Finally, we aim to determine the ability of the $w_{IDILIV3}$ to capture the interannual variability. The interannual variability of the $w_{IDILIV3}$ estimates and the reference over the three representative σ surfaces, considering two spatially-averaged example regions bounded by (55-30°W/15-30°N) and (30-16°W/8-16°N), is displayed in Figure 4.3 . Notably, the reconstruction accuracy is high in terms of the phase and amplitude of the variations. The correlation coefficients between $w_{IDILIV3}$ and the model's w are above 0.9, except for the upwelling over the deep sigma surface. The biases between the $w_{IDILIV3}$ and the OCCITENS simulation w are now quantified concerning the variability amplitude using the RMSE normalised by the standard deviation (std) of the OGCM w (RMSE/std). The synchronisation between the time series and the amplitude of the interannual variability leads to an overall relative minor bias between the $w_{IDILIV3}$ and OGCM output, except for the abysses. The remarkable reconstruction of the interannual

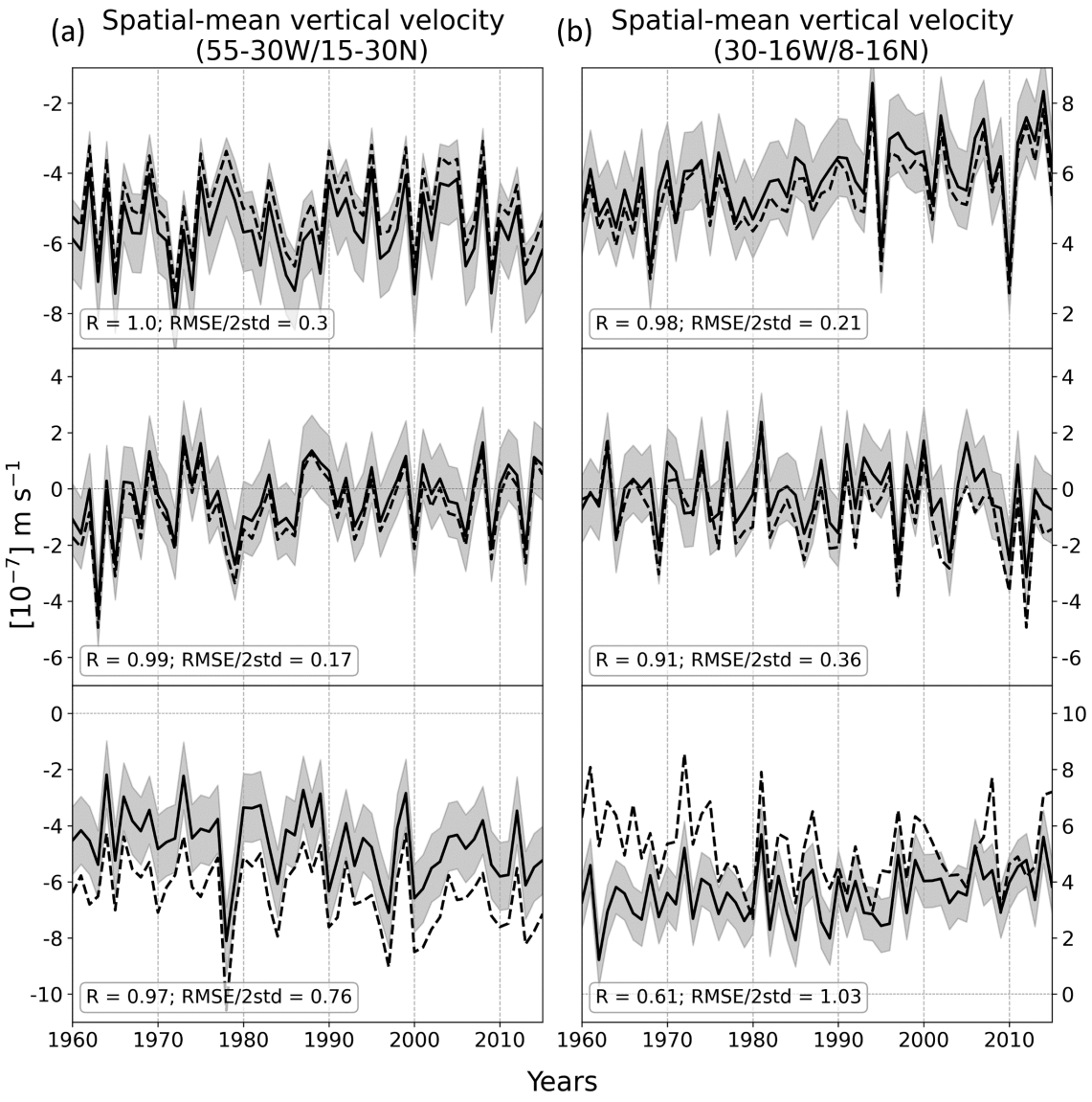

Figure 4.3: Time series of the spatially averaged OGCM w (continuous line) and $w_{IDILIV3}$ estimate (dashed line) over the regions bounded by (55-30°W/15-30°N) (a) and (30-16°W/8-16°N) (b) at σ 26, 27.78 and 28.05 kg m^{-3}. Shading represents the standard deviation of the OGCM w output.

variability of the total w field by the geostrophic LVB, even at periods shorter than the basin-crossing time scale, suggests that the estimated vertical velocities serve as a signal of propagating Rossby waves. The westward-propagating anomalies of sea surface height and w in the ocean interior within the subtropical band (not shown) are synchronised and exhibit a phase speed of approximately 5 cm s^{-1}, consistent with the characteristic phase speed of baroclinic Rossby waves at these latitudes (Chelton et al., 2007; Sanchez-Franks et al., 2021).

Therefore, we now evaluate this accuracy over the entire North Atlantic Basin. Figure 4.4 quantifies the synchronisation between the fields by displaying the correlation coefficient and the normalised RMSE (RMSE/std). In the subtropical band, both the upper and intermediate oceans (Figure 4.4a, b) exhibit correlation coefficients between w_{GLVB} and the model's w are above 0.8, excluding areas close to the western boundary, as well as the eastern tropical and polar bands. However, although the southwestern current between 40-50°N is in GLVB, the reproduced variability does not synchronise with the reference. In

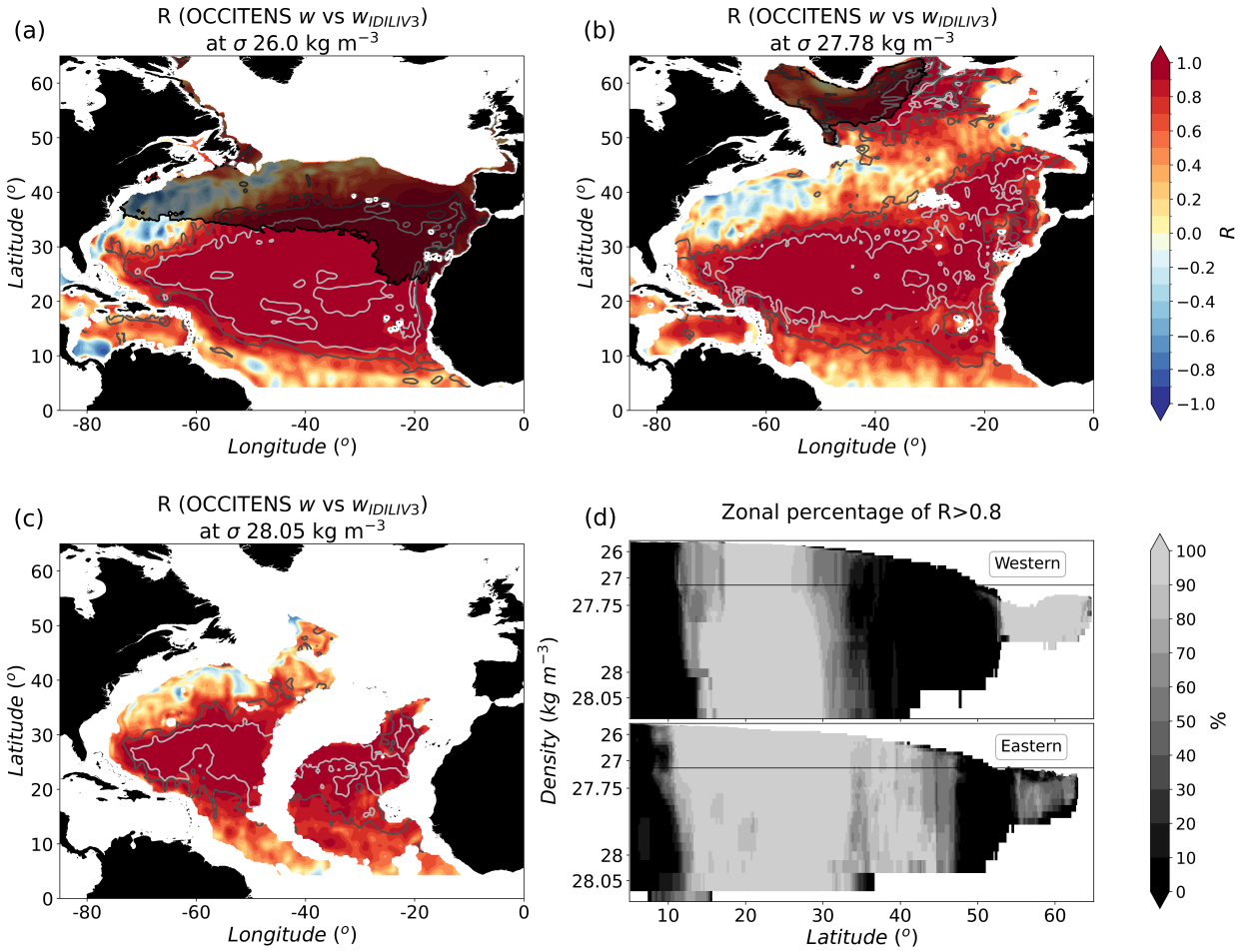

Figure 4.4: Annual correlation coefficient (shading) and normalised RMSE (RMSE/std; white contours for 0.5, black contours for 1) between $w_{IDILIV3}$ and OGCM w output over σ (a) 26, (b) 27.78 and (c) 28.05 kg m^{-3}. The black translucent region indicates the maximum mixed layer mask. The equatorial band has been masked. (d) Zonal extent (%) of correlation coefficient values above 0.8 at each isopycnal level and latitudinal grid point (surface and subsurface tropical band not represented) considering only the western (upper panel) and eastern (lower panel) part of North Atlantic basin defined by the Mid-Atlantic Ridge (Figure 3.7b) within the unmasked region. The distance between σ levels on the y-axis is proportional to their average width within the basin with a zoom between the surface and σ 27.1 kg m^{-3}.

the deep ocean (Figure 4.4c), only the subtropical band maintains correlation coefficient values above 0.8. Within the upper tachocline, note the high correlation even in regions where the flow deviates significantly from the LVB, such as a large portion of the northeastern STG (Figure 4.4a) where the mixed layer reaches this sigma surface, also areas along the Africa coast from 12-20°N. High correlation values are also found in areas with large LVB errors in the deep ocean and in the east and subtropical intermediate ocean. The reconstruction of the interannual variability is, therefore, accurate over a much larger part of the ocean than expected.

However, the variability cannot be derived from the GLVB over two extensive regions characterised by low correlation. The first region encompasses the lower tropical band, extending up to 10°N within the upper tachocline and 15°N at the intermediate and deep ocean. The second region includes the flow near the Gulf Stream (between 35°-55°N in the western basin) and its northeastern extension into the open ocean, reaching the coasts of Northwest Europe (around 50°N in the eastern basin). These two regions

exhibit much larger interannual variability than the region of high correlation. In fact, the ageostrophic circulation accounts for non-negligible interannual variability, preventing an accurate computation based on the GLVB (Figures B.7, B.8 and B.9 in Appendix B).

Examining the entire water column (Figure 4.4d), high correlation is observed from top to bottom from about 12 to 15°N up to 30°N in the western part and near 45°N in the eastern part. Note that in the western part north 55°N, a narrow region in the open ocean bounded by the Mid-Atlantic Ridge and the mixed layer masked exhibit high values across the water column. Overall, these results evidence the paramount contribution of the geostrophic flow, specifically its meridional component, in dominating the interannual variability of the OGCM vertical circulation over the basin, except for the two regions of high ageostrophic variability: one in the deep tropics and the other along the diagonal band extending from Cape Hatteras and Northwest Europe.

One can interpret in two ways the fact that the reconstructed variability is accurate over larger regions than those in LVB. Either the ageostrophic component of w has a negligible contribution to the interannual variability, or it shares the same variability as the geostrophic w. Figure 4.3 shows an almost constant offset between time series across the observed period, suggesting that the ageostrophic component's influence on the interannual variability of w is negligible within these regions.

4.2.1.4 Summary on the OGCM IDILIV framework

The large percentage of the basin explained by the geostrophic LVB has supported the effort to develop a methodology for estimating the three-dimensional geostrophic w field by vertically integrating the geostrophic meridional velocities from the ocean surface. In this study, we have underlined the critical role of the geostrophic flow divergence across the Ekman layer when computing the Ekman pumping at the surface. In climatological mean, the reconstructed geostrophic w (w_{GLVB}) captures at first order the reference w horizontal patterns in the ocean interior below the maximum mixed layer over the tropical, subtropical and extratropical bands, excluding the equatorial band, the Gulf Stream and the subpolar gyre. However, the reconstructed w does not accurately match the model's output in terms of amplitude, which prevents its use for quantitative analyses of the role of time-mean vertical currents.

To the contrary, $w_{IDILIV3}$ effectively captures the interannual variability of the reference w over most of the basin throughout the entire water column far from the Gulf Stream, the North Atlantic Current, and the low tropical band. Therefore, the geostrophic meridional velocities appear to be sufficient to compute the interannual variability of the velocity field to first order over a significant part of the open ocean. The discrepancies between assessing the 56-year average and interannual variability of the vertical velocity field in the open ocean have revealed the dominant role of the geostrophic component of the vertical velocity in the interannual variability. Conversely, the ageostrophic component plays a minor role in the interannual variability but exhibits an important contribution to the time-mean amplitude. Nevertheless, in the Gulf Stream, North Atlantic Current and the low tropics, the ageostrophic circulation mainly controls both the interannual variability and time-mean amplitude of the vertical flow.

This chapter suggests that the Indefinite Depth-Integrated LInear Vorticity (IDILIV) approach can be an effective tool to compute the interannual variability of the vertical velocity field using observation-based geostrophic meridional velocities of the global upper ocean (see Chapter 5).

4.2.2 Complementary diagnostics and analyses over the North Altantic basin

4.2.2.1 Exploring Self-Uncertainty in Estimating Vertical Motions through a Linear Approach

The formalism proposed in the previous section enables the description of vertical movements applying the geostrophic meridional transport to the depth-integrated LVB (Eq. 1.16). While the LVB terms exhibit high agreement over a considerable portion of the basin, it is noteworthy that the time-averaged vertical velocity estimates significantly deviate from the model output (see Section 4.2.1.3.2). To gain further insights into the factors influencing the sources of these errors between the estimation and the model output, a comprehensive study of the regression equation that best approximates the time series of the estimated vertical velocities is conducted.

A first-order regression will adopt the following expression:

$$y = b_0 + b_1 x \tag{4.4}$$

where y represents the dependent variable, x is the independent variable, b_0 is the intercept term and b_1 is the regression coefficient.

When comparing this equation with Eq. 1.16, a clear similarity between the two expressions becomes evident. By subtracting $w_{Ek}(t)$ from both sides of the equation, $-\frac{\beta}{f}V_g(t)$ where V_g represents the meridional transport from the surface to a given level can be considered as the independent variable. Therefore, the intercept term is approximately equal to a constant close to 0, and the regression coefficient (b_1) should ideally be 1.

Figure 4.5 depicts the regression coefficient between the model's output vertical velocities (from which $w_{Ek}(t)$ has been subtracted) and $-\frac{\beta}{f}V_g(t)$ for each grid point. Figure 4.6 displays the ratio (%) between the intercept term and the time mean w_{Ek}. Since $w_{Ek}(t)$ is subtracted from $w(t)$, the constant intercept term should be considerably smaller than the time mean w_{Ek} in the linear case.

Most areas in LVB validity show a regression coefficient ratio between 0.9 and 1.1 within the upper tachocline. However, the linear fit departs from the Eq. 1.16 at denser layers. This degradation is generally given (in the regions where the LVB is valid) by a slope steeper than 1, which would imply that the w experiences a relatively lesser reduction with depth compared with those within the model, leading to a more barotropic field. This could be interpreted as the geostrophic meridional transport adequately absorbing the waters advected by the vertical flow driven by the wind stress at the surface. Therefore, the deviation from the linearity observed in the NEMO OCCITENS model with depth indicates that the non-linear and ageostrophic components of the vertical velocity field are non-negligible. Even when considering the total meridional velocity, there are non-valid LVB layers across the water column, necessitating the inclusion of non-linear contributions. On the other hand, it seems that the choice of w_{Ek} as the initial value for the depth integral is the good one for the upper tachocline (always in the regions where the LVB is valid), with values below 10% between the intercept term that best fits the fit and the Ekman pumping. With increasing depth, this ratio increases, reaching up to 30% in the deep ocean.

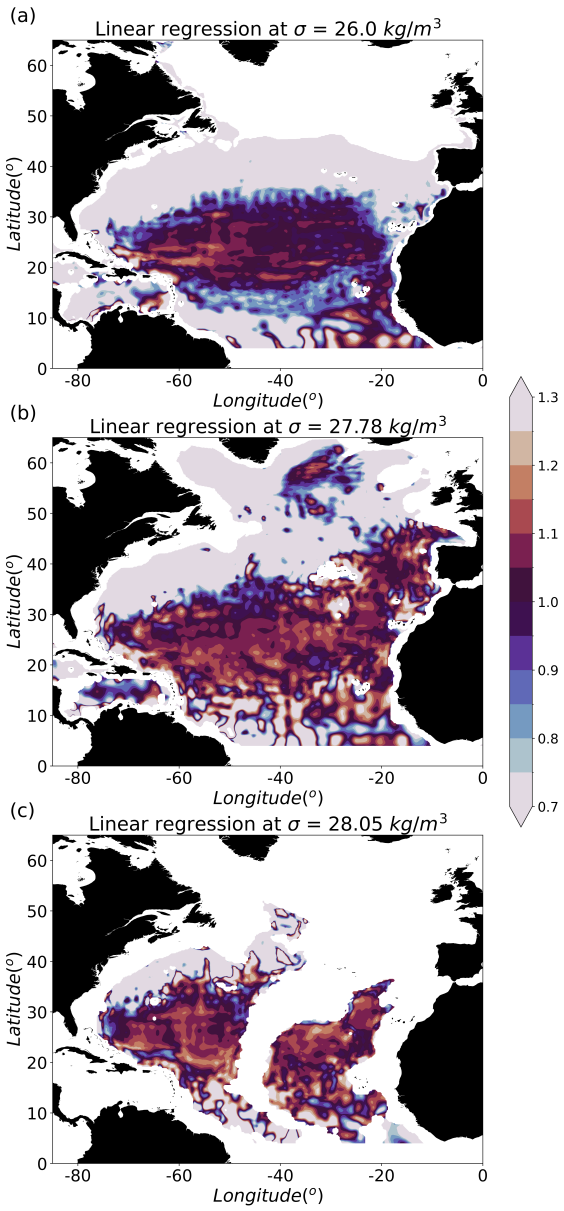

Figure 4.5: Regression coefficient between $w(t)$ - $w_{Ek}(t)$ and $-(\beta/f)V_g(t)$ over σ 26 (a), 27.78 (b) and 28.05 (c) kg m^{-3}.

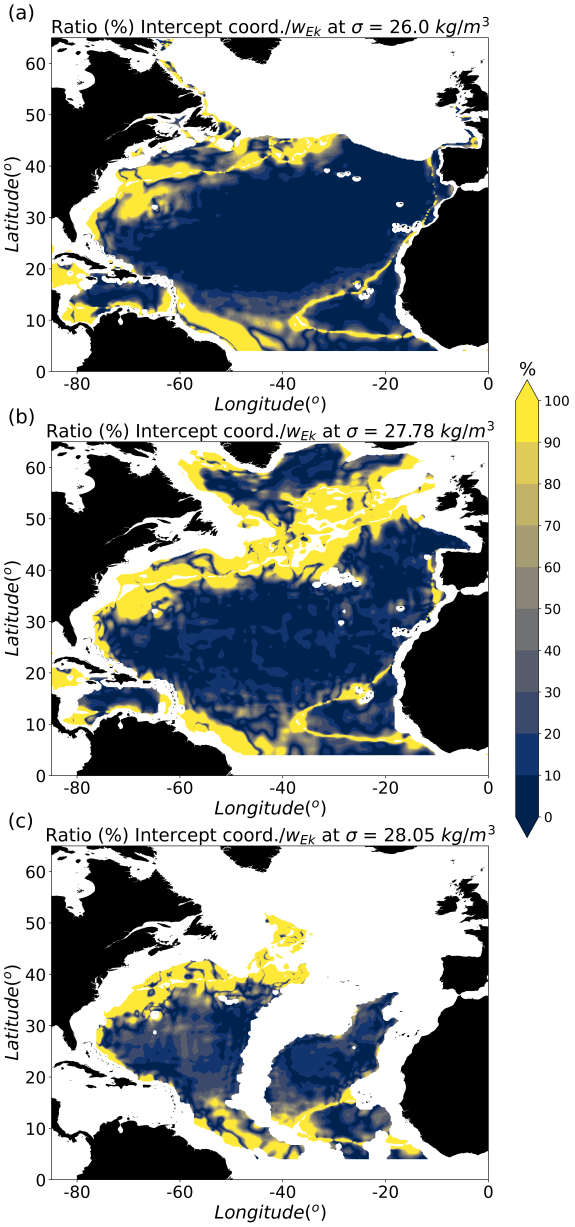

Figure 4.6: Ratio between the intercept term and time mean w_{Ek} in percentage over σ 26 (a), 27.78 (b) and 28.05 (c) kg m^{-3}.

An error in the choice of the surface boundary condition will be transmitted through the entire water column. Even an error below 10% at the surface can severely impact the reconstruction of the vertical flow in the intermediate ocean, where vertical velocity values are at least one order of magnitude smaller than those at the surface.

4.2.2.2 Boundary Forcing Influence on Spatiotemporal Vertical Flow Variability

In Section 4.2.1.3.2, we compared the interannual variability of the vertical velocity estimates and the model output. The IDILIV approach reproduces a highly correlated vertical velocity field compared with the OGCM simulation output throughout the entire water column in the areas where the LVB is valid. On the other hand, the study of the LVB in Chapter 3 has shown that the linear approach is not indepen-

dent of boundary forcing. Although it does not explicitly contain the contribution of the atmospheric and bathymetry interphases, the linear description of the ocean is constrained by these boundary conditions. This condition implies that boundary forcing signals are transmitted to the ocean's interior. Therefore, the spatiotemporal synchronisation between the estimates and the atmospheric and bathymetry forcings is computed to understand better how the pathways of vertical motions at the boundaries are transmitted to the ocean interior.

4.2.2.2.1 Temporal Correspondence between Ekman Pumping and Ocean Interior Vertical Velocity

First, it is studied the contribution of the surface forcing to the vertical motions, analysing the temporal correlation coefficient between the Ekman pumping and the vertical velocity field derived from both the simulation output and the IDILIV3 approach (Figure 4.7). This analysis allows for the assessment of how atmospheric forcing influences vertical motions and the degree of coherence with the model simulation.

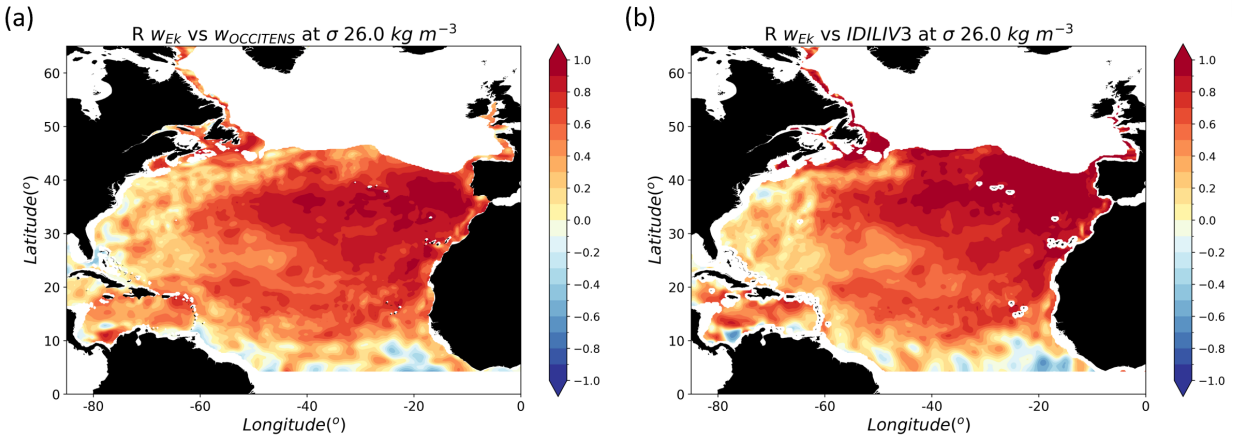

Figure 4.7: Time correlation coefficient between Ekman pumping vertical velocity (w_{Ek}) and the model's output (a) and estimated (b) vertical velocity field over σ 26 kg m^{-3}.

Focusing on the upper tachocline (Figure 4.7), it reveals that a significant portion of the STG exhibits a high correlation between the atmospheric forcing and both vertical velocity fields. However, comparing the depth of the isopycnal surface in Fig. 1.16 with these recent results, a decline in the correlation coefficient towards the west, where the isopycnal surfaces become deeper. This result, together with the findings in Section 4.2.1.3.2, may indicate that not only there is a reduction in the amplitude of the field as we descend in the water column, compared with the surface boundary condition, but also its interannual variability is not sustained. In the tropical gyre, despite its proximity to the surface, we observed that only the northern half of the gyre exhibits positive correlation coefficients. This finding indicates that the interannual variability of the southern half of the TG is not in phase with the atmospheric forcing. The lack of positive correlation in these regions suggests that the variability of the vertical motions is influenced by other factors rather than being directly synchronised with the atmospheric forcing.

The visual comparison between the w field over isopycnal surfaces with the surface forcing in Section 3.2.1.3, together with the results from Figure 4.7 have provided valuable insights into the spatial variability of the vertical motions. Our findings suggest that the surface influence is more homogeneous at horizontal

levels compared to isopycnal levels. This observation indicates that the patterns generated by the surface forcing are better transmitted and more consistently distributed over horizontal levels than isopycnal levels throughout the basin.

4.2.2.2.2 Impact of Upper and Lower Boundaries on Vertical Circulation Pathways

It is essential to understand how and to what extent the vertical velocity patterns forced by the vertical boundaries are transmitted through the water column and how effectively the linear description of the ocean captures them compared to the model's output. To address the extension of the boundary forcing into the ocean interior, the spatial correlation coefficient between the Ekman pumping vertical velocity and the model's bottom vertical velocity with the vertical velocity field in the ocean interior has been computed.

Surface Forcing

Figure 4.8a shows the spatial correlation coefficient between the time-mean vertical velocities at each horizontal level and the time-mean Ekman pumping over LVB valid areas. The imprint of the time-mean atmospheric forcing pattern experiences a decline with depth, reaching a correlation coefficient close to zero at approximately 300 m depth for the simulation output and around 400 m depth for the estimate based on the meridional geostrophic velocities. This finding is consistent with a stronger influence of the surface

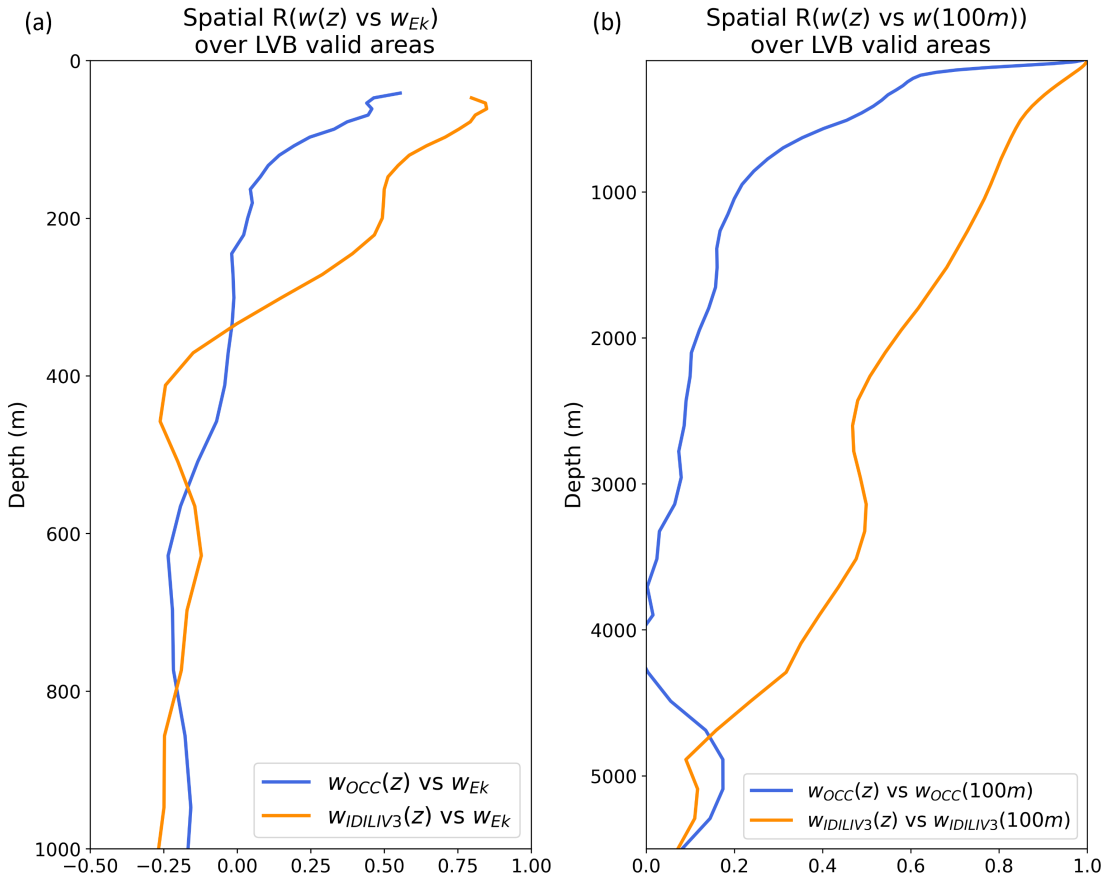

Figure 4.8: Spatial correlation coefficient between time-mean Ekman pumping vertical velocity (w_{Ek}) and the vertical velocity field at each horizontal level (a). Spatial autocorrelation coefficient between time-mean vertical velocity at 100 m depth and the vertical velocity field at each horizontal level (b). The spatial correlation has been computed only over LVB valid areas.

forcing in the IDILIV approach, probably because the depth-integral explicitly uses the Ekman pumping as boundary condition (Eq. 1.16), unlike the simulation output that is a prognostic variable computed depth integrating the continuity equation from the seabed (Madec et al., 2019).

However, the horizontal movements of the model output are, to some extent, directly influenced by the atmospheric forcing. It raises the question of whether the observed rapid decay of the correlation between the vertical velocity and the surface forcing is primarily due to the surface forcing alone or to an increased isolation between the inner layers. To address this question, the spatial autocorrelation over the LVB valid areas between the vertical velocity at 100 m depth and the vertical velocity at each vertical depth level both for the simulation output and IDILIV approach are computed in Figure 4.8b. The rapid decay for the model's simulation (Figure 4.8a) can be attributed not only to greater independence from the surface forcing but also to stronger isolation between the upper tachocline layers and the lower regions (Figure 4.8b). The rapid loss in spatial correlation with depth in the simulation output aligns with previous studies using ECCO reanalysis (e.g. Liang et al., 2017). In the latter study, the surface forcing has a relatively shallow influence, reaching only the first 500 m depth (considered when R reaches a value smaller than 0.5).

Nonetheless, the $w_{IDILIV3}$ exhibit a more barotropic behaviour in the spatial structure features than the NEMO OCCITENS simulation, with weaker changes in its pattern throughout the water column. The correlation coefficient reaches 0.5 below 3000 m depth, indicating a more coherent relationship between the estimated vertical velocities at the surface and intermediate ocean layers. Once more, the disparities between the autocorrelation and the correlation with the Ekman pumping show that the two vertical velocities are not equivalent in intensity and spatial pattern. The more coherent structure of the geostrophic vertical velocity field between the upper and intermediate oceans, in contrast to the total component, suggests that the geostrophic component experiences a lesser degree of isolation between them.

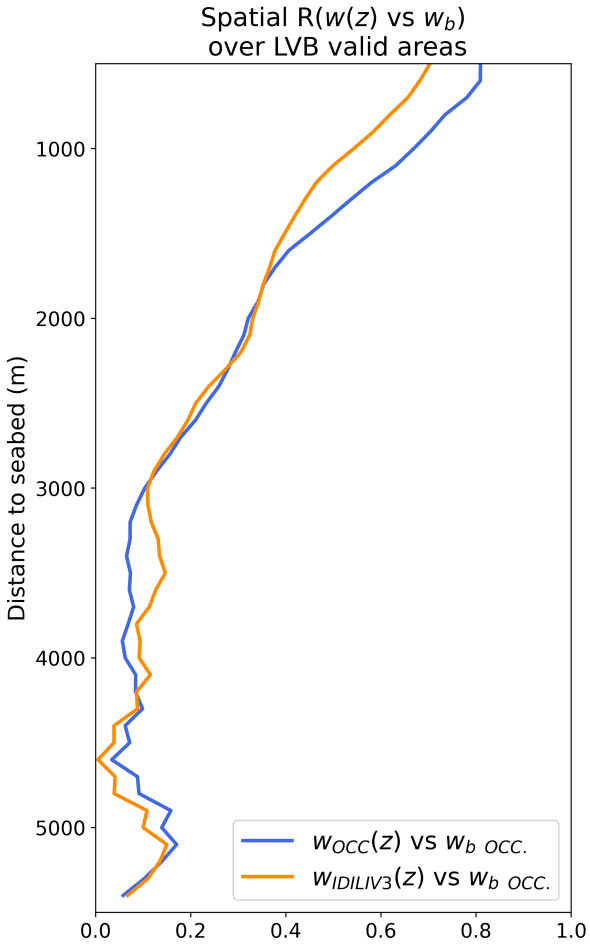

Figure 4.9: Spatial correlation coefficient between time-mean model's output vertical velocity at the deepest level depth and the vertical velocity field at each level above the seafloor. The spatial correlation has been computed only over LVB valid areas.

Bathymetry Forcing

The temporal variability of the deep ocean takes periods much longer than the upper layers (Yeager, 2020). Together with the still coarse knowledge of the varying deep circulation, we will focus only on the influence of the ocean floor in the climatological patterns of the w field. Figure 4.9 shows the spatial correlation between the bottom vertical velocity (vertical velocity at the deepest level in the model's simulation) and both simulation and estimated vertical velocity fields over LVB valid areas. Mimicking the surface forcing, it can be assumed that the bathymetry forcing pathways are transmitted into bathymetry-following levels instead of the natural vertical grid of the model. For this reason, the model's vertical levels were interpolated into bathymetry-following levels to compute the analysis from the bottom of the ocean. The results using the simulation's w output are consistent with the findings from Liang et al. (2017) in the Northern Hemisphere, showing that the model's output has a slightly stronger influence of the bathymetry (up to 1500 m depth above the bottom with R values above 0.5). The $w_{IDILIV3}$ has a correlation coefficient around 0.1 weaker than the simulation. These values for the estimation demonstrate the independence of the deep ocean from the surface forcing, indicating that the forcing of the bathymetry, along with the geostrophic currents, plays a crucial role in modulating the vertical movements at these depths. However, starting the depth-integral from the surface, unlike the NEMO OCCITENS simulation, overestimates the influence of surface patterns in the interior ocean at the expense of maintaining the deep circulation pattern.

These results have facilitated the decomposition and quantification of the persistence of the influence of the surface and bottom forcings on large-scale vertical circulation patterns throughout the water column. It is worth highlighting that the vertical structure correlation obtained, particularly concerning the surface, could be influenced by the average period's length. Here, the wind-driven circulation is confined to the upper tachocline by the first baroclinic mode wave (Tailleux and McWilliams, 2001), encompassing time scales ranging from years to decades. Consequently, any change in the averaging period can also affect the depth of the atmospheric influence.

4.3 Global Expansion of IDILIV Approach

The consistent results for the validity of the LVB in the global ocean in Chapter 3 and the successful estimation of vertical velocities in the upper tachocline North Atlantic basin have motivated us to extend the estimation of the vertical movements to the rest of the ocean.

Due to the increasing errors with depth and the spatiotemporal constraints associated with the availability of the global observation-based geostrophic velocities up the upper 1500 m during the 1993-2019 period (ARMOR3D; Guinehut et al., 2012 and Mulet et al., 2012), this section will primarily focus on the upper ocean during the overlapping ARMOR3D and NEMO OCCITENS simulation period (1993-2015). The methodology used in Section 4.2 of this chapter has been extended to the global ocean using the annual average of meridional velocity field as input for the depth-integrated LVB and the annual average of the Ekman pumping vertical velocity as boundary condition at the surface. In this section, a distance-to-shore filter has been applied to the velocity fields, with maximum filtering of 7° at the centre of the ocean basins and a minimum of 2° at the lateral boundaries, as in Section 3.3 (for further details, please refer to Appendix B). Figure 4.10 shows the time-average of the $w_{IDILIV3}$ over σ 26 kg m^{-3} during the 1993-

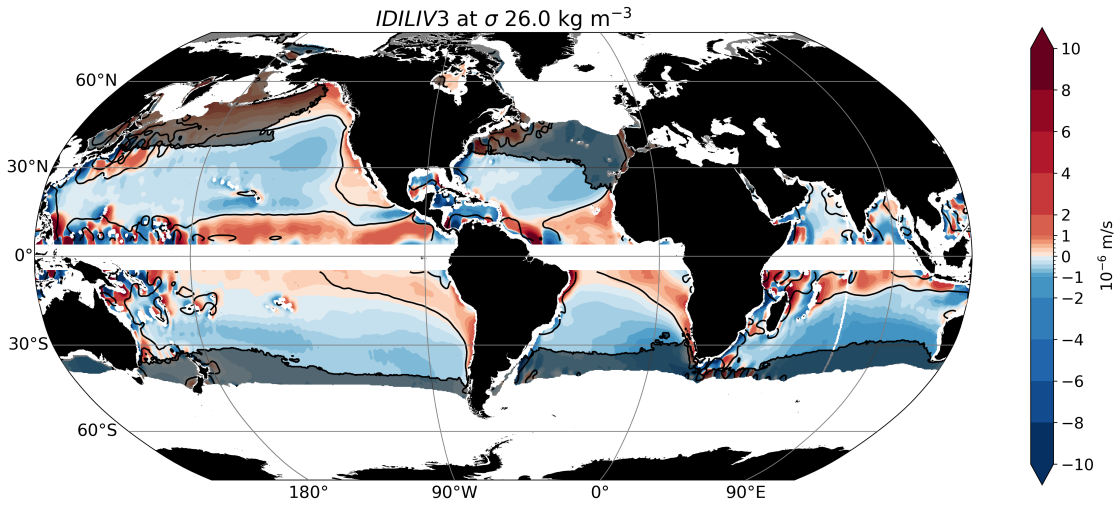

Figure 4.10: Time-mean vertical velocity estimate $w_{IDILIV3}$ over σ 26 kg m^{-3}. $w_{OCCITENS} = 0$ line represented by the black solid contour. The black translucent mask displays the region within the maximum mixed layer. The equatorial band has been masked.

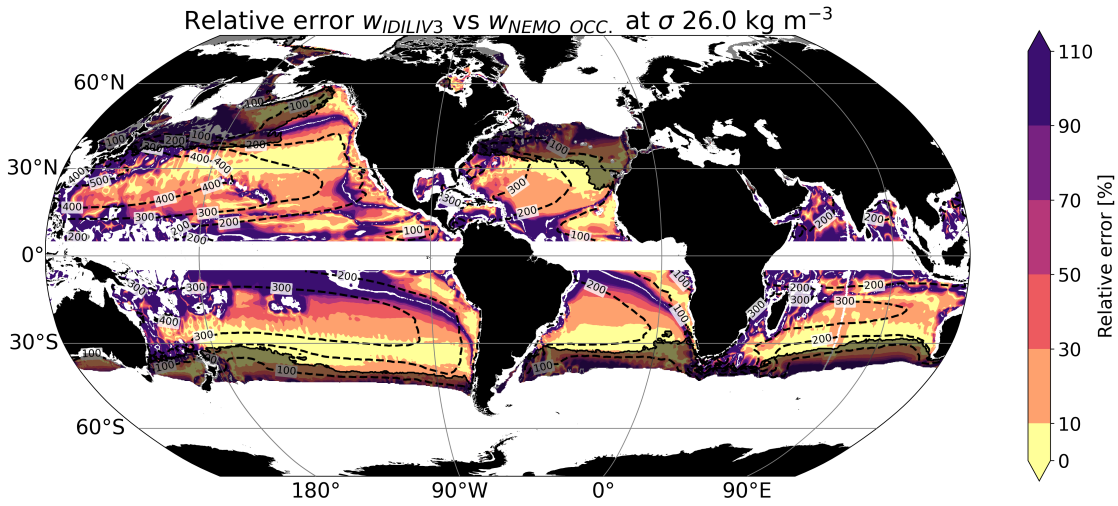

Figure 4.11: Absoolute relative error between $w_{IDILIV3}$ and the model's output over σ 26 kg m^{-3}. The dashed contours represent the depth of the isopycnal surface in meters. The translucent black mask displays the region within the maximum mixed layer. The equatorial band has been masked.

2015 period. The $w_{IDILIV3}$ reproduce the location of the gyres in the model's simulation ($w_{OCCITENS} = 0$ represented by the solid black contour in Figure 4.10), as already observed for the North Atlantic (Figure 4.2a).

However, the $w_{IDILIV3}$ exhibit quantitative relative differences with the NEMO OCCITENS simulation's w (Figure 4.11). The examination of the results indicates that the IDILIV approach reproduces most of the large-scale gyre circulation, with errors below 50%. Within the interior of each tropical and subtropical gyre, the accuracy of the vertical velocity reconstruction progressively improves with latitude. The largest relative errors, above 50%, are primarily found within the upper tachocline in the western boundaries, the equator band and the intergyre regions where the non-linearities, the friction terms and the lateral diffusion are needed to close the vorticity budget.

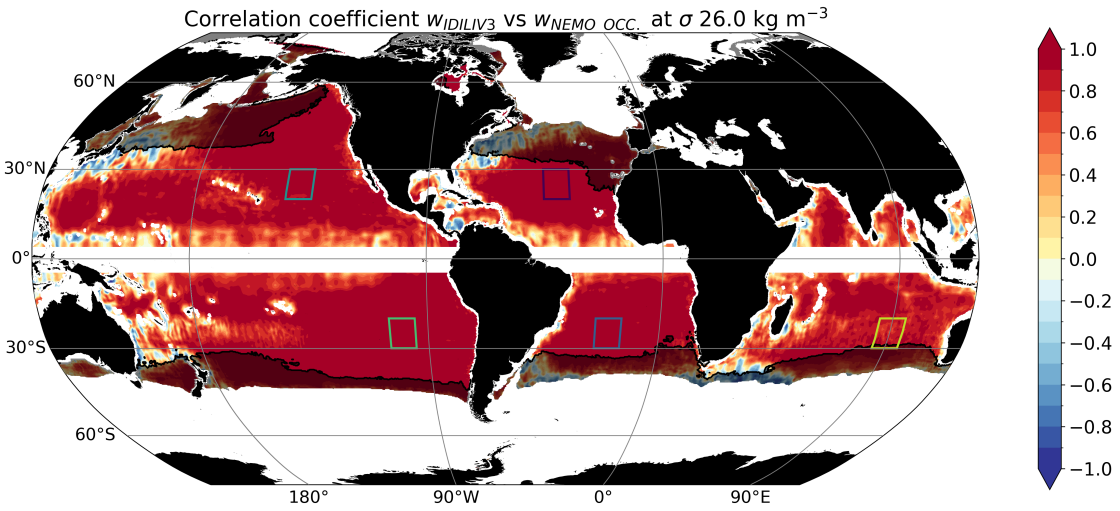

Figure 4.12: Correlation coefficient between $w_{IDILIV3}$ and the model's output over σ 26 kg m^{-3}. The translucent black mask displays the region within the maximum mixed layer. The equatorial band has been masked.

While the time-mean amplitude estimated diverge from the model, the correlation coefficient between the OGCM output simulation and the $w_{IDILIV3}$ (Figure 4.12) exhibit values above 0.8 in most of the global ocean basins (Figure 4.12) over σ 26 kg m^{-3} except for the global equatorial band, the Indian and the western parts of the Pacific and Atlantic tropical bands and the western boundary currents. The high correlation coefficient observed across the global ocean is maintained even in regions where the IDILIV approach does not accurately replicate the time-mean vertical pathways (Figure 4.11) and in regions where the LVB does not hold, such as the mixed layer.

To aid in comprehending the spatiotemporal dynamics, Figure 4.13 allows comparing the time series of the estimated vertical velocity and model's output over five distinct regions corresponding to the subtropical gyres across the global ocean (see rectangles in Figure 4.12). In all regions, the synchronicity and variance of the time series are highly satisfactory (Figure 4.13). However, a consistent deviation between the model's output and the $w_{IDILIV3}$ of less than $1 \cdot 10^{-7}$ m s^{-1} is obtained. Note that despite this deviation between velocity fields is smaller than the amplitude of variation in the field, it contributes to the significant relative errors observed in the mean state (Figure 4.11).

Those results in the synchronisation of the total and geostrophic w fields underscore the robustness of the LVB to simulate and understand the dynamics that lead the vertical motions. However, the discrepancies in extension between time-mean and variability agreement, together with the limited amplitude and mostly constant difference in comparison with the variance of the vertical field between both fields, suggest that the geostrophic component of w dominates the annual variability of the vertical flow. In contrast, the non-linear components of w, while influencing the amplitude of the flow, have a smaller contribution to the interannual variability.

These promising results, coupled with an awareness of its limitations, motivate us to use observation-based geostrophic meridional velocities for estimating a global upper ocean observation-based w product. This pursuit will serve as the main objective of the next chapter.

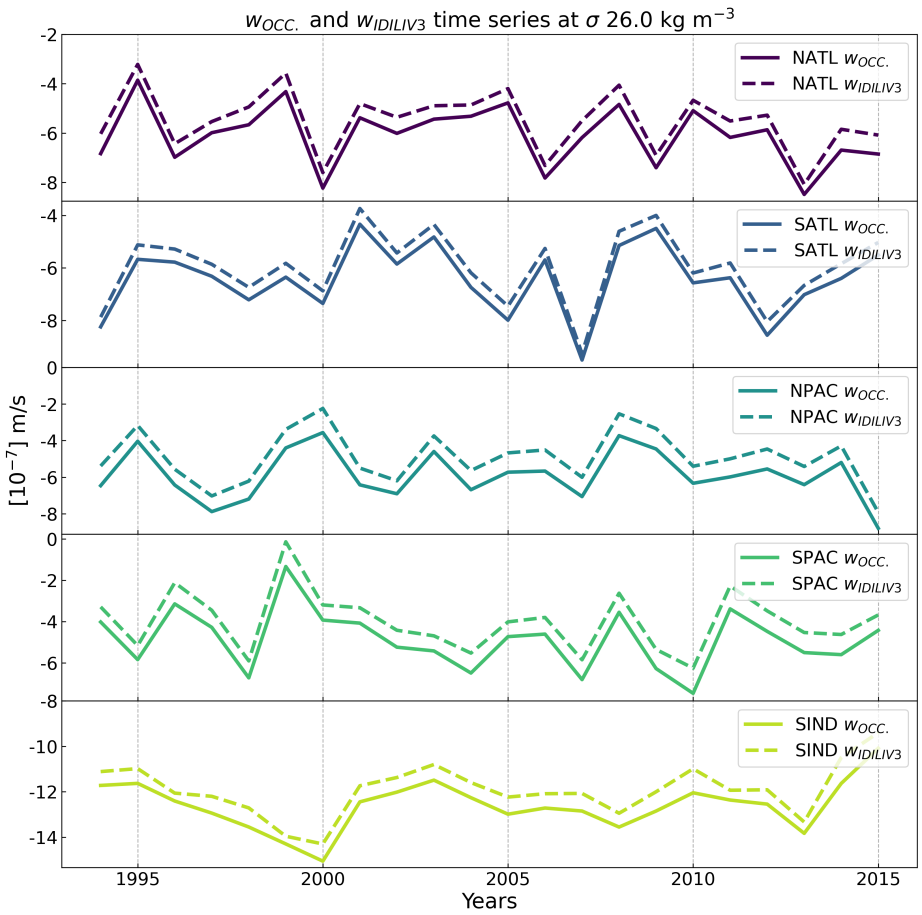

Figure 4.13: Time-series of $w_{IDILIV3}$ (solid line) and NEMO OCCITENS simulation w (dashed line) over the spatial-averaged regions defined in Figure 4.12.

4.4 Conclusions

An attempt to estimate the annual geostrophic vertical velocity field has been conducted by applying the geostrophic meridional velocity field from the NEMO OGCM OCCITENS simulation to the Indefinite Depth-Integrated LInear Vorticity (IDILIV) equation, using the Ekman pumping vertical as boundary condition.

An analysis spanning 56 years (1960-2015) of the North Atlantic water column and 26 years of the global ocean upper tachocline revealed that the estimated time-mean geostrophic vertical flow reproduces the localisation of the time-mean w's large-scale gyre structure compared to the NEMO OGCM OCCITENS simulation used as reference. This alignment occurs below the winter mixed layer over the subtropical and eastern tropical and extratropical bands away from the Western Boundary Current (WBC) regions and the Subpolar Gyres (SPGs). In the North Atlantic, we have shown that the estimated geostrophic velocity field exhibits values of the same order of magnitude as the reference: approximately 10^{-6} m s^{-1} in the upper tachocline and deep ocean, and 10^{-7} m s^{-1} in the intermediate ocean. Nevertheless, the closest agreement with the reference was found within the upper tachocline. In Chapter 3, we defined the threshold for considering the LVB valid in 10%. Therefore, even within the valid areas, there is a certain degree of uncertainty between the estimation of vertical velocities from the LVB and the total vertical velocities of the model. Indeed, these discrepancies in the LVB accumulate at each level during the estimation of w, causing it to deviate further from the model's output. The discrepancies between the reference and our

geostrophic estimate suggest a significant contribution from the non-linear components of w. While the estimated geostrophic w in the ocean interior aligns spatially with the upper ocean's pathways, the total field—encompassing the non-linear terms—deviates from the surface boundary forcing in the intermediate ocean below 1000 m depth. Despite the differences between fields, the estimated geostrophic vertical velocities still exhibit a similar spatial correlation with the bottom boundary features, as observed in the model's case.

The discrepancies between the two representations of the vertical circulation, although within the same order of magnitude as the time average, are smaller ($\sim$ 0.5 of the standard deviation) than the interannual amplitude. The IDILIV method effectively captures the interannual variability of the open-ocean velocity field. Notably, the interannual correlation between the NEMO OCCITENS simulation's output and the estimated w consistently exceeds 0.8 across extensive global ocean regions, excluding areas near western boundaries and the equator band. Distinguishing between estimating the time-mean and variability of the vertical velocity field has unveiled the dominance of the geostrophic meridional transport in interannual variability. Conversely, non-linear components play a lesser role in driving the interannual variability but significantly influence the vertical flow amplitude.

The ability of the LVB to reproduce the global upper open-ocean circulation, coupled with the robustness of the IDILIV approach for estimating the variability of the vertical flow, leads to evaluate in Chapter 5 the question: **Does the available observation-based wind stress and geostrophic meridional transport data allow for the estimation of three-dimensional vertical velocities assuming an ocean in Linear Vorticity Balance?**

¡Pobre mar condenado
a eterno movimiento,
habiendo antes estado
quieto en el firmamento!

— Federico García Lorca, *MAR, 1919*

5

Estimating Vertical Velocities in the Upper Ocean from Observation-based Geostrophic Meridional Transport

The thermocline or upper tachocline, as demonstrated in this study, is fundamental as a transfer layer between a highly variable atmospheric forcing and the slow deep ocean reservoir. Thus, it plays a determining role in driving the physical carbon pump (Iudicone et al., 2011; Lévy et al., 2013; Iudicone et al., 2016), exerting a profound impact on global climate (Le Quéré et al., 2010), ocean biogeochemistry (Freilich and Mahadevan, 2021) and primary production (Lévy et al., 2005).

Since Stommel and Arons (1959), numerous studies have attempted to estimate vertical velocities from observations (see Introduction). Yet, these efforts have predominantly focused on small oceanic regions where the vertical velocities exceed those examined in this study. Despite their importance, only one global vertical velocity product based on observations currently exists: OMEGA3D (Buongiorno Nardelli et al., 2018; Buongiorno Nardelli, 2020). However, without a fully observation-based ground truth, proposing alternative approaches and products of w is imperative.

The extensive capability of the IDILIV approach in the OGCM simulation as an estimator of the vertical flow provides confidence in its application for estimating vertical flow in an observational context (Observation-based Linear Vorticity Vertical Velocities estimates (OLIV3)). This estimation is derived from ARMOR3D geostrophic meridional velocities (Mulet et al., 2012; Guinehut et al., 2012), with ERA5's Ekman pumping vertical velocity employed as boundary condition for the LVB depth-integral. Given the inherent challenge of directly validating the vertical velocity estimates, we explore how they reproduce some of the characteristic oceanic phenomena pointed out from available datasets. These comparisons are made against four estimates of w: including the NEMO OCCITENS simulation output used in previous chapters, two ocean reanalyses, GLORYS (Verezemskaya et al., 2021) and ECCO (Forget et al., 2015; Fukumori et al., 2018), and the OMEGA3D product.

5.1 Preamble

The evaluation of the Linear Vorticity Balance (LVB) validity reveals the potential for a simple description of the circulation in a large portion of the open upper ocean (refer to Chapter 3). Additionally, the geostrophic vertical velocities derived from the Indefinite Depth-Integrated LInear Vorticity (IDILIV) approach accurately reproduce the interannual variability within the LVB valid areas, but only a percentage of the mean amplitude (see Chapter 4). However, it is through the utilisation of observations-derived products that we can gain a more accurate understanding of the behaviour of the real ocean.

These results serve as the foundation for constructing and assessing the Observation-based Linear Vorticity Vertical Velocities estimates (OLIV3). This dataset contains the global upper ocean vertical velocity (w) field spanning the period 1993-2018, computed employing the Indefinite Depth-Integrated LInear Vorticity (IDILIV) formalism applied to a geostrophic meridional velocity field derived from observation-based data (ARMOR3D). The Ekman pumping vertical velocity at surface, calculated using the ERA5's wind stress, has been defined as boundary condition.

We will show that OLIV3 reproduces the order of magnitude and the distribution of the large-scale horizontal pathways and the vertical structure of the climatological upper tachocline (in this Chapter referred as tachocline) vertical velocity field, together with the interannual variability of the vertical flow over the open ocean when compared to the NEMO OGCM OCCITENS simulation and the GLORYS and ECCO reanalyses. The w field estimated in OMEGA3D product contrasts with OLIV3, NEMO OCCITENS simulation and reanalyses' vertical velocities. While OMEGA3D reproduces the horizontal distribution of the vertical flow within the subtropical gyres throughout the tachocline, it captures an almost entirely barotropic ocean. Furthermore, it exhibits the weakest interannual correlation with the rest of the datasets, suggesting that the use of the horizontal gradient of w in the omega equation approach, unlike the only depth integral in the continuity and LVB equations, leads to major differences in the field.

These observational-based estimates of vertical velocity could be pivotal for open ocean research at frequencies lower than annually, particularly for computing tracer fluxes in the ocean.

The chapter is organised as follows: The description of the time-mean OLIV3 over the global upper ocean is presented in Section 5.2. The intercomparison test between the OLIV3 and the validation dataset is performed in Section 5.3. Within Subsection 5.3.2, the four-dimensional features of the various datasets are examined in two averaged regions within the North Atlantic tropical and subtropical gyres. The intercomparison between the various datasets is extended at global scales in Subsection 5.3.3. A general discussion on the possible source origin of discrepancies between the baroclinic/barotropic datasets is conducted in Section 5.4.

5.2 Observation-based Linear Vorticity Vertical Velocities (OLIV3)

The accomplished estimation of the vertical velocity from the surface wind stress using an OGCM simulation in Chapters 3 and 4 allows reconstructing the vertical velocity field from observations (Observation-based Linear Vorticity Vertical Velocities estimates (OLIV3) hereafter). This is achieved by applying observation-based meridional velocities from Argo and satellite measurements (ARMOR3D; Guinehut et al., 2012; Mulet et al., 2012) to the Indefinite Depth-Integrated LInear Vorticity approach, using ERA5's wind product as a boundary condition at the surface (z = 0). These inputs generate a global w reconstruc-

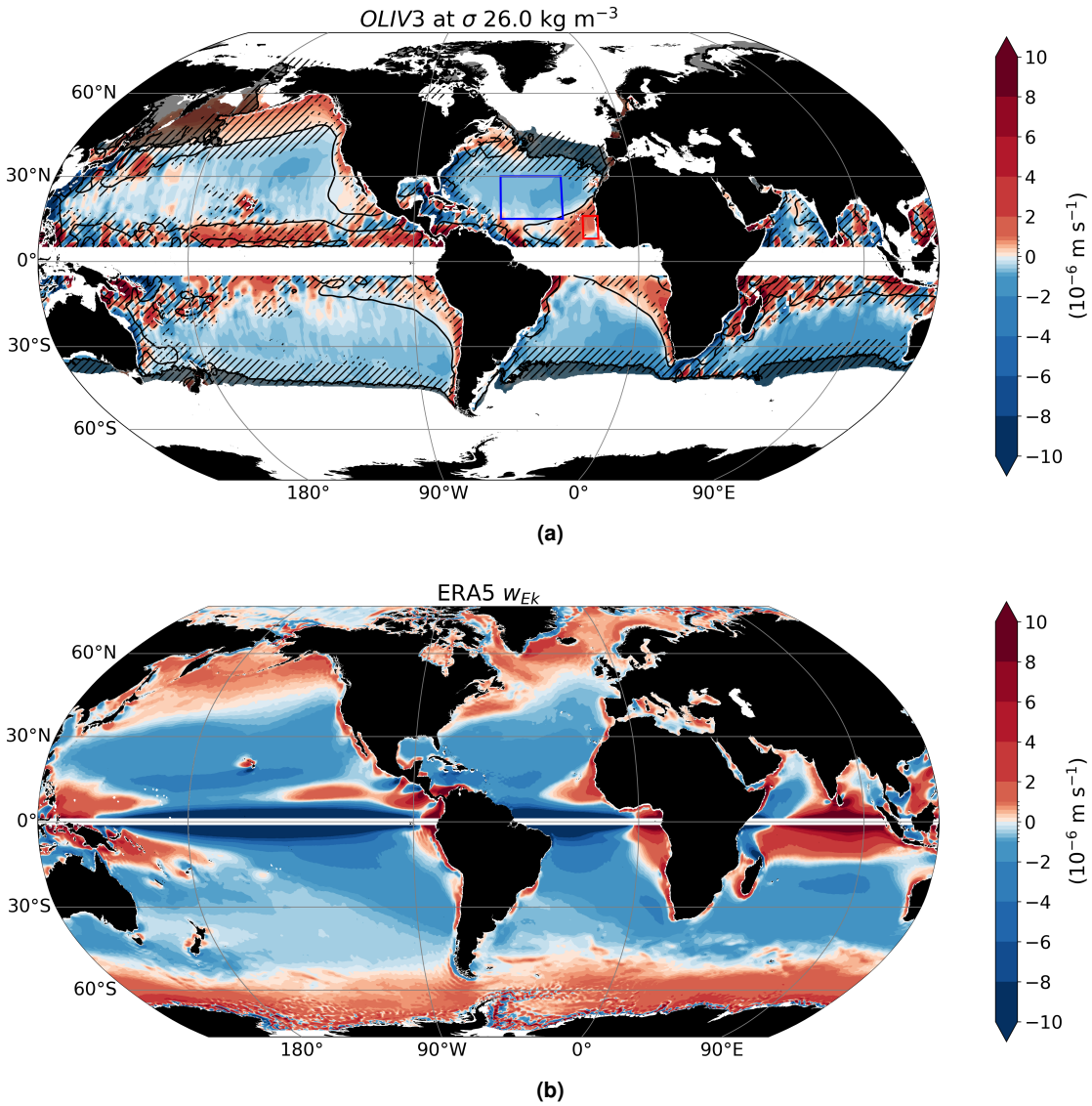

Figure 5.1: Time-mean 1993-2018 vertical velocity estimate from observations (OLIV3) over σ 26 kg m^{-3}. The black solid contour and the black hatching represent the $w = 0$ line and the areas with $|\Delta_{LVB}|$>10, respectively, in the NEMO OCCITENS simulation (a). Time-mean vertical Ekman pumping vertical velocities (w_{Ek}) computed from ERA5 wind stress (b).

tion with a 0.25° horizontal grid and yearly resolution. The 26 years (1993-2018) time-mean OLIV3 over σ 26 kg m^{-3} is represented in Figure 5.1a after applying a distance-to-shore filter. This filter employs a maximum kernel of 7° at the centre of the ocean basins and a minimum of 2° at the lateral boundaries

(for further details, please refer to Appendix B). The solid black contour and the hached areas in Figure 5.1a represent, respectively, the $w = 0$ line (see Figure B.10a in Appendix B) and the non-valid LVB areas ($|\Delta_{LVB}|$ (Eq. 3.4) > 10) within the NEMO OCCITENS simulation (Figure 3.20).

The OLIV3 field within the tachocline reproduces the well-known wind-driven circulation features, exhibiting upwelling in the tropical tachocline and downwelling in the subtropical gyres coherent with the Ekman pumping (Figure 5.1b). However, the amplitude of the tachocline vertical velocity field diminishes with depth (see colorbar in Figure 5.1a). This decrease towards deep layers supports the baroclinic nature of the velocity field within the tachocline coherent with the necessity of a level of no motion at a given depth to close the Sverdrup balance, and the baroclinic nature of the field displayed by the OGCM simulation w field in previous chapters (Figure 3.2).

The upwelling/downwelling structures reproduced by OLIV3 are consistent with the NEMO OCCITENS simulation output (black contours in Figure 5.1a) even in regions characterised by large LVB relative errors areas, such as the North Pacific tropical band, the South Pacific tropical gyre and the western part of the Atlantic tropical gyres (Figure 3.20 and hatching in Figure 5.1a). The ability of the depth-integrated LVB approach to reconstruct the large-scale gyre circulation to a certain level of accuracy, even in regions where the LVB errors are non-negligible, was discussed through the *perfect model test* using the NEMO OCCITENS variables in Chapter 4.

However, despite the relatively good results of OLIV3 in the definition of the time-mean gyres from the OGCM simulation, it exhibits poor accuracy in the reconstruction of the amplitude (see Figure B.14 in Appendix B). In other areas, such as the South Pacific and Indian tropical bands, where the LVB does not hold, the OLIV3 do not reproduce the characteristic upwelling from the model (black contours in Figure 5.1a). In the central region of the South Pacific tropical band characterised by a downward flow and explained by the LVB, the OLIV3 yield positive values.

5.3 Intercomparison Study of Estimated Vertical Velocity Field with Existing Datasets

Large-scale vertical velocities in the open ocean upper ocean pose challenges for direct measurement due to their small magnitudes, typically around 10^{-6} m s^{-1} in the centre of the oceanic gyres, further decreasing to approximately 10^{-7} m s^{-1} near the bottom of the tachocline (see Introduction). Consequently, the validation of OLIV3 using observations becomes inherently problematic. Nevertheless, it is possible to assess the fidelity of OLIV3 in reproducing different oceanic phenomena by comparing them with various existing w estimates.

5.3.1 Methodology

The validation datasets used in this chapter are the model output that served as the foundation for the framework, two reanalyses, GLORYS (Verezemskaya et al., 2021; Jean-Michel et al., 2021) and ECCO (Forget et al., 2015; Fukumori et al., 2018), and an existing observation-based w dataset, namely OMEGA3D (Buongiorno Nardelli et al., 2018; Buongiorno Nardelli, 2020). Please refer to Table 2.1 for a summary of the details of the datasets. Together with these datasets, the geostrophic vertical velocities estimate derived from applying the Indefinite Depth-Integrated LInear Vorticity (IDILIV) approach in

the NEMO OCCITENS simulation (Chapter 4) is included in the intercomparison test. The comparison between the NEMO OCCITENS output with the NEMO OCCITENS IDILIV estimates, referred as *perfect model test* in Chapter 4 provides insights into the theoretical limitations of theIDILIV formalism that can be expected in the OLIV3.

Two fundamental differences should be highlighted among the datasets used in the intercomparison, one involving the methodology followed to acquire the vertical velocity field, while the second concerns the type of vertical field estimated. i) A common feature shared by five of the six datasets presented here, including both model and reanalyses' outputs and IDILIV-based vertical velocity estimates (Chapter 4 and Section 5.2), is the existence of only the vertical derivative of w in their equations. This approach permits the w estimation solely through the vertical integration of horizontal velocity fields. In the case of both the model and reanalyses, vertical velocities are diagnostic variables determined through the vertical integration of the continuity equation (Eq. 1.6). In contrast, the OMEGA3D product, based on the omega equation, incorporates the second-order vertical derivative of w and horizontal derivatives. ii) The OLIV3 and OMEGA3D output are computed employing geostrophic velocity fields, then acquiring the geostrophic component of the vertical velocity field for the OLIV3 case and the quasigeostrophic w for OMEGA3D. In contrast, the model and reanalyses' vertical velocities are derived from total horizontal velocities. However, the ageostrophic component of the horizontal velocity field is minimal within the tachocline (dotted field in Figure 3.20).

Given the potential discrepancies in the thermohaline field across the various datasets used for the intercomparison, the analysis is conducted again using isopycnal levels defined with the neutral density (Jackett et al., 2006) of each dataset. In the case of the OMEGA3D dataset, the ARMOR3D thermohaline field has been employed to interpolate the w estimates on isopycnal levels. Indeed, the ARMOR3D dataset is used in Buongiorno Nardelli et al. (2018) and Buongiorno Nardelli (2020) to compute the w estimates from the omega equation. To ensure a consistent basis for comparison, considering that the different vertical velocities used in the intercomparison are available at varying spatial and temporal resolutions, all datasets will be smoothed using a distance-to-shore filter (Appendix B) before homogenising them to a 5 x 5° horizontal grid with an annual resolution. During this chapter, we show several fundamental metrics over the 23-year overlapping period (1993-2015), excluding the equator band (5°S/N) due to the inapplicability of the LVB. Acknowledging the multidimensional nature of the vertical velocity field (4D), the metrics to be computed and compared include the time-mean, variance, correlation coefficient, RMSE, time-mean vertical gradient and depth of minimum vertical velocity.

Moreover, the LVB, from which the OLIV3 is derived, is not valid within the mixed layer (Figure 3.20). In this region, the mixing term is a leading contributor to the vorticity budget closure as established thanks to the study conducted within the complete vorticity equation (Eq. 3.2; Figure 3.16) in Section 3.2.2.2. Therefore, all areas above the period's maximum winter mixed layer are masked and excluded from the analysis. However, the definitions of the mixed layer slightly differ from one dataset to another. The mixed layer depth provided by the NEMO OCCITENS simulation is computed using a density criterion of 0.01 kg m^{-3} of density change from the surface following the procedure defined by de Boyer Montégut et al. (2004). In the case of ARMOR3D (Guinehut et al., 2012; Mulet et al., 2012), the mixed layer depth is obtained from the minimum of temperature and density threshold equivalent to a 0.2°C decrease. For ECCO reanalysis, the mixed layer depth is defined following the procedure developed by Kara et al. (2000, 2003), which finds

that the optimal estimated of turbulent mixing penetration is obtained with a mixed layer depth definition of $\Delta T = 0.8°$ C. This may be why the mixed layer in ECCO's case is much deeper than in ARMOR3D and NEMO OCCITENS' cases.

5.3.2 North Atlantic Ocean Intercomparison

The North Atlantic basin has been a central focus of this study (see Section 1 of Chapters 3 and 4). Consequently, in this first part of Chapter 5, the North Atlantic basin is chosen for the intercomparison study of the vertical velocity field estimates. In particular, two specific regions of interest within the North Atlantic Ocean will be analysed. These regions are defined as follows: a downwelling region within the STG (55-30°W/15-30°N) and the eastern TG upwelling region (22-16°W/8-16°N) (rectangles in Figure 5.1a).

Figure 5.2 illustrates the vertical structure of time-mean w averaged within the downwelling (panel a) and eastern upwelling regions (panel b). Within these regions, the vertical velocity fields from various datasets, including the model-based fields, GLORYS reanalysis, and the OLIV3, demonstrate a comparable vertical gradient amplitude with values, e.g. around -8.5 x 10^{-6} m s^{-1} / kg m^{-3} and -5.5 x 10^{-6} m s^{-1} / kg m^{-3} between σ 25 and 26.5 kg m^{-3} for the upwelling and downwelling region respectively. This significant vertical gradient of w is referred to as the baroclinicity of the vertical velocity field. The OMEGA3D product differs from the other datasets by presenting a vertical velocity field that is nearly barotropic.

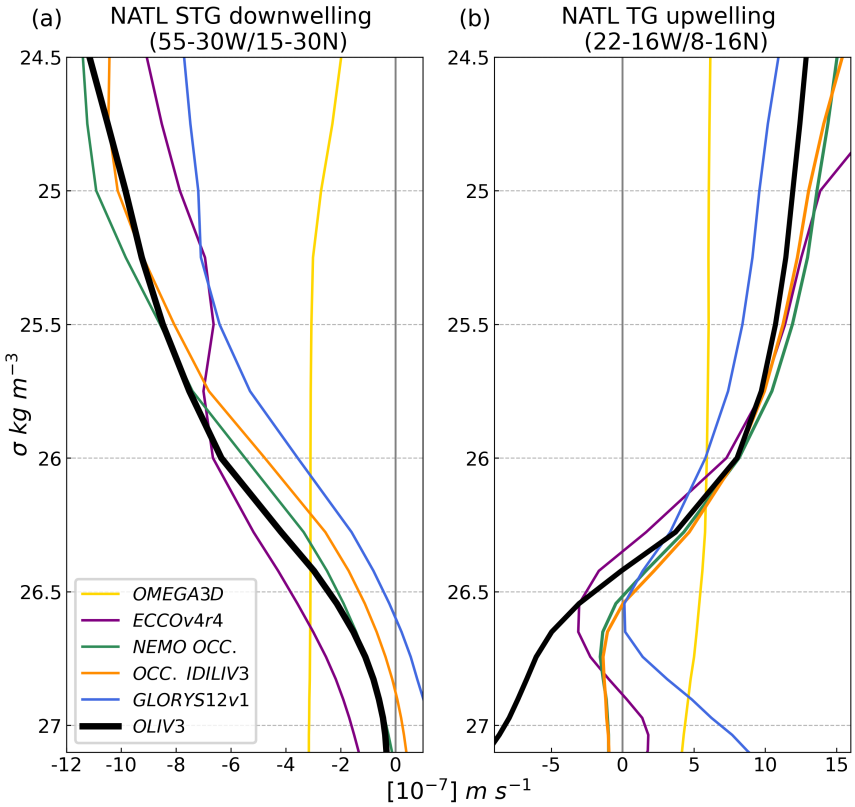

Figure 5.2: Time-mean vertical velocities spatially averaged over the North Atlantic STG downwelling region, bounded by 55-30°W/ 20-35°N (a) and the eastern TG upwelling region (b), bounded by 16-22°W/ 8-16°N for OLIV3, NEMO OCCITENS output, NEMO OCCITENS IDILIV, GLORYS reanalysis output, ECCO reanalysis output and OMEGA3D output.

In the tropics (Figure 5.2b), the minimum vertical velocity level is found around σ 26.5 kg m^{-3}, in contrast to approximately σ 27 kg m^{-3} in the STG (panel a). These two different isopycnal levels illustrate how the fraction of the water column driven by surface atmospheric forcing exhibits different depths within the various North Atlantic regions. Interestingly, in the eastern upwelling region, each dataset group exhibits unique behaviours below the tachocline: the NEMO-based estimates display a more barotropic nature than in the tachocline but with negative values. The reanalysis datasets reproduce a relative velocity minimum, then a transition to positive values with increasing depth. The OMEGA3D product remains predominantly barotropic, always with positive values. Conversely, the OLIV3 exhibits an increasing downward motion at deeper levels. The loss of the capacity of the LVB to close the vorticity budget below the tropical tachocline (Figure 3.9) results in a vertical flow heading to the opposite direction than the reanalyses. At these depths, the geostrophic component of the w is not the main component of the vertical flow. Therefore, relying solely on the LVB to estimate vertical velocities in these regions yields inaccurate results, as evident from the observed outcomes. A logical next step, which unfortunately remains unexplored due to time constraints, would involve estimating the vertical velocity field by adding the horizontal advection of relative vorticity terms to the depth-integral of the meridional transport of planetary vorticity. Such an approach would contribute to balance the LVB residue, especially in regions where the linear description is not valid (Section 3.2.2.2).

Comparing the vertical velocity field estimates at various depths (Figure 5.2), it is evident that the amplitude of the vertical velocity field is reduced with depth within the tachocline. Consequently, focusing solely on one specific depth can potentially lead to a misinterpretation of the field's behaviour concerning other datasets. For example, when assessing the error between the mean values of various datasets in the upwelling and downwelling regions at a given depth, such as σ 26 and 25.75 kg m^{-3} respectively, a close alignment is observed between OMEGA3D values and those from the model simulation and the OLIV3. However, this error is inconsistent throughout the tachocline and primarily arises from the intersection between the most barotropic field of OMEGA3D and the more baroclinic fields of the OLIV3, GLORYS, ECCO and NEMO OCCITENS.

Now that the spatial structure of the velocity field has been analysed, it remains to assess how the OLIV3 captures the temporal dimension of vertical velocities in the North Atlantic regions defined here. The annual time series of the spatially averaged vertical velocities within the same downwelling and eastern upwelling regions as Figure 5.2 are presented in Figure 5.3 over two different depths for the upwelling and downwelling regions that represent the upper and lower tachocline: σ 25.5 (panel a) and σ 26 kg m^{-3} (panel b) for the upwelling and σ 25.75 (panel c) and σ 26.5 kg m^{-3} (panel d) for the downwelling. Interannual frequencies primarily influence the variability within the selected regions. This intrinsic variability of each dataset is also maintained throughout the tachocline, with little change in depth (comparing panels a, b and c, d in Figure 5.3. Within the downwelling region (panels c and d), there is generally a relatively good agreement among most of the datasets. In the eastern upwelling region (panels a and b), the OLIV3 estimate reproduces a field with larger amplitude variations than the model and OMEGA3D outputs, but within the uncertainty of the reanalysis ensemble (by a factor of ~ 10)[1].

[1] Please refer to the values in cells in the diagonal in Figure 5.4

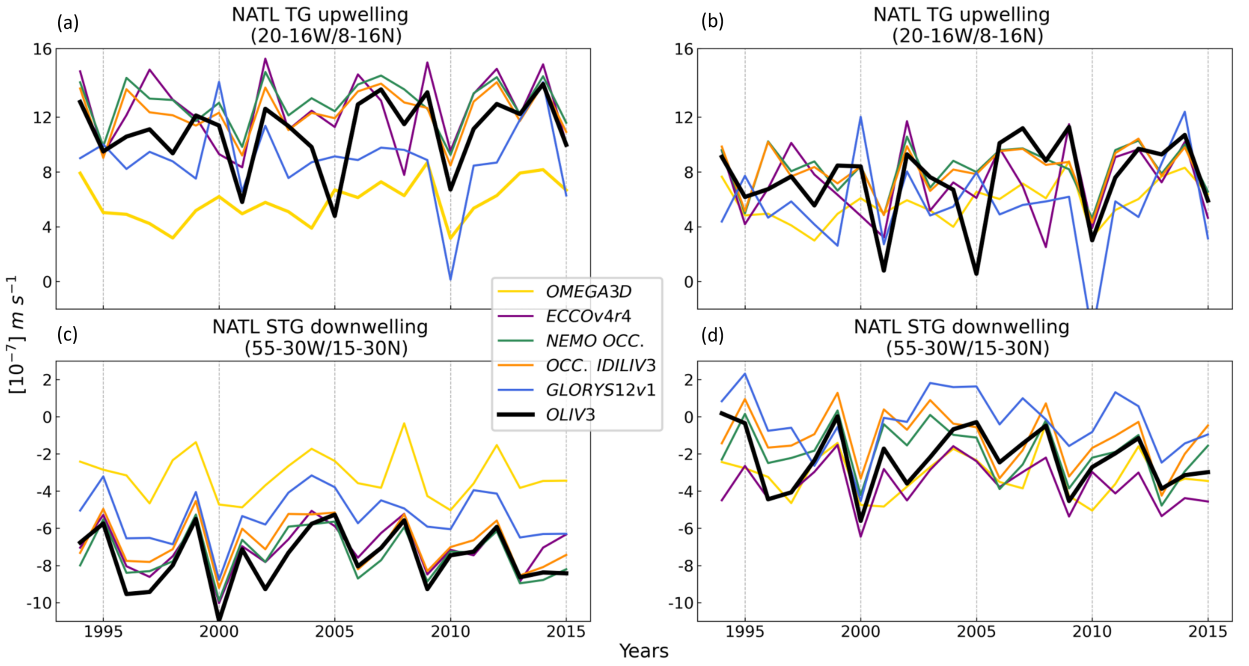

Figure 5.3: Time series of the spatially averaged vertical velocity field for the North Atlantic eastern TG upwelling region, bounded by 16-22°W/ 8-16°N over σ 25.5 (a) and σ 26 (b) kg m^{-3}, and STG downwelling region, bounded by 55-30°W/ 20-35°N, over σ 25.75 (c) and σ 26.5 (d) kg m^{-3} for OLIV3, NEMO OCCITENS output, NEMO OCCITENS IDILIV, GLORYS reanalysis output, ECCO reanalysis output and OMEGA3D output.

Figure 5.4 presents the crosscorrelation (upper diagonal half), cross-RMSE (lower diagonal half) and variance (diagonal) of the vertical velocity fields among the different datasets for the upwelling (panel a) and downwelling (panel b) regions. The upper and lower triangles in each cell within Figure 5.4 contain the values for the upper and lower tachocline: σ 25.5 and σ 26 kg m^{-3} for the upwelling (panel a) and σ 25.75 and σ 26.5 kg m^{-3} for the downwelling (panel b).

A robust correlation is evident among the different dataset time series, with the highest correlation occurring in the downwelling region of the subtropical gyre (upper diagonal half in panels a and b in Figure 5.4). In most cases, the upper triangle in each cell representing a shallower level exhibits a higher correlation than the lower triangle corresponding to a deeper level, indicating a decrease in the synchronicity between the dataset with increasing depth. This trend is also observed in the correlation coefficient between the datasets when comparing the NEMO OCCITENS IDILIV estimate and the model's output (Figure 4.4). However, the reduction of the correlation coefficient is less pronounced in the case of the perfect model, with an R above 0.9 throughout the tachocline (see rectangle corresponding to the "perfect model test" in Figure 5.4). Comparing OLIV3 with the validation set, depicted in the cells within the top row of Figure 5.4, it exhibits correlation values with the rest of the validation datasets ranging between 0.4 and 0.6 in the upwelling areas (panel a) and exceeding 0.7 in the downwelling region (panel b). The correlation values between OLIV3 and the two reanalyses are higher than the correlation coefficient between the reanalyses themselves. Specifically, the correlation coefficient values are approximately 0.25 for the upwelling region (panel a) and 0.4 for the downwelling region (panel b). Hence, OLIV3 falls within the range of uncertainty observed between the reanalyses. Simultaneously, within the selected areas over the North Atlantic basin, OMEGA3D estimates (right column in Figure 5.4) closely reproduce the velocity field variability of the various products studied, achieving a level of accuracy comparable to the OLIV3.

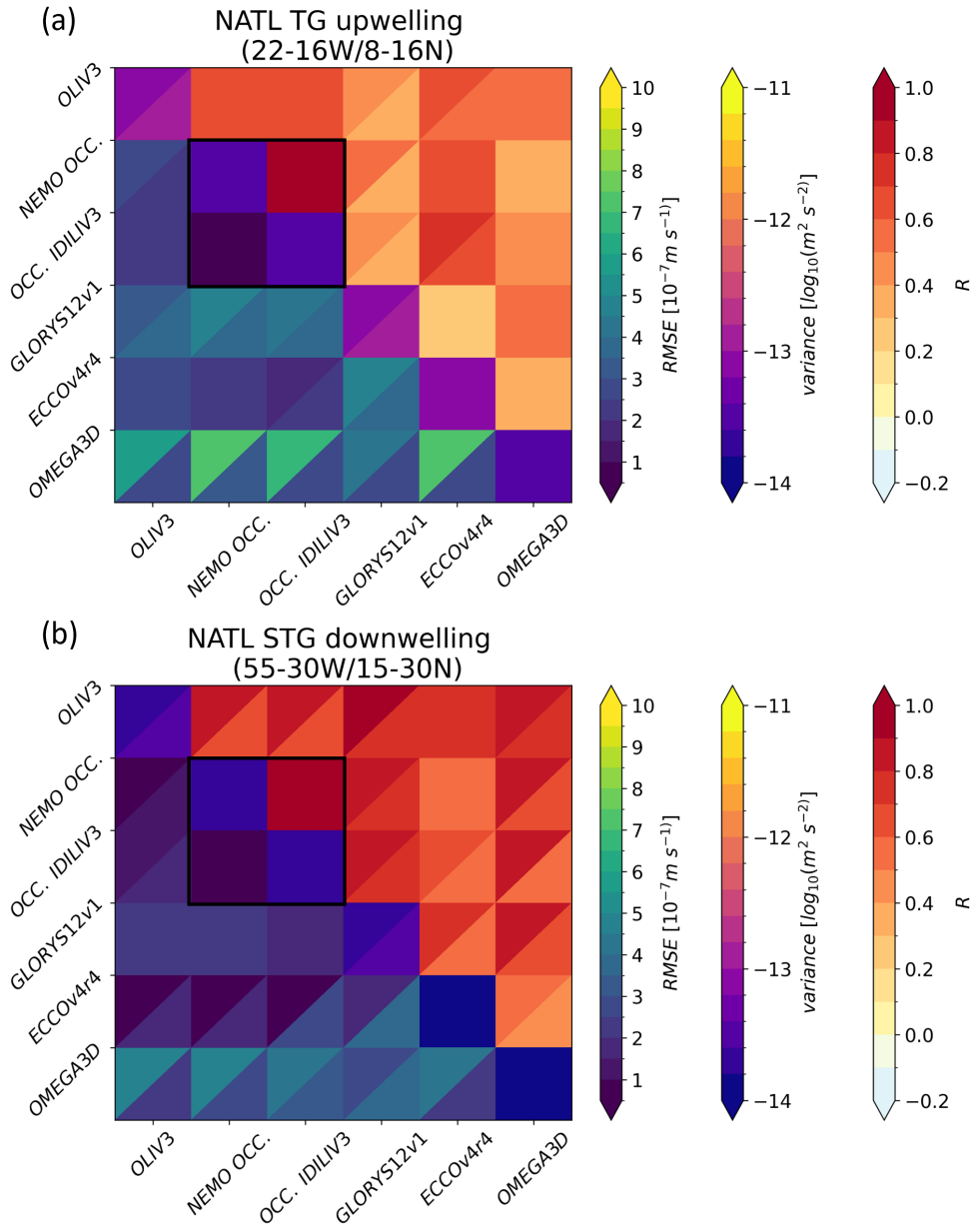

Figure 5.4: Cross correlation coefficient (R) (upper diagonal) and root mean square error (RMSE) (lower diagonal) of the various vertical velocity fields for the North Atlantic eastern TG upwelling region, bounded by 22-16°W/ 8-16°N (a) and the STG downwelling region, bounded by 55-30°W/ 20-35°N (b) over σ 25.5 kg m^{-3} (upper cell triangle) and σ 26 kg m^{-3} (lower cell triangle) for the upwelling, and σ 25.75 kg m^{-3} (upper cell triangle) and σ 26.5 kg m^{-3} (lower cell triangle) kg m^{-3} for the downwelling. From left to right and up to bottom, the compared fields are: OLIV3, NEMO OCCITENS output, NEMO OCCITENS IDILIV, GLORYS reanalysis output, ECCO reanalysis output and OMEGA3D output. The black rectangle illustrates the *perfect model test*.

Comparing the RMSE values within the upper and lower triangles at each cell for OMEGA3D product (bottom row Figure 5.4), it is evident from the difference between levels that the OMEGA3D exhibits a predominantly barotropic behaviour in comparison to the OLIV3, NEMO OCCITENS and GLORYS w. At depths near σ 25.75 and 26 kg m^{-3} in the downwelling (upper cell triangles in panel b) and upwelling (lower cell triangles in the panel a), respectively, the large-scale field reconstructed by the omega equation crosses the rest of the fields, causing the relative RMSE to be reduced compared to other isopycnal levels.

The zoom-in over the two regions of the North Atlantic (Figures 5.2, 5.3 and 5.4) has provided valuable visual aid into the differences between the two observation-based vertical velocity products presented in this study (OLIV3 and OMEGA3D) compared with existing model and reanalysis reconstructions (NEMO OCCITENS, GLORYS12, ECCOv4r4), particularly in describing the vertical structure of climatological large-scale movements. Regarding this last characteristic of the flow, the OLIV3 aligns more closely with the baroclinic ocean representation found in the model and within the uncertainty of the reanalyses, unlike the OMEGA3D product.

Nonetheless, this study's ultimate goal is to offer the scientific community a vertical velocities product based on observation with an acceptable level of confidence in its descriptive capabilities of large-scale ocean features. To achieve this goal, it is imperative to extend the analysis beyond a single representative example within the open ocean North Atlantic gyres and to encompass a comprehensive global-scale study of the four-dimensional properties of ocean dynamics.

5.3.3 Intercomparison of Estimated Vertical Velocity Field at Global Scales

The outcomes of various metrics for the existing datasets discussed above (Table 2.1) will be presented at global scales. The diverse spatial and temporal resolutions of the different validation and validated datasets will be homogenised to 5 x 5° and annual frequencies for comparative purposes after applying a distance-to-shore dependent smoothing (see B.1 in Appendix B for further details about the filtering). This section will permit us to evaluate the robustness of the OLIV3 compared to products already available for the community and examine their overall consistency in the global ocean, with particular attention to the uncertainties between the reanalyses.

5.3.3.1 Time-mean Vertical Velocities

5.3.3.1.1 Large-Scale Horizontal Patterns

The OLIV3 (Figure 5.5a) reproduces the large-scale time-mean patterns and the range of amplitudes observed in velocities obtained from the model (panel c) and reanalysis state estimates (panels d and f) are well. Similarly, OMEGA3D (panel b) also reproduces the dipole tropical upwelling/subtropical downwelling.

Focusing on the Pacific and Atlantic tropical bands, the OMEGA3D vertical velocities (panel b) display a stronger and shifted to the west upwelling compared to the rest of the datasets that exhibit the TG upwelling maximum closer to the eastern boundaries. Within the South Indian Ocean, no clear agreement exists between reanalyses and the model in the pattern nor the amplitude of the vertical flow sign, unlike their Pacific and Atlantic counterparts. In the South Indian tropical band, OLIV3 (panel a) does not exhibit a clearly defined large-scale upwelling region, aligning with GLORYS12 estimates (panel d). However, it fails to replicate the horizontal pattern obtained by the NEMO OCCITENS simulation (panel c) and ECCO reanalysis (panel f). In this region, OMEGA3D (panel b) displays a substantial upwelling exhibiting the most distinct field among the datasets. While the reproduced upward motions by the OMEGA3D product differ from the other datasets, it exhibits consistency with its reconstruction of the tropical region across different ocean basins. This overestimation of the global tropical upwelling was already highlighted by Buongiorno Nardelli (2020) when compared not only with ECCOv4r4 but also with SODA3 reanalysis (Carton et al., 2018).

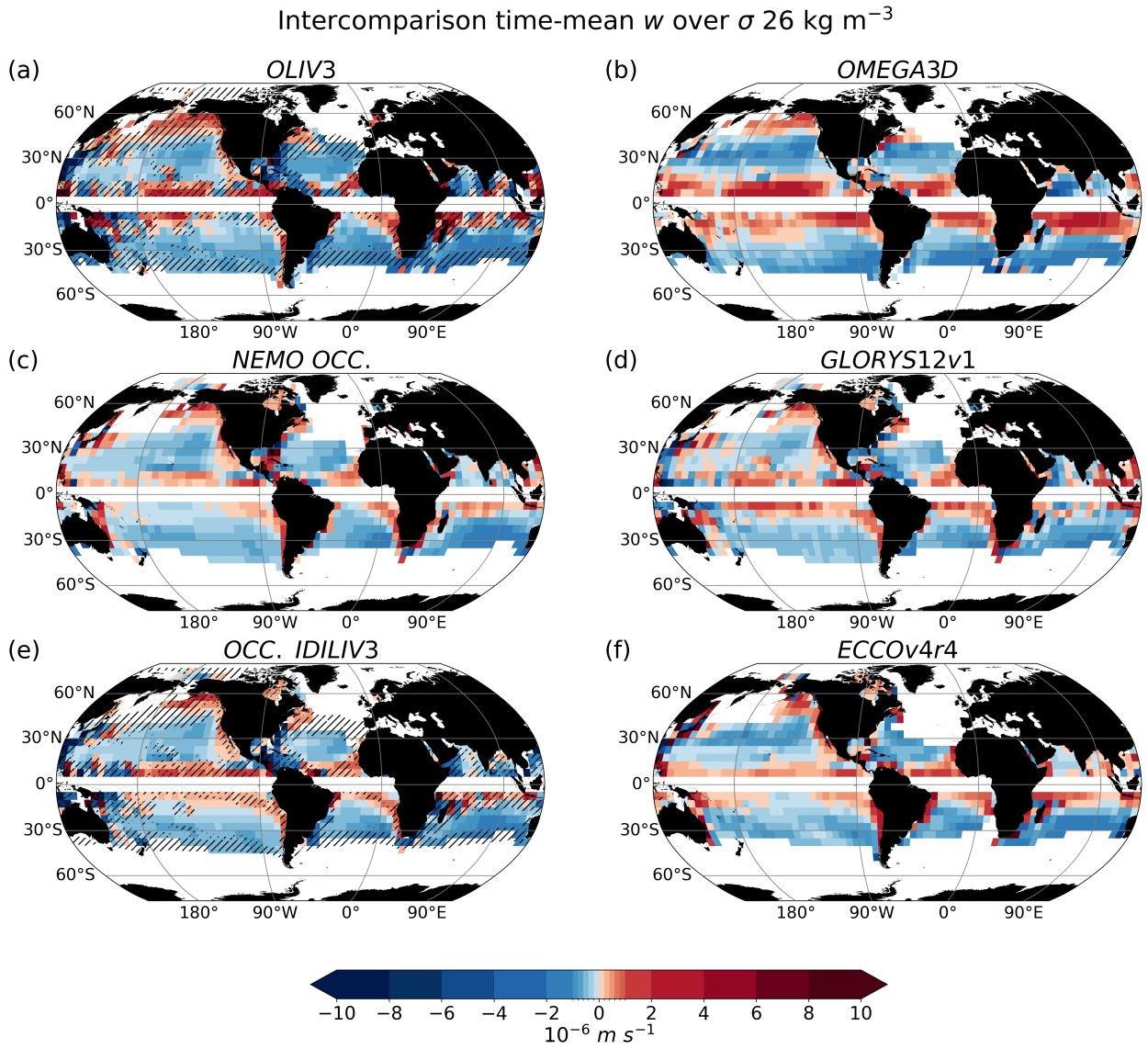

Figure 5.5: Time-mean (a) OLIV3, (b) OMEGA3D output, (c) NEMO OCCITENS output, (d) GLORYS reanalysis output, (e) NEMO OCCITENS IDILIV3 and (f) ECCO reanalysis output over σ 26 kg m^{-3} at 5 x 5° resolution. The hatched regions in panels (a) and (e) represent the areas with $|\Delta_{LVB}|$ (Eq. 3.4) < 10. Note that the maximum mixed layer defined by each dataset has been removed.

In the Pacific tropics, both estimates based on the IDILIV approach (panels a and e in Figure 5.5) and the GLORYS reanalysis (panel d) depict large upwellings although their intensity is lower compared to the OMEGA3D (panel b). In the case of the NEMO OCCITENS IDILIV (panel e), the intensity of the upward flow falls within the reanalysis ensemble unlike OLIV3. In these regions the LVB values exceed $|\Delta_{LVB}|$>10 (hatching region in panels a and e in Figure 5.5). In the equator band, the western boundary currents and the SPGs where the approximations that lead to the LVB cannot be considered, the geostrophic component of the w is not the sole contributor to the total w. Despite the disparities observed in the vertical velocity fields produced by the reanalyses, the time-mean OLIV3 values between 10°S/N do not fall within the range of uncertainty associated with the reanalyses.

One potential explanation for the discrepancies between reanalyses is their native spatial resolution. Even if both fields have been averaged at the same spatial scales, certain phenomena's resolution could have been retained across scales and not entirely removed by the smoothing process (Yeager, 2015). The higher spatial resolution at 1/12° in the GLORYS12 reanalysis might capture the imprint of events at a smaller spatial scale compared to the parameterisation in the 1° ECCOv4r4 reanalysis. In addition, events characterised by smaller spatial scales are inherently associated with shorter time scales. With GLORYS12's spatial resolution, the reanalysis could capture and preserve events at seasonal and sub-seasonal levels through the smoothing process.

Studies focusing on the intercomparison of reanalyses using different spatial resolutions (e.g. Balmaseda et al., 2015; Carton et al., 2019) point out that the tropical band shows the most significant differences in the temperature and salinity variables of the ensemble. Carton et al. (2018) shows how the ECCO coarser spatial resolution is key to its divergence from other datasets with eddy-permitting horizontal resolution. In Balmaseda et al. (2015), the interval of spatial resolution spans from 1/4° to 1°. Therefore, the uncertainty obtained here between the GLORYS12 results, with a horizontal grid of 1/12°, and ECCOv4r4, with a spatial resolution of 1°, may not only reproduce the spread observed in the latter study but potentially magnify it. Conversely, Masina et al. (2017), which compares reanalyses with the same spatial grid but different assimilation techniques, demonstrates robust agreement between them. Despite the differences in the methodology of these intercomparison studies, they emphasise that the general ensemble mean usually provides better estimates of ocean properties than any individual ocean reanalysis.

Considering now subtropical latitudes, the amplitude of downward movements within the five STGs has the same order of magnitude throughout the various datasets. OLIV3 (panel a) generally overestimates the vertical flow (except for the Pacific Ocean in ECCOv4r4) compared to the values obtained by the reanalyses (panels d and f) and the model (panel c). Nonetheless, OLIV3 tends to be closer to these values than OMEGA3D (panel b), that exhibits even larger values. Specifically, in the Northern basins, the maximum downward flow is located in the southeastern part of the gyres within all the datasets except for the ECCO and OMEGA3D cases. In the latter fields, the northern STGs exhibit a maximum downwelling close to the border with the western boundary currents. In the case of the South Atlantic and Indian Oceans, the maximum downwelling is found close to the upper mixed layer boundary for all the datasets. However, only the OMEGA3D case presents this behaviour in the Pacific Ocean, with a more feasible amplitude for the rest of the datasets.

Although the uncertainty between the reanalyses is typically smaller in subtropical latitudes compared to the tropical band, a substantial difference is notably observed in the North Pacific region. This difference aligns with the findings reported by Carton et al. (2019) for SODA3 (Carton et al., 2018) and ORAS5 (Zuo et al., 2019) with a horizontal resolution of 1/4°.

5.3.3.1.2 Assessing the Vertical Dimension of w

When evaluating the vertical velocities, two critical aspects are their vertical structure and the depth where the field vanishes. Indeed, in constructing the Sverdrup balance and its aim to define the areas and volumes of water it can account for, a primordial consideration is determining a depth at which the vertical velocity field reaches zero, if it exists. This depth's existence means that the meridional transport driven by the atmospheric forcing above it effectively evacuates the input of the wind stress curl into the

ocean, validating the Sverdrup balance. Simultaneously, this level of no vertical motion allows defining the volumetric regions of the ocean that can interact and communicate with the atmosphere. Therefore, it is crucial to assess how well OLIV3 approximate the vertical structure of w until an effective level of no vertical motion.

5.3.3.1.2.1 Vertical Structure of Vertical Movements

Using the LVB as a reference, the vertical velocities in the ocean's interior can be understood as a residue of the evacuation by meridional transport of the vertical flow input in the layer above them. The vertical structure is the missing dimension in Sverdrup's analysis that integrates the ocean circulation throughout the wind-forced layer, needing a level of no vertical motion to close the vorticity budget as largely discussed in Chapter 4. However, the studies focused on the Sverdrup balance do not worry about the vertical gradient of the vertical velocity field in the wind-driven layer.

The vertical gradient of the vertical velocities between the maximum mixed layer depth-isopycnal outcrop and σ 27 kg m^{-3} has been calculated at low resolution (Figure 5.6). In the centre of the subtropical gyres, the vertical velocities of the model (panels c, e), reanalyses (panels d, f) and the OLIV3 (panel a) exhibit a reduction in the magnitude of the field with depth with maximum values close to -10·10 $^{-6}$ m s^{-1} / kg m^{-3} in the centre of the Atlantic and Indian subtropical gyres and close to -5·10 $^{-6}$ m s^{-1} / kg m^{-3} in the Pacific Ocean. The OLIV3 fall within the reanalyses values in the areas where we are confident of the reconstruction values. In contrast, the OMEGA3D product (panel b) displays a relatively less negative gradient, indicating a more barotropic nature of the estimated velocity field. The reduction in the amplitude of the w field with depth highlights the baroclinic nature of the field within the tachocline, with systematically greater values at the bottom of the mixed layer than those at deeper layers.

5.3.3.1.2.2 Defining a level of no vertical motions

The baroclinic field depicted in five out of six datasets in the previous section raises the question of the existence of vertical velocity values small enough to define a level of no motion. To address the possible existence of this level, three vertical velocity field thresholds have been established: 10^{-8}, 5 × 10^{-8}, and 10^{-7} m s^{-1}. The lower limit was determined based on the order of magnitude of the minimum velocity values reported by Wunsch (2011) for ECCOv3 (a previous version of the ECCO reanalysis utilised in this study). The upper limit of 10^{-7} m s^{-1} indicates vertical motions that are one order of magnitude smaller than those in the tachocline (Figure 3.2). The isopycnal level where the vertical motion reaches 10^{-8}, 5 × 10^{-8} or 10^{-7} m s^{-1} is illustrated in Figure 5.7. It is specified when the field reaches 10^{-8} m s^{-1} (5 × 10^{-8} m s^{-1}) with a black (grey) dot. The regions with values smaller than 10^{-7} m s^{-1} but larger than the previous two thresholds are not marked. On the other hand, the gaps in the maps display the areas where the vertical velocity field does not reach a minimum value smaller than 10^{-7} m s^{-1}. Please note that the OMEGA3D w field (panel b) is only accessible for the upper 1500 m depth, which differs from the other datasets encompassing the entire water column.

A limited map coverage of the observation-based datasets OLIV3 (panel a) and OMEGA3D (panel b) in comparison to the model (panels c, e) and reanalyses (panels d, f) can be observed in Figure 5.7. This disparity suggests that the observation-based fields contain relatively fewer small values than the reanal-

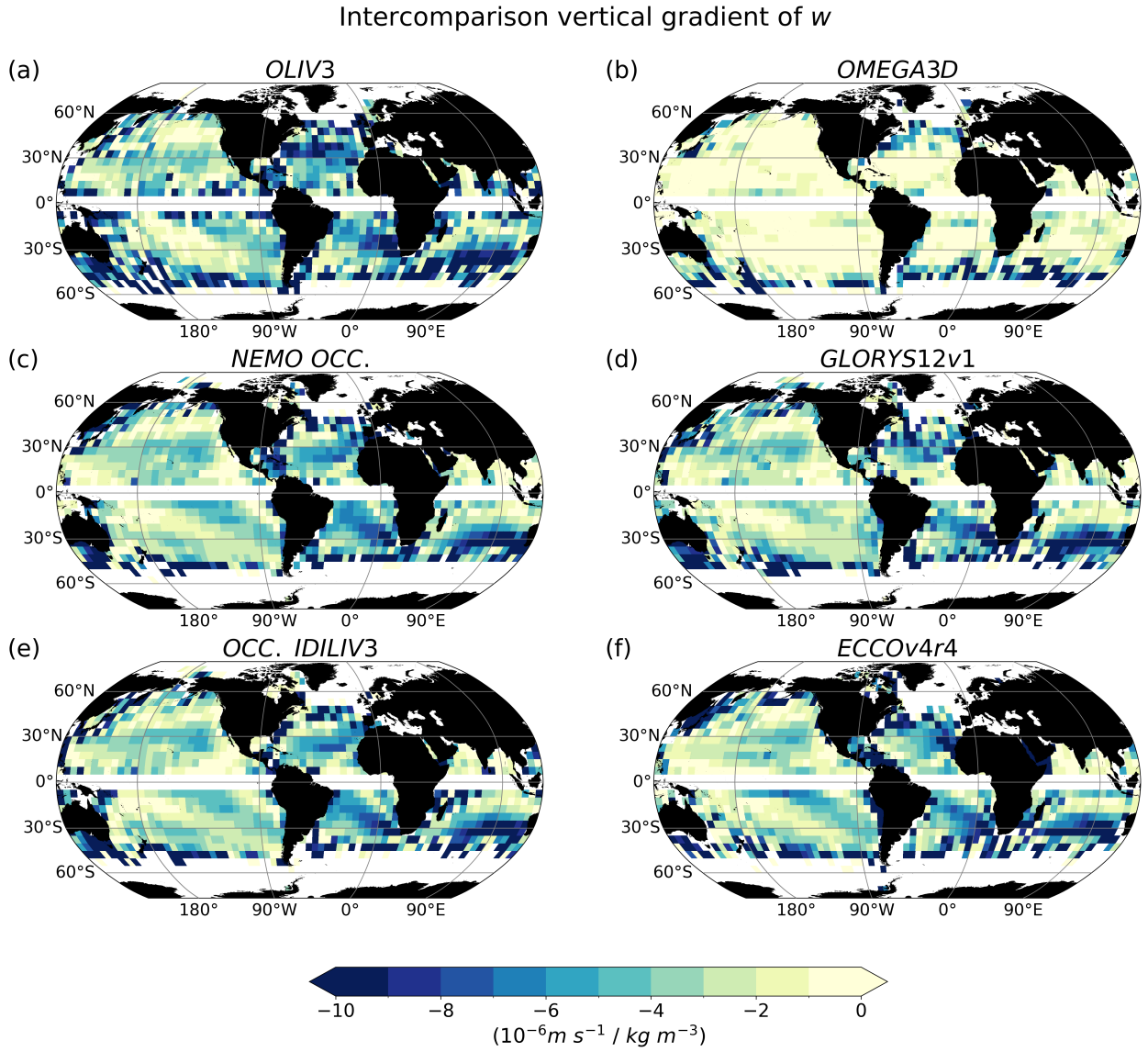

Figure 5.6: Vertical gradient of vertical velocities between the maximum mixed layer depth and σ 27 kg m^{-3} in (a) OLIV3, (b) OMEGA3D output, (c) NEMO OCCITENS output, (d) GLORYS reanalysis output, (e) NEMO OCCITENS IDILIV3 and (f) ECCO reanalysis output at 5 x 5° resolution. The hatched regions in panels (a) and (e) represent the areas with Δ_{LVB}(LVB relative error; Eq. 3.4) < 10. Note that the maximum mixed layer has been defined by each dataset.

yses or the model. When comparing the two observation-based datasets, OLIV3 display smaller vertical velocity values than OMEGA3D. The larger vertical velocity values, together with the smaller vertical gradient observed in the OMEGA3D product compared to other vertical velocity fields, further underscores the barotropic nature of the OMEGA3D field in the upper 1500 m depth. When examining the OLIV3 product (panel a in Figure 5.7), the depths at which it reaches values below the defined limits are more similar to GLORYS12 (panel d) than to the other datasets. However, the OLIV3 field exhibits fewer points than the GLORYS12 field, indicating that the minimum values in OLIV3 are generally larger than those in GLORYS12.

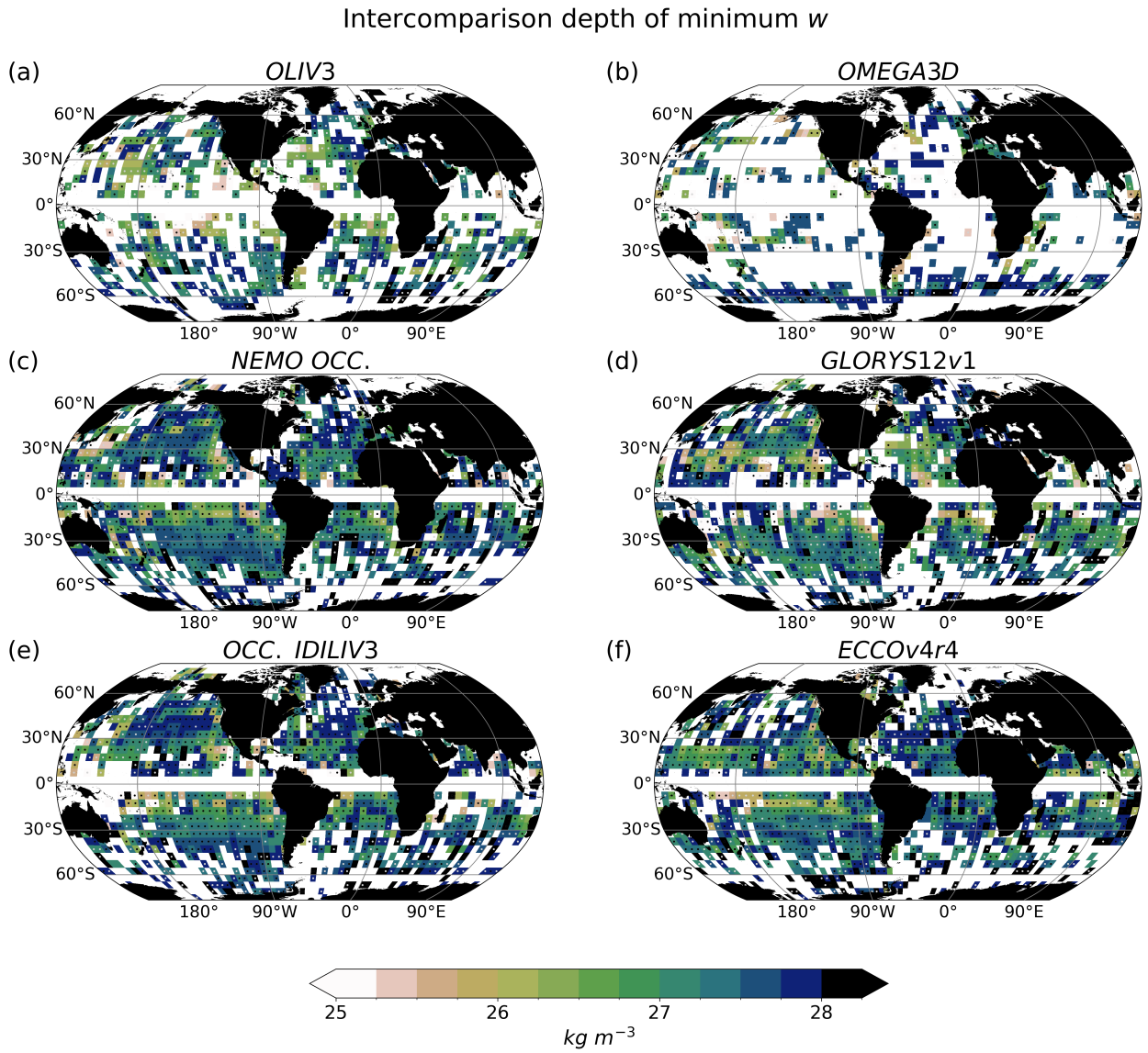

Figure 5.7: Isopycnal level where the vertical velocity field reaches 10^{-8} m s^{-1} (black dot), 5×10^{-8} m s^{-1} (grey dot) and 10^{-7} m s^{-1} (no dot) in (a) OLIV3, (b) OMEGA3D output, (c) NEMO OCCITENS output, (d) GLORYS reanalysis output, (e) NEMO OCCITENS IDILIV3 and (f) ECCO reanalysis output over σ 26 kg m^{-3} at 5 x 5° resolution. Note that the maximum mixed layer has been defined by each dataset.

The consistent minimum values of vertical velocities, their coverage and locations between the model-based vertical velocity fields (panels c and e) indicate that the LVB accurately replicates the vertical structure of the velocity field. However, the disparities observed between the two IDILIV-based fields (panels a and e) suggest that the observation-based meridional transport alone is insufficient to capture the entire atmospheric forcing at the surface to an effective level of no vertical motions.

In the vertical velocity fields provided by the reanalyses and the model, the different datasets exhibit a varying map coverage (panels c, d and f). Notably, the GLORYS12 reanalysis (panel c) contains fewer regions with vertical velocities below 10^{-7} m s^{-1} compared to the other two datasets. However, all three datasets identify regions with vertical velocities below 10^{-8} m s^{-1} at the centres of the tropical gyres. The

depth at which these low values are located varies between the reanalyses and the model. In most cases, GLORYS12 locates the minimum values at shallower depths than the ECCO reanalysis and the NEMO OCCITENS simulation output (lighter colours in colorbar Figure 5.7).

Comparing the reanalyses and the model output, they reveal a trend in the global ocean's tropics and subtropics, where the boundary of minimum vertical velocities extends deeper towards the centre of the subtropical gyre, reaching levels deeper than σ 27.1 kg m^{-3} at mid-latitudes. In contrast, this boundary is considerably shallower within the tropical gyres, at around σ 26.5 kg m^{-3}. This latitudinal-dependent deepening behaviour of the level of minimum vertical velocities aligns with the findings reported by Gray and Riser (2014). The change can be attributed to the variation of the tachocline boundary, which, as discussed in Chapter 3, cannot be accurately defined by a single isopycnal level. Nevertheless, this observed variation with latitude in the depth of the level of no vertical motion does not appear to align with previous studies on the localisation of the minimum w in the water column (Wunsch, 2011). In this latter study, the depth of the vertical velocity minimum in the tropical and subtropical gyres exhibited values between 1000-2500 m depth without a clear dependency on latitude.

5.3.3.2 Vertical Velocity Resolved Variability

The *perfect model test* conducted in Chapter 4, addressing the comparison between NEMO OCCITENS IDILIV estimates and output, emphasises the accurate temporal variability reproduced by the estimated OLIV3. To evaluate the capability of the observation-based geostrophic meridional velocity field to capture the temporal variability of the vertical velocity field, the annual variance of the various datasets and the correlation coefficient (R) and root mean square error (RMSE) between them are computed.

5.3.3.2.1 Variance

The variance reproduced by the various datasets (Figure 5.8) present common properties. Within each dataset, the variance is larger in the western boundary current regions and the equatorial-tropical band. In the centre of the subtropical gyres, the variance exhibits a relative minimum. Comparing the variance between the different datasets, it is apparent that the six datasets presented here exhibit similar variances in the centre of the gyres and WBC regions (except ECCO (panel f) in these latter regions, where it reproduces a field with weaker variance). The discrepancies observed within the WBC region between ECCO and the rest of the fields are consistent with Buongiorno Nardelli (2020). This study compares OMEGA3D with ECCO at 100 m depth and includes SODA reanalysis, which exhibits values closer to OMEGA3D than ECCO. However, at 100 m depth, most of the subtropical gyres are above the mixed layer, so the properties compared in that study may not necessarily be extrapolated to the tachocline studied here.

The differences in the variance obtained for OMEGA3D (panel b) and ECCO reanalysis (panel f) may be attributed to the spatial and temporal resolution variations between them. ECCO has a lower spatial and temporal resolution than the OMEGA3D product. While the spatial resolution of the OLIV3 (panel a) matches that of OMEGA3D, the temporal constraints of the LVB limit the estimation of the vertical velocities

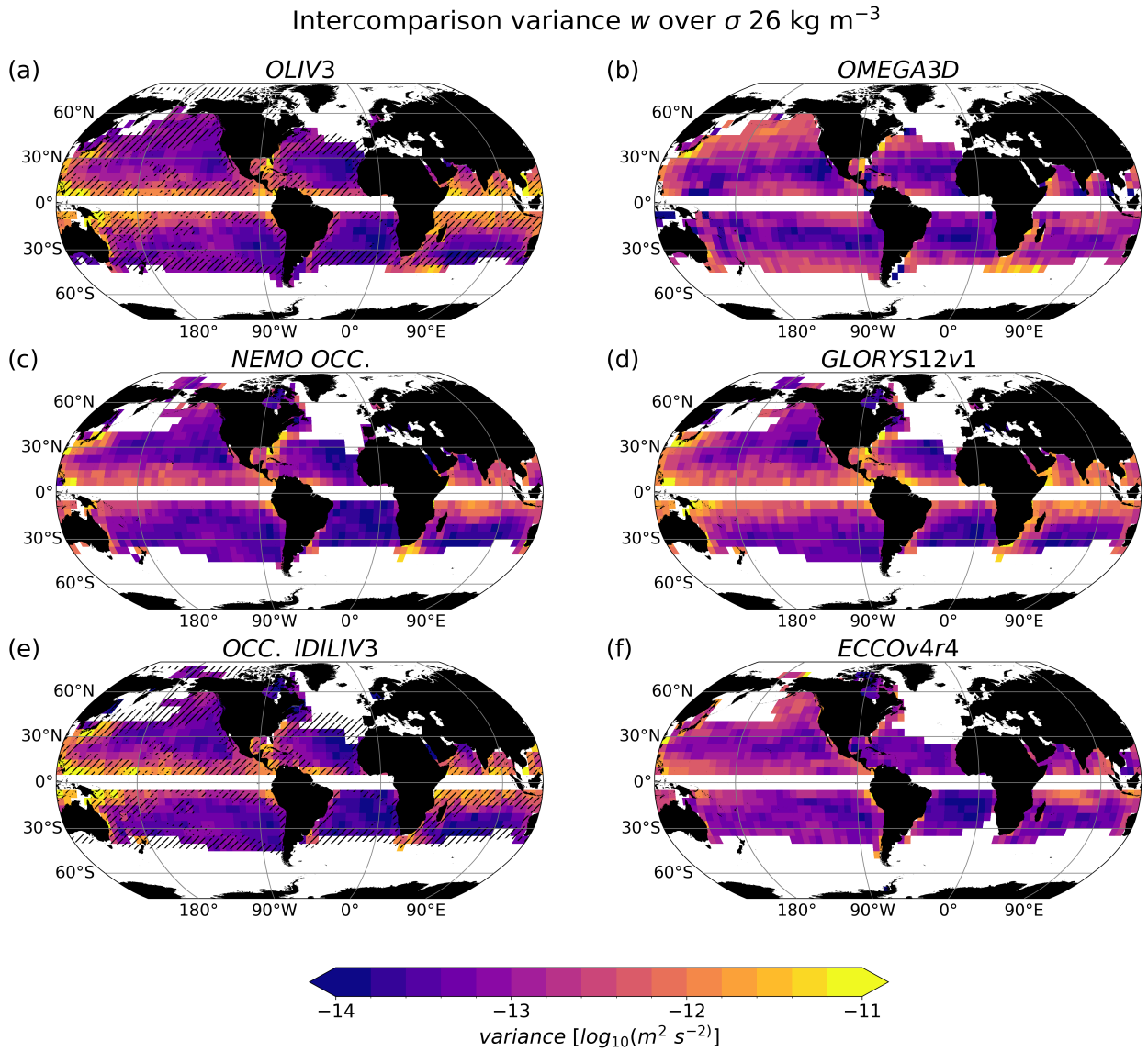

Figure 5.8: Annual variance in logarithmic scale of (a) OLIV3, (b) OMEGA3D output, (c) NEMO OCCITENS output, (d) GLORYS reanalysis output, (e) NEMO OCCITENS IDILIV3 and (f) ECCO reanalysis output over σ 26 kg m^{-3} at 5 x 5° resolution. The hatched regions in panels (a) and (e) represent the areas with $|\Delta_{LVB}|$ (Eq. 3.4) < 10. Note that the maximum mixed layer has been defined by each dataset.

with a minimum frequency of one year, further reducing the variance of the field. However, the NEMO OCCITENS simulation, with the same spatiotemporal resolution as OMEGA3D, generally reproduces a lower interannual variability.

The different amplitude of the time signals reproduced by the two reanalyses becomes apparent when their variance is analysed (panels d, f). This contrast is particularly noticeable in the WBC regions and tropical regions. In the tropical Indian Ocean region and the western tropical Pacific and Atlantic Ocean, characterised by large displacements of the LVB from the equilibrium, the OLIV3 and the NEMO OCCITENS IDILIV3 have a similar variance to the GLORYS reanalysis. This finding demonstrates that even in regions where the LVB cannot fully explain the climatological circulation, the IDILIV approach can capture the temporal variance according to the GLORYS reanalysis.

5.3.3.2.2 Syncronicity

Figure 5.9 shows the annual correlation coefficient (R) between the different products on the upper diagonal half and the RMSE on the lower diagonal half with 5 x 5° spatial resolution over σ 26 kg m^{-3}. Within the rectangle in Figure 5.9, the *perfect model test* exhibits the constraints of the IDILIV methodology to reproduce the vertical velocity field. Here, it is obtained a very accurate reproduction of the model variability with RMSE values smaller than 10^{-7} m s^{-1} almost everywhere, except for the regions where the LVB does not hold.

In the panels included in the upper row in Figure 5.9 the OLIV3 is compared with the rest of the datasets. The OLIV3 velocities are correlated with the reanalyses and the model with significative R above 0.6 in practically the entire ocean, reaching significative values above 0.8 in the centre of the subtropical gyres (significative values above 95% of the confident level are indicated by dotted regions in Figure 5.9). In the tropical regions where the LVB is not maintained (hatched areas), this correlation is generally reduced below R 0.4.

The near-perfect synchronisation observed in the *perfect model test* above 0.9 across the global ocean, even within regions where the LVB does not hold, together with the similar spatial distribution of the level of synchronicity of the NEMO OCCITENS output simulation, NEMO OCCITENS IDILIV estimates, and OLIV3 fields in relation to the reanalyses, indicates that the vertical velocities within the NEMO OCCITENS output simulation lean significantly more towards linearity/geostrophy compared to the reanalyses.

The observed deterioration in the OLIV3 time-dependent metrics compared to the *perfect model test* was expected due to variations in spatiotemporal resolutions and the applied forcing among the different datasets.

In addition, the reduction in the correlation coefficient when comparing OLIV3 in the non-valid LVB areas could provide insights into the differences between the simulated and the observed ocean. The reanalyses exhibit lower correlation coefficients in the tropics and WBCs with the NEMO OCCITENS simulation output and IDILIV3 estimate fields than OLIV3. This suggests that although the geostrophic component strongly influences the tropical variability of the total vertical circulation, the NEMO OCCITENS simulation (even when considering the total w) generally portrays it less accurately than OLIV3.

Moreover, note the limited synchronicity across all sites among the reanalyses when compared to OLIV3. This discrepancy might stem from a lack of synchronisation within the nonlinear vertical velocity components among the reanalysis fields, thereby reducing the correlation, while the geostrophic components remain highly correlated. Notably, the nonlinear terms in the GLORYS dataset seem to contribute significantly more to the temporal variability than ECCO, where areas within the tropical band exhibit correlation values akin to those in the open ocean.

The lowest correlation coefficient values are found with OMEGA3D (panels within the rightest column in Figure 5.9), reaching a significative maximum R 0.7 with the OLIV3 in some areas within the open ocean (Pacific and North Atlantic STGs). Nonetheless, OMEGA3D is poorly correlated with the reanalyses, in a similar way that in the time series of the regional examples (Figure 5.3). In these regional averages, the variability of the OMEGA3D field does not synchronise as effectively with the other datasets as they do with each other.

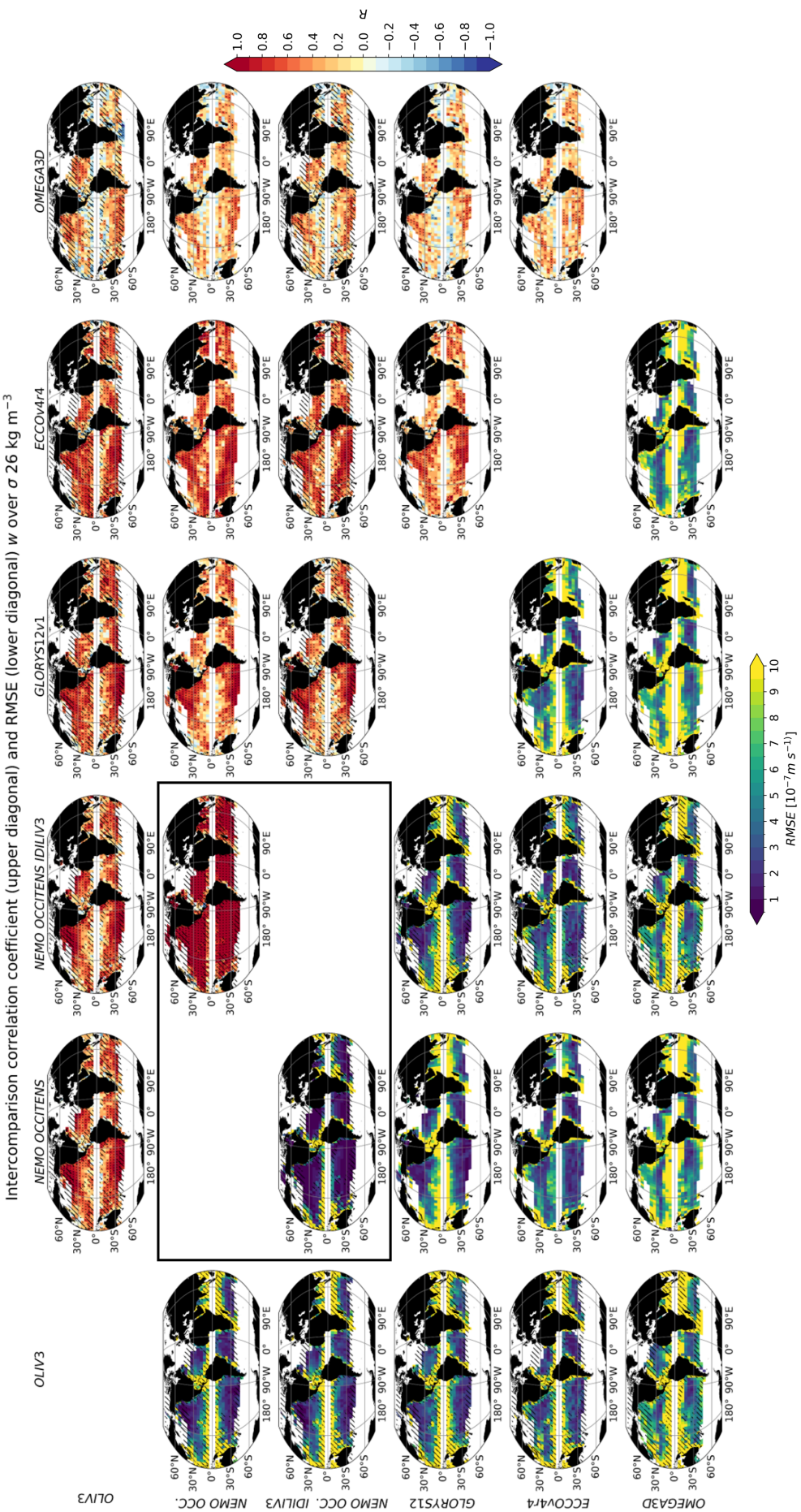

Figure 5.9: Cross correlation coefficient (upper diagonal half) and root mean square error (lower diagonal half) between the OLIV3, NEMOS OCCITENS output, NEMO OCCITENS IDILIV, GLORYS reanalysis output, ECCO reanalysis output and OMEGA3D output over σ 26 kg m^{-3} at 5 x 5° resolution. Hatched areas represent the regions with $|\Delta_{LVB}|$ (Eq. 3.4) < 0. Dotted areas in the R panels (upper diagonal half) indicate significant values at the 95% confidence level based on the Student t-test. Note that the maximum mixed layer has been defined by each dataset.

The OLIV3's RMSE (panels included in the left column in Figure 5.9) remains approximately one order of magnitude smaller than the mean values (Figure 5.5) in the centre of the oceanic gyres, far from the western boundaries. OLIV3's RMSE is smaller with the model-based datasets than the reanalyses. Again, the OLIV3 and reanalyses' RMSE fall within the RMSE uncertainty among reanalyses. The RMSE between OMEGA3D and the reanalyses (bottom row in Figure 5.9) is often larger than the difference between reanalyses except for the South Atlantic and Pacific STG with RMSE values of similar magnitude.

5.4 Discussion

While the OLIV3, model and reanalysis estimates exhibit reasonable agreement on the climatological baroclinic structure and the synchronicity of the vertical movements, OMEGA3D is less consistent. What could be the underlying causes of these differences? Three factors could potentially account for the distinctions between the relatively coherent fields of the model, reanalyses, OLIV3, and OMEGA3D: the methodology employed for the vertical motion estimation, the atmospheric forcing, and the three-dimensional horizontal velocity fields applied in the equations.

Starting with the horizontal velocities applied to the various methodologies (Table 2.1), both the OLIV3 estimate and the OMEGA3D product are based on the ARMOR3D geostrophic velocity field (Guinehut et al., 2012; Mulet et al., 2012). However, these fields exhibit prominent differences. In contrast, the NEMO OCCITENS simulation and OLIV3 share common features despite their distinct origin in either purely modelled or observation-based horizontal velocity fields. On the other hand, all the datasets presented here employ various versions of the same ERA atmospheric forcing product. The homogeneity in the forcing sources suggests that neither this aspect nor the meridional velocity input is the primary source of differences among the datasets.

Finally, the equations used to retrieve w in OLIV3, NEMO OCCITENS IDILIV3, NEMO OCCITENS simulation output and reanalyses outputs only use the vertical derivative of w: LVB (Eq. 1.12) and continuity equation (Eq. 1.6). Conversely, OMEGA3D uses the omega equation (Eq. 1.1) that incorporates the second-order vertical derivative of w and horizontal derivatives. Consequently, Dirichlet (vertical velocities are set to zero) and Neumann (partial derivatives of vertical velocity are set to zero) conditions are imposed at the bottom and lateral boundaries. In addition, the omega equation includes turbulent terms (Buongiorno Nardelli et al., 2018; Buongiorno Nardelli, 2020). This fundamental methodology difference could account for the "barotropic" character of the OMEGA3D estimate. However, a comprehensive examination of the sources of these differences would require a separate in-depth investigation, given the complex physics, constraints and assumptions underlying the omega equation.

5.5 Conclusions

In this chapter, we evaluate our Observation-based Linear Vorticity Vertical Velocities estimates (OLIV3). OLIV3 contains the global upper ocean vertical velocity (w) field spanning the period 1993-2018, computed applying the Indefinite Depth-Integrated LInear Vorticity (IDILIV) formalism to a geostrophic meridional velocity field derived from observational data (ARMOR3D). The Ekman pumping vertical velocity at surface, calculated from wind stress (ERA5's), has been defined as boundary condition.

To ascertain the consistency of OLIV3's vertical currents with existing estimates, we evaluated the four-dimensional vertical velocities from five different datasets, encompassing two model-based, two reanalyses and one observation-based estimates, covering the 23-year overlapping period (1993-2015). OLIV3 aligns well with the horizontal patterns and vertical structure of the climatological tachocline vertical velocity field, and it captures the interannual variability over the open ocean when compared to the NEMO OCCITENS model and the GLORYS and ECCO reanalyses. Our analysis on synchronicity among model, reanalyses, and IDILIV-based estimates reveals three key findings. First, the NEMO OCCITENS w variability is predominantly driven by its geostrophic component, evidenced by higher synchronicity with NEMO OCCITENS IDILIV3 and OLIV3 compared to the reanalyses. Second, despite the geostrophic component's dominance in the NEMO OCCITENS's interannual variability, it does not perfectly synchronise with OLIV3. Lastly, the reduced synchronicity between the reanalyses compared to the geostrophic fields (NEMO OCCITENS IDILIV estimate and OLIV3) suggests that the interannual variability of reanalyses' nonlinear vertical velocity fields is not negligible and not correlated.

While the omega equation method is commonly used in the scientific community to estimate vertical velocities, the w field in OMEGA3D differs significantly from OLIV3, NEMO OCCITENS simulation and reanalyses' vertical velocities. Notably, OMEGA3D captures an almost entirely barotropic ocean—with no effective LONM—, which contrasts with the agreement on baroclinicity among the rest of the datasets and the necessity of baroclinic ocean to uphold the Sverdrup balance theory. In terms of interannual variability, OMEGA3D exhibits the least synchronisation with other datasets. The discrepancies between OMEGA3D and OLIV3, along with other validation datasets, may be attributed to various factors, such as the type and source of the horizontal velocity field, wind-forcing, or the use of the horizontal gradient of w in the omega equation.

In conclusion, two observation-based estimates of the vertical velocity field are currently available for future applications: one based on the linear vorticity equation and the other on the omega equation. Despite inherent limitations in each methodology, the estimates derived from the LVB exhibit characteristics closely aligned with the NEMO OCCITENS simulation and two widely used reanalyses. However, while capable of accurately reproducing many multidimensional features of w, it falls short in describing motions at scales smaller than 5°. This underscores the need to incorporate additional terms of the vorticity equation, such as the horizontal advection of relative vorticity. This expansion would allow exploring and exploiting smaller spatiotemporal scales and extend the potential for estimations in regions closer to the coast while maintaining the simple only depth-integrated formalism.

Dove inizia la fine del mare? O addirittura: cosa diciamo quando diciamo: mare? Diciamo l'immenso mostro capace di divorarsi qualsiasi cosa, o quell'onda che ci schiuma intorno ai piedi? L'acqua che puoi tenere nel cavo della mano o l'abisso che nessuno può vedere? Diciamo tutto in una parola sola o in un sola parola tutto nascondiamo?

— Alessandro Baricco, *Oceanomare, 1993*

6 General Conclusions

6.1 General Conclusions

The crucial role of the large-scale vertical ocean movements in the Earth's climatic system is often obscured by technological limitations hindering their direct observation. Simultaneously, the Sverdrup balance is widely recognised for its robustness and simplicity. Yet, understanding its baroclinic characteristics, expressed through the linear vorticity balance (LVB), i.e. the relation between the vertical gradient of vertical velocities and meridional transport, remains limited. The convergence of these two aspects has provided a compelling motivation for this thesis: the computation and evaluation of a global estimation of the large-scale geostrophic vertical flow, subsequently framing the central question of the thesis: **Can the geostrophic component of vertical velocity account for the large-scale vertical circulation in the "real" ocean, where "real" refers to the ocean as replicated by models and reanalyses?**

The global upper ocean's geostrophic vertical velocity field has been successfully estimated from observations (Observation-based Linear Vorticity Vertical Velocities estimates (OLIV3)). This estimation accurately reproduces the known large-scale climatological (1993-2018) horizontal and vertical structures of the vertical circulation and its interannual variability. This dataset has been computed by applying the Indefinite Depth-Integrated LInear Vorticity (IDILIV) formalism to a geostrophic meridional velocity field evaluated from observation-based data (ARMOR3D[1]). The Ekman pumping vertical velocity at surface, computed from wind stress (ERA5[2]), serves as boundary condition.

[1] Guinehut et al., 2012; Mulet et al., 2012
[2] ECMWF Re-Analysis v5

Does the available observation-based wind stress and geostrophic meridional transport data allow for the estimation of three-dimensional vertical velocities assuming an ocean in Linear Vorticity Balance? OLIV3 exhibits a remarkable level of agreement with various datasets (a NEMO OGCM simulation, GLORYS and ECCO renalyses[3]) across the open ocean, far from the Western Boundary Currents (WBC)s, the equator band, the western part of the tropical band and the subpolar gyres. This consistency is evident when examining their time-mean horizontal patterns and vertical baroclinicity during the 1993-2015 period. In contrast, the observation (ARMOR3D)-based dataset computed using the omega equation (OMEGA3D[4]) deviates from this latter agreement.

The OLIV3 relies on the Linear Vorticity Balance (LVB) validity at each depth level. Therefore, understanding OLIV3 necessitated a thorough understanding of the underlying principles governing the Linear Vorticity Balance (LVB). The LVB successfully explains the 1960-2015 climatological large-scale ocean flow (at scales larger than 5°) within the upper tachocline, extending below the mixed layer across most of the global subtropical gyres, eastern Atlantic and Pacific tropical gyres and the eastern side of the Pacific subpolar gyre. In the intermediate ocean, the spatial extent over tropical and subtropical latitudes where the LVB describes the ocean to a good level of approximation diminishes compared to the upper layers. Nonetheless, the LVB partially explains the Northern Hemisphere extratropics at these depths. In the deep ocean, the topography-induced circulation is largely explained by the LVB, particularly evident over abyssal plains and the austral circulation.

Across the water column, significant deviations from the equilibrium occur within the Western Boundary Current (WBC), the equatorial band (including the Indian Ocean tropical band), the western halves of the Pacific and Atlantic subtropical gyres and the Atlantic subpolar gyre. Within the intermediate ocean, the reduction in the extent of valid LVB is especially pronounced at tropical and Pacific subtropical latitudes and the circumpolar circulation. Reducing the averaging period promotes small-scale circulation (<5°), leading to the emergence of nonlinear vorticity contributions. Nevertheless, even when considering annual time scales, the LVB formulation remains robust enough to accurately depict the ocean dynamics. The validity of the Geostrophic Linear Vorticity Balance (GLVB) follows the constraints outlined by the LVB, covering nearly all regions in LVB in both the upper and deep oceans. Nonetheless, the validity of the GLVB in the intermediate ocean is restricted to the extratropical regions where the LVB is valid. The localisation of the regions where the LVB can be considered valid, obtained through a NEMO OGCM simulation, has addressed the fundamental question posed in the Introduction: **To what spatial and temporal extent is the ocean in Linear Vorticity Balance?**

A connection between the LVB and the Sverdrup and Topographic Sverdrup balances can be established due to the similarities in the description of atmospheric and bathymetry-driven circulation observed in previous studies. This suggests a transport of the forcing patterns throughout the water column. In particular, the link established between the Sverdrup and Topographic Sverdrup balance, and the LVB within the upper and deep oceans provides an alternative and simpler explanation for the direction of the flow compared to the classical potential vorticity scheme. In the upper tachocline-thermocline case, the LVB supports that a convergent/divergent flow is needed to feed/absorb the Ekman layer's upward/downward atmospheric-driven motions. This, establishes the direction of the geostrophic meridional flow since only

[3] See Chapter 2 for details in the datasets
[4] See footnote 3

the poleward flows are convergent, and the equatorward flows are divergent. Although the extension of the LVB and Sverdrup balance applicability are nearly identical, certain discrepancies emerge between the valid areas defined by the LVB and the Sverdrup balance, such as the Atlantic eastern boundary. These differences highlight the need for the existence and precise localisation of the assumed LONM[5] to close the Sverdrup balance, emphasising the importance of addressing the ocean dynamics from a baroclinic perspective to determine to what extent they penetrate into the water column. This holds true, even in regions where the ocean can be accurately described by the LVB, potentially offering a vertical level up to which the equation can be depth-integrated to retain a linear barotropic ocean.

Similarly to the accurate reproduction of the magnitude of both the horizontal and vertical structure of the time-mean vertical velocity field, OLIV3 effectively captures the interannual temporal variability of the model and reanalyses in the LVB valid areas. Conversely, OMEGA3D displays lower synchronisation with the datasets used in the intercomparison study. The Indefinite Depth-Integrated LInear Vorticity Vertical Velocities Estimates (IDILIV3) derived from the NEMO OGCM simulation accurately captures the interannual variability of the NEMO simulation output field. The latter finding suggests that the geostrophic component of w, estimated through the IDILIV approach, predominantly governs the variability, resulting in the geostrophic meridional transport driving the variability of the ocean dynamics. While influencing the flow's amplitude, the nonlinear components of the w exhibit a minor contribution to the variability. Two conclusions emerge regarding the interannual variability of the various datasets within the intercomparison test. Firstly, the NEMO OGCM simulation output field exhibits a more linear and geostrophic nature compared to the reanalyses, yet it remains unsynchronised with OLIV3 beyond the area validated by the LVB. Secondly, the reanalyses are less synchronised among themselves compared to the geostrophic fields (NEMO OGCM IDILIV3 estimate and OLIV3) and the NEMO OGCM simulation output. This implies a lack of interannual correlation between the nonlinear components of the vertical velocity field.

However, even in regions where the LVB has demonstrated to explain three-dimensional circulation, there is a lack of agreement in the time-mean amplitudes of the vertical velocity fields among the different datasets, including OLIV3. The IDILIV methodology employed to estimate vertical velocities has revealed, through the model simulation, that while maintaining a coherent order of magnitude, errors accumulate in the vertical integration. This results in a deviation that exceeds 10% within most of the upper tachocline and surpasses 50% below it when compared to the time-mean output of total w from the NEMO OGCM simulation in the North Atlantic basin. Consequently, this constraint to the interannual variability and order of magnitude of the time-mean vertical velocities is the answer to the question asked in the Introduction: **Can the geostrophic meridional transport effectively explain the vertical motions?**.

In regions within the upper tachocline where the LVB does not hold, such as WBC, the equatorial band (including the tropical band in the Indian Ocean case), the western halves of the Pacific and Atlantic subtropical gyres, and the Atlantic subpolar gyre, the field reproduced by OLIV3 exhibits distinct characteristics compared to other datasets. Significant departures from the linear equilibrium have been demonstrated in these regions using a NEMO OGCM simulation. These departures result from the dominance of other terms in the vorticity budget, such as the horizontal advection of relative vorticity within the upper tachocline, balancing the linear vorticity residue demonstrated in the one-year CROCO OGCM simulation analysis. In the open ocean at scales larger than 5°, contributions from vortex tilting, vortex

[5] Level Of No Motion

stretching due to the relative vorticity, vertical advection of relative vorticity, time evolution of relative vorticity, vertical mixing and horizontal diffusivity terms are entirely negligible. However, in regions such as the WBC and western tropical band, where the LVB is not valid, the vorticity contribution from nonlinear and mixing terms, except for the time evolution of relative vorticity, have shown a non-negligible but relatively small contribution to the vorticity closure compared to the horizontal advection of relative vorticity. Particularly, the vertical mixing term largely balances the LVB and horizontal advection of relative vorticity residue in the eastern boundary currents and the mixed layer.

At the end of this work, we introduce a new dataset containing annual estimations of the global upper ocean's geostrophic vertical velocities, offering an alternative to the established OMEGA3D product for public access. The intercomparison study highlights a fundamental difference between the various estimations of the vertical movements. Estimations using equations that solely rely on the indefinite depth integration of the horizontal circulation retrieve a baroclinic ocean. This approach is adopted in the LVB for OLIV3 and the continuity equation for the NEMO OGCM simulation, as well as in the GLORYS and ECCO reanalyses. In contrast, OMEGA3D derived from the omega equation, which also includes the horizontal gradient of w, yields a notably more barotropic field. This divergence prompts further study, focusing on exploring the connections between these methodologies and understanding why they produce such different representations of vertical circulation.

The robustness and simplicity of the four-dimensional observation-based vertical velocity product proposed in this study open up new paths of research in the open ocean, particularly at lower frequencies than annually. This enables scientists from various domains to utilise these vertical velocity estimations in their respective studies. The broader and near future prospect for the OLIV3 lies in computing the three-dimensional advection of tracers at scales larger than 5° at annual frequency within the open ocean upper tachocline far from the Western Boundary Currents (WBC)s, the equator band, the western part of the tropical band and the subpolar gyres. This advancement would indeed enhance our comprehension of biogeochemical interactions within the ocean interior.

6.2 Perspectives

The baroclinic perspective of the LVB introduces a novel approach for deriving vertical velocities. Nonetheless, our research has spawned new questions, paving the way for future work: The OLIV3 is suitable for calculating large-scale vertical flow variability. Additionally, theoretical approaches could potentially resolve certain limitations inherent to the LVB for describing ocean circulation. This, in turn, would enable the incorporation of additional components in reconstructing vertical velocities. Employing total meridional velocities and expanding observations of both the thermohaline and total horizontal velocity fields allows further enhancing and extending the OLIV3 within and below the upper tachocline. These perspectives will be further explained in the subsequent sections.

Exploring the Possibilities of Observation-Based Vertical Velocities in Tracer Flux Studies

Research demonstrates the potential and necessity to address the vertical component of the advective flux to derive large-scale tracer trends in the ocean interior such as temperature (Stammer et al., 2003), salinity (Freeland, 2013) or carbon (Rödenbeck et al., 2022). In particular, the temporal evolution of temperature within a volume in the ocean responds to the contribution of vertical mixing, horizontal diffusivity and external forcings. But, when assuming a volume within the ocean interior, the sources and sinks for heat, vertical mixing and horizontal diffusivity can be considered negligible. Thus, the material derivative of the temperature can be expressed as:

$$\frac{\partial T}{\partial t} = -u\frac{\partial T}{\partial x} - v\frac{\partial T}{\partial y} - w\frac{\partial T}{\partial z} \tag{6.1}$$

To illustrate the contribution of the advection terms to the time variation of temperature, employing the annual vertical velocities from OLIV3, we have computed the terms in Eq. 6.1 using data from the NEMO OCCITENS simulation[6] as an illustrative example. The spatially averaged annual time series for the region bounded by 55-30° W/ 20-35° N at a depth of 300 m (Figure 6.1a), as defined in Chapter 5, is presented for each of the terms in Equation 6.1 calculated at annual (dashed lines) and monthly frequencies (solid lines).

The total horizontal advection (blue line in Figure 6.1a) contribution is not negligible and exhibits, in this layer and region, a negative contribution to the temperature budget throughout the whole period. The difference between the horizontal advection and the time ratio (black line in Figure 6.1a) illustrates that the contribution of vertical advection cannot be ignored (red line in Figure 6.1). Here, the downward vertical flow transports the surface temperature to lower layers while the horizontal circulation subtracts it. Discrepancies between these vertical and horizontal flows result in the system gaining or losing heat.

The total temperature advection (dashed blue line), calculated with annual frequencies, reproduces the interannual variability of the temperature time ratio. However, it falls short of fully balancing the temperature time ratio (comparing the purple and black dashed lines in Figure 6.1a).

The relationship between the total advection and the temperature time-ratio is evaluated by computing the Correlation coefficient (R) and Root Mean Squared Error (RMSE) between the two sides of Eq. 6.1 from the surface to a depth of 1000 m (Figure 6.1b). The results reveal two distinct regions, characterised

[6] See Chapter 2 for details in the datasets

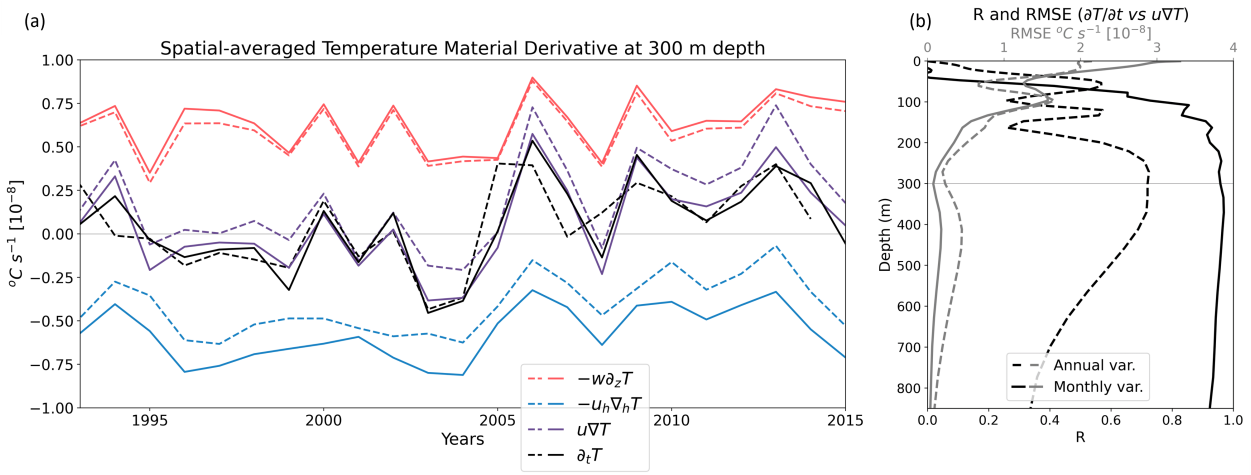

Figure 6.1: (a) Annual time-series at 300 m depth and (b) correlation coefficient (R) (black) and RMSE (grey) of the spatially averaged NEMO OCCITENS output terms of Eq. 6.1 calculated at monthly (solid lines) and annual (dashed lines) timescales within the North Atlantic STG downwelling region, bounded by 55-30° W/ 20-35° N.

by different R and RMSE vertical gradients, bounded around 200 m depth. The relatively higher RMSE values and low correlation coefficient above 200 m depth than below support that the contribution of mixing terms is non-negligible for closing the temperature budget in the mixing layer. The annual-computed total advection of temperature exhibits a maximum correlation coefficient above 0.7 at 300 m depth, which decreases with increasing.

Increasing the frequency of the variables used to compute the advection of temperature to monthly scales results in improved correlation (Figure 6.1b). As previously shown in Section 3.2.2.2, the cross anomaly terms are crucial in closing the budget when using observations. Reducing the time step from annual to monthly scales when computing the advection terms would reduce the influence of cross anomaly terms. Furthermore, the close agreement between the temperature time rate (black solid line) and the monthly computed total advection (purple solid line) in Figure 6.1a confirms that, according to the model, mixing is negligible in the centre of the STG upper ocean.

When using observations, two issues would arise from the use of the observation-based products presented in this study. First, the Indefinite Depth-Integrated LInear Vorticity approach presented here is limited by annual frequencies, causing the advection of the temperature not to be well correlated with the temperature time ratio. Second, using the ARMOR3D thermohaline field to study temperature and salinity fluxes in the ocean interior can be problematic. The ARMOR3D geostrophic velocities are calculated by applying the thermohaline fields to the thermal wind equation (Chapter 2). Therefore, the three-dimensional velocity field used to estimate the temperature advection is explicitly estimated from the thermohaline field. This computation could result in an artificial positive correlation between the material derivative terms.

In conclusion, while using model data offers promising possibilities for calculating tracer fluxes in the ocean interior, there is still a long way to go to harness the full potential of the OLIV3 product to estimate the fluxes accurately. To accomplish this, developing a less spatiotemporal constrained OLIV3 vertical velocities is crucial.

Overcoming Spatial Linear Vorticity Balance Constraints: Characterising Small-Mesoscale and Submesoscale Features

The spatial and temporal scale is one of the principal constraints we have encountered when applying the linear vorticity balance equation to oceanic motions. The equation's descriptive capacity diminishes as we delve into spatial scales finer than 1° and at timescales smaller than a year as the spatial and temporal scales of the oceanic phenomena are linked.

The analysis of the full vorticity equation over the North Atlantic upper ocean, conducted using a one-year high-resolution model simulation, has revealed that the horizontal advection term of relative vorticity holds the potential to balance the residue from the linear terms. The contribution of these terms will improve the description of open-ocean oceanic motions at meso- and submesoscale, at timescales even shorter than one year, compared with the linear case. Furthermore, it allows for the extension of the reconstruction of vertical velocities to regions that conventionally lie beyond the validity of the linear vorticity balance, such as the western boundary current regions, equatorial band, or subpolar latitudes.

However, even considering the linear vorticity alone, a considerable body of work remains ahead: Detailed analyses are required to assess the extent of validity of the vorticity balance validity at each depth level. Khatri et al. (2023) explore the sensitivity of the contribution of the barotropic vorticity balance terms to the vorticity budget at different spatial scales, offering a pivotal demonstration of the imperative to unveil the role of each term across scales of the oceanic circulation.

The limitations of the Indefinite Depth-Integrated LInear Vorticity (IDILIV) approach have been shown to be related not only to the constraints of the equation itself at different depths but also to the fact that the reconstruction relies on the vertical integration from the surface, resulting in systematic errors in describing ocean dynamics at increasing depths. Employing a more comprehensive vorticity equation could mitigate these errors and enhance the accuracy of vertical velocity estimation across all locations, even in areas where the LVB holds, increasing both spatial and temporal resolutions. Therefore, incorporating the horizontal advection of relative vorticity terms, identified to have a significant impact on closing the vorticity budget, would extend the range of the LVB valid regions identified in this study. This extension would be achieved while retaining the depth-integration framework to retrieve the vertical motions.

This line of work offers a direct opportunity to establish connections between different formalisms of the depth-integrated vorticity equation (Waldman and Giordani, 2023), facilitating the examination of the ocean from either a barotropic or baroclinic perspective.

Enhancing Vertical Velocity Estimates through ADCP Data and Extending Observations Coverage to Greater Depths

Adding nonlinear terms into the linear vorticity balance will enhance the precision of the vertical circulation description. Nonetheless, without significant advancements in observations, all efforts will remain limited to theoretical comprehension of ocean dynamics. The ARMOR3D global horizontal geostrophic velocity product has demonstrated its proficiency to retrieve the vertical component of the circulation not only in our study but also when applied to the omega equation (e.g. Buongiorno Nardelli et al., 2018; Buongiorno Nardelli, 2020). However, the model-based analysis of the LVB (Section 3.2) emphasises the critical importance of utilising the total horizontal velocity, as opposed to solely relying on the geostrophic component, especially below the upper tachocline. Observations of the total horizontal velocities via, e.g. ADCPs, are crucial for achieving a more accurate estimation of vertical velocities. Hence, it would be highly valuable for future projects to update the presented observation-based vertical velocity product by incorporating total horizontal velocities obtained from current meter datasets, such as those assembled by Scott et al. (2010).

Moreover, the ARMOR3D product's relatively satisfactory observation coverage of the upper ocean, particularly within tropics, subtropics, and extratropics, contrasts with the sparse observations available below the 2000-meter depth. This emphasises the urgency of expanding the observation coverage of the water column at greater depths. Currently, the Argo float network's coverage at depth is remarkably limited (see https://argo.ucsd.edu/about/status/). Of the nearly 4000 operational units currently in the Argo network, less than 10% are deep Argo (sampling far below 2000 meters to the ocean bottom). The necessity for such requirement has been emphasised in the scientific literature for several decades (e.g. Heuzé et al., 2022[7]).

[7]The author of Heuzé et al. (2022) was honoured with the 2022 Outstanding Early Career Scientist Award

Scientific activities during the PhD

Publications in peer-reviewed scientific journals

Cortés-Morales, D., and Lazar, A. (2024) *Vertical velocity 3D estimates from the Linear Vorticity Balance in the North Atlantic.*, Journal of Physical Oceanography.

Seminars and International conferences

Cortés-Morales, D., and Lazar, A. *Observation-based study of vertical velocities within the global thermocline: interannual variability and subsequent tracer fluxes.* TAV-PIRATA/TRIATLAS meeting, 2023, poster online.

Cortés-Morales, D., and Lazar, A. *LVBW-3DClim: Estimating the interannual variability of vertical velocities within the global ocean thermocline from observation-based geostrophic meridional velocities.* LEFE/GMMC Scientific days, 2023, online oral presentation.

Cortés-Morales, D., and Lazar, A. *Estimating the interannual variability of vertical velocities within the global ocean thermocline from observation-based geostrophic meridional velocities.* EGU General Assembly, 2023, online oral presentation.

Cortés-Morales, D., and Lazar, A. *Global open ocean vertical velocity reconstruction from observation-based geostrophic meridional velocity field.* AGU General Assembly in Chicago, USA, 2022, poster on-site.

Cortés-Morales, D., and Lazar, A. *North Atlantic thermocline vertical velocity reconstruction from observation-based geostrophic meridional velocity field.* WOCEAN workshop, LOCEAN, 2022, online oral presentation.

Cortés-Morales, D., and Lazar, A. *North Atlantic thermocline vertical velocity reconstruction from observation-based geostrophic meridional velocity field.* EGU General Assembly in Vienna, Austria, 2022, on-site oral presentation

Cortés-Morales, D., and Lazar, A. *Estimates of large-scale vertical velocities in the tropical Atlantic Ocean.* PIRATA-24/TAV meeting, 2021, online oral presentation.

Courses received

Machine Learning Introduction, 2023, *LOCEAN* (12h)

Phytoplanctonic Biomass Spatial Teledetection, 2023, *LOCEAN* (18h)

Numerical Modelling and Assimilation of Atmospheric Observations, 2023, *Ecole Normale Supérieure* (20h)

Activities in the laboratory

Participation in the organization and animation of the "Month of Paleoclimatology" and "Month of Mediterranean Sea" (Journal Clubs, seminars and "goûter-débat") of the laboratory.

Participation in Fête de la Science (Scientific week) during two years where we have shown experiments aimed at children, teenagers, and families to demonstrate the ocean circulation and the impact of climate change in the ocean.

Organization of and participation in the WOCEAN workshop held at LOCEAN in September 2022.

Founded projects

My director Alban Lazar and I, as co-PI, received funding of 10 000€ from LEFE MERCATOR for the LVBW-3Dclim project, spanning from 2022 to 2023.

Teaching

I conducted English and Spanish conversation workshops, mentored students in English, and fulfilled responsibilities at the Language Department Library as part of my teaching mission in the Languages Department (64h/yr x 3yr).

A

Appendix A: VERTICAL VELOCITY 3D ESTIMATES FROM THE LINEAR VORTICITY BALANCE IN THE NORTH ATLANTIC OCEAN

VERTICAL VELOCITY 3D ESTIMATES FROM THE LINEAR VORTICITY BALANCE IN THE NORTH ATLANTIC OCEAN

Diego Cortés Morales and Alban Lazar

LOCEAN, IPSL

Corresponding author: Diego Cortés Morales, dcortes@locean.ipsl.fr

ABSTRACT: Large-scale three-dimensional vertical movements of the world's oceans play a fundamental role in their functioning, yet they are still overlooked. This study aims to enhance our understanding of the relationship between horizontal and vertical flows as a function of depth to derive some major characteristics of the w field from a relatively well-constrained variable. For this purpose, we analyse an eddy-permitting ocean general circulation model simulation, focusing on the linear vorticity balance (LVB) over the North Atlantic basin. For spatial scales greater than 5°, over more than 50-year average, the LVB holds with less than 10% error over the whole depth range of most of the subtropical upper tachocline-upper ocean and part of the tropical one, away from western boundary currents and zonal tropical flows. The spatial extent of the balance diminishes in the intermediate ocean, particularly in the western half of the basin. Within the deep tachocline, the balance holds over large portions of the abyssal plains. Based on these results, the β-plane geostrophic vertical velocities are derived from the vertical indefinite integral of the geostrophic LVB from the surface. While its time-mean aligns only qualitatively with the model reference w, it accurately captures the interannual variability over most of the basin, even close to eastern boundaries. However, it cannot reproduce the variability in the lower tropics, the western boundary, and the North Atlantic Current system. Our results emphasise the dominance of geostrophy in establishing most of the ocean model vertical flow variability.

1. Introduction

One of the most influential theories that explain the ocean's general circulation is the Sverdrup balance, which connects the meridional geostrophic transport with the wind stress at basin scales (Sverdrup 1947). The Sverdrup balance theory describes the time-mean barotropic ocean transport over the subtropical and tropical gyres (STG and TG), assuming a level of no vertical motion. Sverdrup (1947) proposes that the Sverdrup balance should emerge after extended time-averaging. Subsequent research on this theory has suggested that the oceanic response to the atmospheric forcing needed for the Sverdrup balance to hold can occur within the first-mode baroclinic Rossby wave propagation timescales (Tailleux and McWilliams 2001). Hence, the Sverdrup balance approach fails to explain the vertically integrated circulation in regions where the Rossby wave has longer timescales than the studied period, such as in high latitudes. This formulation is also inadequate near the coasts, where the assumption of a level of no vertical motion is no longer valid (Wunsch 2011; Gray and Riser 2014 and Thomas et al. 2014).

Recent studies have examined the limitations of the Sverdrup balance through the complete vorticity balance, which includes viscosity, frictional, non-linear, and bottom pressure torque terms to close the vorticity budget. The importance of frictional and bottom pressure torque terms in the North Atlantic subpolar gyre interior has been highlighted by Spence et al. (2012), Yeager (2015) and Le Corre et al. (2020). In the Gulf Stream, it is necessary to add the non-linearities to the bottom pressure torque term to accurately account for the atmospheric forcing (Hughes and De Cuevas 2001, Gula et al. 2015 and Schoonover et al. 2016). The global ocean exhibits similar features, as noted by Hughes and De Cuevas (2001) and Sonnewald et al. (2019). Remarkably, the depth dependency of the vorticity balance is little studied. In an ocean circulation general model (OGCM), Lu and Stammer (2004) and Waldman and Giordani (2023) identify the Sverdrupian nature of the centre of the oceanic gyres within the upper and intermediate oceans and show that topographic forcing drives the vorticity budget closure in the deep ocean.

In order to conduct a baroclinic analysis of the basin-scale circulation, the linear vorticity balance (LVB) serves as an appropriate and well-known starting point:

$$\beta v = f \partial_z w \tag{1}$$

Where f is the Coriolis parameter, β is the meridional gradient of f. v and w are the meridional and vertical components of the velocity. When the flow is in LVB, it becomes possible to relate the shear of the vertical velocity field directly and locally to the meridional velocities. When integrated vertically from the surface to a level of no vertical motion, the LVB results in the Sverdrup balance. For a geostrophic and incompressible flow on a β-plane, the LVB represents the continuity equation and expresses a local mass balance between meridional divergent flow and an opposing vertical convergent movement, and vice-versa. Figure 1 illustrates this interpretation schematically for the geostrophic component of two stationary tropical and subtropical circulation gyres in the North Atlantic upper ocean.

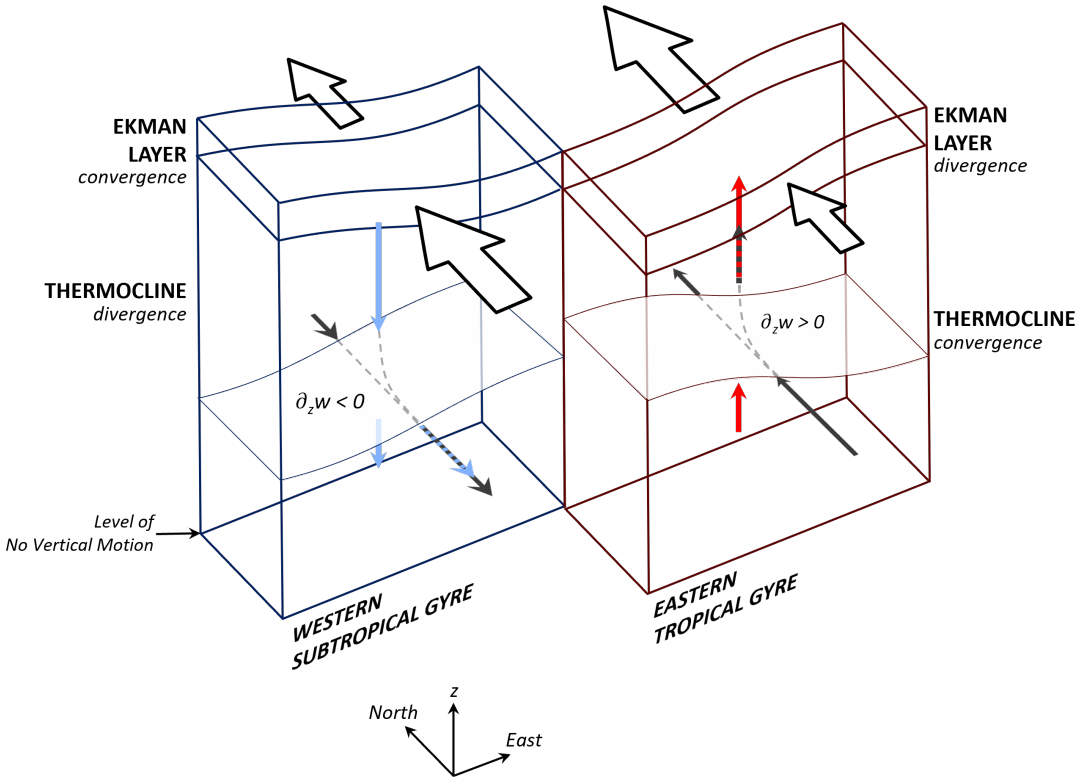

FIG. 1. Vertical and geostrophic meridional circulation over a typical Northern Hemisphere STG (northernmost cube) and TG (southernmost cube) within the thermocline. The tendency to reduce the amplitude of the downward (upward) flow in the thermocline must be offset by a divergent (convergent) flow in the STG (TG) to absorb (feed) the Ekman transport to the oceanic surface. Thus, the meridional circulation in the thermocline is determined by the divergence of equatorward transport and the convergence of poleward transport.

Indeed, the inverse dependence on latitude of the meridional geostrophic transport (v_g) results in the convergence of the poleward transport within the cyclonic tropical gyre (TG) thermocline, pushing up the thermocline waters and supplying mass to the diverging Ekman flow, forced by the Trade winds, whose intensity increases with latitude. Further north, the intrinsic divergence of the equatorward transport of the subtropical gyre (STG) progressively absorbs the Ekman layer mass excess from the converging flow, leading to downward movements (Tomczak and Godfrey 1994). A comparable logic can be used in the geostrophic deep ocean and the bottom Ekman layer. However, there is no independent forcing like wind stress in the deep ocean to estimate a boundary condition for the ageostrophic component of w.

As illustrated for the thermocline, geostrophic vertical movements are essential to global circulation. They redistribute water masses between layers, shaping them (Stramma and England 1999), they ventilate the thermocline (Gordon 1981), and also participate in driving the deep circulation (Drake et al. 2020). However, the w field in the open ocean is several orders of magnitude smaller than the horizontal circulation (approximately 10^{-6} m s^{-1} in the centre of oceanic gyres). Currently, direct observations of such weak intensities are not yet technically possible (e.g., Comby et al. 2022).

The reconstruction of horizontal geostrophic velocities, derived from observed thermohaline fields, in conjunction with data collected by current metres, expands the possibilities for connecting the three components of ocean circulation.

Many early estimations of w utilised measured profiles of tracers to estimate tracer fluxes (e.g. Stommel and Arons 1959; Robinson and Stommel 1959; Wyrtki 1961; Munk 1966; Wunsch 1984), or the application of mooring measurements of horizontal currents to the continuity equation (Stommel and Schott 1977; Schott and Stommel 1978; Wyrtki 1981; Roemmich 1983; Bubnov 1987; Halpern and Freitag 1987; Halpern et al. 1989; Weingartner and Weisberg 1991). These studies reached a consensus on the order of magnitude of the w in the different ocean layers ranging from 10^{-5} m s^{-1} near the surface, gradually decreasing to 10^{-6} m s^{-1} within the upper ocean, and reaching values between 10^{-7} and 10^{-8} m s^{-1} in the intermediate and deep oceans. However, while the vertical velocity field can be diagnosed in primitive equation numerical models by solving the

continuity equation, this approach has been limited by the scarcity of observation-based data at global scale and the potential for prominent instrumental errors when computing the divergence from measured horizontal velocities. One example of retrieving the vertical flow from observations via continuity equation is presented by Freeland (2013), who calculated observation-based barotropic w at 700 dbar within an approximately 25x20° horizontal box. Over the last decade, researchers have explored alternative approaches for assessing large-scale baroclinic vertical velocities. These include the use of observations of isopycnal displacement (Giglio et al. 2013; Christensen et al. 2023), moorings data applied to the momentum and density equations (Sévellec et al. 2015) and biogeochemical tracers (Garcia-Jove et al. 2022). More theoretical approaches have now gained more attention, such as using the Bernoulli function to estimate w (Tailleux 2023). In recent years, several attempts have been made to compute the w field using the omega equation ($f^2 \frac{\partial^2 w}{\partial z^2} + \nabla_h (N^2 \cdot \nabla_h w) = \nabla \cdot Q$; Giordani et al. 2006), as demonstrated by studies conducted by Buongiorno Nardelli et al. (2018); Ruiz et al. (2019) and Buongiorno Nardelli (2020). Buongiorno Nardelli et al. (2018) developed a three-dimensional w product within the upper ocean (OMEGA3D) from an Argo and satellite based dataset (Mulet et al. 2012; Guinehut et al. 2012).

An alternative approach to estimate the w field from observations is theoretically possible within the geostrophic LVB framework, as suggested by Charney (1955). This alternative also offers a simple and intuitive method to understand basin-scale motions in LVB. In the present paper, we aim to develop a comprehensive baroclinic analysis of the LVB and its geostrophic case at all depths, in climatological and interannual scales across the North Atlantic, in an OGCM simulation. This analysis will address the oceanic circulation patterns' ability to react to the surface and bottom boundaries forcing, transmitting the forcing to the ocean interior. Lastly, and from the perspective of future developments based on the use of global geostrophic currents computed from observations, we will assess the feasibility of using an indefinite vertical integration of the geostrophic LVB in order to reconstruct the three-dimensional distribution of the OGCM's vertical flow.

2. Methodology and Data

a. The Linear Vorticity Balance

The vorticity balance can be obtained by applying the continuity equation to the vertical component of the curl of the steady-state momentum Navier-Stokes equations under Boussinesq approximation:

$$\partial_t \zeta + \beta v + \mathbf{u}\nabla\zeta + [(\partial_x w \partial_z v) - (\partial_y w \partial_z u)] = (f+\zeta)\partial_z w + \frac{1}{\rho}\nabla \times [\rho A_H \nabla^2 \mathbf{u}_H + \rho A_V \partial_z^2 \mathbf{u}_H] \quad (2)$$

Where ζ is the relative vorticity, $\mathbf{u}$ and $\mathbf{u}_H$ are the three-dimensional and horizontal velocity fields, respectively. u, v and w represent the zonal, meridional and vertical components of the velocity. A_H and A_V are the horizontal and vertical turbulent viscosity coefficients, respectively. The terms on the left-hand side of Eq. 2 are the relative vorticity time variation, the planetary vorticity advection, the relative vorticity advection and vortex tilting term. On the right side of Eq. 2, the terms are the vortex stretching term and the horizontal and vertical eddy viscosity terms (Vallis 2006).

The Rossby number ($Ro = V/fL$, where L and V are the characteristic length and horizontal component of the flow) relates the inertial to Coriolis forces. Therefore, this ratio can be used for a magnitude analysis of the vorticity equation. Most term dimensions in Eq. 2 can be expressed in terms of Ro. The continuity equation indicates that the vertical velocity scale is related to the horizontal velocity by $V/L = W/D$ where W and D are the vertical component and thickness of the flow. With T the characteristic time of the flow and expressed as $T = 1/fRo$:

$$\left[\partial_t \zeta = \frac{fRo}{T}\right] = f^2Ro^2; \quad [\mathbf{u}\nabla\zeta] = f^2Ro^2; \quad \left[(\partial_x w \partial_z v) - (\partial_y w \partial_z u)\right] = f^2Ro^2; \quad [\zeta\partial_z w] = f^2Ro^2$$
$$[\beta v] = f^2Ro; \qquad [f\partial_z w] = f^2Ro; \quad (3)$$

Considering a low Rossby number ($Ro << 1$) describes large-scale ocean flow of $O(100km)$, the terms explicitly dependent on the Coriolis force are dominant contributors in the balance of forces

(Pedlosky 1979). Far from frictional boundaries, the Ekman numbers (horizontal $Ek = 2A_H/fL^2$ and vertical $Ek = 2A_V/fD^2$) are low (Ek << 1), and rotation dominates over friction. Therefore, the eddy viscosity-related terms ($\frac{1}{\rho}\nabla \times [\rho A_H \nabla^2 \mathbf{u}_H] = f^2 RoEk$; $\frac{1}{\rho}\nabla \times [\rho A_V \partial_z^2 \mathbf{u}_H] = f^2 RoEk$) can be overlooked. Taking the first-order balance of Eq. 2 while considering the regime flows mentioned above and averaging over a sufficiently long period to neglect time-variation contribution, the Eq. 1 emerges.

In this paper, both sides of Eq. 1 are first estimated to assess the extent to which the LVB describes the circulation in the OCGM. Their relative error (Δ_{LVB}) relative to the mean between both terms in Eq. 1 is estimated as follows:

$$\Delta_{LVB} = \frac{(\beta v - f\partial_z w)}{\frac{1}{2}(|\beta v| + |f\partial_z w|)} \cdot 100 \tag{4}$$

Δ_{LVB} measures the deviation of Eq. 1 from the perfect equilibrium and is zero where the LVB is exactly correct. The regions where the $|\Delta_{LVB}|$ is smaller than 10% are considered LVB-valid areas at first order.

The western boundary region (4° width-band), characterised by a high Rossby number, as well as the equatorial band (0-5°N), where the Coriolis parameter f becomes too small, have been masked and not considered in our quantitative analyses. Additionally, given the significant impact of mixing terms within the mixed layer, we exclude the region between the surface and the maximum mixed layer depth from our analysis when determining the zonal percentage of the basin explained by the LVB.

In this model study, we will divide the tropical and subtropical oceans into three distinct dynamic layers visible in Figure 2. First, we introduce a new concept: the tachocline. This concept represents a region in a dynamically stratified water column which separates rapid flowing waters from an almost steady region, with velocity amplitude decreasing rapidly with depth. The name "tachocline" is inspired by the construction of concepts such as thermocline, halocline or pycnocline. "Tacho-", from Greek "tachos", refers to "velocity, speed", and "-cline", from Greek klinein, means "to

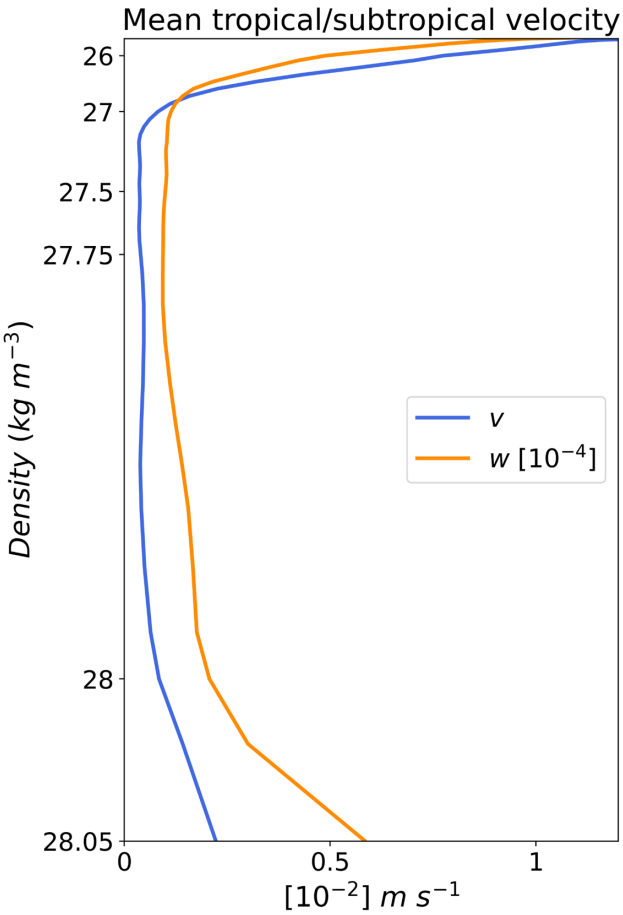

171 FIG. 2. Spatial-mean of absolute velocity field over the tropical and subtropical bands (5°-35°N), excluding
172 the 4° width-band along the western boundary as well as the mixed layer. The distance between σ levels on the
173 y-axis is proportional to their average width within the basin.

161 slope". Therefore, in Figure 2, we observe an upper tachocline covering the depth range of the
162 thermocline (not shown) and a lower tachocline within the deep ocean. Between these layers,
163 the intermediate ocean is characterised by minimal and barotropic velocities. In this study, we
164 have identified the maximum mixed layer as the upper boundary condition of the upper tachocline
165 and the isopycnal surface σ 27.1 kg m^{-3}, averaged across the subtropical (20-35°N) and tropical
166 bands (5-20°N), as the lower boundary. Note that the subtropical upper tachocline extends to
167 approximately σ 27.1 kg m^{-3}, while the tropical upper tachocline reaches around σ 26.75 kg m^{-3}.
168 In the mid-latitudes (35°-50°N), the upper tachocline extends to σ 27.5 kg m^{-3} (not shown). The
169 intermediate ocean is bounded by σ 27.1 and 28 kg m^{-3}. Lastly, the lower tachocline in the deep
170 ocean is bounded from above by σ 28 kg m^{-3} and from below by the seabed.

Given our interest in assessing the horizontal circulation patterns and the extension of the LVB description of each of these three domains, we identified three representative isopycnal surfaces at σ 26, 27.78 and 28.05 kg m^{-3}.

b. Vertical Velocity Estimation from the Linear Vorticity Balance

The current state of the observations at basin scales only allows retrieving geostrophic flows. Although we are assessing the validity of the total LVB, this study aims to evaluate the feasibility of reconstructing w from observation-based data and LVB. Therefore, we derive the three-dimensional w by vertically integrating the geostrophic component of the LVB (GLVB):

$$w_{GLVB}(z) = w(z_{ref}) - \int_{z}^{z_{ref}} \frac{\beta v_g}{f} dz' \tag{5}$$

In fact, the geostrophic LVB and the w_{GLVB} can be derived from the divergence of the geostrophic flow in a β-plane (Pedlosky 1996):

$$\frac{\partial u_g}{\partial x} + \frac{\partial v_g}{\partial y} + \frac{\partial w_g}{\partial z} = 0 \tag{6}$$

Where $u_g = -1/f\rho_0 \ \partial_y p$, $v_g = 1/f\rho_0 \ \partial_x p$, and p is the pressure. Considering a β-plane, the GLVB is retrieved:

$$\beta v_g = \frac{\partial w_g}{\partial z} \tag{7}$$

Where w_g is the geostrophic component of the vertical flow. According to the GLVB, when accounting for the β-plane effect, the geostrophic meridional transport of the planetary vorticity is compensated by the vortex stretching induced by the vertical transport. By applying the indefinite depth-integral to Eq. 7, we obtain the equation for $w_{GLVB}(z)$ (Eq. 5):

$$w_g(z) = w_g(z_{ref}) - \int_{z}^{z_{ref}} \frac{\beta v_g}{f} dz' \tag{8}$$

In order to compute $w_g(z_{ref})$, one method assumes a level of no motion where all velocity vector components are null. However, while recent studies (e.g. Koelling et al. 2020) support this assumption, the depth of this level is uncertain for computations based on data from the real

ocean. Alternatively, satellite observations provide variables with extensive spatial and temporal coverage, making them adequate for use as boundary conditions. Therefore, we propose estimating $w_g(z_{ref})$ at the surface.

The total vertical velocity (w) is the sum of the ageostrophic (w_{ag}) and the geostrophic (w_g) components. Since the vertical velocity must vanish at the ocean surface in a steady state, both components are opposite (Pedlosky 1996). For this purpose, let us recall that w_{ag} is generated by the divergence of the wind-driven ageostrophic flow. When neglecting any other ageostrophic flow, it is therefore sufficient to estimate the Ekman pumping vertical velocity at the surface ($w_{Ek}(z=0)$). Within the Ekman Layer, dissipation brings the wind-driven flow to zero at its bottom, allowing us to consider its vertical component as null there (Ekman 1905). Therefore, vertically integrating the Ekman transport over this layer thickness yields:

$$w_{Ek}(z=0) = -\frac{1}{\rho_0} curl\left(\frac{\tau^{surf}}{f}\right) \tag{9}$$

Where $z=0$ denotes the surface (Pedlosky 1996), ρ_0 represents the water density at the surface, and τ_{surf} is the wind stress.

The classical view of the Ekman pumping vertical velocity locates it at the bottom of the Ekman layer, neglecting the geostrophic contribution to the horizontal flow (Marshall and Plumb 2007). However, the contribution of the geostrophic flow divergence in the Ekman layer is found to be about 10 (30)% of the Ekman pumping amplitude in the upper 50 (100) m depth (not shown). In the context of the Ekman pumping described in Eq. 9, e.g. over the downwelling gyre, the Ekman transport convergence within the Ekman layer is balanced by a downward vertical flow from the Ekman layer into the ocean interior, evacuating water masses accumulating due to the Ekman flow.

Thus, we derive the expression for the GLVB vertical velocity (or geostrophic vertical velocity) as a function of depth:

$$w_{GLVB}(z) = w_g(z) = -w_{Ek}(z=0) - \int_z^0 \frac{\beta v_g}{f} dz' \tag{10}$$

c. The Reference Ocean Model and the Spatial Filtering

The OGCM of reference for this study is the Nucleus for European Modelling of the Ocean (NEMO; Madec et al. 2017). It embeds an ocean general circulation model (OPA, Océan PArallélisé) and a sea-ice model (LIM, Louvain-la-Neuve ice model); see http://www.nemo-ocean.eu/. The dataset used in this study originates from the OCCITENS simulation (Bessières et al. 2017), conducted over the period 1960-2015, after a spin-up of 26 years, at eddy-permitting resolution 1/4° (ORCA025 grid Arakawa type C cell) and forced by DFS5.2 set (Dussin et al. 2016). The OCCITENS simulation provides monthly 3D estimates of oceanic variables that would be impossible to produce from observations alone, such as the vertical velocity field. Thermohaline and sea surface height fields are used to compute the neutral density field following Jackett et al. (2006) formula. Furthermore, the wind stress is used to compute w_{Ek} (Eq. 9). The geostrophic velocity field is computed using the geostrophic equation applied to the pressure field, which is calculated using sea surface height and integration of the hydrostatic equation. The code used to compute the geostrophic velocities is available at https://github.com/meom-group/CDFTOOLS.

Previous studies on the validity of the Sverdrup balance, including Thomas et al. (2014), Wunsch (2011) and Gray and Riser (2014), and studies analysing the complete barotropic vorticity, such as Gula et al. (2015), Le Bras et al. (2019), Sonnewald et al. (2019) and Khatri et al. (2023), have highlighted the significant impact of model spatial resolution and horizontal low-pass filtering on the role and assessment of each term of the vorticity balance. To account for the spatial resolution dependency of the LVB, we conducted a low-pass sensitivity analysis with filter kernel sizes ranging from 1 to 7° (Figure 3). The w in the OGCM is a diagnostic variable derived from the horizontal flow in the continuity equation, exhibiting smaller structures than the horizontal velocity field. Hence, prior to the above analysis, a 1° filter is applied to the w field to remove the spatial high-frequency and match its scale to that of the horizontal flow components.

Figure 3 displays the 56-year average LVB validity extension as a function of depth and filter scale ranging from 1 to 7°. As the filtering kernel size increases, the LVB validity extension for a given isopycnal surface expands within the intermediate and deep oceans. This occurs because the

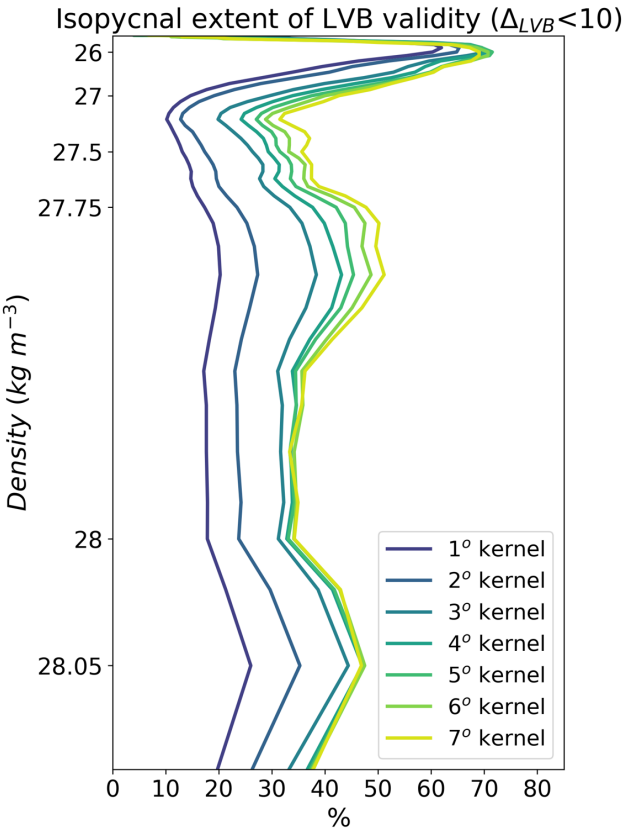

239 FIG. 3. 56-year average LVB validity extent (%) over isopycnal levels in the unmasked region outside the 4°
240 belt from the western boundary, as a function of spatial smoothing size from 1 to 7 ° kernel.

244 filter ensures that the motion is of a sufficiently large scale for the LVB to remain valid. However,
245 for larger scales, particularly within the upper ocean where the open ocean circulation already
246 exhibits basin-scale features at its native resolution, the filter extends the error near the coasts.
247 Thus, 5° filter maximises the LVB validity extension across the water column. It reduces errors
248 along the lateral boundaries, smooths out small-scale structures within the intermediate and deep
249 oceans, and preserves the core circulation patterns. This choice lets us focus on the large-scale
250 ocean dynamics the LVB formulation can successfully describe.

251 3. The Climatological Velocity Field in OCCITENS Simulation

252 The 56-year average of the OGCM vertical and horizontal velocity field is presented in Figures
253 4, 5 and 6 over three isopycnal surfaces (σ 26, 27.78 and 28.05 kg m^{-3}), representing the upper
254 tachocline, corresponding to the upper tachocline in the upper ocean, the intermediate ocean, and

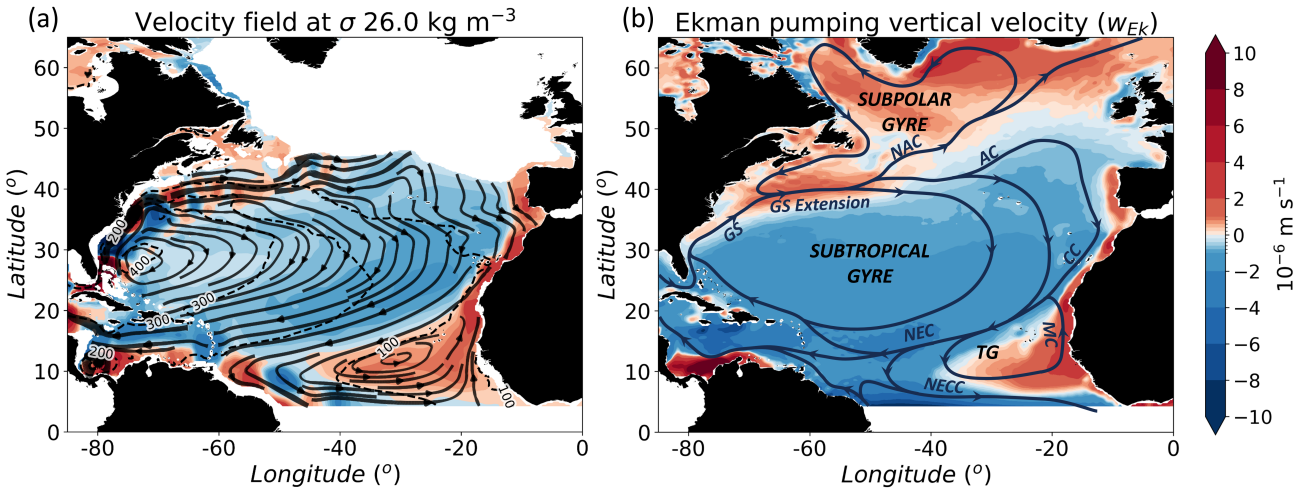

FIG. 4. (a) 56-year averaged velocity field from OGCM simulation over σ 26 kg m^{-3} representative of the upper tachocline-upper ocean. Vertical velocities are represented with coloured-filled contours, and horizontal velocities are represented with streamlines. The black-dashed contours represent the depth of the isopycnal surface (in metres). (b) 56-year Ekman pumping vertical velocity (w_{Ek}; Eq. 9) computed from OGCM simulation wind stress. The schematic streamlines represent the main upper ocean gyres and currents of the North Atlantic Ocean. Adapted from Schmitz Jr and McCartney (1993) and Tomczak and Godfrey (1994). [AC, Açores Current; CC, Canary Current; GS, Gulf Stream; GS Extension, Gulf Stream Extension; MC, Mauritania Current; NAC, North Atlantic Current; NEC, North Equatorial Current; NECC, North Equatorial Countercurrent; TG, Tropical Gyre] The equatorial band (0-5°N) has been masked.

the lower tachocline in the deep ocean. Figures 4 and 6 also depict the Ekman pumping vertical velocity (w_{Ek}) and the bottom vertical velocity, respectively, offering insights into how boundary conditions influence the circulation in the ocean interior.

The tropical gyre (TG; Figure 4(a)), as described by Schott et al. (2004), displays a counterclockwise circulation around the Guinea Dome (Stramma et al. 2005). On the other hand, the subtropical gyre (STG; Schmitz Jr and McCartney 1993) is characterised by a clockwise circulation. Strong zonal flow is evident in the southern part of both gyres, the equatorial band and the open ocean Gulf Stream extension.

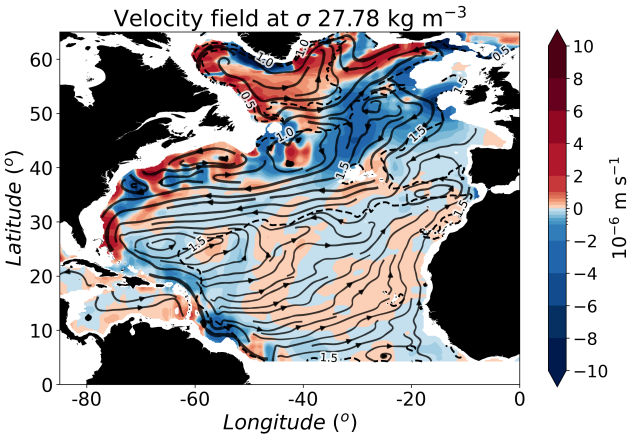

290 FIG. 5. Same as Figure 4(a) over σ 27.78 kg m^{-3}, representative example of the intermediate ocean. The
291 black-dashed contours represent the depth of the isopycnal surface (in kilometres).

272 The Ekman pumping vertical velocity (w_{Ek}) (Figure 4(b)) shows an upwelling over the TG
273 with its maximum occurring near the eastern boundary from between 10-20°N. Over the STG,
274 the downwelling is centred at 50°W over the southern part of the STG. The Gulf Stream region,
275 including its separation from the coast and its open ocean extension, is characterised by upward
276 movements. The subpolar gyre (SPG) exhibits an upwelling centred in the southeastern part of
277 Greenland with a coastal downwelling along Greenland. These results are consistent with previous
278 computations of w_{Ek} using observed datasets (e.g. Xie and Hsieh 1995).

279 The vertical velocity field within the upper tachocline-upper ocean (shading in Figure 4(a)) is
280 largely similar to w_{Ek} spatial patterns (Figure 4(b)), evidencing the role of the atmospheric forcing
281 as the primary contributor to the vertical flow within the upper ocean (Huang and Russell 1994).
282 The sign and amplitude of w_{Ek} evidently shape the isopycnal surfaces (Gill 1982). Over σ 26
283 kg m^{-3}, the cyclonic circulation of the TG is associated with positive w (Lazar et al. 2002) with
284 maximum upwelling values within the Canary upwelling system (Arístegui et al. 2009). Conversely,
285 the anticyclonic circulation of the STG is characterised by negative velocities, which deepen the
286 isopycnal surfaces. In addition, the Gulf Stream is associated with an overall downwelling along
287 the coast and an upwelling after its separation from the continent, featuring meanders and eddies.
288 The differences in intensity between the upper ocean w and w_{Ek} illustrate the baroclinic nature of
289 the field within the upper tachocline, as depicted in Figure 2.

Let us examine now the intermediate ocean that we chose to bound by σ 27.1 kg m^{-3}, representing the bottom of the upper tachocline and 28 kg m^{-3} where the circulation starts significantly intensifying as shown in Figure 2. The σ 27.78 kg m^{-3} surface (Figure 5) extends across the entire basin, revealing the cyclonic SPG and northernmost anticyclonic STG circulation. Comparing the tropical and subtropical bands in Figures 4(b) and 5, it is evident that the influence of surface circulation is limited to north of 35°N. South 35°N the w_{Ek} no longer dominates the spatial patterns of the vertical motions in the intermediate ocean. Here, the w field has a spatial scale of a few degrees without coherent large-scale structure, in accordance with Ollitrault and De Verdière (2014). While the magnitude of the w field changes rapidly with depth within the upper tachocline, it remains relatively constant in the intermediate ocean (Figure 2). Between 40 and 50 °N, the vertical flow exhibits values of the same order of magnitude as within the upper tachocline. The equatorward and downward flow is associated with the STG shifted towards the north with depth (Stramma 1984). In subpolar latitudes, the SPG cyclonic circulation is associated with upwelling.

Regarding the deep tachocline circulation in the deep ocean, Figure 6(a) displays the three-dimensional flow pathways over σ 28.05 kg m^{-3}. The western and eastern basins, separated by the Mid-Atlantic Ridge (Figure 6(b)), show clockwise basin scale circulations constrained by the topography. Indeed, the interaction of the deep horizontal circulation with bathymetry generates a vertical velocity field at the bottom (Figure 6(b)), expressed as $w_B = -\mathbf{u}_B \cdot \nabla D$ (where $\mathbf{u}_B$ is the horizontal velocity vector at the seabed, and ∇D is the spatial gradient of the bathymetry) (Zhang and Vallis 2007). Again, the similarities between the deep ocean and bottom vertical velocity fields (panels (a) and (b) in Figure 6) highlight that the deep ocean vertical flow is controlled by the bottom horizontal circulation and the varying bathymetry. This result is consistent with the high spatial correlation between the bottom and deep ocean vertical velocities obtained by Liang et al. 2017. However, note that the OGCM's reconstruction of the deep circulation has limited confidence. The deep and abyssal flows remain undersampled with scarce observations in the real ocean (Levin et al. 2019). Therefore, obtaining a clear large-scale picture of the climatological circulation within the deep ocean is challenging, and the patterns and amplitudes shown in Figure 6(a) should be interpreted with caution, as they are specific for the OGCM's case.

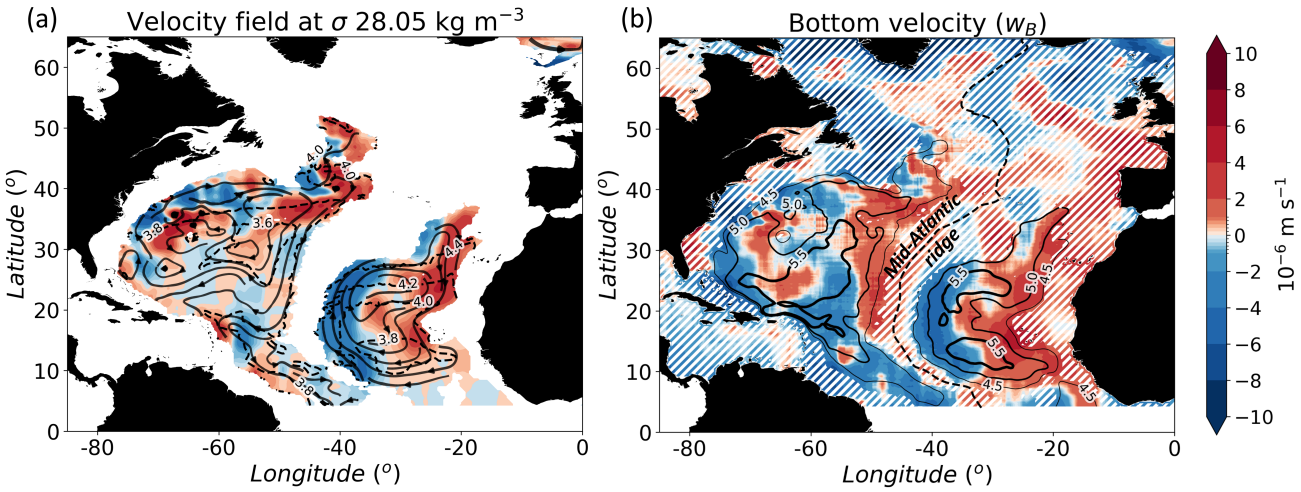

FIG. 6. Same as Figure 4(a) over σ 28.05 kg m^{-3}, representative of the deep ocean. The black-dashed contours in panel (a) represent the depth of the isopycnal surface (in kilometres). OGCM simulation vertical velocities on the deepest level (b). Note that Madec et al. (2017) uses the topographic induced vertical velocity (Zhang and Vallis (2007)). The contours in panel (b) indicate the seafloor depth at 4500, 5000 and 5500 m (from thinner to thicker contours). The dashed line in panel (b) represents the Mid-Atlantic Ridge border used to split the North Atlantic basin into western and eastern sub-basins. White hatching masks the regions above σ 28.05 kg m^{-3} for comparison purposes.

Given these three large circulation patterns, we aim to assess the extent to which the LVB characterises them and allows a relationship between the meridional and vertical flows.

4. Linear Vorticity Balance Validity

First, we analyse the multidecadal climatology of the two LVB terms within the upper tachocline-upper ocean, intermediate ocean and lower tachocline-deep ocean. This section seeks to evaluate the LVB as a function of depth, quantifying its ability to capture climatological ocean dynamics in layers that are remote from the impact of wind and bathymetry forcings. Moreover, this approach is expected to offer insights into regions within the basin where reconstructing the w field using an indefinite integral of the LVB is feasible, thus enhancing our understanding of circulation patterns. In the final subsection, we will explore the dependency of the extension of LVB validity to the average period.

a. Upper Tachocline-Upper Ocean

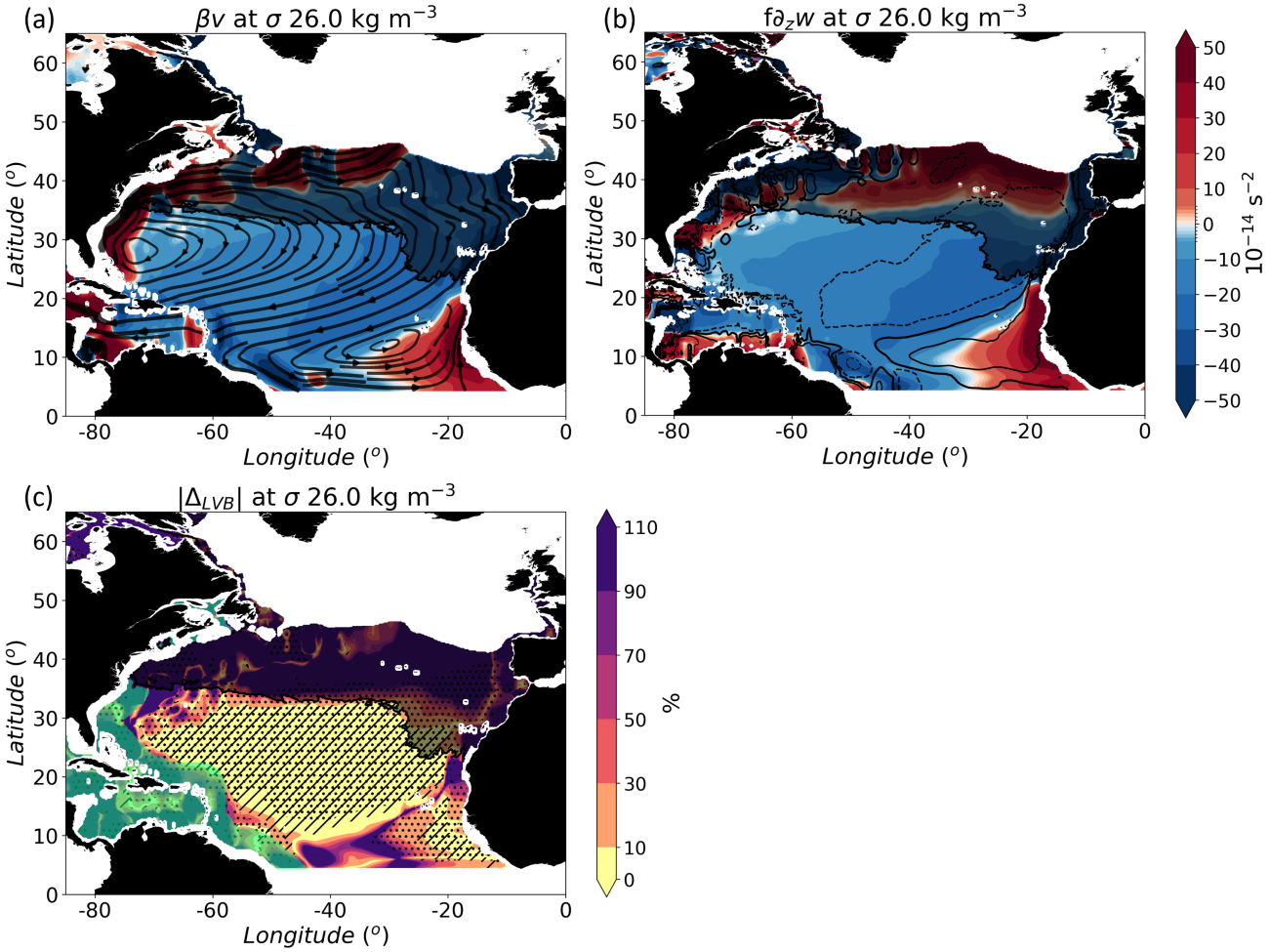

FIG. 7. 56-year averaged filtered LVB terms (advection of planetary vorticity and vortex stretching) and $|\Delta_{LVB}|$ (Eq. 1) (c) over σ 26 kg m^{-3} (a,b). Horizontal velocities are represented with streamlines over (a) panel (Same as Figure 4). Positive (continuous contours) and negative (dashed contours) vertical velocities have been plotted on panel (b). Dotted areas in panel (c) represent regions where the meridional velocity field is in geostrophic balance with a relative error smaller than 10%. Hatched areas represent the regions where the geostrophic LVB is valid at 10%. The black and green translucent regions indicate the maximum mixed layer mask and the 4° width-band along the western boundary masked region for the zonal percentage extent of valid area computation.

The $|\Delta_{LVB}|$ displayed over σ 26 kg m^{-3} in Figure 7(c) allows us to unveil where and to what extent this balance characterises the 56-year averaged meridional and vertical circulation. The $|\Delta_{LVB}|$ exhibits values smaller than 10%, considered as LVB-valid regions, in the eastern part of the TG where the poleward Mauritanian Current (MC; Figure 4(b); Fernandes et al. 2005) and the

basin-wide equatorward North Equatorial Current (NEC; Figure 4(b); Schott et al. 2002), except for the recirculation core of the gyre, adjacent to the Gulf Stream, with a much weaker flow. For these LVB-valid areas, it appears that the vortex stretching ($f\partial_z w$; Figure 7(b)) is balanced by the planetary vorticity transport (βv; Figure 7(a)). It corresponds to positive (negative) vorticity contribution over poleward (equatorward) flow regions. The sign of the vortex stretching term corresponds to the general downward decrease of the amplitude of the upper tachocline flow (Figure 2). In the northwestern part of the TG (solid contours in Figure 7(b) from 30-50°W and 10-15°N), the LVB holds within the NEC exhibiting negative $\partial_z w$ values, unlike the rest of the TG. The divergence of the equatorward flow in shallow layers (not shown) evacuates the downwelling waters from the Ekman layer, changing the sign of the vertical flow. This change displaces the gyre to the north and west with depth, as shown by Elmoussaoui et al. (2005). Note that the Ekman pumping-induced upwelling reaches 35°W at the surface, while the σ 26 kg m^{-3} upwelling in the upper tachocline's tropical gyre extends up to 50°W.

In order to integrate the LVB from the surface to the depth or sigma of interest, it must hold throughout the entire depth range. Therefore, we now examine the vertical extension of the LVB regimes in more detail. Figure 8 shows the zonal fraction of LVB-valid area at each isopycnal surface and latitude. To address the Eastern Atlantic currents separately from the contribution of the western boundary currents that reduce this fraction, the North Atlantic basin is divided between western and eastern halves separated by the Mid-Atlantic Ridge (Figure 6(b)). To the south, it confirms that the TG departs largely from the LVB, except south of 12°N (Figure 8(b)) where the flow, corresponding to the MC, is essentially meridional. At tropical latitudes, the thermocline (and therefore the upper tachocline) is thin (Salmon 1982), and consequently, the LVB holds over a shallower extension. However, in the North Equatorial Counter Current (NECC; Figure 4(b); Schott et al. 2002), with a predominantly zonal character, the zonal extent LVB's validity drops to a few spots with a maximum of 60% in the western tropical upper tachocline (Figure 8(a)). The LVB validity extends zonally across up to 90% of the basin until σ 27.1 in the central region of the subtropical band, between 20-30°N. Currents such as the equatorward Canary Current (CC; Figure 4(b); Stramma et al. 2005) and the NEC in the interior of the STG are almost entirely in LVB. At higher subtropical latitudes, between 30-35°N, in the vicinity of the Azores Current (AC;

Figure 4(b); Klein and Siedler 1989), the LVB accounts for about 80% of the zonal extent of the eastern and western sub-basins. The limited extent of LVB validity in the western half of the North Atlantic basin between 35-40°N (Figure 8(a)) illustrates the importance of non-linearities in the Gulf Stream. Moving between 40-50°N, the LVB also plays a significant role in the region where the poleward flow of the North Atlantic Current (NAC; Figure 4(b); Rossby 1996) is found. It covers up to 90% of the zonal extent near the surface in the western basin below and more than 50% around σ 27.5 in the eastern basin.

In addition, to evaluate the capability of observation-based geostrophic meridional transport in describing vertical motions, we analysed the extent where the geostrophic component of the LVB (GLVB; Eq. 7) and the geostrophic balance (GB) can be considered valid ($|\Delta_{GLVB} = |0.5 \cdot (\beta v_g - f\partial_z w)/(|\beta v_g| + |f\partial_z w|) \cdot 100||$, $|\Delta_{GB}| = |0.5 \cdot (v_g - v_t)/(|v_g| + |v_t|) \cdot 100| < 10\%$) (depicted by hatched and dotted areas in Figure 7(c)). This analysis demonstrates that the LVB is geostrophic within the STG and the eastern part of the TG. The overall overlap of the areas where the GLVB and geostrophic balance are valid suggests that while the geostrophic balance is necessary to close the geostrophic linear vorticity balance, it may not be needed for the total case.

b. Intermediate Ocean

As the flow decreases below the upper tachocline, one expects the smaller terms of the vorticity balance to become more important compared to the linear terms. However, there is a qualitative agreement between βv and $f\partial_z w$ terms over σ 27.78 kg m^{-3} (Figure 9(a),(b)) away from the western boundaries where both terms are mainly positive. Further north, the sign changes, but the terms still agree quite well at first glance. Their values are one order of magnitude larger there than over the tropical and subtropical bands, associated with a more intense circulation. This circulation is predominantly southwestward between 30-50°N, below the NAC, and northeastward at higher latitudes. They contribute respectively with positive and negative vorticity to the LVB.

Figure 9(c) shows that the LVB holds irregularly across most of the eastern tropical, subtropical and extratropical bands, away from lateral boundaries. The discrepancy in the eastern boundaries, evident in the upper and intermediate ocean, is likely a result of the diabatic effect of eddy fluxes

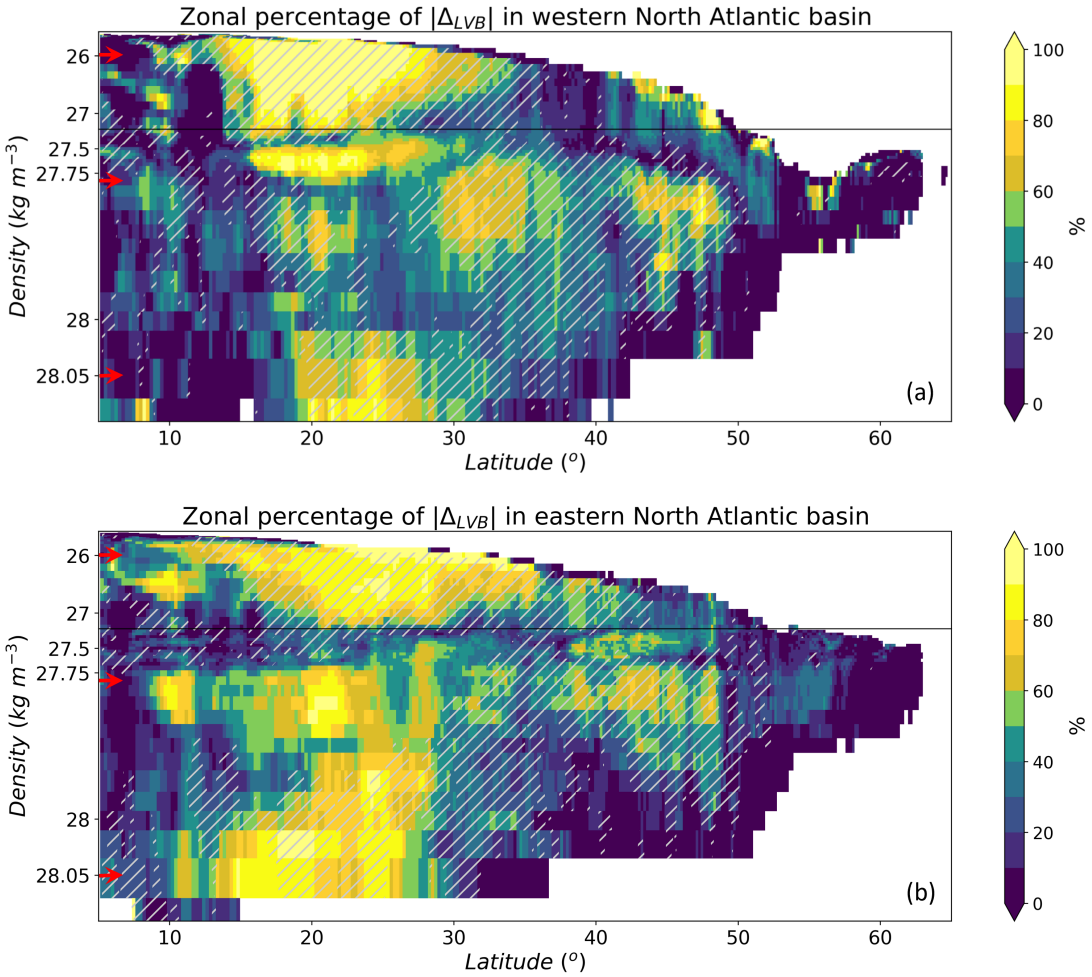

394 FIG. 8. Zonal extent (%) of LVB validity ($|\Delta_{LVB}|$ <10%) at each isopycnal surface level and latitudinal grid
395 point (surface and subsurface tropical band not represented) considering only the western (a) and eastern (b) part
396 of the North Atlantic basin defined by the Mid-Atlantic Ridge (Figure 6(b)) within the unmasked region. The
397 hatching represents net equatorward circulation when the meridional circulation is zonally averaged over solely
398 LVB-valid regions. The distance between σ levels on the y-axis is proportional to their average width within the
399 basin with a zoom between the surface and σ 27.1 kg m^{-3}. The red arrows indicate the isopycnal levels chosen
400 as representative of the upper, intermediate and deep oceans.

413 originating from the eastern boundary currents (Cessi and Wolfe 2013). The intermediate ocean
414 exhibits smaller LVB-valid areas than the upper layers, particularly in the western half of the
415 tropical-subtropical domain, where alternative meridional bands with relative error larger than
416 10% are visible. However, the LVB validity extends until reaching the northernmost region of
417 the anticyclonic STG, around 55°N. The zonal extent of LVB validity reaches up to 70% of the

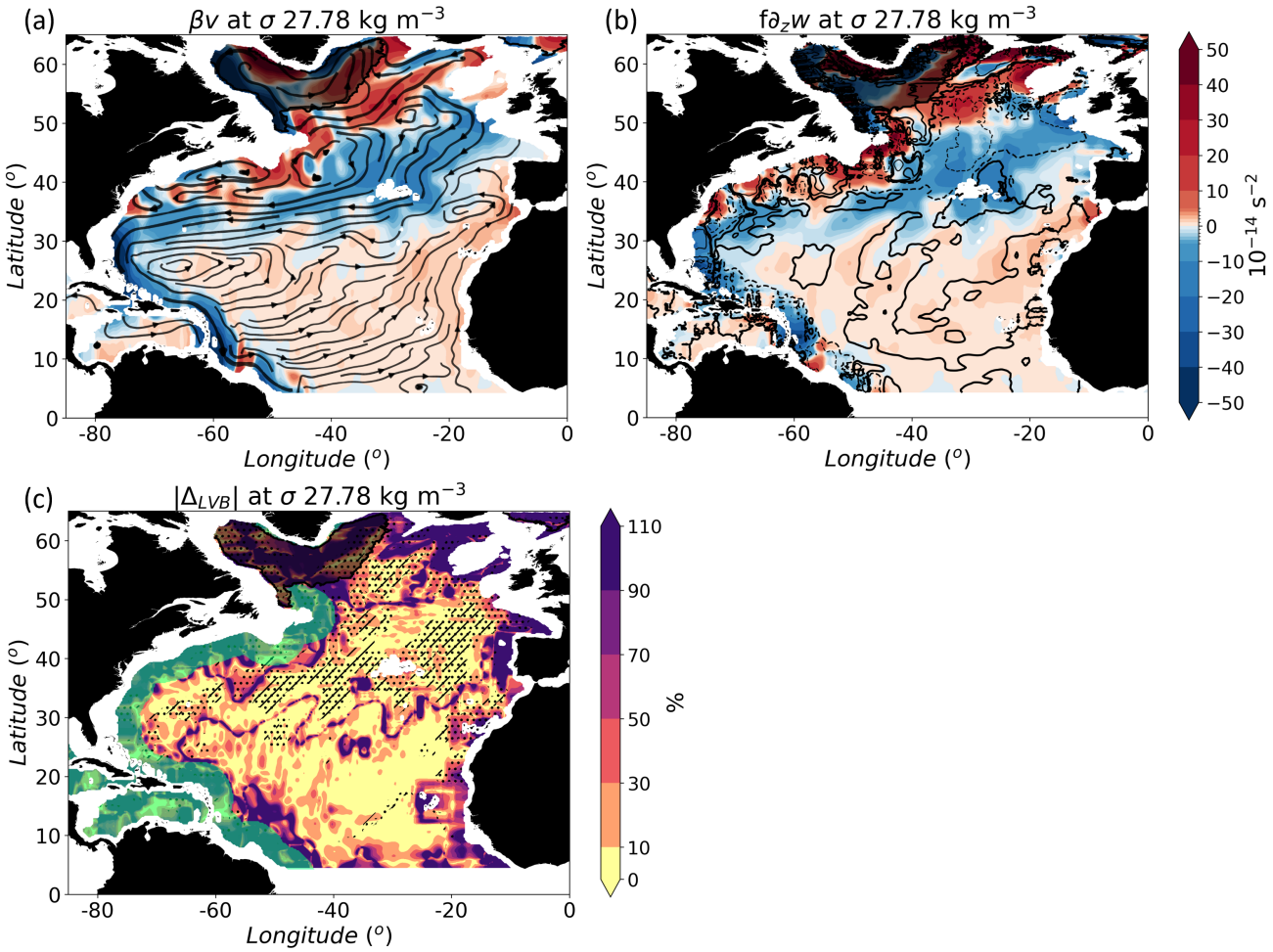

FIG. 9. Same as Figure 7 over σ 27.78 kg m^{-3}, representative example of the intermediate ocean.

basin width away from the masked regions within the subtropical, extratropical and eastern tropical latitudes (Figure 8). Moreover, poleward of 50°N, the zonal extent of the LVB drops drastically, accounting for only a maximum of 50% in the eastern half of the basin.

Regarding the nature of the LVB, as expected, one notices that the geostrophic component of LVB is dominant for geostrophic flow north of about 30° (Figure 9(c)). There, the steeper isopycnal surfaces (contours in Figure 5) compared with the subtropical and tropical bands drive more intense geostrophic currents.

c. Lower tachocline-Deep Ocean

In the lower tachocline-deep ocean, the validity of the LVB holds over most of the basin except in the Gulf Stream, its adjacent recirculation region and the narrower regions of the abyssal sub-basins

within the tropics and mid-latitudes (Figures 8 and 10). The deep ocean upwelling and downwelling horizontal distribution is generally associated with negative and positive vortex stretching values, respectively, in contrast with the sign of this term in the upper ocean. Drawing a parallel with the upper tachocline within the upper ocean, the velocity field in the deep ocean, induced by the interaction of the varying topography and the horizontal circulation ocean bottom, diminishes towards shallower depths (see also Figure 2). This vertical shear matches the meridional transport direction in the areas where the LVB is valid within the deep ocean. In such proximity to the seabed, the isopycnal surfaces are highly influenced by the topography, promoting larger horizontal density gradients (closer and topography following contours in Figure 5 compared with Figure 6(a)). Note that the GLVB (hatched regions in panel (c)) characterise large fractions of the deep circulation, particularly those associated with steeper topography.

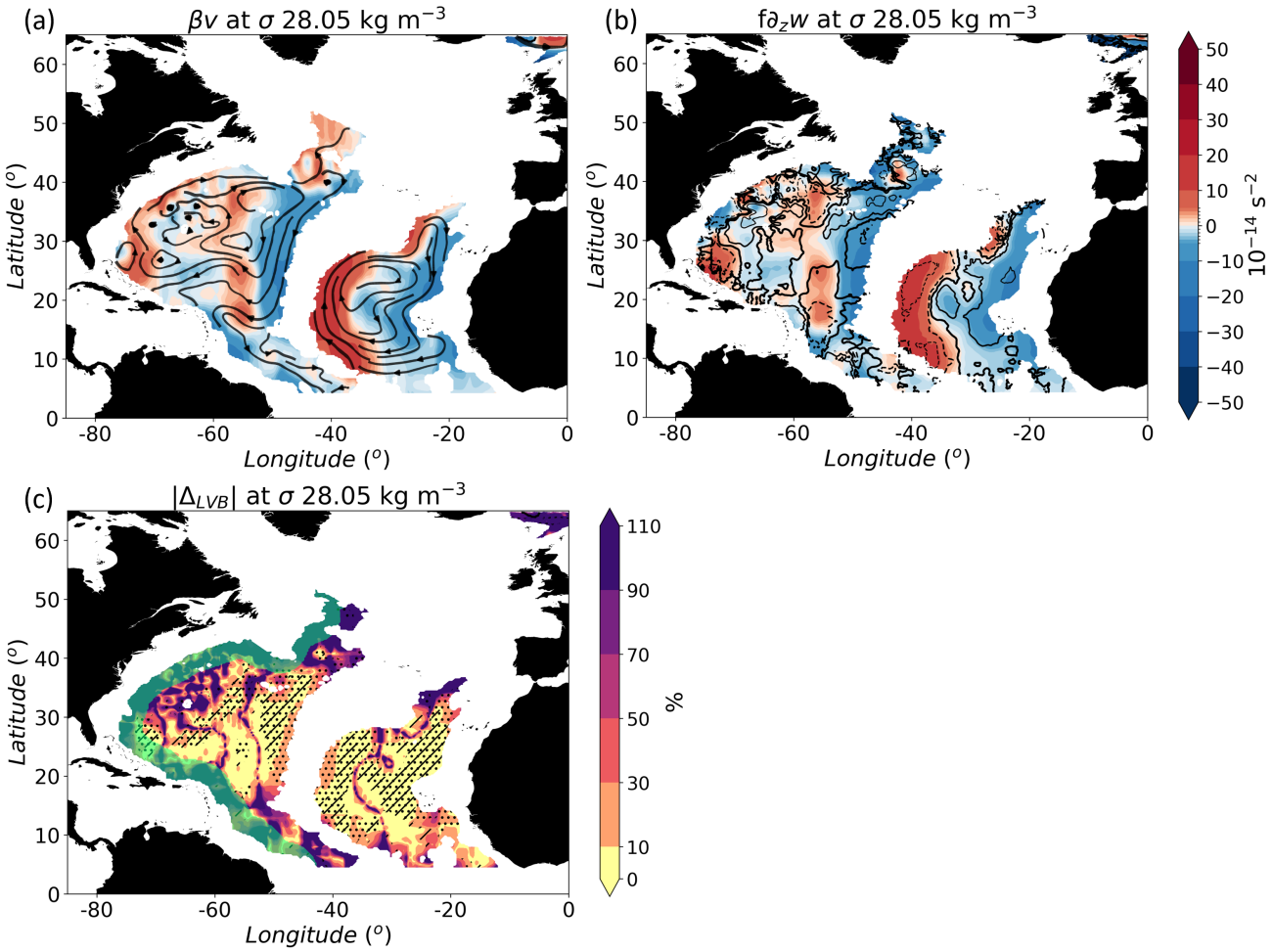

FIG. 10. Same as Figure 7 over σ 28.05 kg m^{-3}, representative example of the deep ocean.

d. Sensitivity to Averaged Period Length

The LVB validity analysis was conducted so far on the longest multidecadal climatological dataset available to us. However, it is often not feasible to obtain such a long time frame when using observations, reanalyses, or shorter runs. One limitation in the linear vorticity description of the ocean lies in the time required for the ocean adjustment, determined to first order by the propagation velocity of the first baroclinic Rossby wave, which decreases towards higher latitudes (Hughes and De Cuevas 2001; Wunsch 2011 and Thomas et al. 2014). Therefore, a sensitivity study as a function of the averaging period lengths and latitude is advocated.

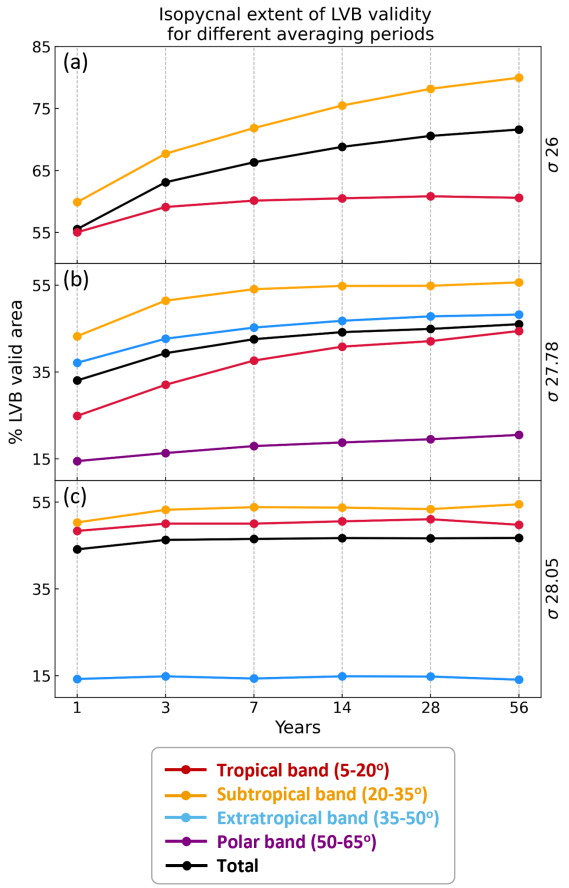

FIG. 11. Mean zonal extent (%) of LVB validity dependent on the averaged period over the 5-20°N, 20-35°N, 35-50°N, 50-65°N bands and the full basin over σ 26 (a), 27.78 (b) and 28.05 (c) kg m^{-3}.

In Figure 11, the temporal dependence of the LVB validity is assessed by computing its zonal extent as a function of the number of years in the climatology for three representative σ levels

in the unmasked region, and averaged meridionally over four different latitudinal bands. Within the upper tachocline, particularly the subtropical band, a large difference of about 20% is found between 1-year and 56-year climatologies, and each increment up to about 14 years significantly improves the results. Nevertheless, the extension of the LVB validity shows only a marginal increase of up to 7 years in the intermediate ocean and 3 years in the deep ocean. The decay of the extent of LVB validity in the upper tachocline is more noticeable in the subtropical band than in the tropical band (by a factor of ~ 4). However, the decrease in the validity extension within the intermediate ocean at shorter timescales is more pronounced in the tropics than in extratropics.

Our results, based on annual climatologies, assessed the spatiotemporal extension of the LVB and GLVB throughout the North Atlantic Basin. In the following section, we tackle the possibility of estimating vertical velocities using GLVB and observation-based meridional geostrophic velocity products by assessing the computation of such geostrophic component in our reference simulation.

5. Estimation of Vertical Velocities

a. 56-year average

Following the methodology presented in Section 2, we computed the geostrophic vertical velocity (w_{GLVB} hereafter) applying the Eq. 5 to the geostrophic meridional velocities and w_{Ek} (Figure 4 (b)) as surface boundary condition at an annual frequency. The multidecadal mean of w_{GLVB} is presented in Figure 12 over the three representative σ surfaces.

The w_{GLVB} field appears to be qualitatively similar to the reference OGCM output in the open ocean throughout the water column, as illustrated in Figure 12. It captures the horizontal patterns across most of the subtropical, extratropical and eastern tropical bands, far from the western boundary and the western part of the tropical band, where large LVB errors were observed. However, when quantitatively evaluating our estimate with the mean square error (RMSE) normalised by the 56-averaged target model output (RMSE/$\overline{w}$; contours in Figure 12), it shows significant amplitude biases.

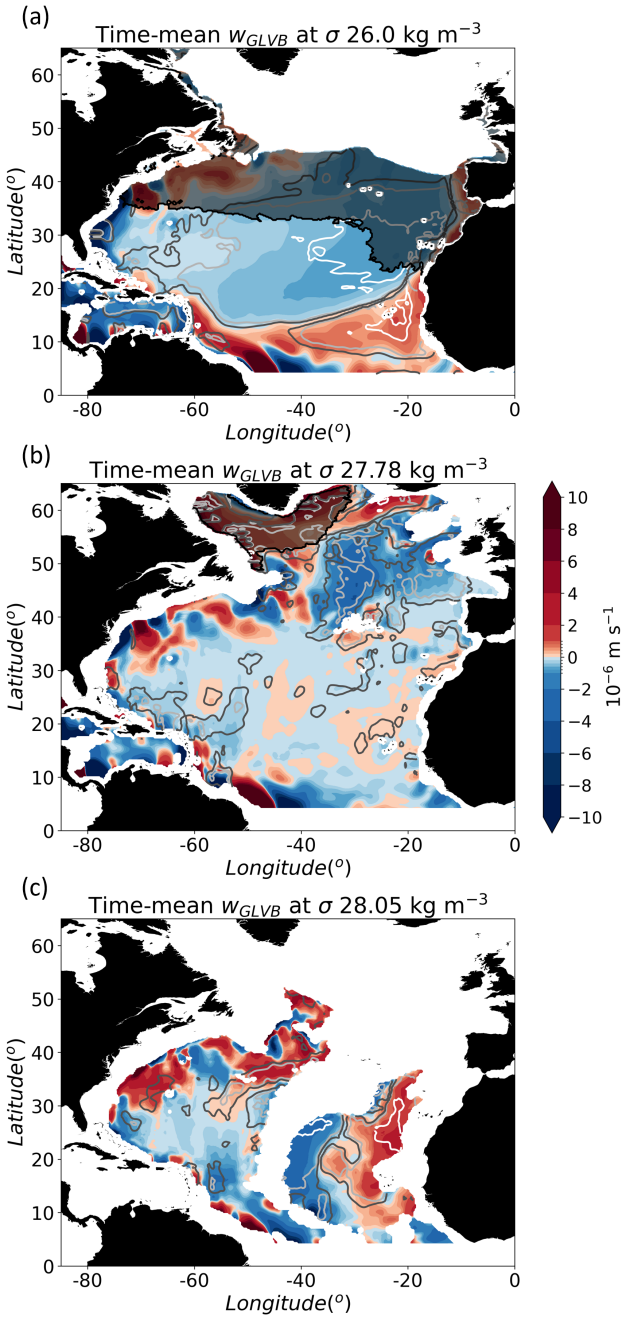

464 FIG. 12. 56-year averaged vertical velocity estimate (w_{GLVB}) and normalised RMSE (RMSE/$\overline{w}$; 0.1 (white),
465 0.5 (light grey), 1 (dark grey) contours) of w_{GLVB} estimate with OGCM w output over σ 26 (a), 27.78 (b) and
466 28.05 (c) kg m^{-3} using OGCM data. The black translucent region indicates the maximum mixed layer mask.
467 The equatorial band has been masked.

483 Within the upper tachocline, RMSE/$\overline{w}$ (contours in Figure 12(a)) shows values below 0.5 in
484 most of the STG and TG, with values above 1 found in the western boundaries and zonal tropical

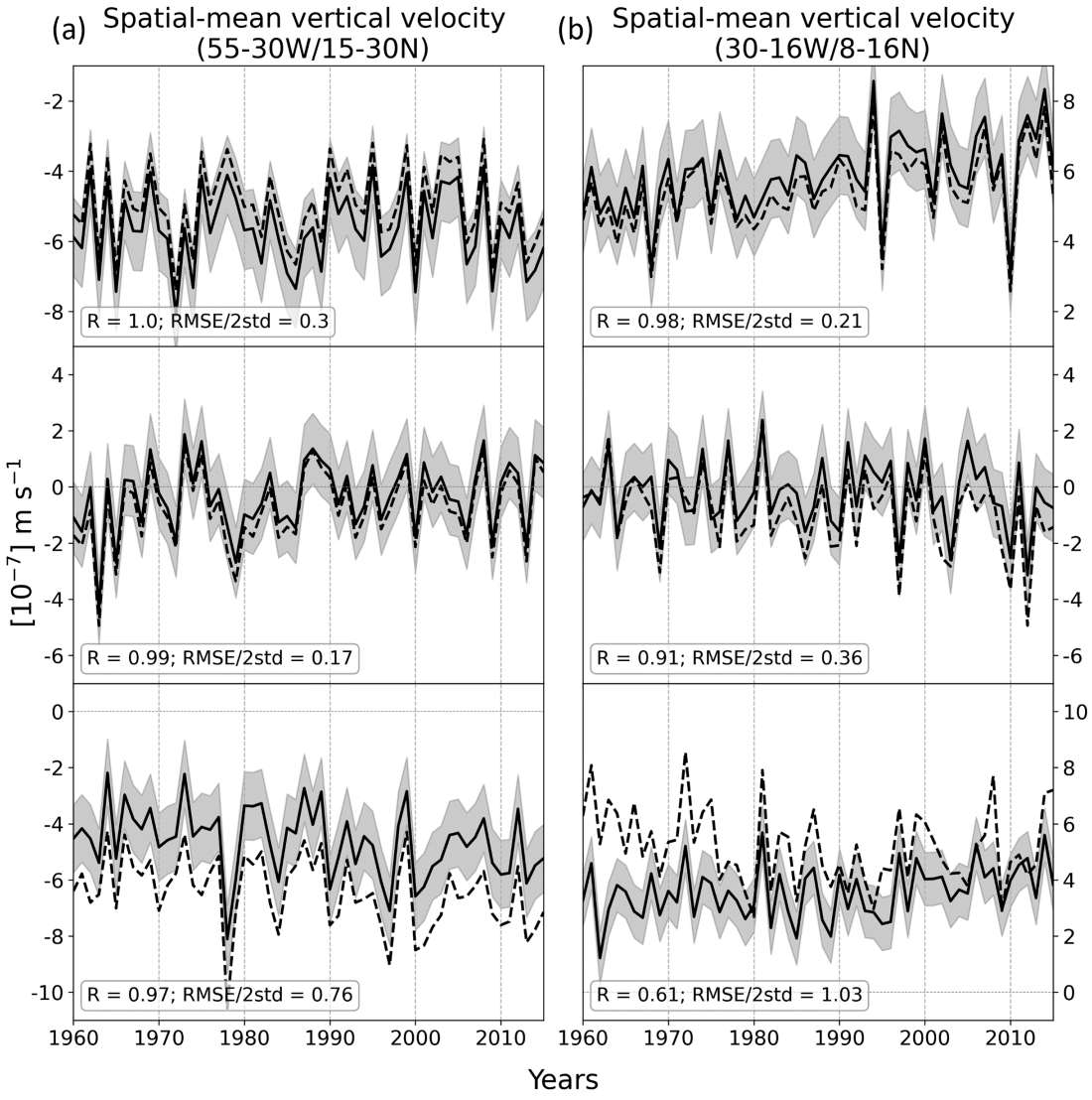

468 FIG. 13. Time series of the spatially averaged OGCM w (continuous line) and w_{GLVB} estimate (dashed line)
469 over the regions bounded by (55-30°W/15-30°N) (a) and (30-16°W/8-16°N) (b) at σ 26, 27.78 and 28.05 kg
470 m^{-3}. Shading represents the standard deviation of the OGCM w output.

485 currents where flow is not in GLVB. The bias exceeds the 56-year averaged reference within
486 most of the intermediate ocean (Figure 12 (b)). Only in some regions of the eastern part of the
487 extratropical bands the w_{GLVB} reproduce the vertical motion of the OGCM's simulation output with
488 a normalised RMSE smaller than 0.5. These regions in extratropical latitudes coincide with areas
489 described by GLVB (Figure 9(c)). The overall coherence of the deep vertical pathways between
490 the w_{GLVB} (Figure 12(c)) and the reference evidences the lesser influence of the Ekman forcing
491 compared with the bathymetry. However, w_{GLVB} fails in accurately reproducing the amplitude of

the OGCM w in most of the basin. Overall, despite the very satisfying qualitative agreement of the reconstruction, the relatively large biases indicate that while the geostrophic component of w establishes the order of magnitude of the total vertical flow, the ageostrophic component (coming from the ageostophic planetary vorticity advection and the non-linear contribution of the vorticity balance) is necessary to close the vorticity budget.

After analysing the average of the entire available period, the feasibility of employing the LVB at timescales shorter than the longest multidecadal climatological dataset available enables an exploration of the temporal dimension in the vertical velocity estimates.

b. Temporal Variability

Finally, we aim to determine the ability of the w_{GLVB} to capture the interannual variability. The interannual variability of the w_{GLVB} estimates and the reference over the three representative σ surfaces, considering two spatially-averaged example regions bounded by (55-30°W/15-30°N) and (30-16°W/8-16°N), is displayed in Figure 13 . Notably, the reconstruction accuracy is high in terms of the phase and amplitude of the variations. The correlation coefficients between w_{GLVB} and the model's w are above 0.9, except for the upwelling over the deep sigma surface. The biases between the w_{GLVB} and the OGCM w are now quantified concerning the variability amplitude using the RMSE normalised by the standard deviation (std) of the OGCM w (RMSE/std). The synchronisation between the time series and the amplitude of the interannual variability leads to an overall relative minor bias between the w_{GLVB} and OGCM output, except for the abysses. The remarkable reconstruction of the interannual variability of the total w field by the geostrophic LVB, even at periods shorter than the basin-crossing time scale, suggests that the estimated vertical velocities serve as a signal of propagating Rossby waves. The westward-propagating anomalies of sea surface height and w in the ocean interior within the subtropical band (not shown) are synchronised and exhibit a phase speed of approximately 5 cm s^{-1}, consistent with the characteristic phase speed of baroclinic Rossby waves at these latitudes (Chelton et al. 2007; Sanchez-Franks et al. 2021).

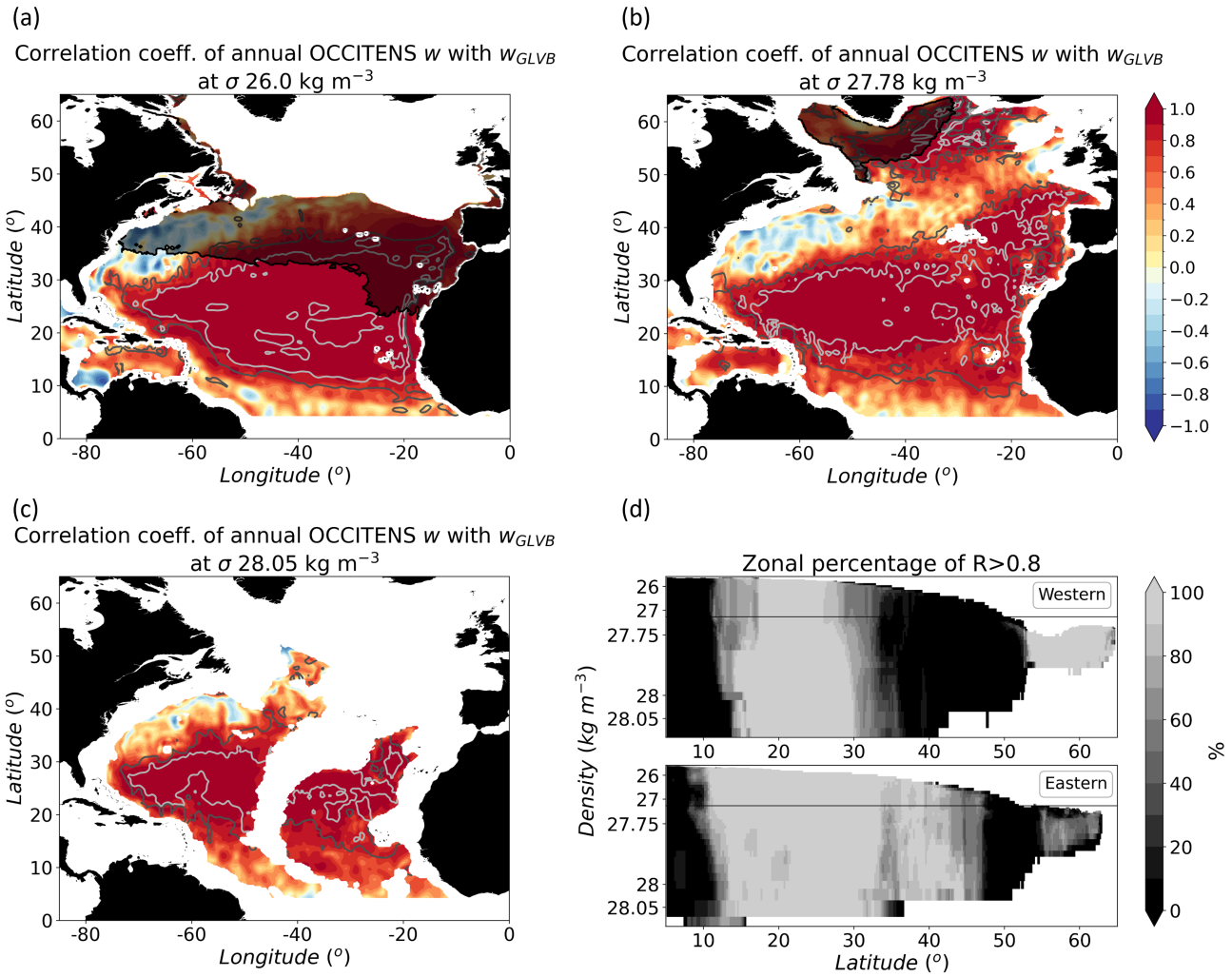

501 FIG. 14. Annual correlation coefficient (shading) and normalised RMSE (RMSE/std; white contours for 0.5,
502 black contours for 1) between the w_{GLVB} and the OGCM w output over σ (a) 26, (b) 27.78 and (c) 28.05 kg m^{-3}.
503 The black translucent region indicates the maximum mixed layer mask. The equatorial band has been masked.
504 (d) Zonal extent (%) of correlation coefficient values above 0.8 at each isopycnal surface level and latitudinal
505 grid point (surface and subsurface tropical band not represented) considering only the western (upper panel) and
506 eastern (lower panel) part of the North Atlantic basin defined by the Mid-Atlantic Ridge (Figure 6(b)) within the
507 unmasked region. The distance between σ levels on the y-axis is proportional to their average width within the
508 basin with a zoom between the surface and σ 27.1 kg m^{-3}.

526 Therefore, we now evaluate this accuracy over the entire North Atlantic Basin. Figure 14
527 quantifies the synchronisation between the fields by displaying the correlation coefficient and the
528 normalised RMSE (RMSE/std). In the subtropical band, both the upper and intermediate oceans

(Figure 14(a), (b)) exhibit correlation coefficients between w_{GLVB} and the model's w are above 0.8, excluding areas close to the western boundary, as well as the eastern tropical and polar bands. However, although the southwestern current between 40-50°N is in GLVB, the reproduced variability does not synchronise with the reference. In the deep ocean (Figure 14(c)), only the subtropical band maintains correlation coefficient values above 0.8. Within the upper tachocline, note the high correlation even in regions where the flow deviates significantly from the LVB, such as a large portion of the northeastern STG (Figure 14(a)) where the mixed layer reaches this sigma surface, also areas along the Africa coast from 12-20°N. High correlation values are also found in areas with large LVB errors in the deep ocean and in the east and subtropical intermediate ocean. The reconstruction of the interannual variability is, therefore, accurate over a much larger part of the ocean than expected.

However, the variability cannot be derived from the GLVB over two extensive regions characterised by low correlation. The first region encompasses the lower tropical band, extending up to 10°N within the upper tachocline and 15°N at the intermediate and deep ocean. The second region includes the flow near the Gulf Stream (between 35°-55°N in the western basin) and its northeastern extension into the open ocean, reaching the coasts of Northwest Europe (around 50°N in the eastern basin). These two regions exhibit much larger interannual variability than the region of high correlation. In fact, the ageostrophic circulation accounts for non-negligible interannual variability, preventing an accurate computation based on the GLVB.

Examining the whole water column (Figure 14(d)), high correlation is observed from top to bottom from about 12 to 15°N up to 30°N in the western part and near 45°N in the eastern part. Note that in the western part north 55°N, a narrow region in the open ocean bounded by the Mid-Atlantic Ridge and the mixed layer masked exhibit high values across the water column. Overall, these results evidence the paramount contribution of the geostrophic flow, specifically its meridional component, in dominating the interannual variability of the OGCM vertical circulation over the basin, except for the two regions of high ageostrophic variability: one in the deep tropics and the other along the diagonal band extending from Cape Hatteras and Northwest Europe.

One can interpret in two ways the fact that the reconstructed variability is accurate over larger regions than those in LVB. Either the ageostrophic component of w has a negligible contribution to the interannual variability, or it shares the same variability as the geostrophic w. Figure 13 shows an almost constant offset between time series across the observed period, suggesting that the ageostrophic component's influence on the interannual variability of w is negligible within these regions.

6. Discussion on the Relevance of the Linear Vorticity Balance for Interpreting the Ocean Circulation

The large domain within the upper tachocline in GLVB allowed us to explain the major currents of the North Atlantic by revisiting the principles of the linear theory of large-scale circulation. By flowing equatorward, the geostrophic component of currents like the NEC, the CC and the AC are divergent, absorbing downwelling Ekman Layer waters accordingly. To the contrary, poleward currents like the NECC and the MC converge and provide upper ocean waters to balance the divergent Ekman transport above, feeding the local TG upwelling. Thus, the applicability of the LVB suggests that the direction of the geostrophic meridional component of the flow of the upper tachocline is influenced by both the sign of the divergence of the Ekman transport above and the decrease in vertical velocity amplitude with depth across the upper tachocline. This latter view corresponds to the classic interpretation of the Sverdrup balance when applied to the upper ocean.

The LVB brings a novel baroclinic analysis of the classical barotropic description of the ocean made by the Sverdrup balance. However, let's recall that the Sverdrup balance needs the LVB and proper boundary conditions. The extensive areas within the upper tachocline identified in LVB are comparable to valid regions observed in Sverdrup balance studies using reanalyses (Wunsch 2011 and Thomas et al. 2014) or observation-based dataset (Gray and Riser 2014). Nevertheless, the eastern part of the TG, described by the LVB in this study, does not satisfy the Sverdrup balance according to previous studies such as Wunsch (2011) and Gray and Riser (2014). Such apparent contradiction for flow in LVB occurs when the w field, chosen as boundary condition to close the Sverdrup balance, is inaccurately estimated. This poorly constrained boundary w field is often at the bottom thermocline (e.g. Kounta et al. 2018), but it can also be the surface w field. The latter

generally suffers from considering the Ekman pumping as the sole contributor to the vertical flow in the Ekman layer while neglecting the contribution of the β-plane geostrophic divergence, as explained in the present study.

The departure from the LVB at the large spatiotemporal scales analysed in the present paper can be only explained by the importance of non-linear terms in the vorticity balance (Eq. 2). Previous researchers have turned to a barotropic approach to investigate their contribution. Numerous studies have studied the barotropic vorticity balance (BVB) to address the vorticity source and sink mechanisms that the Sverdrupian description of the ocean cannot fully account for.

In both the Gulf Stream region and the SPG, the LVB does not hold along the entire water column (panels (c) in Figures 7, 9 and 10). In these areas, additional terms are needed to close the vorticity budget. In the Gulf Stream, the bottom pressure torque (BPT) effectively balances the barotropic planetary vorticity advection, with the wind forcing being negligible (e.g. Hughes and De Cuevas 2001, Gula et al. 2015 and Schoonover et al. 2016). Regarding the SPG, Le Corre et al. (2020) demonstrates that the bathymetry forcing (bottom drag curl) and atmospheric forcing, although with lesser influence, are needed to balance the BPT contribution. The observed reduction in the validity extent of the LVB at shorter timescales, visible in Figure 11, may be attributed to the influence of small-scale non-linear flows within the open ocean. Similarly, a model study by Khatri et al. 2023 evidences an increase in non-linear dynamics when diminishing the scale of the low-pass filter. These results are coherent with the fact that oceanic flows' temporal and spatial dimensions often vary with a certain level of proportionality (e.g. Dickey 1991). A key question remains whether OGCM grid's spatial resolution might change the vorticity balance significantly, even after low-pass space filtering. Ongoing research on the vorticity equation in a high-resolution OGCM suggests that the non-linear advection term is responsible for the first-order balancing of the LVB residual across the upper ocean (J. Gula, personal communication, 2023).

Over a substantial portion of the open ocean STG where we have shown that the LVB holds, previous studies (e.g., Khatri et al. 2023 or Sonnewald et al. 2019) evidence the necessity of the

BPT to close the vorticity budget. To further compare our baroclinic results with barotropic studies, we may also refer to studies considering the depth integration of the vorticity balance (DIVB; see Waldman and Giordani (2023)). In Waldman and Giordani (2023), a comparison between the BVB and DIVB approaches supports the equivalence at first order between the bottom pressure torque (BPT) term and the bottom vortex stretching (fw_b; where w_b is the vertical velocity at the bottom of the ocean, being the bottom boundary condition of the $f\partial_z w$ term). The mainly geostrophic horizontal velocities at the deep ocean close to the lateral boundaries (dotted surfaces in Figure 10(c)), together with the minimal contribution of non-linear terms to the deep ocean vorticity budget (small $|\Delta_{LVB}|$ in Figure 10(c)), allows considering that the BPT is equal to the bottom vortex stretching (Zhang and Vallis 2007). Consequently, the large volume of tropical and subtropical ocean explained by the LVB throughout the water column aligns with the regions where the Sverdrup and Topographic Sverdrup (where BPT closes the Sverdrup balance budget; Holland (1967)) balances hold within the open ocean (Khatri et al. 2023).

7. Conclusions

In this numerical study based on an eddy-permitting OGCM simulation, we have shown that the linear vorticity balance (LVB) approximation, spatially filtered with a 5° low-pass filter and averaged over 56 years, is valid within the upper ocean across most of the STG and eastern TG. The dominance of the LVB diminishes in the intermediate ocean, particularly at tropical latitudes and the western half of the basin. In the deep ocean, the topography-induced circulation is largely explained by the LVB, notably over the abyssal plains. Throughout the entire water column, significant departures from the balance are observed in the Gulf Stream region, the equatorial band, the subpolar gyre, and regions with a mainly zonal flow. Here, the vorticity equation can no longer be assumed linear, and the non-linear terms, not studied in the present work, become essential to close the vorticity budget. Over the upper ocean, the mainly geostrophic nature of the LVB determines how the meridional component of the flow responds to the geostrophic vertical divergence. However, the geostrophic LVB holds over more limited extensions within the intermediate ocean and the deep tachocline, reducing its a priori usefulness in deriving the geostrophic w from the geostrophic flow below the upper tachocline.

The duration of the averaging period conditions the occurrence of the LVB, although not in a uniform way. A general degradation in the extent of LVB validity occurs when the average period is reduced, with the maximum reduction observed being 20% within the upper ocean. This reduction may be attributed to the enhancement of small-scale structures at shorter timescales. Nevertheless, the increase in LVB-valid extension becomes marginal after several decades, decreasing to 3 years in the intermediate and deep ocean.

The extensive validity of the geostrophic LVB within the upper and lower tachoclines implies that the linear theory of large-scale circulation offers a simple yet reliable explanation for the direction of the meridional geostrophic flow. In the upper tachocline, a convergent (divergent) flow is needed to feed (absorb) the Ekman layer's upward (downward) pumping. This condition, in turn, establishes the direction of the geostrophic meridional flow since only the poleward (equatorward) flows are convergent (divergent). It corresponds to the mere satisfaction of the continuity equation for geostrophic circulation. A similar interpretation can be applied to circulation in vast portions of the deep ocean tachocline when considering the sign of the bottom vertical velocity.

The large percentage of the basin explained by the geostrophic LVB has supported the effort to develop a methodology for estimating the three-dimensional geostrophic w field by vertically integrating the geostrophic meridional velocities from the ocean surface. In this study, we have underlined the critical role of the geostrophic flow divergence across the Ekman layer when computing the Ekman pumping at the surface. In climatological mean, the reconstructed geostrophic w (w_{GLVB}) captures at first order the reference w horizontal patterns in the ocean interior below the maximum mixed layer over the tropical, subtropical and extratropical bands, excluding the equatorial band, the Gulf Stream and the subpolar gyre. However, the reconstructed w does not accurately match the model's output in terms of amplitude, which prevents its use for quantitative analyses of the role of time-mean vertical currents.

To the contrary, w_{GLVB} effectively captures the interannual variability of the reference w over most of the basin throughout the entire water column far from the Gulf Stream, the North Atlantic

Current, and the low tropical band. Therefore, the geostrophic meridional velocities appear to be sufficient to compute the interannual variability of the velocity field to first order over a significant part of the open ocean. The discrepancies between assessing the 56-year average and interannual variability of the vertical velocity field in the open ocean have revealed the dominant role of the geostrophic component of the vertical velocity in the interannual variability. Conversely, the ageostrophic component plays a minor role in the interannual variability but exhibits an important contribution to the time-mean amplitude. Nevertheless, in the Gulf Stream, North Atlantic Current and the low tropics, the ageostrophic circulation mainly controls both the interannual variability and time-mean amplitude of the vertical flow.

It is left to future projects to assess how non-linear terms could improve the accuracy of the baroclinic vorticity balance in describing the ocean flow. Our OGCM study suggests that the geostrophic LVB could serve as a powerful tool to estimate the interannual variability of the upper tachocline vertical movements using observation-based geostrophic meridional velocities away from the specific regions identified in the OGCM. Consequently, an observation-based w product might potentially offer valuable insights into the interannual variations of the physical and biogeochemical advective fluxes in the real-world upper ocean.

Acknowledgments. We kindly thank Juliette Mignot, Gilles Reverdin and Diana Ruiz-Pino who have read and commented on versions of this paper. This work was supported by the INSU LEFE Mercator.

Data availability statement. The outputs of the OCCITENS simulation used in the current study to estimate the neutral density and geostrophic velocity fields, the Linear Vorticity Balance terms, the Ekman pumping vertical velocity, and w_{GLVB} are available upon request. Please contact Thierry Penduff at thierry.penduff@cnrs.fr.

References

Arístegui, J., and Coauthors, 2009: Sub-regional ecosystem variability in the canary current upwelling. *Progress in Oceanography*, **83 (1-4)**, 33–48.

Bessières, L., and Coauthors, 2017: Development of a probabilistic ocean modelling system based on nemo 3.5: application at eddying resolution. *Geoscientific Model Development*, **10 (3)**, 1091–1106.

Bubnov, V. A., 1987: Vertical motions in the central equatorial pacific. *Oceanologica Acta, Special issue*.

Buongiorno Nardelli, B., 2020: A multi-year time series of observation-based 3d horizontal and vertical quasi-geostrophic global ocean currents. *Earth System Science Data*, **12 (3)**, 1711–1723.

Buongiorno Nardelli, B., S. Mulet, and D. Iudicone, 2018: Three-dimensional ageostrophic motion and water mass subduction in the southern ocean. *Journal of Geophysical Research: Oceans*, **123 (2)**, 1533–1562.

Cessi, P., and C. L. Wolfe, 2013: Adiabatic eastern boundary currents. *Journal of physical oceanography*, **43 (6)**, 1127–1149.

Charney, J., 1955: The generation of oceanic currents by wind. https://doi.org/https://elischolar.library.yale.edu/journal_of_marine_research/858.

Chelton, D. B., M. G. Schlax, R. M. Samelson, and R. A. de Szoeke, 2007: Global observations of large oceanic eddies. *Geophysical Research Letters*, **34 (15)**.

706 Christensen, K. M., A. Gray, and S. Riser, 2023: Global estimates of mesoscale vertical velocity near 1000 m from argo observations. *Authorea Preprints*, https://doi.org/10.22541/essoar.168500356.69644187/v1.

709 Comby, C., S. Barrillon, J.-L. Fuda, A. M. Doglioli, R. Tzortzis, G. Grégori, M. Thyssen, and A. A. Petrenko, 2022: Measuring vertical velocities with adcps in low-energy ocean. *Journal of Atmospheric and Oceanic Technology*, **39 (11)**, 1669–1684, https://doi.org/doi.org/10.1175/JTECH-D-21-0180.1.

713 Dickey, T. D., 1991: The emergence of concurrent high-resolution physical and bio-optical measurements in the upper ocean and their applications. *Reviews of Geophysics*, **29 (3)**, 383–413.

715 Drake, H. F., R. Ferrari, and J. Callies, 2020: Abyssal circulation driven by near-boundary mixing: Water mass transformations and interior stratification. *Journal of Physical Oceanography*, **50 (8)**, 2203–2226.

718 Dussin, R., B. Barnier, L. Brodeau, and J. M. Molines, 2016: Drakkar forcing set dfs5. *MyOcean Report*.

720 Ekman, V. W., 1905: On the influence of the earth's rotation on ocean-currents.

721 Elmoussaoui, A., M. Arhan, and A.-M. Tréguier, 2005: Model-inferred upper ocean circulation in the eastern tropics of the north atlantic. *Deep Sea Research Part I: Oceanographic Research Papers*, **52 (7)**, 1093–1120.

724 Fernandes, M., C. Lázaro, A. Santos, and P. Oliveira, 2005: Oceanographic characterization of the cape verde region using multisensor data. *Envisat & ERS Symposium*, Vol. 572.

726 Freeland, H. J., 2013: Vertical velocity estimates in the north pacific using argo floats. *Deep Sea Research Part II: Topical Studies in Oceanography*, **85**, 75–80.

728 Garcia-Jove, M., B. Mourre, N. D. Zarokanellos, P. F. Lermusiaux, D. L. Rudnick, and J. Tintoré, 2022: Frontal dynamics in the alboran sea: 2. processes for vertical velocities development. *Journal of Geophysical Research: Oceans*, **127 (3)**, e2021JC017 428.

731 Giglio, D., D. Roemmich, and B. Cornuelle, 2013: Understanding the annual cycle in global steric height. *Geophysical research letters*, **40 (16)**, 4349–4354.

Gill, A. E., 1982: *Atmosphere-ocean dynamics*. Academic press, 662 pp.

Giordani, H., L. Prieur, and G. Caniaux, 2006: Advanced insights into sources of vertical velocity in the ocean. *Ocean Dynamics*, **56 (5)**, 513–524.

Gordon, A. L., 1981: South atlantic thermocline ventilation. *Deep Sea Research Part A. Oceanographic Research Papers*, **28 (11)**, 1239–1264.

Gray, A. R., and S. C. Riser, 2014: A global analysis of sverdrup balance using absolute geostrophic velocities from argo. *Journal of Physical Oceanography*, **44 (4)**, 1213–1229.

Guinehut, S., A.-L. Dhomps, G. Larnicol, and P.-Y. Le Traon, 2012: High resolution 3-d temperature and salinity fields derived from in situ and satellite observations. *Ocean Science*, **8 (5)**, 845–857.

Gula, J., M. J. Molemaker, and J. C. McWilliams, 2015: Gulf stream dynamics along the southeastern us seaboard. *Journal of Physical Oceanography*, **45 (3)**, 690–715.

Halpern, D., and H. P. Freitag, 1987: Vertical motion in the upper ocean of the equatorial eastern pacific. *Oceanologica Acta, Special Issue*.

Halpern, D., R. A. Knox, D. S. Luther, and S. G. H. Philander, 1989: Estimates of equatorial upwelling between 140 and 110 w during 1984. *Journal of Geophysical Research: Oceans*, **94 (C6)**, 8018–8020.

Holland, W. R., 1967: On the wind-driven circulation in an ocean with bottom topography. *Tellus*, **19 (4)**, 582–600.

Huang, R. X., and S. Russell, 1994: Ventilation of the subtropical north pacific. *Journal of Physical Oceanography*, **24 (12)**, 2589–2605.

Hughes, C. W., and B. A. De Cuevas, 2001: Why western boundary currents in realistic oceans are inviscid: A link between form stress and bottom pressure torques. *Journal of Physical Oceanography*, **31 (10)**, 2871–2885.

Jackett, D. R., T. J. McDougall, R. Feistel, D. G. Wright, and S. M. Griffies, 2006: Algorithms for density, potential temperature, conservative temperature, and the freezing temperature of seawater. *Journal of Atmospheric and Oceanic Technology*, **23 (12)**, 1709–1728.

760 Khatri, H., S. M. Griffies, B. A. Storer, M. Buzzicotti, M. Aluie, Hussein nd Sonnewald, R. Dussin,
761 and A. Shao, 2023: A scale-dependent analysis of the barotropic vorticity budget in a global
762 ocean simulation. *Journal of Advances in Modeling Earth System (JAMES)*.

763 Klein, B., and G. Siedler, 1989: On the origin of the azores current. *Journal of Geophysical*
764 *Research: Oceans*, **94 (C5)**, 6159–6168.

765 Koelling, J., U. Send, and M. Lankhorst, 2020: Decadal strengthening of interior flow of north
766 atlantic deep water observed by grace satellites. *Journal of Geophysical Research: Oceans*,
767 **125 (11)**, e2020JC016 217.

768 Kounta, L., X. Capet, J. Jouanno, N. Kolodziejczyk, B. Sow, and A. T. Gaye, 2018: A model
769 perspective on the dynamics of the shadow zone of the eastern tropical north atlantic–part 1: the
770 poleward slope currents along west africa. *Ocean Science*, **14 (5)**, 971–997.

771 Lazar, A., T. Inui, P. Malanotte-Rizzoli, A. J. Busalacchi, L. Wang, and R. Murtugudde, 2002:
772 Seasonality of the ventilation of the tropical atlantic thermocline in an ocean general circulation
773 model. *Journal of Geophysical Research: Oceans*, **107 (C8)**, 18–1.

774 Le Bras, I. A.-A., M. Sonnewald, and J. M. Toole, 2019: A barotropic vorticity budget for the
775 subtropical north atlantic based on observations. *Journal of Physical Oceanography*, **49 (11)**,
776 2781–2797.

777 Le Corre, M., J. Gula, and A.-M. Tréguier, 2020: Barotropic vorticity balance of the north atlantic
778 subpolar gyre in an eddy-resolving model. *Ocean Science*, **16 (2)**, 451–468.

779 Levin, L. A., and Coauthors, 2019: Global observing needs in the deep ocean. *Frontiers in Marine*
780 *Science*, **6**, 241.

781 Liang, X., M. Spall, and C. Wunsch, 2017: Global ocean vertical velocity from a dynamically
782 consistent ocean state estimate. *Journal of Geophysical Research: Oceans*, **122 (10)**, 8208–8224.

783 Lu, Y., and D. Stammer, 2004: Vorticity balance in coarse-resolution global ocean simulations.
784 *Journal of physical oceanography*, **34 (3)**, 605–622.

785 Madec, G., and Coauthors, 2017: Nemo ocean engine.

Marshall, J., and R. Plumb, 2007: Atmosphere, ocean and climate dynamic, an introduction. Academic Press New York.

Mulet, S., M.-H. Rio, A. Mignot, S. Guinehut, and R. Morrow, 2012: A new estimate of the global 3d geostrophic ocean circulation based on satellite data and in-situ measurements. *Deep Sea Research Part II: Topical Studies in Oceanography*, **77**, 70–81.

Munk, W. H., 1966: Abyssal recipes. *Deep sea research and oceanographic abstracts*, Elsevier, Vol. 13, 707–730, https://doi.org/doi.org/10.1016/0011-7471(66)90602-4.

Ollitrault, M., and A. C. De Verdière, 2014: The ocean general circulation near 1000-m depth. *Journal of Physical Oceanography*, **44 (1)**, 384–409.

Pedlosky, J., 1979: *Geophysical Fluid Dynamics*. Springer New York, 710 pp.

Pedlosky, J., 1996: *Ocean circulation theory*. Springer Science & Business Media.

Robinson, A., and H. Stommel, 1959: The oceanic thermocline and the associated thermohaline circulation 1. *Tellus*, **11 (3)**, 295–308, https://doi.org/https://.

Roemmich, D., 1983: The balance of geostrophic and ekman transports in the tropical atlantic ocean. *Journal of Physical Oceanography*, **13 (8)**, 1534–1539.

Rossby, T., 1996: The north atlantic current and surrounding waters: At the crossroads. *Reviews of Geophysics*, **34 (4)**, 463–481.

Ruiz, S., and Coauthors, 2019: Effects of oceanic mesoscale and submesoscale frontal processes on the vertical transport of phytoplankton. *Journal of Geophysical Research: Oceans*, **124 (8)**, 5999–6014.

Salmon, R., 1982: The shape of the main thermocline. *Journal of Physical Oceanography*, **12 (12)**, 1458–1479.

Sanchez-Franks, A., E. Frajka-Williams, B. I. Moat, and D. A. Smeed, 2021: A dynamically based method for estimating the atlantic meridional overturning circulation at 26° n from satellite altimetry. *Ocean Science*, **17 (5)**, 1321–1340.

Schmitz Jr, W. J., and M. S. McCartney, 1993: On the north atlantic circulation. *Reviews of Geophysics*, **31 (1)**, 29–49.

Schoonover, J., and Coauthors, 2016: North atlantic barotropic vorticity balances in numerical models. *Journal of Physical Oceanography*, **46 (1)**, 289–303.

Schott, F. A., P. Brandt, M. Hamann, J. Fischer, and L. Stramma, 2002: On the boundary flow off brazil at 5–10 s and its connection to the interior tropical atlantic. *Geophysical Research Letters*, **29 (17)**, 21–1.

Schott, F. A., J. P. McCreary Jr, and G. C. Johnson, 2004: Shallow overturning circulations of the tropical-subtropical oceans. *Washington DC American Geophysical Union Geophysical Monograph Series*, **147**, 261–304.

Schott, F. A., and H. Stommel, 1978: Beta spirals and absolute velocities in different oceans. *Deep Sea Research*, **25 (11)**, 961–1010, https://doi.org/doi.org/10.1016/0146-6291(78)90583-0.

Sévellec, F., A. N. Garabato, J. Brearley, and K. Sheen, 2015: Vertical flow in the southern ocean estimated from individual moorings. *Journal of Physical Oceanography*, **45 (9)**, 2209–2220.

Sonnewald, M., C. Wunsch, and P. Heimbach, 2019: Unsupervised learning reveals geography of global ocean dynamical regions. *Earth and Space Science*, **6 (5)**, 784–794.

Spence, P., O. A. Saenko, W. Sijp, and M. England, 2012: The role of bottom pressure torques on the interior pathways of north atlantic deep water. *Journal of Physical Oceanography*, **42 (1)**, 110–125.

Stommel, H., and A. Arons, 1959: On the abyssal circulation of the world ocean—i. stationary planetary flow patterns on a sphere. *Deep Sea Research (1953)*, **6**, 140–154.

Stommel, H., and F. Schott, 1977: The beta spiral and the determination of the absolute velocity field from hydrographic station data. *Deep Sea Research*, **24 (3)**, 325–329, https://doi.org/doi.org/10.1016/0146-6291(77)93000-4.

Stramma, L., 1984: Geostrophic transport in the warm water sphere of the eastern subtropical north atlantic. *Journal of Marine Research*, **42 (3)**, 537–558.

Stramma, L., and M. England, 1999: On the water masses and mean circulation of the south atlantic ocean. *Journal of Geophysical Research: Oceans*, **104 (C9)**, 20 863–20 883.

Stramma, L., M. Rhein, P. Brandt, M. Dengler, C. Böning, and M. Walter, 2005: Upper ocean circulation in the western tropical atlantic in boreal fall 2000. *Deep Sea Research Part I: Oceanographic Research Papers*, **52 (2)**, 221–240.

Sverdrup, H. U., 1947: Wind-driven currents in a baroclinic ocean; with application to the equatorial currents of the eastern pacific. *Proceedings of the National Academy of Sciences*, **33 (11)**, 318–326.

Tailleux, R., 2023: On the determination of the 3d velocity field in terms of conserved variables in a compressible ocean. *Fluids*, **8 (3)**, 94, https://doi.org/doi.org/10.3390/fluids8030094.

Tailleux, R., and J. C. McWilliams, 2001: The effect of bottom pressure decoupling on the speed of extratropical, baroclinic rossby waves. *Journal of physical oceanography*, **31 (6)**, 1461–1476.

Thomas, M. D., A. M. De Boer, H. L. Johnson, and D. P. Stevens, 2014: Spatial and temporal scales of sverdrup balance. *Journal of Physical Oceanography*, **44 (10)**, 2644–2660.

Tomczak, M., and J. S. Godfrey, 1994: The coriolis force, geostrophy, rossby waves and the westward intensification. *Regional Oceanography*, M. Tomczak, and J. S. Godfrey, Eds., Pergamon, 29–37.

Vallis, G., 2006: *Atmospheric and Oceanic Fluid Dynamics: Fundamentals and Large-scale Circulation*. Cambridge University Press.

Waldman, R., and H. Giordani, 2023: Ocean barotropic vorticity balances: theory and application to numerical models. *Journal of Advances in Modeling Earth Systems*, **15 (4)**, e2022MS003 276.

Weingartner, T. J., and R. H. Weisberg, 1991: On the annual cycle of equatorial upwelling in the central atlantic ocean. *Journal of Physical Oceanography*, **21 (1)**, 68–82.

Wunsch, C., 1984: An estimate of the upwelling rate in the equatorial atlantic based on the distribution of bomb radiocarbon and quasi-geostrophic dynamics. *Journal of Geophysical Research: Oceans*, **89 (C5)**, 7971–7978.

Wunsch, C., 2011: The decadal mean ocean circulation and sverdrup balance. *Journal of Marine Research*, **69 (2-3)**, 417–434.

865 Wyrtki, K., 1961: The thermohaline circulation in relation to the general circulation in the
866 oceans. *Deep Sea Research (1953)*, **8 (1)**, 39–64, https://doi.org/doi.org/10.1016/0146-6313(61)
867 90014-4.

868 Wyrtki, K., 1981: An estimate of equatorial upwelling in the pacific. *Journal of Physical Oceanog-*
869 *raphy*, **11 (9)**, 1205–1214.

870 Xie, L., and W. W. Hsieh, 1995: The global distribution of wind-induced upwelling. *Fisheries*
871 *Oceanography*, **4 (1)**, 52–67.

872 Yeager, S., 2015: Topographic coupling of the atlantic overturning and gyre circulations. *Journal*
873 *of Physical Oceanography*, **45 (5)**, 1258–1284.

874 Zhang, R., and G. K. Vallis, 2007: The role of bottom vortex stretching on the path of the north
875 atlantic western boundary current and on the northern recirculation gyre. *Journal of Physical*
876 *Oceanography*, **37 (8)**, 2053–2080.

B

Appendix B: Supplementary Materials

B.1 Distance-to-Shore Filter

In Section 3.2.1.2.2, a sensitivity analysis was conducted to assess the LVB's capability to describe the North Atlantic's dynamics across the entire water column. Figure 3.3 illustrates the percentage of valid areas for the LVB at each isopycnal level for spatially averaged displacements ranging from 1 to 7°. Furthermore, an additional case, which was not included in the version submitted to the JPO journal, involves the application of a filter based on the distance to the coast (Figure B.1). The motivation behind this filter is to optimize the results obtained with uniform filters.

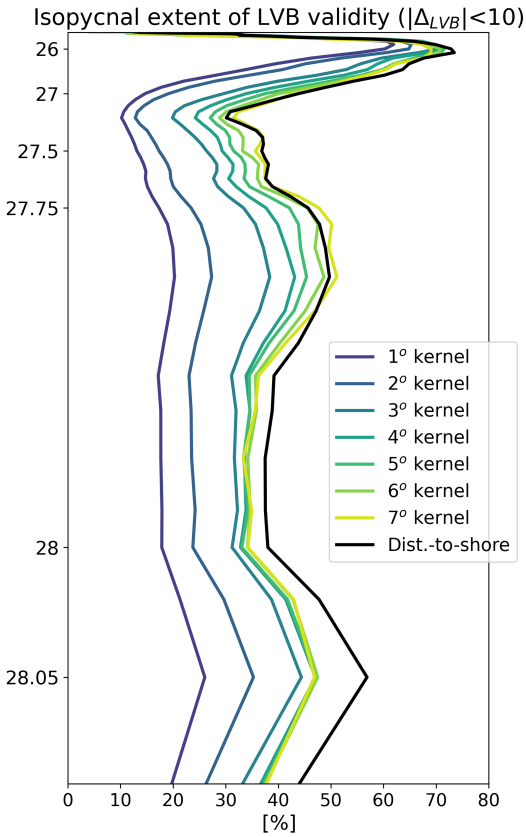

Figure B.1: 56-year average LVB validity extent (%) over isopycnal levels in the unmasked region outside the 4° width band from the western boundary, as a function of spatial smoothing size from 1 to 7 ° kernel.

A two-step filter has been applied to enhance the performance of the LVB in describing large-scale oceanic structures. The first step involves suppressing high-frequency spatial noise that appears in the original output and bringing w closer to v. The second step implies filtering out structures that are too small for LVB. This first filter is based on a running mean of 1° over w. Once filtered, the w spatial structures are of comparable size to those of the meridional velocity field. The LVB terms (Eq. 3.1) are then calculated. Before computing Δ_{LVB} (Eq. 3.4), another spatial filter is applied over isopycnal surfaces. Being $I(x, y, z)$ any term from the LVB expression, the smoothed field ($I_l(x, y, z)$) can be retrieved applying a discrete convolution:

$$I_l(x, y, z) = I(x, y, x) * K_l \tag{B.1}$$

The normalized variable kernel (K_l) smooths out scales smaller than l with a minimum filtering of 2° near the coast and the equator, and maximum filtering of 7° in the open ocean (Figure B.2). At the same time, each point within the normalized kernel ($\int_l k_l = 1$) is weighted depending on the distance to the shore, being heavier for the mean, the points furthest from the boundaries (Figure B.3). Employing the distance-to-shore dependent filter makes it possible to enlarge the LVB valid areas everywhere, particularly in the intermediate and abyssal oceans, while constraining the error from the lateral boundaries to its source regions. Note that the discrete convolution maintains the size of the initial field without considering NaN elements from the lateral boundaries.

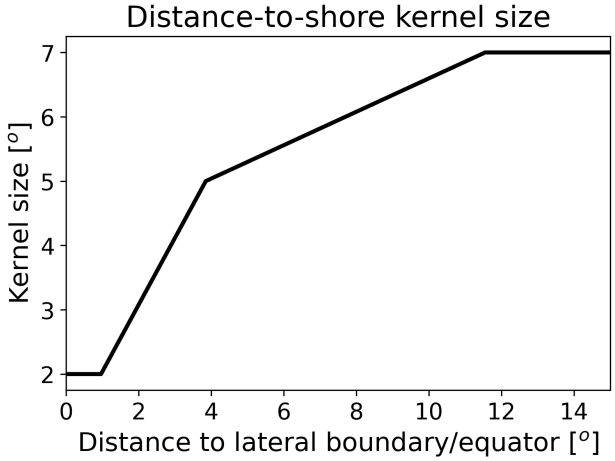

Figure B.2: Size kernel dependent on the absolute distance to the equator and lateral boundaries for the distance-to-shore filter.

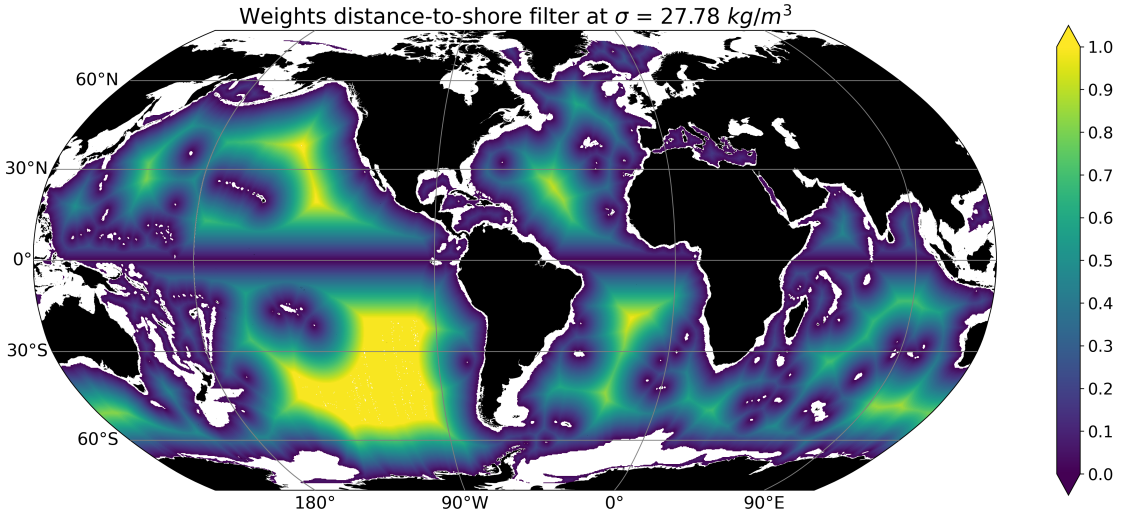

Figure B.3: Example of the distance to lateral boundaries and equator dependent weights normalized to the North Atlantic basin for σ 27.78 kg m^{-3}.

B.2 Derivation of the Depth-Integrated Vorticity Balance (DIVB)

The ocean's four-dimensional vorticity budget is retrieved by taking the curl of the Navier-Stokes equations for momentum and applying the Bousinesq approximation.

$$\frac{\partial(1.5)}{\partial x} - \frac{\partial(1.4)}{\partial y} \tag{B.2}$$

The vorticity balance equation then arises after considering the continuity equation:

$$\partial_t \zeta + \beta v + \mathbf{u}\nabla\zeta + [(\partial_x w \partial_z v) - (\partial_y w \partial_z u)] = (f+\zeta)\partial_z w + \frac{1}{\rho}\nabla \times [\rho A_h \nabla^2 \mathbf{u}_H + \rho A_v \partial_z^2 \mathbf{u}_H] \tag{B.3}$$

The pressure-dependent momentum terms that appear in Eqs. 1.4 and 1.5 cancel each other out. Integrating from the surface to the seabead the Depth-Integrated Vorticity Balance (DIVB) is retrieved:

$$\overline{\frac{\partial \zeta}{\partial t}} + \beta V + \overline{\mathbf{u}\nabla\zeta} + \overline{\hat{\mathbf{k}}(\nabla_h w \times \partial_z \mathbf{u}_h)} = -f w_b + \overline{\zeta \partial_z w} + \overline{\frac{1}{\rho}\nabla \times [\rho A_h \nabla^2 \mathbf{u}_h]} + \overline{\frac{1}{\rho}\nabla \times [\rho A_v \partial_z^2 \mathbf{u}_h]} \tag{B.4}$$

Therefore, there is no equivalent term to the BPT from the BVB (Eq. 1.10) in the Depth-Integrated Vorticity Balance (DIVB). However, extending the depth integral of the vorticity equation across the entire water column can recover a vortex stretching term due to the bottom vertical velocity. This bottom vertical velocity can, in turn, be derived from the varying bathymetry and the bottom horizontal circulation through the kinematic boundary condition ($w_{bot} = -u_{bot} \cdot \nabla H$; with w, u_{bot} being the vertical and horizontal velocity above the seafloor and H the varying bathymetry).

Using the Leibniz integration formula, it is possible to link both expressions of the vorticity balance considering a barotropic ocean (e.g. Zhang and Vallis, 2007; Waldman and Giordani, 2023):

$$\frac{d}{dx}\left(\int_{h(x)}^{\eta(x)} f(x,z)dz\right) = f(x,\eta(x)) \cdot \frac{d}{dx}\eta(x) - f(x,h(x)) \cdot \frac{d}{dx}h(x) + \left(\int_{h(x)}^{\eta(x)} \frac{\partial}{\partial x} f(x,z)dz\right) \tag{B.5}$$

Where η and h represent, respectively, the free surface and the topography. Therefore, the difference between applying the curl before or after the depth-integral is due to the varying vertical boundaries. Neglecting the horizontal variations of the free surface and combining the terms derived from the nonlinear advection of momentum: $\overline{(\mathbf{u}\cdot\nabla)\mathbf{u}} = \overline{\mathbf{u}\nabla\zeta} + \overline{\hat{\mathbf{k}}(\nabla_h w \times \partial_z \mathbf{u}_h)} - \overline{\zeta \partial_z w}$; the difference between the BVB and the DIVB is obtained subtracting the Eq. B.4 to Eq. 1.10:

$$-f w_b = \frac{1}{\rho_0} J(P_b, h) + k \times \left[(\mathbf{u}\cdot\nabla)\mathbf{u} + A_h \nabla^2 \mathbf{u}_h + A_v \partial_z^2 \mathbf{u}_h - \frac{\partial \mathbf{u}_h}{\partial t}\right]_b \cdot \nabla_h h \tag{B.6}$$

Assuming an idealised case with the geostrophic bottom flow, it is possible to establish that $BPT = -f w_b$ (Lu and Stammer, 2004; Spence et al., 2012). Therefore, any non-zero BPT can lead to vertical velocities through bottom vortex stretching. In more general cases, ageostrophic and viscous effects at the bottom influence this relationship (e.g. Le Bras et al., 2019). However, idealised flow scenarios have been constructed in which there is no need for viscous effects to permit a meridional flow (Salmon, 1992; Becker and Salmon, 1997; Griffiths and Veronis, 1997; Becker, 1999; Ford, 2000).

B.3 LVB Relative Error at Snapshot 1996-1998

In this section, it is displayed an example of the 5° filtered LVB relative error (Δ_{LVB}) averaged for the 1996-1998 period as a visual aid to understand the source of the decrease of LVB validity extension when reducing the averaged period.

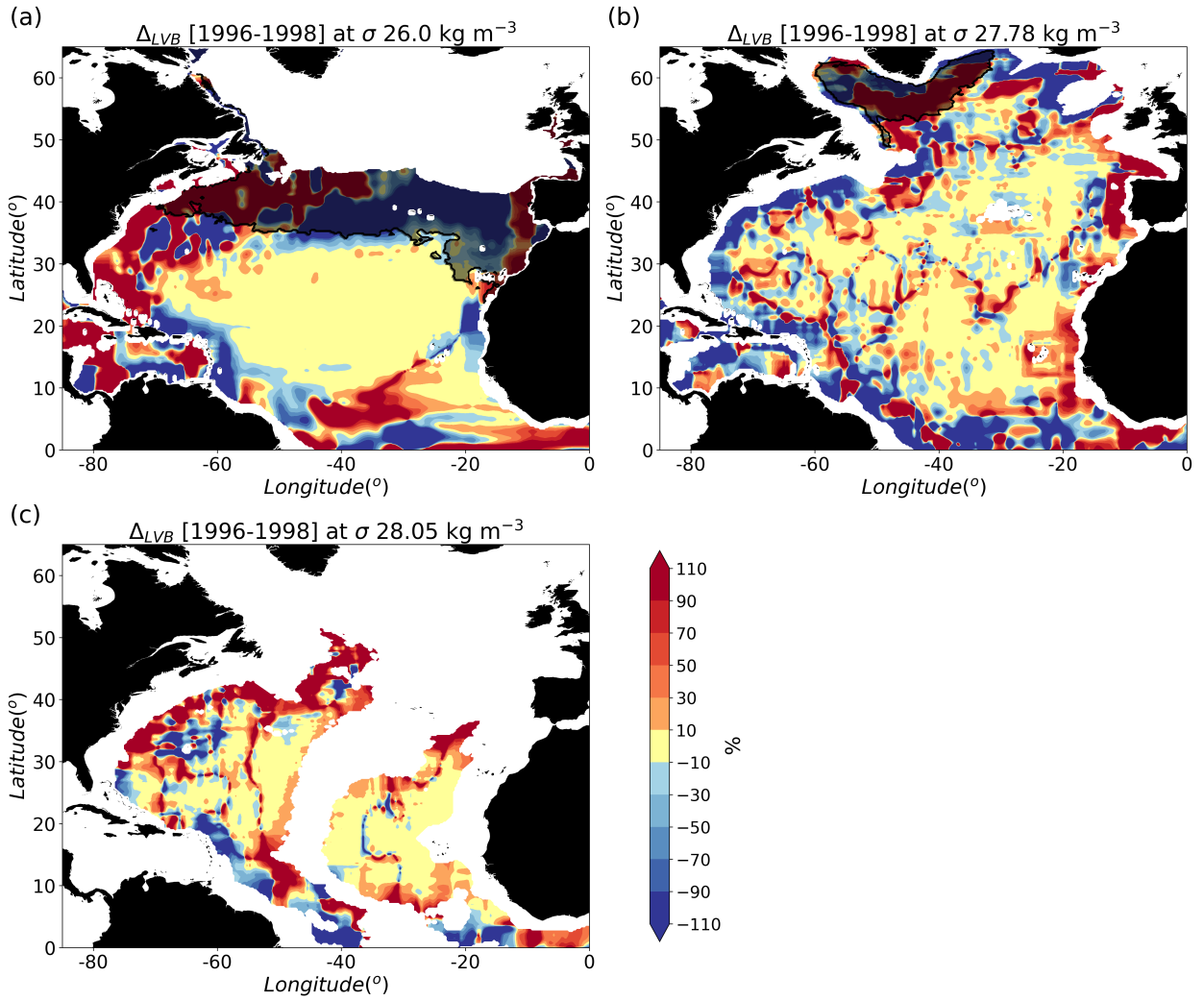

Figure B.4: 1996-1998 time-mean 5° filtered LVB relative error (Δ_{LVB}; Eq. 3.1) over (a) σ 26, (b) 27.78 and (c) 28.05 kg m^{-3}. The black translucent regions indicate the maximum mixed layer mask.

B.4 Ekman pumping vertical velocity localization discussion

Ekman pumping is derived from the divergence of Ekman transport through the Ekman layer. Considering Ekman transport as the only contributor to the ageostrophic circulation:

$$\mathbf{u}_h = \mathbf{u}_{hg} + \mathbf{u}_{hEk} \tag{B.7}$$

where $\mathbf{u}_h$, $\mathbf{u}_{hg}$ and $\mathbf{u}_{hEk}$ are the total, geostrophic and Ekman components of the horizontal velocity respectively. In a f-plane (as considered in the classical version), it is assumed that the geostrophic flow is non-divergent, so only the ageostrophic component of the horizontal flow can generate a vertical component:

$$\nabla_h \times \mathbf{u}_{hEk} + \partial_z w_{Ek} = 0 \tag{B.8}$$

Therefore, in the absence of a geostrophic component of the vertical circulation and under the assumption that the vertical velocity at the surface is 0, the ageostrophic component must also be 0 ($w_{Ek}(z=0)=0$) at the surface. Integrating over the Ekman layer thickness yields the Ekman pumping at the bottom of the Ekman layer (D_{Ek}):

$$w_{Ek}(z = D_{Ek}) = \nabla \times \left(\frac{\tau}{\rho_0 f}\right) \tag{B.9}$$

However, considering a β-plane, the geostrophic flow is divergent and generates a vertical velocity.

Assuming that the ageostrophic velocity follows the Ekman transport profile in the Ekman layer, the vertical velocity vanishes at the base of the Ekman layer (Pedlosky, 1996). The ageostrophic component of the flow is retrieved at the ocean surface integrating the Eq. B.8:

$$w_{Ek}(0) = -\nabla \times \left(\frac{\tau}{\rho_0 f}\right) \tag{B.10}$$

Therefore, as the total velocity ($w_{tot} = w_g + w_{ag}$) must be 0 at the surface:

$$w_g(0) = -w_{Ek}(0) = \nabla \times \left(\frac{\tau}{\rho_0 f}\right) \tag{B.11}$$

This is explained as the convergence of the wind-forced mass flux is compensated by a vertical flow into the ocean.

Both relations converge if we consider that the geostrophic flux divergence is zero in the Ekman layer, obtaining that $w_g(D_{Ek}) = w_{Ek}(D_{Ek})$. However, the divergence of the geostrophic flow is not negligible across the Ekman Layer. At the base of the Ekman layer, we find a total vertical velocity, which can be assumed geostrophic since all the ageostrophic contribution has vanished at the bottom of the Ekman layer:

$$w(D_{Ek}) = w_g(z = D_{Ek}) = w_g(z = 0) - \int_{D_{Ek}}^{0} \frac{\beta v_g}{f} dz' \tag{B.12}$$

We have checked the assumption that the divergence of the geostrophic flow is not negligible in the Ekman layer using the ratio between the absolute value of the Ekman pumping (Eq. B.10) and the divergence of the geostrophic flow (or w_g) for the 56-year average of the OCCITENS simulation (Figure B.5). In Figure B.6, where the ratio has been plotted for two depths of 50 and 100 m, the divergence of the geostrophic flow contributes to the vertical circulation with values above 10 (30)% of the Ekman pumping in the tropical and subtropical gyre regions at 50 (100) m. Note that these depths are often taken to define the base of the Ekman layer, although an increasing depth with latitude is more accurate.

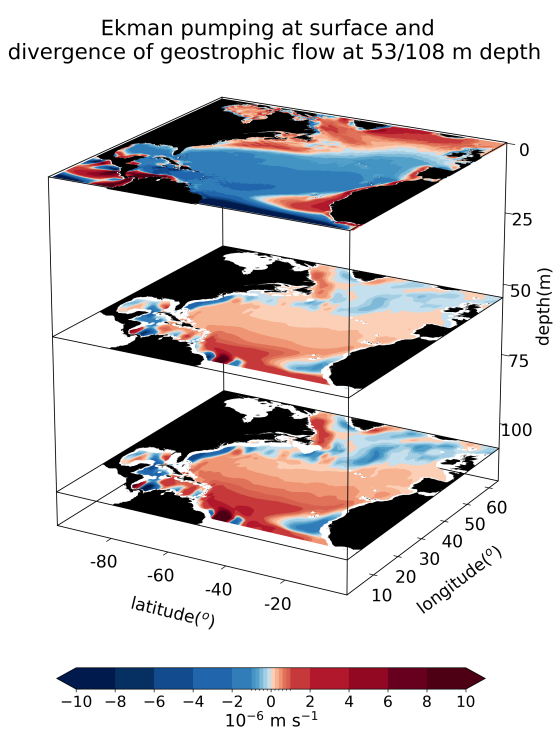

Figure B.5: Time mean Ekman pumping and the divergence of geostrophic flow over 53 and 108 m depth.

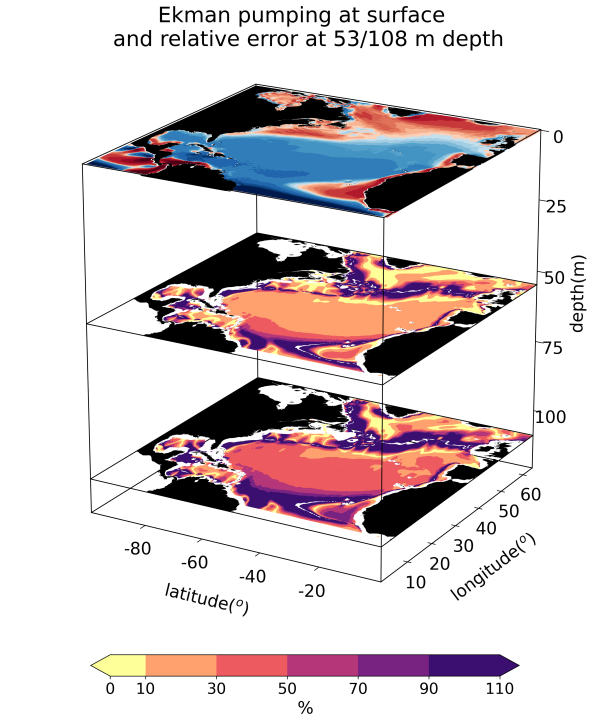

Figure B.6: Time mean Ekman pumping and relative error between divergence of geostrophic flow and Ekman pumping over 53 and 108 m depth.

B.5 Standard deviation of the total, geostrophic and ageostrophic component of the vertical velocity

In this section, we display the standard deviation of the total, geostrophic and ageostrophic components of the vertical velocity during the 1960-2015 period over σ 26 (Figure B.7), 27.78 (Figure B.8) and 28.05 kg m^{-3} (Figure B.9).

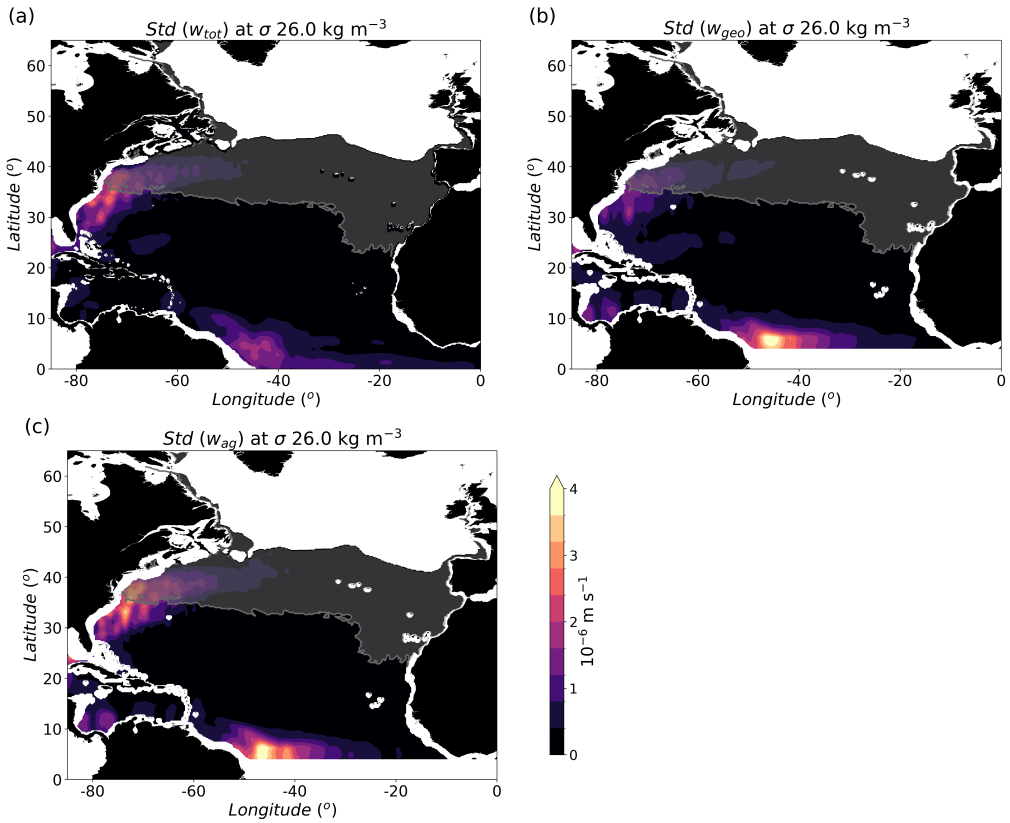

Figure B.7: Standard deviation during the 1960-2015 period for (a) total, (b) geostrophic and (c) ageostrophic vertical velocities in the OGCM simulation over σ 26 kg m^{-3}. The grey translucent regions indicate the maximum mixed layer mask.

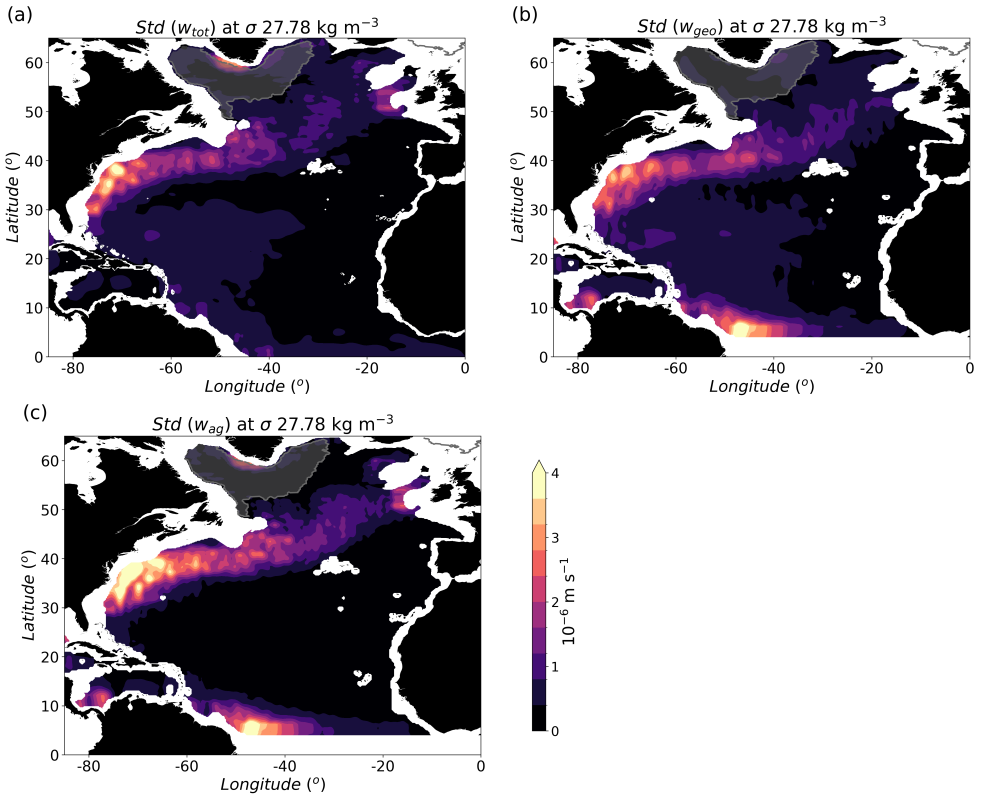

Figure B.8: Standard deviation during the 1960-2015 period for (a) total, (b) geostrophic and (c) ageostrophic vertical velocities in the OGCM simulation over σ 27.78 kg m^{-3}. The grey translucent regions indicate the maximum mixed layer mask.

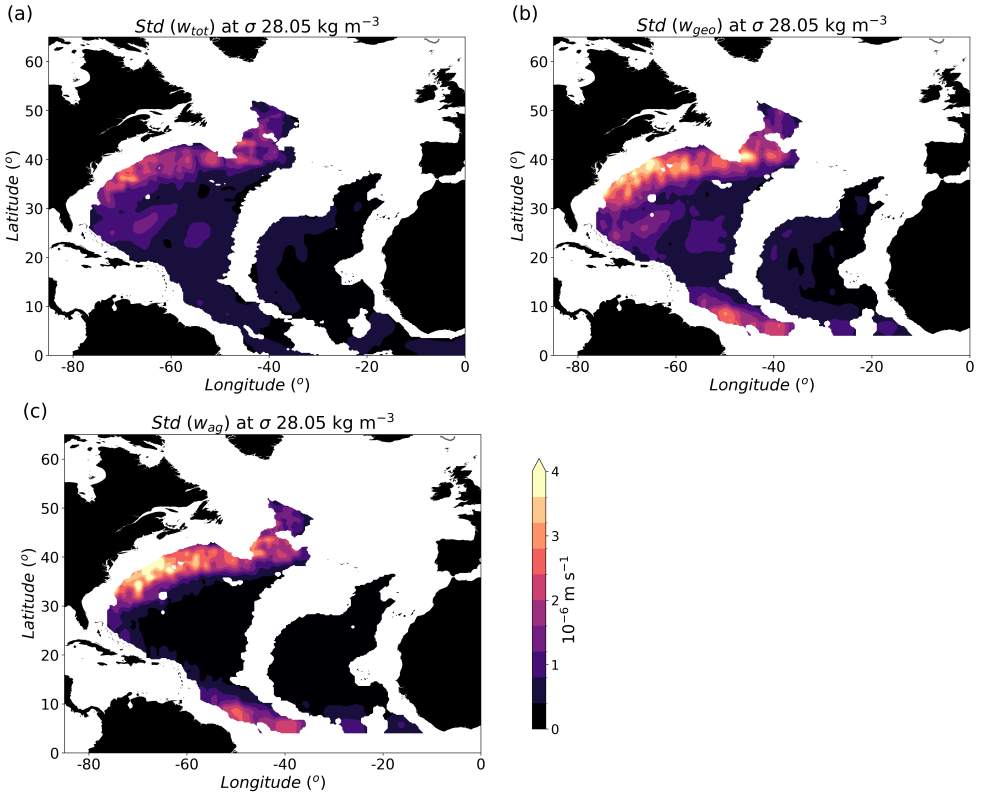

Figure B.9: Standard deviation during the 1960-2015 period for (a) total, (b) geostrophic and (c) ageostrophic vertical velocities in the OGCM simulation over σ 28.05 kg m^{-3}. The grey translucent regions indicate the maximum mixed layer mask.

B.6 Time-mean Vertical Velocities and Terms of the Linear Vorticity Balance in the OGCM Simulation at Global Scales

This section illustrates the vertical velocity field alongside the corresponding terms of the linear vorticity equation over the global ocean across various σ levels and meridional sections. The objective is to enhance the comprehension of the discussion in the main text by offering visual representations of the relevant variables and their links.

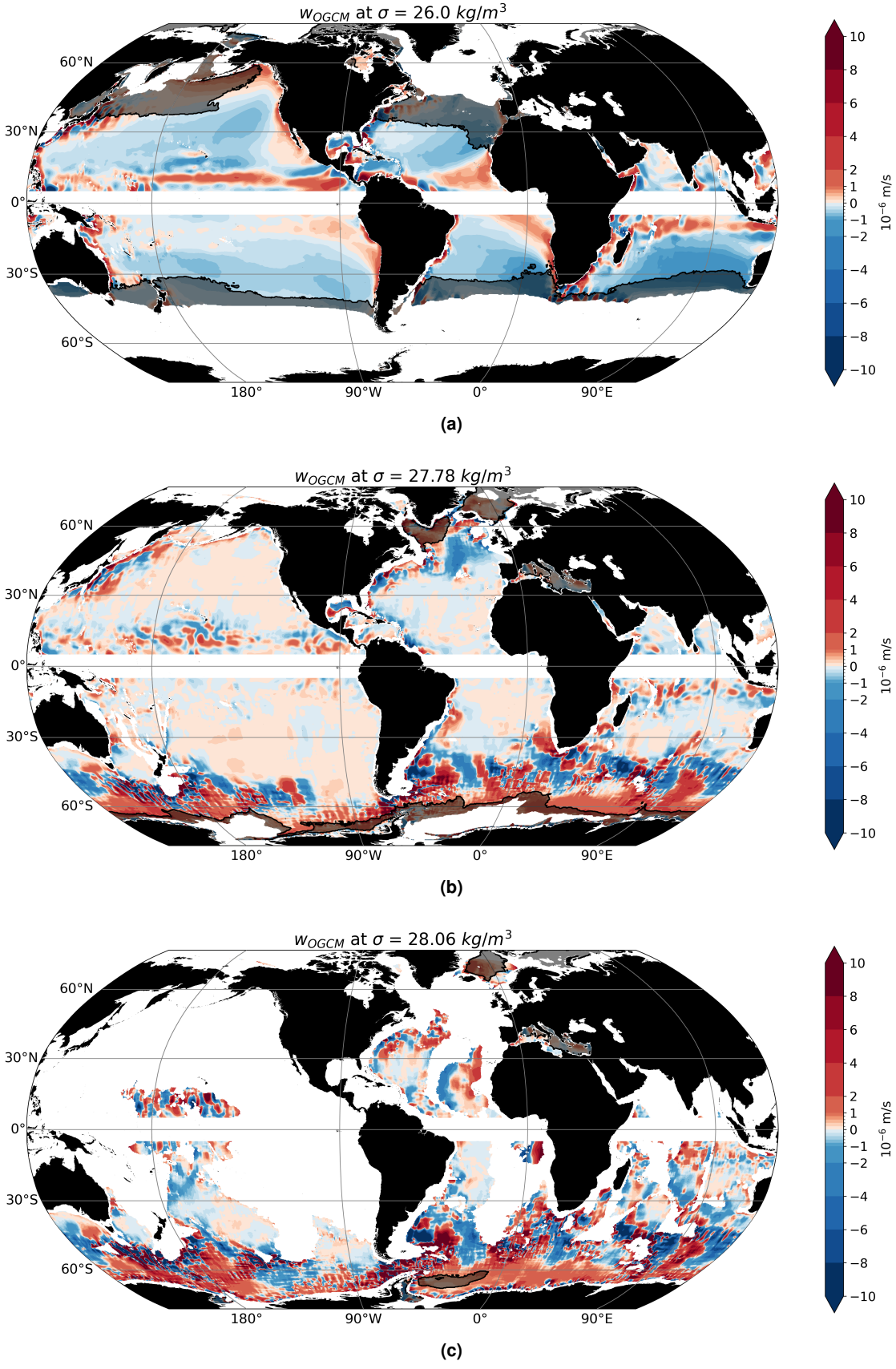

Figure B.10: 56-year time-mean vertical velocities in the OGCM simulation over σ 26 (a), 27.78 (b) and 28.05 (c) kg m^{-3}.

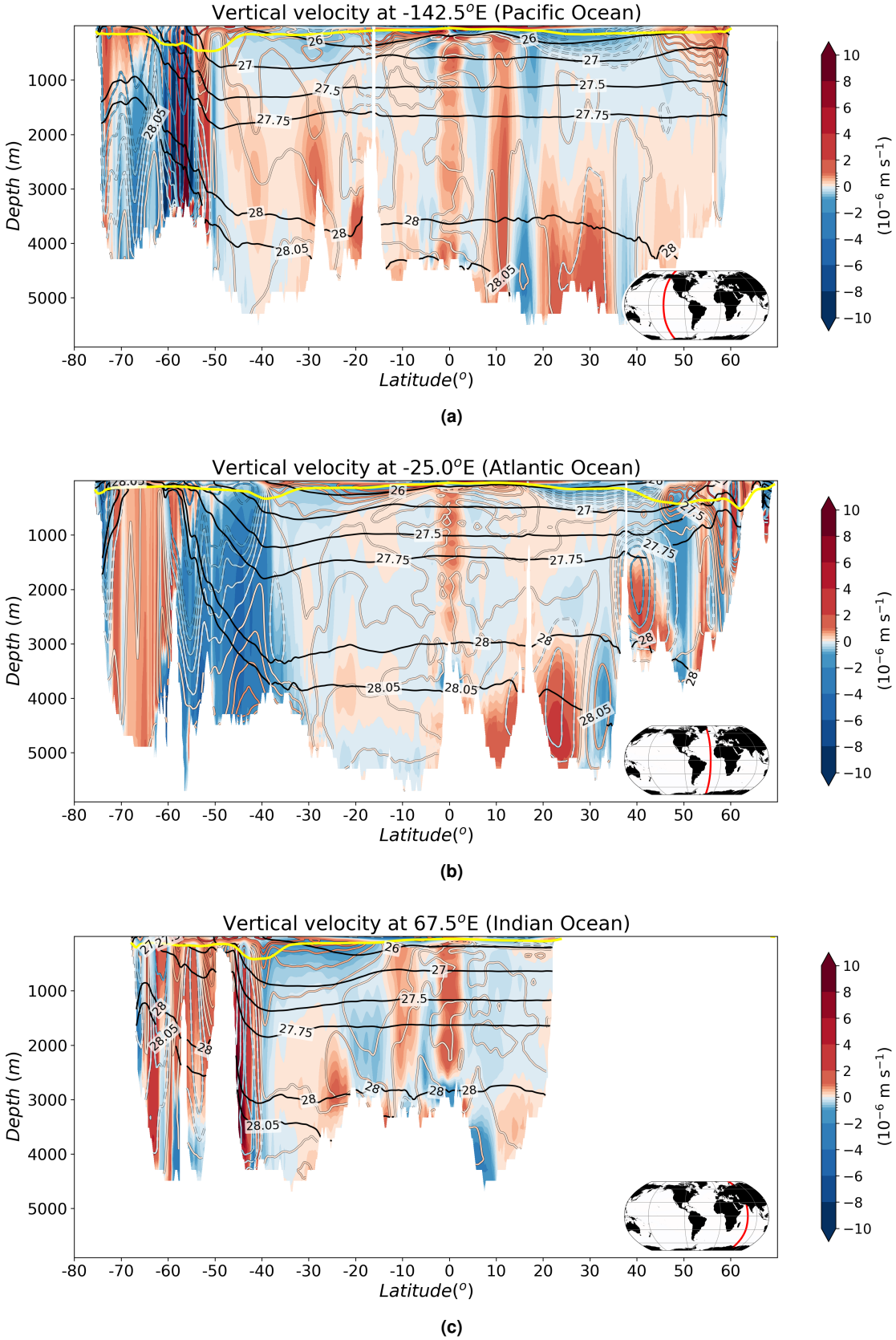

Figure B.11: 56-year time-mean vertical velocities in the OGCM simulation over 142.5°W (a), 25.5°W (b) and 67°E (c) meridional sections. Coloured contours represent the meridional flow (see colorbar multiply by 10^4), black contours illustrate the neutral density and yellow contours the maximum MLD.

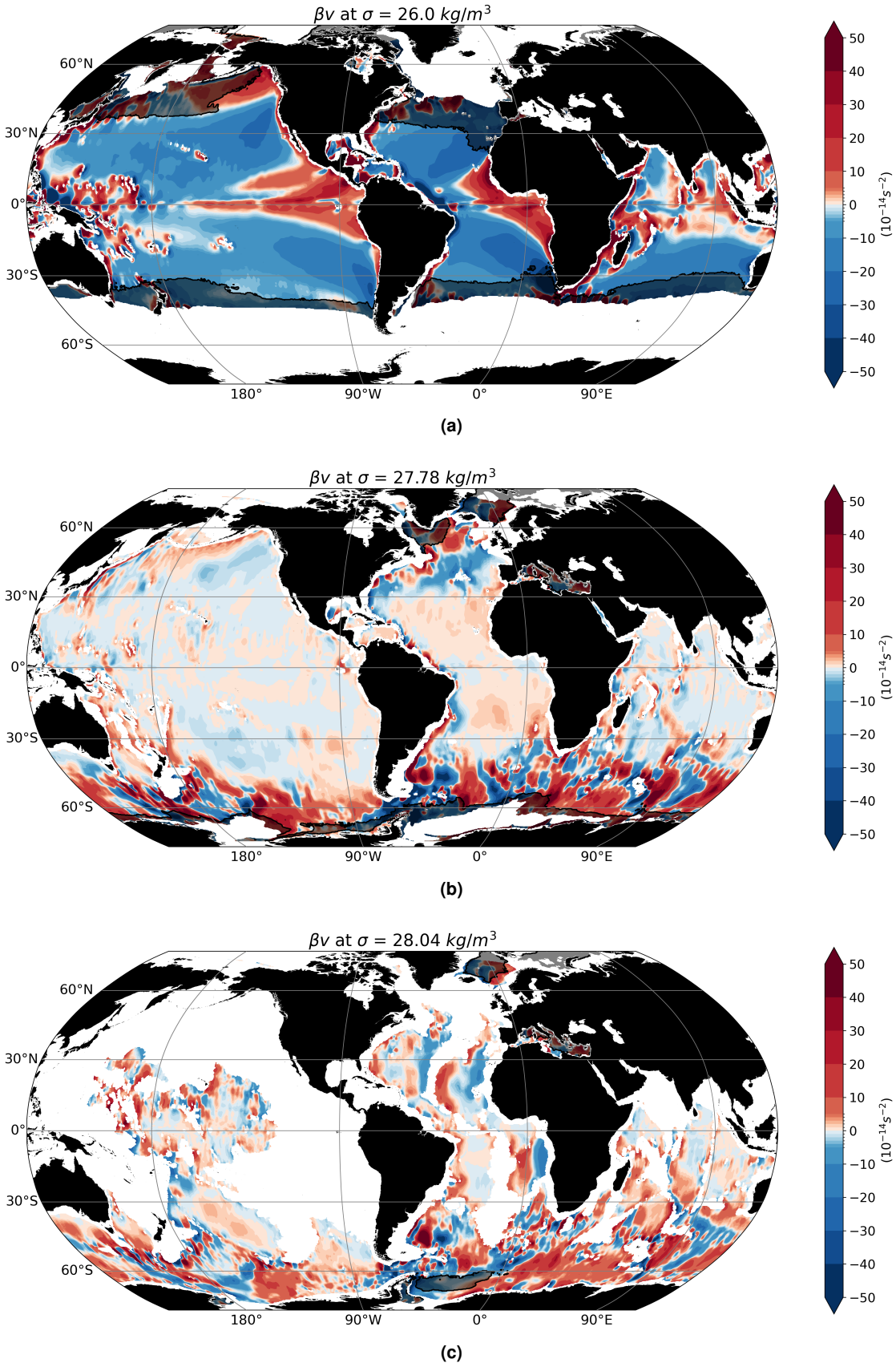

Figure B.12: βv term from Eq. 3.1 in the OGCM simulation over σ 26 (a), 27.78 (b) and 28.05 (c) kg m^{-3}.

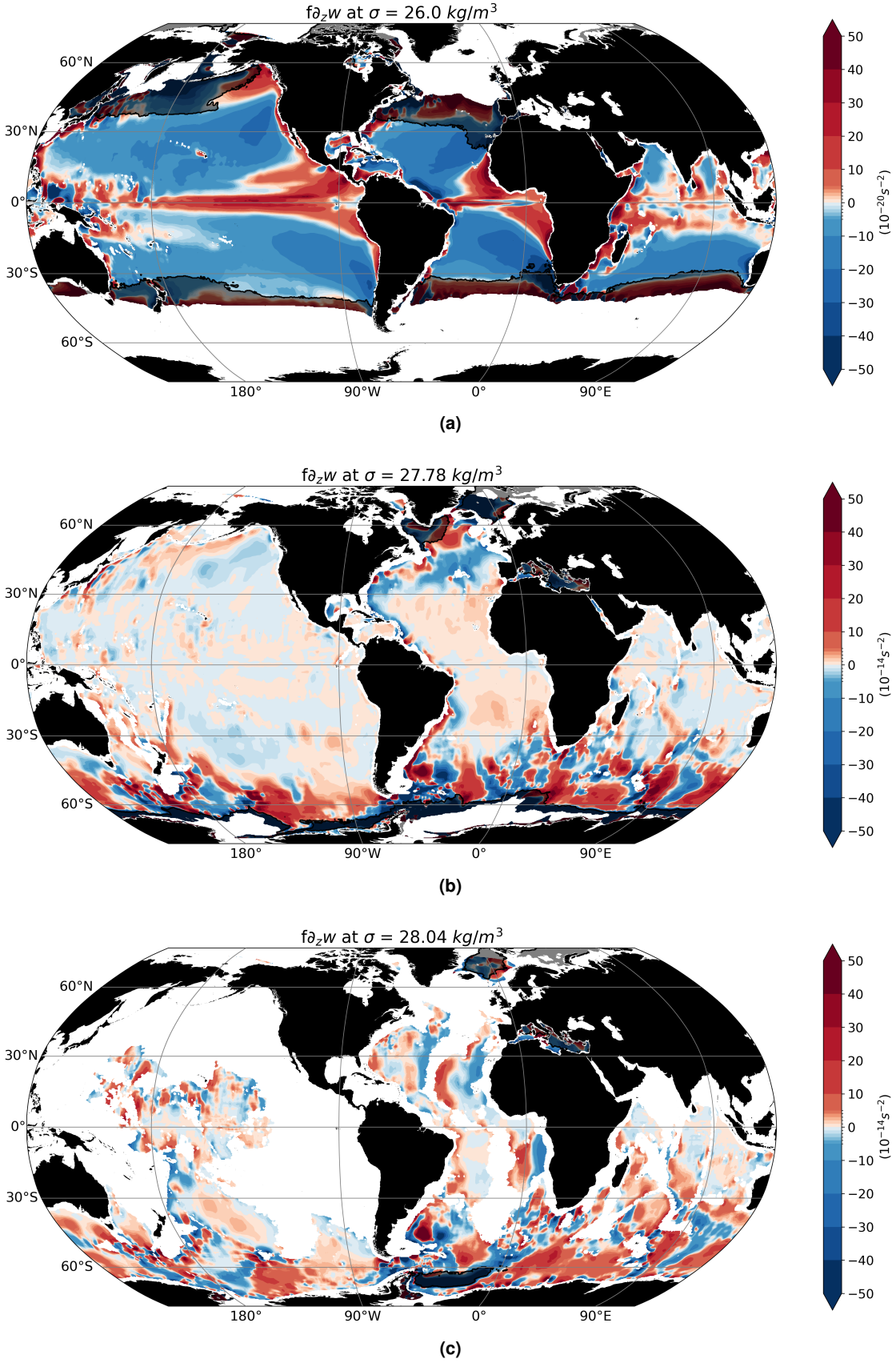

Figure B.13: $f\partial_z w$ term from Eq. 3.1 in the OGCM simulation over σ 26 (a), 27.78 (b) and 28.05 (c) kg m^{-3}.

B.7 Relative Error between NEMO OCCITENS simulation output and OLIV3

This section depicts the relative error between the 27-year mean NEMO OCCITENS simulation's output and OLIV3 at σ 26 kg m^{-3}.

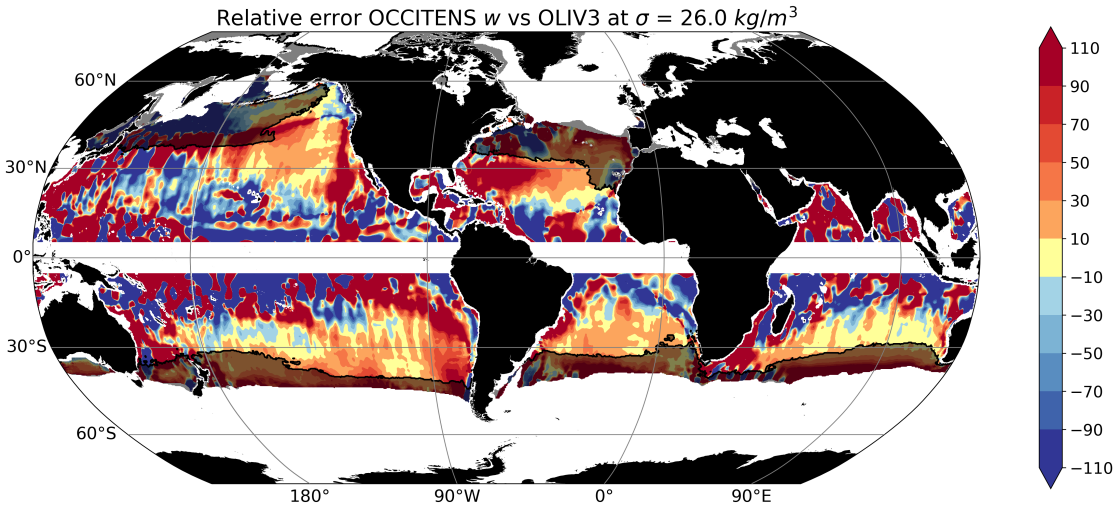

Figure B.14: 27-year time-mean relative error between the NEMO OCCITENS simulation w output and OLIV3 at σ 26 kg m^{-3}.

Bibliography

Adcroft A., Hill C., Campin J.-M., Marshall J., Heimbach P. (2004) Overview of the formulation and numerics of the mit gcm. In: Proceedings of the ECMWF seminar series on Numerical Methods, Recent developments in numerical methods for atmosphere and ocean modelling, pp. 139–149

Allen J., Smeed D., Nurser A., Zhang J., Rixen M. (2001) Diagnosis of vertical velocities with the qg omega equation: An examination of the errors due to sampling strategy. Deep Sea Research Part I: Oceanographic Research Papers 48(2):315–346, DOI: doi.org/10.1016/S0967-0637(00)00035-2

Anderson D. L., Gill A. E. (1975) Spin-up of a stratified ocean, with applications to upwelling. In: Deep Sea Research and Oceanographic Abstracts, Elsevier, vol 22, pp. 583–596, DOI: doi.org/10.1016/0011-7471(75)90046-7

Anderson D. L., Killworth P. D. (1977) Spin-up of a stratified ocean, with topography. Deep Sea Research 24(8):709–732, DOI: doi.org/10.1016/0146-6291(77)90495-7

Andres M., Kwon Y.-O., Yang J. (2011) Observations of the kuroshio's barotropic and baroclinic responses to basin-wide wind forcing. Journal of Geophysical Research: Oceans 116(C4), DOI: doi.org/10.1029/2010JC006863

Andres M., Yang J., Kwon Y.-O. (2012) Adjustment of a wind-driven two-layer system with mid-basin topography. Journal of Marine Research 70(6):851–882

Arístegui J., Barton E. D., Álvarez-Salgado X. A., Santos A. M. P., Figueiras F. G., Kifani S., Hernández-León S., Mason E., Machú E., Demarcq H. (2009) Sub-regional ecosystem variability in the canary current upwelling. Progress in Oceanography 83(1-4):33–48, DOI: doi.org/10.1016/j.pocean.2009.07.031

AVISO+ (2015) SSALTO/DUACS User Handbook, CLS-DOS-NT-06- 034, Issue 4.4, SALP-MU-P-EA-21065-CLS

Bachman S. D., Fox-Kemper B., Pearson B. (2017) A scale-aware subgrid model for quasi-geostrophic turbulence. Journal of Geophysical Research: Oceans 122(2):1529–1554, DOI: doi.org/10.1002/2016JC012265

Balmaseda M. A., Hernandez F., Storto A., Palmer M., Alves O., Shi L., Smith G. C., Toyoda T., Valdivieso M., Barnier B., et al. (2015) The ocean reanalyses intercomparison project (ora-ip). Journal of Operational Oceanography 8(sup1):s80–s97, DOI: doi.org/10.1080/1755876X.2015.1022329

Barceló-Llull B., Mason E., Capet A., Pascual A. (2016) Impact of vertical and horizontal advection on nutrient distribution in the southeast pacific. Ocean Science 12(4):1003–1011, DOI: doi.org/10.5194/os-12-1003-2016

Becker J. M. (1999) Effect of a western continental slope on the wind-driven circulation. Journal of physical oceanography 29(3):512–518, DOI: doi.org/10.1175/1520-0485(1999)029<0512:EOAWCS>2.0.CO;2

Becker J. M., Salmon R. (1997) Eddy formation on a continental slope. Journal of marine research 55(2):181–200

Bessières L., Leroux S., Brankart J.-M., Molines J.-M., Moine M.-P., Bouttier P.-A., Penduff T., Terray L., Barnier B., Sérazin G. (2017) Development of a probabilistic ocean modelling system based on nemo 3.5: application at eddying resolution. Geoscientific Model Development 10(3):1091–1106, DOI: doi.org/10.5194/gmd-10-1091-2017

Blumen W. (1978) Uniform potential vorticity flow: Part i. theory of wave interactions and two-dimensional turbulence. Journal of the Atmospheric Sciences 35(5):774–783, DOI: doi.org/10.1175/1520-0469(1978)035<0774:UPVFPI>2.0.CO;2

Bower A. S., Rossby T. (1989) Evidence of cross-frontal exchange processes in the gulf stream based on isopycnal rafos float data. Journal of Physical Oceanography 19(9):1177–1190, DOI: doi.org/10.1175/1520-0485(1989)019<1177:EOCFEP>2.0.CO;2

de Boyer Montégut C., Madec G., Fischer A. S., Lazar A., Iudicone D. (2004) Mixed layer depth over the global ocean: An examination of profile data and a profile-based climatology. Journal of Geophysical Research: Oceans 109(C12), DOI: doi.org/10.1029/2004JC002378

Bretherton F. P., Davis R. E., Fandry C. (1976) A technique for objective analysis and design of oceanographic experiments applied to mode-73. In: Deep Sea Research and Oceanographic Abstracts, Elsevier, vol 23, pp. 559–582, DOI: doi.org/10.1016/0011-7471(76)90001-2

Bryan F. O., Böning C. W., Holland W. R. (1995) On the midlatitude circulation in a high-resolution model of the north atlantic. Journal of physical oceanography 25(3):289–305, DOI: doi.org/10.1175/1520-0485(1995)025<0289:OTMCIA>2.0.CO;2

Bryan K., Cox M. D. (1972) The circulation of the world ocean: a numerical study. part i, a homogeneous model. Journal of Physical Oceanography 2(4):319–335, DOI: doi.org/10.1175/1520-0485(1972)002<0319:TCOTWO>2.0.CO;2

Bryden H. L. (1980) Geostrophic vorticity balance in midocean. Journal of Geophysical Research: Oceans 85(C5):2825–2828, DOI: doi.org/10.1029/JC085iC05p02825

Bubnov V. A. (1987) Vertical motions in the central equatorial pacific. Oceanologica Acta, Special issue DOI: archimer.ifremer.fr/doc/00267/37841/

Buongiorno Nardelli B. (2020) A multi-year time series of observation-based 3d horizontal and vertical quasi-geostrophic global ocean currents. Earth System Science Data 12(3):1711–1723, DOI: doi.org/10.5194/essd-12-1711-2020

Buongiorno Nardelli B., Mulet S., Iudicone D. (2018) Three-dimensional ageostrophic motion and water mass subduction in the southern ocean. Journal of Geophysical Research: Oceans 123(2):1533–1562, DOI: doi.org/10.1002/2017JC013316

Cabanes C., Grouazel A., von Schuckmann K., Hamon M., Turpin V., Coatanoan C., Guinehut S., Boone C., Ferry N., Reverdin G., et al. (2012) The cora dataset: validation and diagnostics of ocean temperature and salinity in situ measurements. Ocean Science Discussions 9(2):1273–1312, DOI: doi.org/10.5194/os-9-1-2013,2013.

Canuto V. (2015) Pv dynamics: The role of small-scale turbulence, submesoscales and mesoscales. Journal of Geophysical Research: Oceans 120(10):6971–6985, DOI: doi.org/10.1002/2015JC011043

Carton J. A., Chepurin G. A., Chen L. (2018) Soda3: A new ocean climate reanalysis. Journal of Climate 31(17):6967–6983, DOI: doi.org/10.1175/JCLI-D-18-0149.1

Carton J. A., Penny S. G., Kalnay E. (2019) Temperature and salinity variability in the soda3, ecco4r3, and oras5 ocean reanalyses, 1993–2015. Journal of Climate 32(8):2277–2293, DOI: doi.org/10.1175/JCLI-D-18-0605.1

Cessi P., Wolfe C. L. (2013) Adiabatic eastern boundary currents. Journal of physical oceanography 43(6):1127–1149, DOI: doi.org/10.1175/JPO-D-12-0211.1

Charney J. (1955) The generation of oceanic currents by wind. Journal of Marine Research DOI: https://elischolar.library.yale.edu/journal_of_marine_research/858

Chelton D. B., Schlax M. G., Samelson R. M., de Szoeke R. A. (2007) Global observations of large oceanic eddies. Geophysical Research Letters 34(15), DOI: doi.org/10.1029/2007GL030812

Christensen K. M., Gray A., Riser S. (2023) Global estimates of mesoscale vertical velocity near 1000 m from argo observations. Authorea Preprints DOI: 10.22541/essoar.168500356.69644187/v1

Comby C., Barrillon S., Fuda J.-L., Doglioli A. M., Tzortzis R., Grégori G., Thyssen M., Petrenko A. A. (2022) Measuring vertical velocities with adcps in low-energy ocean. Journal of Atmospheric and Oceanic Technology 39(11):1669–1684, DOI: doi.org/10.1175/JTECH-D-21-0180.1

Cortés-Morales D., Lazar A. (submitted) Vertical velocity 3d estimates from the linear vorticity balance in the north atlantic ocean. Journal of Physical oceanography

Davis R., Regier L., Dufour J., Webb D. (1992) The autonomous lagrangian circulation explorer (alace). Journal of atmospheric and oceanic technology 9(3):264–285, DOI: doi.org/10.1175/1520-0426(1992)009<0264:TALCE>2.0.CO;2

Davis R. E. (1991) Observing the general circulation with floats. Deep Sea Research Part A Oceanographic Research Papers 38:S531–S571, DOI: doi.org/10.1016/S0198-0149(12)80023-9

Dee D. P., Uppala S. M., Simmons A. J., Berrisford P., Poli P., Kobayashi S., Andrae U., Balmaseda M., Balsamo G., Bauer d. P., et al. (2011) The era-interim reanalysis: Configuration and performance of the data assimilation system. Quarterly Journal of the royal meteorological society 137(656):553–597, DOI: doi.org/10.1002/qj.828

DeVries T., Holzer M., Primeau F. (2017) Recent increase in oceanic carbon uptake driven by weaker upper-ocean overturning. Nature 542(7640):215–218, DOI: doi.org/10.1038/nature21068

Dickey T. D. (1991) The emergence of concurrent high-resolution physical and bio-optical measurements in the upper ocean and their applications. Reviews of Geophysics 29(3):383–413, DOI: doi.org/10.1029/91RG00578

Drake H. F., Ferrari R., Callies J. (2020) Abyssal circulation driven by near-boundary mixing: Water mass transformations and interior stratification. Journal of Physical Oceanography 50(8):2203–2226, DOI: doi.org/10.1175/JPO-D-19-0313.1

Droghei R., Buongiorno Nardelli B., Santoleri R. (2018) A new global sea surface salinity and density dataset from multivariate observations (1993–2016). Frontiers in Marine Science 5:84, DOI: doi.org/10.3389/fmars.2018.00084

Dussin R., Barnier B., Brodeau L., Molines J. M. (2016) Drakkar forcing set dfs5. MyOcean Report DOI: FR-330-715-368-00032-IFR_DRAKKAR_DFS5.2

D'Asaro E. A., Lien R.-C., Henyey F. (2007) High-frequency internal waves on the oregon continental shelf. Journal of physical oceanography 37(7):1956–1967, DOI: doi.org/10.1175/JPO3096.1

D'Asaro E. A., Shcherbina A. Y., Klymak J. M., Molemaker J., Novelli G., Guigand C. M., Haza A. C., Haus B. K., Ryan E. H., Jacobs G. A., et al. (2018) Ocean convergence and the dispersion of flotsam. Proceedings of the National Academy of Sciences 115(6):1162–1167, DOI: doi.org/10.1073/pnas.1718453115

Ekman V. W. (1905) On the influence of the earth's rotation on ocean-currents DOI: jhir.library.jhu.edu/handle/1774.2/33989

Elmoussaoui A., Arhan M., Tréguier A.-M. (2005) Model-inferred upper ocean circulation in the eastern tropics of the north atlantic. Deep Sea Research Part I: Oceanographic Research Papers 52(7):1093–1120, DOI: doi.org/10.1016/j.dsr.2005.01.010

Fernandes M., Lázaro C., Santos A., Oliveira P. (2005) Oceanographic characterization of the cape verde region using multisensor data. In: Envisat & ERS Symposium, vol 572

Fischer J., Leach H., Woods J. (1989) A synoptic map of isopycnic potential vorticity in the seasonal thermocline. Journal of physical oceanography 19(4):519–531, DOI: doi.org/10.1175/1520-0485(1989)019<0519:ASMOIP>2.0.CO;2

Ford R. (2000) A baroclinic western boundary current over a continental slope. Journal of marine research 58(3):327–373

Forget G., Ponte R. M. (2015) The partition of regional sea level variability. Progress in Oceanography 137:173–195, DOI: doi.org/10.1016/j.pocean.2015.06.002

Forget G., Campin J.-M., Heimbach P., Hill C., Ponte R., Wunsch C. (2015) Ecco version 4: An integrated framework for non-linear inverse modeling and global ocean state estimation. Geoscientific Model Development 8(10):3071–3104, DOI: doi.org/10.5194/gmd-8-3071-2015

Freeland H. J. (2013) Vertical velocity estimates in the north pacific using argo floats. Deep Sea Research Part II: Topical Studies in Oceanography 85:75–80, DOI: doi.org/10.1016/j.dsr2.2012.07.019

Freilich M., Mahadevan A. (2019) Decomposition of vertical velocity for nutrient transport in the upper ocean. Journal of Physical Oceanography 49(6):1561–1575, DOI: doi.org/10.1175/JPO-D-19-0002.1

Freilich M., Mahadevan A. (2021) Coherent pathways for subduction from the surface mixed layer at ocean fronts. Journal of Geophysical Research: Oceans 126(5), DOI: doi.org/10.1029/2020JC017042

Fukumori I., Heimbach P., Ponte R. M., Wunsch C. (2018) A dynamically consistent, multivariable ocean climatology. Bulletin of the American Meteorological Society 99(10):2107–2128, DOI: doi.org/10.1175/BAMS-D-17-0213.1

Garabato A. C. N., Leach H., Allen J. T., Pollard R. T., Strass V. H. (2001) Mesoscale subduction at the antarctic polar front driven by baroclinic instability. Journal of Physical Oceanography 31(8):2087–2107, DOI: doi.org/10.1175/1520-0485(2001)031<2087:MSATAP>2.0.CO;2

Garcia-Jove M., Mourre B., Zarokanellos N. D., Lermusiaux P. F., Rudnick D. L., Tintoré J. (2022) Frontal dynamics in the alboran sea: 2. processes for vertical velocities development. Journal of Geophysical Research: Oceans 127(3), DOI: doi.org/10.1029/2021JC017428

Garrett C., MacCready P., Rhines P. (1993) Boundary mixing and arrested ekman layers: Rotating stratified flow near a sloping boundary. Annual Review of Fluid Mechanics 25(1):291–323, DOI: doi.org/10.1146/annurev.fl.25.010193.001451

Giglio D., Roemmich D., Cornuelle B. (2013) Understanding the annual cycle in global steric height. Geophysical research letters 40(16):4349–4354, DOI: doi.org/10.1002/grl.50774

Gill A. E. (1982) Atmosphere-ocean dynamics. Academic press

Giordani H., Prieur L., Caniaux G. (2006) Advanced insights into sources of vertical velocity in the ocean. Ocean Dynamics 56(5):513–524, DOI: doi.org/10.1007/s10236-005-0050-1

Gomis D., Ruiz S., Pedder M. A. (2001) Diagnostic analysis of the 3d ageostrophic circulation from a multivariate spatial interpolation of ctd and adcp data. Deep Sea Research Part I: Oceanographic Research Papers 48(1):269–295, DOI: doi.org/10.1016/S0967-0637(00)00060-1

Gordon A. L. (1981) South atlantic thermocline ventilation. Deep Sea Research Part A Oceanographic Research Papers 28(11):1239–1264, DOI: doi.org/10.1016/0198-0149(81)90033-9

Gray A. R., Riser S. C. (2014) A global analysis of sverdrup balance using absolute geostrophic velocities from argo. Journal of Physical Oceanography 44(4):1213–1229, DOI: doi.org/10.1175/JPO-D-12-0206.1

Griffiths R. W., Veronis G. (1997) A laboratory study of the effects of a sloping side boundary on wind-driven circulation in a homogeneous ocean model. Journal of marine research 55(6):1103–1126

Guinehut S., Dhomps A.-L., Larnicol G., Le Traon P.-Y. (2012) High resolution 3-d temperature and salinity fields derived from in situ and satellite observations. Ocean Science 8(5):845–857, DOI: doi.org/10.5194/os-8-845-2012

Gula J., Molemaker M. J., McWilliams J. C. (2015) Gulf stream dynamics along the southeastern us seaboard. Journal of Physical Oceanography 45(3):690–715, DOI: doi.org/10.1175/JPO-D-14-0154.1

Halpern D., Freitag H. P. (1987) Vertical motion in the upper ocean of the equatorial eastern pacific. Oceanologica Acta, Special Issue DOI: archimer.ifremer.fr/doc/00267/37842/

Halpern D., Knox R. A., Luther D. S., Philander S. G. H. (1989) Estimates of equatorial upwelling between 140 and 110 w during 1984. Journal of Geophysical Research: Oceans 94(C6):8018–8020, DOI: doi.org/10.1029/JC094iC06p08018

Hamlington P. E., Van Roekel L. P., Fox-Kemper B., Julien K., Chini G. P. (2014) Langmuir–submesoscale interactions: Descriptive analysis of multiscale frontal spindown simulations. Journal of Physical Oceanography 44(9):2249–2272, DOI: doi.org/10.1175/JPO-D-13-0139.1

Hausmann U., Czaja A. (2012) The observed signature of mesoscale eddies in sea surface temperature and the associated heat transport. Deep Sea Research Part I: Oceanographic Research Papers 70:60–72, DOI: doi.org/10.1016/j.dsr.2012.08.005

Hautala S. L., Roemmich D. H., Schmilz Jr W. J. (1994) Is the north pacific in sverdrup balance along 24°n? Journal of Geophysical Research: Oceans 99(C8):16,041–16,052, DOI: doi.org/10.1029/94JC01084

Held I. M., Pierrehumbert R. T., Garner S. T., Swanson K. L. (1995) Surface quasi-geostrophic dynamics. Journal of Fluid Mechanics 282:1–20, DOI: doi.org/10.1017/S0022112095000012

Hellerman S., Rosenstein M. (1983) Normal monthly wind stress over the world ocean with error estimates. Journal of Physical Oceanography 13(7):1093–1104, DOI: doi.org/10.1175/1520-0485(1983)013<1093:NMWSOT>2.0.CO;2

Heuzé C., Purkey S. G., Johnson G. C. (2022) It is high time we monitor the deep ocean. Environmental Research Letters 17(12):121,002, DOI: doi.org/10.1088/1748-9326/aca622

Holland W. R. (1967) On the wind-driven circulation in an ocean with bottom topography. Tellus 19(4):582–600, DOI: doi.org/10.3402/tellusa.v19i4.9825

Holland W. R. (1973) Baroclinic and topographic influences on the transport in western boundary currents. Geophysical Fluid Dynamics 4(3):187–210, DOI: doi.org/10.1080/03091927208236095

Holton J. R. (1973) An introduction to dynamic meteorology. American Journal of Physics 41(5):752–754, DOI: doi.org/10.1119/1.1987371

Hoskins B., Draghici I., Davies H. (1978) A new look at the ω-equation. Quarterly Journal of the Royal Meteorological Society 104(439):31–38, DOI: doi.org/10.1002/qj.49710443903

Hoskins B. J., Draghici I. (1977) The forcing of ageostrophic motion according to the semi-geostrophic equations and in an isentropic coordinate model. Journal of Atmospheric Sciences 34(12):1859–1867, DOI: doi.org/10.1175/1520-0469(1977)034<1859:TFOAMA>2.0.CO;2

Huang R. X., Russell S. (1994) Ventilation of the subtropical north pacific. Journal of Physical Oceanography 24(12):2589–2605, DOI: doi.org/10.1175/1520-0485(1994)024<2589:VOTSNP>2.0.CO;2

Hughes C. W. (2000) A theoretical reason to expect inviscid western boundary currents in realistic oceans. Ocean Modelling 2(1-2):73–83, DOI: doi.org/10.1016/S1463-5003(00)00011-1

Hughes C. W., De Cuevas B. A. (2001) Why western boundary currents in realistic oceans are inviscid: A link between form stress and bottom pressure torques. Journal of Physical Oceanography 31(10):2871–2885, DOI: doi.org/10.1175/1520-0485(2001)031<2871:WWBCIR>2.0.CO;2

Ingleby B., Huddleston M. (2007) Quality control of ocean temperature and salinity profileshistorical and real-time data. Journal of Marine Systems 65(1-4):158–175, DOI: doi.org/10.1016/j.jmarsys.2005.11.019

Iudicone D., Rodgers K. B., Stendardo I., Aumont O., Madec G., Bopp L., Mangoni O., Ribera d'Alcala' M. (2011) Water masses as a unifying framework for understanding the southern ocean carbon cycle. Biogeosciences 8(5):1031–1052, DOI: doi.org/10.5194/bg-8-1031-2011

Iudicone D., Rodgers K. B., Plancherel Y., Aumont O., Ito T., Key R. M., Madec G., Ishii M. (2016) The formation of the ocean's anthropogenic carbon reservoir. Scientific Reports 6(1):35,473, DOI: doi.org/10.1038/srep35473

Jackett D. R., McDougall T. J., Feistel R., Wright D. G., Griffies S. M. (2006) Algorithms for density, potential temperature, conservative temperature, and the freezing temperature of seawater. Journal of Atmospheric and Oceanic Technology 23(12):1709–1728, DOI: doi.org/10.1175/JTECH1946.1

Jackson L., Hughes C. W., Williams R. G. (2006) Topographic control of basin and channel flows: The role of bottom pressure torques and friction. Journal of physical oceanography 36(9):1786–1805, DOI: doi.org/10.1175/JPO2936.1

Jean-Michel L., Eric G., Romain B.-B., Gilles G., Angélique M., Marie D., Clément B., Mathieu H., Olivier L. G., Charly R., et al. (2021) The copernicus global 1/12 oceanic and sea ice glorys12 reanalysis. Frontiers in Earth Science 9:698,876, DOI: doi.org/10.3389/feart.2021.698876

Jones M. S., Allen M., Guymer T., Saunders M. (1998) Correlations between altimetric sea surface height and radiometric sea surface temperature in the south atlantic. Journal of Geophysical Research: Oceans 103(C4):8073–8087, DOI: doi.org/10.1029/97JC02177

Kara A. B., Rochford P. A., Hurlburt H. E. (2000) An optimal definition for ocean mixed layer depth. Journal of Geophysical Research: Oceans 105(C7):16,803–16,821, DOI: doi.org/10.1029/2000JC900072

Kara A. B., Rochford P. A., Hurlburt H. E. (2003) Mixed layer depth variability over the global ocean. Journal of Geophysical Research: Oceans 108(C3), DOI: doi.org/10.1029/2000JC000736

Khatri H., Griffies S. M., Storer B. A., Buzzicotti M., Aluie H., Sonnewald M., Dussin R., Shao A. E. (2023) A scale-dependent analysis of the barotropic vorticity budget in a global ocean simulation. Journal of Advances in Modeling Earth Systems DOI: 10.22541/essoar.168394747.71837050/v1

Killworth P. D., Chelton D. B., de Szoeke R. A. (1997) The speed of observed and theoretical long extratropical planetary waves. Journal of Physical Oceanography 27(9):1946–1966, DOI: doi.org/10.1175/1520-0485(1997)027<1946:TSOOAT>2.0.CO;2

Klein B., Siedler G. (1989) On the origin of the azores current. Journal of Geophysical Research: Oceans 94(C5):6159–6168, DOI: doi.org/10.1029/JC094iC05p06159

Klein P., Lapeyre G. (2009) The oceanic vertical pump induced by mesoscale and submesoscale turbulence. Annual review of marine science 1:351–375, DOI: doi.org/10.1146/annurev.marine.010908.163704

Klein P., Isern-Fontanet J., Lapeyre G., Roullet G., Danioux E., Chapron B., Le Gentil S., Sasaki H. (2009) Diagnosis of vertical velocities in the upper ocean from high resolution sea surface height. Geophysical Research Letters 36(12), DOI: doi.org/10.1029/2009GL038359

Koelling J., Send U., Lankhorst M. (2020) Decadal strengthening of interior flow of north atlantic deep water observed by grace satellites. Journal of Geophysical Research: Oceans 125(11), DOI: doi.org/10.1029/2020JC016217

Kounta L., Capet X., Jouanno J., Kolodziejczyk N., Sow B., Gaye A. T. (2018) A model perspective on the dynamics of the shadow zone of the eastern tropical north atlantic–part 1: the poleward slope currents along west africa. Ocean Science 14(5):971–997, DOI: doi.org/10.5194/os-14-971-2018

LaCasce J. H., Mahadevan A. (2006) Estimating subsurface horizontal and vertical velocities from sea-surface temperature. Journal of Marine Research 64(5):695–721

Lapeyre G., Klein P. (2006) Dynamics of the upper oceanic layers in terms of surface quasigeostrophy theory. Journal of physical oceanography 36(2):165–176, DOI: doi.org/10.1175/JPO2840.1

Large W. G., Yeager S. G. (2004) Diurnal to decadal global forcing for ocean and sea-ice models: The data sets and flux climatologies. DOI: dx.doi.org/10.5065/D6KK98Q6

Lazar A., Inui T., Malanotte-Rizzoli P., Busalacchi A. J., Wang L., Murtugudde R. (2002) Seasonality of the ventilation of the tropical atlantic thermocline in an ocean general circulation model. Journal of Geophysical Research: Oceans 107(C8):18–1, DOI: doi.org/10.1029/2000JC000667

Le Bras I. A.-A., Sonnewald M., Toole J. M. (2019) A barotropic vorticity budget for the subtropical north atlantic based on observations. Journal of Physical Oceanography 49(11):2781–2797, DOI: doi.org/10.1175/JPO-D-19-0111.1

Le Corre M., Gula J., Tréguier A.-M. (2020) Barotropic vorticity balance of the north atlantic subpolar gyre in an eddy-resolving model. Ocean Science 16(2):451–468, DOI: doi.org/10.5194/os-16-451-2020

Le Quéré C., Takahashi T., Buitenhuis E. T., Rödenbeck C., Sutherland S. C. (2010) Impact of climate change and variability on the global oceanic sink of co2. Global Biogeochemical Cycles 24(4), DOI: doi.org/10.1029/2009GB003599

Leach H. (1987) The diagnosis of synoptic-scale vertical motion in the seasonal thermocline. Deep Sea Research Part A Oceanographic Research Papers 34(12):2005–2017, DOI: doi.org/10.1016/0198-0149(87)90095-1

Lellouche J.-M., Greiner E., Le Galloudec O., Garric G., Regnier C., Drevillon M., Benkiran M., Testut C.-E., Bourdalle-Badie R., Gasparin F., et al. (2018) Recent updates to the copernicus marine service global ocean monitoring and forecasting real-time 1/12 high-resolution system. Ocean Science 14(5):1093–1126, DOI: doi.org/10.5194/os-14-1093-2018

Levin L. A., Bett B. J., Gates A. R., Heimbach P., Howe B. M., Janssen F., McCurdy A., Ruhl H. A., Snelgrove P., Stocks K. I., et al. (2019) Global observing needs in the deep ocean. Frontiers in Marine Science 6:241, DOI: doi.org/10.3389/fmars.2019.00241

Levitus S. (1982) Climatological atlas of the world ocean, vol 13. US Department of Commerce, National Oceanic and Atmospheric Administration

Lévy M., Gavart M., Mémery L., Caniaux G., Paci A. (2005) A four-dimensional mesoscale map of the spring bloom in the northeast atlantic (pomme experiment): Results of a prognostic model. Journal of Geophysical Research: Oceans 110(C7), DOI: doi.org/10.1029/2004JC002588

Lévy M., Bopp L., Karleskind P., Resplandy L., Éthé C., Pinsard F. (2013) Physical pathways for carbon transfers between the surface mixed layer and the ocean interior. Global Biogeochemical Cycles 27(4):1001–1012, DOI: doi.org/10.1002/gbc.20092

Li Q., Fox-Kemper B., Breivik Ø., Webb A. (2017) Statistical models of global langmuir mixing. Ocean Modelling 113:95–114, DOI: doi.org/10.1016/j.ocemod.2017.03.016

Liang X., Spall M., Wunsch C. (2017) Global ocean vertical velocity from a dynamically consistent ocean state estimate. Journal of Geophysical Research: Oceans 122(10):8208–8224, DOI: doi.org/10.1002/2017JC012985

Locarnini R. A., Baranova O. K., Mishonov A. V., Boyer T. P., Reagan J. R., Dukhovskoy D., Seidov D., Garcia H. E., Bouchard C., Cross S., Paver C. R., Wang Z. (2023) World ocean atlas 2023, volume 1: Temperature. NOAA Atlas NESDIS

Lu Y., Stammer D. (2004) Vorticity balance in coarse-resolution global ocean simulations. Journal of physical oceanography 34(3):605–622, DOI: doi.org/10.1175/2504.1

Luyten J., Stommel H., Wunsch C. (1985) A diagnostic study of the northern atlantic subpolar gyre. Journal of physical oceanography 15(10):1344–1348, DOI: doi.org/10.1175/1520-0485(1985)015<1344:ADSOTN>2.0.CO;2

Madec G., Bourdallé-Badie R., Bouttier P.-A., Bricaud C., Bruciaferri D., Calvert D., Chanut J., Clementi E., Coward A., Delrosso D., et al. (2017) Nemo ocean engine DOI: 10.5281/zenodo.3248739

Madec G., Bourdallé-Badie R., Chanut J., Clementi E., Coward A., Éthé C., Iovino D., Lea D., Lévy C., Lovato T., et al. (2019) Nemo ocean engine, scientific notes of climate modelling center

Mahadevan A. (2016) The impact of submesoscale physics on primary productivity of plankton. Annual review of marine science 8:161–184, DOI: doi.org/10.1146/annurev-marine-010814-015912

Marshall J., Plumb R. (2007) Atmosphere, ocean and climate dynamic, an introduction

Marshall J., Speer K. (2012) Closure of the meridional overturning circulation through southern ocean upwelling. Nature geoscience 5(3):171–180, DOI: doi.org/10.1038/ngeo1391

Masina S., Storto A., Ferry N., Valdivieso M., Haines K., Balmaseda M., Zuo H., Drevillon M., Parent L. (2017) An ensemble of eddy-permitting global ocean reanalyses from the myocean project. Climate Dynamics 49:813–841, DOI: doi.org/10.1007/s00382-015-2728-5

Mason E., Pascual A., Gaube P., Ruiz S., Pelegrí J. L., Delepoulle A. (2017) Subregional characterization of mesoscale eddies across the b razil-m alvinas c onfluence. Journal of Geophysical Research: Oceans 122(4):3329–3357, DOI: doi.org/10.1002/2016JC012611

Mulet S., Rio M.-H., Mignot A., Guinehut S., Morrow R. (2012) A new estimate of the global 3d geostrophic ocean circulation based on satellite data and in-situ measurements. Deep Sea Research Part II: Topical Studies in Oceanography 77:70–81, DOI: doi.org/10.1016/j.dsr2.2012.04.012

Munk W. H. (1950) On the wind-driven ocean circulation. Journal of Atmospheric Sciences 7(2):80–93, DOI: doi.org/10.1175/1520-0469(1950)007<0080:OTWDOC>2.0.CO;2

Munk W. H. (1966) Abyssal recipes. In: Deep sea research and oceanographic abstracts, Elsevier, vol 13, pp. 707–730, DOI: doi.org/10.1016/0011-7471(66)90602-4

Nagai T., Tandon A., Rudnick D. L. (2006) Two-dimensional ageostrophic secondary circulation at ocean fronts due to vertical mixing and large-scale deformation. Journal of Geophysical Research: Oceans 111(C9), DOI: doi.org/10.1029/2005JC002964

Nardelli B. B., Santoleri R., Sparnocchia S. (2001) Small mesoscale features at a meandering upper-ocean front in the western ionian sea (mediterranean sea): Vertical motion and potential vorticity analysis. Journal of physical oceanography 31(8):2227–2250, DOI: doi.org/10.1175/1520-0485(2001)031<2227:SMFAAM>2.0.CO;2

Niiler P. P., Koblinsky C. J. (1985) A local time-dependent sverdrup balance in the eastern north pacific ocean. Science 229(4715):754–756, DOI: doi.org/10.1126/science.229.4715.754

Ollitrault M., De Verdière A. C. (2014) The ocean general circulation near 1000-m depth. Journal of Physical Oceanography 44(1):384–409, DOI: doi.org/10.1175/JPO-D-13-030.1

Ollitrault M., Rannou J.-P. (2013) Andro: An argo-based deep displacement dataset. Journal of Atmospheric and Oceanic Technology 30(4):759–788, DOI: doi.org/10.1175/JTECH-D-12-00073.1

Pascual A., Ruiz S., Buongiorno Nardelli B., Guinehut S., Iudicone D., Tintoré J. (2014) Net primary production in the gulf stream sustained by quasi-geostrophic vertical exchanges. Geophysical Research Letters 42(2):441–449, DOI: doi.org/10.1002/2014GL062569

Pedlosky J. (1979) Geophysical Fluid Dynamics. Springer New York

Pedlosky J. (1996) Ocean circulation theory. Springer Science & Business Media

Penduff T., Barnier B., Terray L., Bessières L., Sérazin G., Gregorio S., Brankart J., Moine M., Molines J., Brasseur P. (2014) Ensembles of eddying ocean simulations for climate. CLIVAR Exchanges, Special Issue on High Resolution Ocean Climate Modelling 19

Pollard R. T., Regier L. A. (1992) Vorticity and vertical circulation at an ocean front. Journal of Physical Oceanography 22(6):609–625, DOI: doi.org/10.1175/1520-0485(1992)022<0609:VAVCAA>2.0.CO;2

Polzin K., Toole J., Ledwell J., Schmitt R. (1997) Spatial variability of turbulent mixing in the abyssal ocean. Science 276(5309):93–96, DOI: doi.org/10.1126/science.276.5309.93

Ponte A. L., Klein P. (2013) Reconstruction of the upper ocean 3d dynamics from high-resolution sea surface height. Ocean Dynamics 63(7):777–791, DOI: doi.org/10.1007/s10236-013-0611-7

Poole R., Tomczak M. (1999) Optimum multiparameter analysis of the water mass structure in the atlantic ocean thermocline. Deep Sea Research Part I: Oceanographic Research Papers 46(11):1895–1921, DOI: doi.org/10.1016/S0967-0637(99)00025-4

Qiu B., Chen S., Klein P., Torres H., Wang J., Fu L.-L., Menemenlis D. (2020) Reconstructing upper-ocean vertical velocity field from sea surface height in the presence of unbalanced motion. Journal of Physical Oceanography 50(1):55–79, DOI: doi.org/10.1175/JPO-D-19-0172.1

Reagan J. R., Dukhovskoy D., Seidov D., Boyer T. P., Locarnini R. A., Baranova O. K., Mishonov A. V., Garcia H. E., Bouchard C., Cross S., Paver C. R., Wang Z. (2023) World ocean atlas 2023, volume 2: Salinity. NOAA Atlas NESDIS

Reul N., Chapron B., Lee T., Donlon C., Boutin J., Alory G. (2014) Sea surface salinity structure of the meandering gulf stream revealed by smos sensor. Geophysical Research Letters 41(9):3141–3148, DOI: doi.org/10.1002/2014GL059215

Reynolds R. W., Smith T. M., Liu C., Chelton D. B., Casey K. S., Schlax M. G. (2007) Daily high-resolution-blended analyses for sea surface temperature. Journal of climate 20(22):5473–5496, DOI: doi.org/10.1175/2007JCLI1824.1

Rhines P. B. (1986) Vorticity dynamics of the oceanic general circulation. Annual review of fluid mechanics 18(1):433–497, DOI: doi.org/10.1146/annurev.fl.18.010186.002245

Rio M.-H., Santoleri R., Bourdalle-Badie R., Griffa A., Piterbarg L., Taburet G. (2016) Improving the altimeter-derived surface currents using high-resolution sea surface temperature data: a feasability study based on model outputs. Journal of Atmospheric and Oceanic Technology 33(12):2769–2784, DOI: doi.org/10.1175/JTECH-D-16-0017.1

Robinson A., Stommel H. (1959) The oceanic thermocline and the associated thermohaline circulation 1. Tellus 11(3):295–308, DOI: doi.org/10.1111/j.2153-3490.1959.tb00035.x

Rödenbeck C., DeVries T., Hauck J., Le Quéré C., Keeling R. F. (2022) Data-based estimates of interannual sea–air co 2 flux variations 1957–2020 and their relation to environmental drivers. Biogeosciences 19(10):2627–2652, DOI: doi.org/10.5194/bg-19-2627-2022

Rodriguez J., Tintoré J., Allen J. T., Blanco J. M., Gomis D., Reul A., Ruiz J., Rodríguez V., Echevarría F., Jiménez-Gómez F. (2001) Mesoscale vertical motion and the size structure of phytoplankton in the ocean. Nature 410(6826):360–363, DOI: doi.org/10.1038/35066560

Roemmich D. (1983) The balance of geostrophic and ekman transports in the tropical atlantic ocean. Journal of Physical Oceanography 13(8):1534–1539, DOI: doi.org/10.1175/1520-0485(1983)013<1534:TBOGAE>2.0.CO;2

Roemmich D., Wunsch C. (1985) Two transatlantic sections: Meridional circulation and heat flux in the subtropical north atlantic ocean. Deep Sea Research Part A Oceanographic Research Papers 32(6):619–664, DOI: doi.org/10.1016/0198-0149(85)90070-6

Roemmich D., Boebel O., Desaubies Y., Freeland H., King B., LeTraon P.-Y., Molinari R., Owens B., Riser S., Send U., et al. (1999) Argo: The global array of profiling floats. CLIVAR Exchanges 13(4 (3)):4–5

Rossby T. (1996) The north atlantic current and surrounding waters: At the crossroads. Reviews of Geophysics 34(4):463–481, DOI: doi.org/10.1029/96RG02214

Rossby T. (2016) Visualizing and quantifying oceanic motion. Annual review of marine science 8:35–57, DOI: doi.org/10.1146/annurev-marine-122414-033849

Rudnick D. L. (1996) Intensive surveys of the azores front: 2. inferring the geostrophic and vertical velocity fields. Journal of Geophysical Research: Oceans 101(C7):16,291–16,303, DOI: doi.org/10.1029/96JC01144

Ruiz S., Pelegrí J. L., Emelianov M., Pascual A., Mason E. (2014) Geostrophic and ageostrophic circulation of a shallow anticyclonic eddy off cape bojador. Journal of Geophysical Research: Oceans 119(2):1257–1270, DOI: doi.org/10.1002/2013JC009169

Ruiz S., Claret M., Pascual A., Olita A., Troupin C., Capet A., Tovar-Sánchez A., Allen J., Poulain P.-M., Tintoré J., et al. (2019) Effects of oceanic mesoscale and submesoscale frontal processes on the vertical transport of phytoplankton. Journal of Geophysical Research: Oceans 124(8):5999–6014, DOI: doi.org/10.1029/2019JC015034

Salmon R. (1982) The shape of the main thermocline. Journal of Physical Oceanography 12(12):1458–1479, DOI: doi.org/10.1175/1520-0485(1982)012<1458:TSOTMT>2.0.CO;2

Salmon R. (1992) A two-layer gulf stream over a continental slope. Journal of marine research 50(3):341–365

Sanchez-Franks A., Frajka-Williams E., Moat B. I., Smeed D. A. (2021) A dynamically based method for estimating the atlantic meridional overturning circulation at 26° n from satellite altimetry. Ocean Science 17(5):1321–1340, DOI: doi.org/10.5194/os-17-1321-2021

Sanz E. P., Viúdez Á. (2005) Diagnosing mesoscale vertical motion from horizontal velocity and density data. Journal of physical oceanography 35(10):1744–1762, DOI: doi.org/10.1175/JPO2784.1

Schmitz Jr W. J., McCartney M. S. (1993) On the north atlantic circulation. Reviews of Geophysics 31(1):29–49, DOI: doi.org/10.1029/92RG02583

Schoonover J., Dewar W., Wienders N., Gula J., McWilliams J. C., Molemaker M. J., Bates S. C., Danabasoglu G., Yeager S. (2016) North atlantic barotropic vorticity balances in numerical models. Journal of Physical Oceanography 46(1):289–303, DOI: doi.org/10.1175/JPO-D-15-0133.1

Schott F. A., Stommel H. (1978) Beta spirals and absolute velocities in different oceans. Deep Sea Research 25(11):961–1010, DOI: doi.org/10.1016/0146-6291(78)90583-0

Schott F. A., Brandt P., Hamann M., Fischer J., Stramma L. (2002) On the boundary flow off brazil at 5–10 s and its connection to the interior tropical atlantic. Geophysical Research Letters 29(17):21–1, DOI: doi.org/10.1029/2002GL014786

Schott F. A., McCreary Jr J. P., Johnson G. C. (2004) Shallow overturning circulations of the tropical-subtropical oceans. Washington DC American Geophysical Union Geophysical Monograph Series 147:261–304, DOI: doi.org/10.1029/147GM15

Scott R. B., Arbic B. K., Chassignet E. P., Coward A. C., Maltrud M., Merryfield W. J., Srinivasan A., Varghese A. (2010) Total kinetic energy in four global eddying ocean circulation models and over 5000 current meter records. Ocean Modelling 32(3-4):157–169, DOI: doi.org/10.1016/j.ocemod.2010.01.005

Sévellec F., Garabato A. N., Brearley J., Sheen K. (2015) Vertical flow in the southern ocean estimated from individual moorings. Journal of Physical Oceanography 45(9):2209–2220, DOI: doi.org/10.1175/JPO-D-14-0065.1

Shchepetkin A. F., McWilliams J. C. (2005) The regional oceanic modeling system (roms): a split-explicit, free-surface, topography-following-coordinate oceanic model. Ocean modelling 9(4):347–404, DOI: doi.org/10.1016/j.ocemod.2004.08.002

Sheen K., Brearley J., Naveira Garabato A. C., Smeed D., Waterman S., Ledwell J. R., Meredith M. P., St. Laurent L., Thurnherr A. M., Toole J. M., et al. (2013) Rates and mechanisms of turbulent dissipation and mixing in the southern ocean: Results from the diapycnal and isopycnal mixing experiment in the southern ocean (dimes). Journal of Geophysical Research: Oceans 118(6):2774–2792, DOI: doi.org/10.1002/jgrc.20217

Siedler G., Griffies S. M., Gould J., Church J. A. (2013) Ocean circulation and climate: a 21st century perspective. Academic Press

Siegel D. A., Buesseler K. O., Behrenfeld M. J., Benitez-Nelson C. R., Boss E., Brzezinski M. A., Burd A., Carlson C. A., D'Asaro E. A., Doney S. C., et al. (2016) Prediction of the export and fate of global ocean net primary production: The exports science plan. Frontiers in Marine Science 3:22, DOI: doi.org/10.3389/fmars.2016.00022

Smith G. C., Allard R., Babin M., Bertino L., Chevallier M., Corlett G., Crout J., Davidson F., Delille B., Gille S. T., et al. (2019) Polar ocean observations: a critical gap in the observing system and its effect on environmental predictions from hours to a season. Frontiers in Marine Science 6:429, DOI: doi.org/10.3389/fmars.2019.00429

Smith R. D., Maltrud M. E., Bryan F. O., Hecht M. W. (2000) Numerical simulation of the north atlantic ocean at 1/10. Journal of Physical oceanography 30(7):1532–1561, DOI: doi.org/10.1175/1520-0485(2000)030<1532:NSOTNA>2.0.CO;2

Song T., Rossby T., Carter E. (1995) Lagrangian studies of fluid exchange between the gulf stream and surrounding waters. Journal of physical oceanography 25(1):46–63, DOI: doi.org/10.1175/1520-0485(1995)025<0046:LSOFEB>2.0.CO;2

Sonnewald M., Lguensat R. (2021) Revealing the impact of global heating on north atlantic circulation using transparent machine learning. Journal of Advances in Modeling Earth Systems 13(8), DOI: doi.org/10.1029/2021MS002496

Sonnewald M., Wunsch C., Heimbach P. (2019) Unsupervised learning reveals geography of global ocean dynamical regions. Earth and Space Science 6(5):784–794, DOI: doi.org/10.1029/2018EA000519

Spence P., Saenko O. A., Sijp W., England M. (2012) The role of bottom pressure torques on the interior pathways of north atlantic deep water. Journal of Physical Oceanography 42(1):110–125, DOI: doi.org/10.1175/2011JPO4584.1

Stammer D., Wunsch C., Giering R., Eckert C., Heimbach P., Marotzke J., Adcroft A., Hill C., Marshall J. (2003) Volume, heat, and freshwater transports of the global ocean circulation 1993–2000, estimated from a general circulation model constrained by world ocean circulation experiment (woce) data. Journal of Geophysical Research: Oceans 108(C1):7–1, DOI: doi.org/10.1029/2001JC001115

Stommel H. (1948) The westward intensification of wind-driven ocean currents. Eos, Transactions American Geophysical Union 29(2):202–206, DOI: doi.org/10.1029/TR029i002p00202

Stommel H., Arons A. (1959) On the abyssal circulation of the world oceani. stationary planetary flow patterns on a sphere. Deep Sea Research (1953) 6:140–154, DOI: doi.org/10.1016/0146-6313(59)90065-6

Stommel H., Schott F. (1977) The beta spiral and the determination of the absolute velocity field from hydrographic station data. Deep Sea Research 24(3):325–329, DOI: doi.org/10.1016/0146-6291(77)93000-4

Stramma L. (1984) Geostrophic transport in the warm water sphere of the eastern subtropical north atlantic. Journal of Marine Research 42(3):537–558, DOI: 10.1357/002224084788506022.

Stramma L., England M. (1999) On the water masses and mean circulation of the south atlantic ocean. Journal of Geophysical Research: Oceans 104(C9):20,863–20,883, DOI: doi.org/10.1029/1999JC900139

Stramma L., Rhein M., Brandt P., Dengler M., Böning C., Walter M. (2005) Upper ocean circulation in the western tropical atlantic in boreal fall 2000. Deep Sea Research Part I: Oceanographic Research Papers 52(2):221–240, DOI: doi.org/10.1016/j.dsr.2004.07.021

Styles A. F., Bell M. J., Marshall D. P., Storkey D. (2022) Spurious forces can dominate the vorticity budget of ocean gyres on the c-grid. Journal of Advances in Modeling Earth Systems 14(5), DOI: doi.org/10.1029/2021MS002884

Sverdrup H. U. (1947) Wind-driven currents in a baroclinic ocean; with application to the equatorial currents of the eastern pacific. Proceedings of the National Academy of Sciences 33(11):318–326, DOI: doi.org/10.1073/pnas.33.11.318

Tailleux R. (2023) On the determination of the 3d velocity field in terms of conserved variables in a compressible ocean. Fluids 8(3):94, DOI: doi.org/10.3390/fluids8030094

Tailleux R., McWilliams J. C. (2001) The effect of bottom pressure decoupling on the speed of extratropical, baroclinic rossby waves. Journal of physical oceanography 31(6):1461–1476, DOI: doi.org/10.1175/1520-0485(2001)031<1461:TEOBPD>2.0.CO;2

Thomas M. D., De Boer A. M., Johnson H. L., Stevens D. P. (2014) Spatial and temporal scales of sverdrup balance. Journal of Physical Oceanography 44(10):2644–2660, DOI: doi.org/10.1175/JPO-D-13-0192.1

Thompson B., Crease J., Gould J. (2001) The origins, development and conduct of woce. In: International Geophysics, vol 77, Elsevier, pp. 31–VIII, DOI: doi.org/10.1016/S0074-6142(01)80110-8

Tintoré J., Gomis D., Alonso S., Parrilla G. (1991) Mesoscale dynamics and vertical motion in the alboran sea. Journal of Physical Oceanography 21(6):811–823, DOI: doi.org/10.1175/1520-0485(1991)021<0811:MDAVMI>2.0.CO;2

Tomczak M., Godfrey J. S. (1994) The coriolis force, geostrophy, rossby waves and the westward intensification. In: Tomczak M., Godfrey J. S. (eds) Regional Oceanography, Pergamon, pp. 29–37

Tzortzis R., Doglioli A. M., Barrillon S., Petrenko A. A., d'Ovidio F., Izard L., Thyssen M., Pascual A., Barceló-Llull B., Cyr F., et al. (2021) Impact of moderately energetic fine-scale dynamics on the phytoplankton community structure in the western mediterranean sea. Biogeosciences 18(24):6455–6477, DOI: doi.org/10.5194/bg-18-6455-2021

Uchida T., Balwada D., Abernathey R., McKinley G., Smith S., Levy M. (2019) The contribution of submesoscale over mesoscale eddy iron transport in the open southern ocean. Journal of Advances in Modeling Earth Systems 11(12):3934–3958, DOI: doi.org/10.1029/2019MS001805

Vallis G. (2006) Atmospheric and Oceanic Fluid Dynamics: Fundamentals and Large-scale Circulation. Cambridge University Press

Verezemskaya P., Barnier B., Gulev S. K., Gladyshev S., Molines J.-M., Gladyshev V., Lellouche J.-M., Gavrikov A. (2021) Assessing eddying (1/12) ocean reanalysis glorys12 using the 14-yr instrumental record from 59.5 n section in the atlantic. Journal of Geophysical Research: Oceans 126(6), DOI: doi.org/10.1029/2020JC016317

Veronis G. (1966) Wind-driven ocean circulationpart 2. numerical solutions of the non-linear problem. In: Deep sea research and oceanographic abstracts, Elsevier, vol 13, pp. 31–55, DOI: doi.org/10.1016/0011-7471(66)90004-0

Vivier F., Kelly K. A., Thompson L. (1999) Contributions of wind forcing, waves, and surface heating to sea surface height observations in the pacific ocean. Journal of Geophysical Research: Oceans 104(C9):20,767–20,788, DOI: doi.org/10.1029/1999JC900096

Waldman R., Giordani H. (2023) Ocean barotropic vorticity balances: theory and application to numerical models. Journal of Advances in Modeling Earth Systems 15(4), DOI: doi.org/10.1029/2022MS003276

Wang J., Flierl G. R., LaCasce J. H., McClean J. L., Mahadevan A. (2013) Reconstructing the ocean's interior from surface data. Journal of Physical Oceanography 43(8):1611–1626, DOI: doi.org/10.1175/JPO-D-12-0204.1

Waterman S., Naveira Garabato A. C., Polzin K. L. (2013) Internal waves and turbulence in the antarctic circumpolar current. Journal of Physical Oceanography 43(2):259–282, DOI: doi.org/10.1175/JPO-D-11-0194.1

Weingartner T. J., Weisberg R. H. (1991) On the annual cycle of equatorial upwelling in the central atlantic ocean. Journal of Physical Oceanography 21(1):68–82, DOI: doi.org/10.1175/1520-0485(1991)021<0068:OTACOE>2.0.CO;2

Willebrand J., Philander S., Pacanowski R. (1980) The oceanic response to large-scale atmospheric disturbances. Journal of Physical Oceanography 10(3):411–429, DOI: doi.org/10.1175/1520-0485(1980)010<0411:TORTLS>2.0.CO;2

Williams R. G., Roussenov V., Smith D., Lozier M. S. (2014) Decadal evolution of ocean thermal anomalies in the north atlantic: The effects of ekman, overturning, and horizontal transport. Journal of Climate 27(2):698–719, DOI: doi.org/10.1175/JCLI-D-12-00234.1

Wilson E. A., Riser S. C., Campbell E. C., Wong A. P. (2019) Winter upper-ocean stability and ice–ocean feedbacks in the sea ice–covered southern ocean. Journal of Physical Oceanography 49(4):1099–1117, DOI: doi.org/10.1175/JPO-D-18-0184.1

Wong A. P., Wijffels S. E., Riser S. C., Pouliquen S., Hosoda S., Roemmich D., Gilson J., Johnson G. C., Martini K., Murphy D. J., et al. (2020) Argo data 1999–2019: Two million temperature-salinity profiles and subsurface velocity observations from a global array of profiling floats. Frontiers in Marine Science 7:700, DOI: doi.org/10.3389/fmars.2020.00700

Wunsch C. (1984) An estimate of the upwelling rate in the equatorial atlantic based on the distribution of bomb radiocarbon and quasi-geostrophic dynamics. Journal of Geophysical Research: Oceans 89(C5):7971–7978, DOI: doi.org/10.1029/JC089iC05p07971

Wunsch C. (2011) The decadal mean ocean circulation and sverdrup balance. Journal of Marine Research 69(2-3):417–434

Wunsch C. (2015) Modern observational physical oceanography: understanding the global ocean. Princeton University Press

Wunsch C., Roemmich D. (1985) Is the north atlantic in sverdrup balance? Journal of Physical Oceanography 15(12):1876–1880, DOI: doi.org/10.1175/1520-0485(1985)015<1876:ITNAIS>2.0.CO;2

Wyrtki K. (1961) The thermohaline circulation in relation to the general circulation in the oceans. Deep Sea Research (1953) 8(1):39–64, DOI: doi.org/10.1016/0146-6313(61)90014-4

Wyrtki K. (1981) An estimate of equatorial upwelling in the pacific. Journal of Physical Oceanography 11(9):1205–1214, DOI: doi.org/10.1175/1520-0485(1981)011<1205:AEOEUI>2.0.CO;2

Wyville Thomson C., Murray J. (1885a) The voyage of hms challenger 1873-1876. narrative vol. i. first part. chapter xii DOI: archimer.ifremer.fr/doc/00000/4763/

Wyville Thomson C., Murray J. (1885b) The voyage of hms challenger 1873-1876. narrative vol. i. first part. introduction DOI: archimer.ifremer.fr/doc/00000/4746/

Xie L., Hsieh W. W. (1995) The global distribution of wind-induced upwelling. Fisheries Oceanography 4(1):52–67, DOI: doi.org/10.1111/j.1365-2419.1995.tb00060.x

Yang P., Jing Z., Sun B., Wu L., Qiu B., Chang P., Ramachandran S. (2021) On the upper-ocean vertical eddy heat transport in the kuroshio extension. part i: Variability and dynamics. Journal of Physical Oceanography 51(1):229–246, DOI: doi.org/10.1175/JPO-D-20-0068.1

Yeager S. (2015) Topographic coupling of the atlantic overturning and gyre circulations. Journal of Physical Oceanography 45(5):1258–1284, DOI: doi.org/10.1175/JPO-D-14-0100.1

Yeager S. (2020) The abyssal origins of north atlantic decadal predictability. Climate Dynamics 55(7):2253–2271, DOI: doi.org/10.1007/s00382-020-05382-4

Zhang R., Vallis G. K. (2007) The role of bottom vortex stretching on the path of the north atlantic western boundary current and on the northern recirculation gyre. Journal of Physical Oceanography 37(8):2053–2080, DOI: doi.org/10.1175/JPO3102.1

Zuo H., Balmaseda M. A., Tietsche S., Mogensen K., Mayer M. (2019) The ecmwf operational ensemble reanalysis–analysis system for ocean and sea ice: a description of the system and assessment. Ocean science 15(3):779–808, DOI: doi.org/10.5194/os-15-779-2019